Coating, Degrading and Testing of Organic Polymer Devices - Reducing the route from Laboratory to Production scale devices

Dam, Henrik Friis; Krebs, Frederik C

Publication date:
2013

Document Version
Publisher's PDF, also known as Version of record

Technical University of Denmark

Coating, Degrading and Testing of Organic Polymer Devices - Reducing the route from Laboratory to Production scale devices

Henrik Friis Dam
Department of Energy Conversion and Storage

Ph.D. Thesis, August 2013

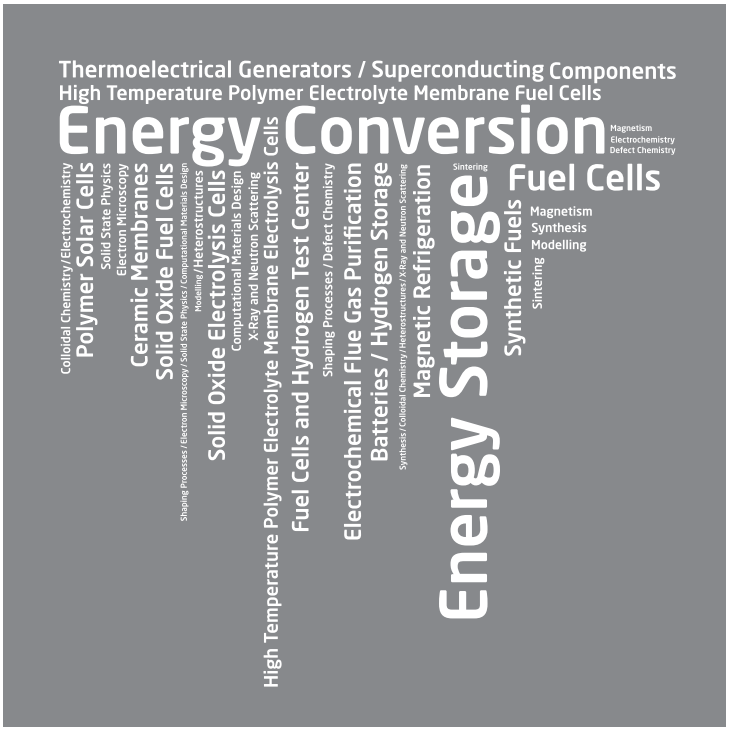

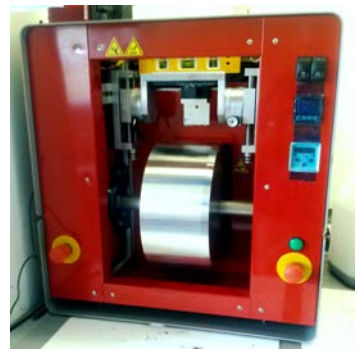

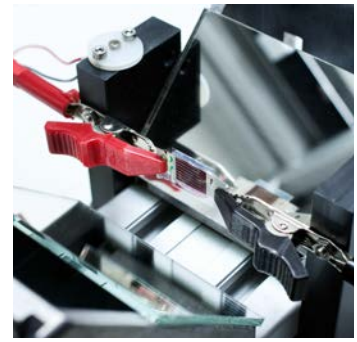

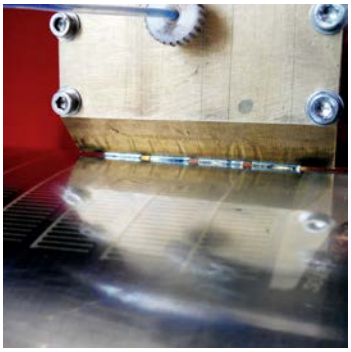

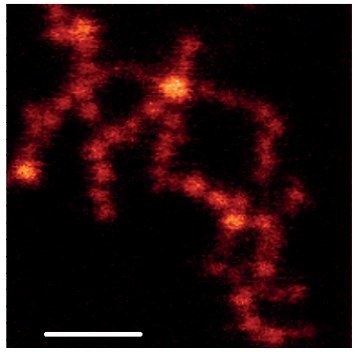

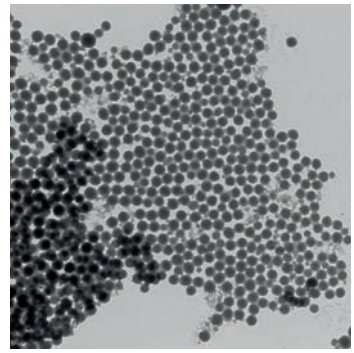

DTU Energy Conversion
Department of Energy Conversion and Storage

Coating, Degrading and Testing of Organic Polymer Devices

Reducing the route from Laboratory to Production scale devices

Ph.D. Thesis

Henrik Friis Dam

August 2013

Coating, Degrading and Testing of Organic Polymer Devices
Reducing the route from Laboratory to Production scale devices

August 2013

By
Henrik Friis Dam

Sponsorship: The project was financed through the Danish Strategic Research Council (2104-07-0022).

Academic advisor: Professor Frederik C. Krebs
Functional Organic Materials, Department of Energy Conversion and Storage

Cover photo: Images on the cover shows: Mini Roll Coater (MRC), as presented in chapter 2; Polymer tandem solar cell, as presented in chapter 5; Solar Cell Test Platform, as presented in chapter 8.

Published by: Department of Energy Conversion and Storage, Frederiksborgvej 399, Building 775, 4000 Roskilde, Denmark

ISBN: 978-87-92986-06-1

Preface

This thesis presents the highlights of my work carried out as a Ph.D. student at the Technical University of Denmark in the period from August 9, 2010 until August 1, 2013 in the Functional Organic Materials section in the Department of Energy Conversion and Storage. The work has been funded by the Danish Strategic Research Council (2104-07-0022) and completed under the supervision of Prof. Frederik C. Krebs.

During my three years as a Ph.D. student I have had the chance to work with some really great people and spend my time with a wide range of subjects as is also reflected by the range of the subjects within this thesis.

I want to thank my supervisor Frederik C. Krebs for the support of this work and for the possibility of working on so many different subjects for the last three years. For his countless ideas and suggestions, and for allowing me the freedom to be my own guide, through the topics and ideas that have been spawned.

A special thanks goes to David M. Tanenbaum, who while visiting as a guest researcher had a tremendous influence on my introduction to the field of organic materials and to Thomas Andersen, who has been a faithful lab partner during the last year through both ups and downs of making an uncountable number of solar cells. I would like to thank all the colleagues from the Functional Organic Materials section

For my stay abroad, which was completed in the Newcastle University Australia group of Paul Dastoor, to whom I owe gratitude for a wonderful time learning about a different approach to organic photovoltaics, and about the Australian culture and their warmth. A special mention goes to Ben Vaughan, Nicolas Nicolaidis, Natalie Holmes and Glenn Bryant.

Finally, a thanks to my friends and my family, for their support and acceptance of the very limited communication coming out of the thesis writing bubble.

Roskilde, August 2013

Abstract

Organic electronics is a vast and fast improving research area, with widespread uses proposed since the 1991 discovery of semiconducting polymers.

The premise of this thesis is based on finding more effective ways towards making cheap organic electronics and enabling a shorter path from the lab scale manufacturing of organic electronics to the large scale manufacturing, by downscaling some of the methods used in full size roll to roll (R2R) coating techniques into a lab scale setting. The enabling of similar techniques in both lab and production settings allows an optimization in the lab to be more directly transferred to the production environment, in contrast to the presently often used spin coating technique, for which optimizations of parameters are close to impossible to transfer to the larger scale operations.

Therefore a mini lab scale roll coating system was developed to enable lab scale fabrication of organic electronic devices, using the techniques of the larger R2R systems.

The lab scale slot-die roll coating technique reported, not only allow a faster route from lab scale to production scale, but also has the added advantage of a smaller material consumption. The solution volume, which for spin coating allowed making a single 1 cm^2 device, using the mini roll coater (MRC) enable the coating of a 100 cm^2 area, resulting in 60 1cm^2 devices with the present mask designs. With the relative expensive polymers, this translates into a large saving for performing the same amount of tests, not to mention the saved time in the preparation of the devices.

The lab scale roll coater system was used to manufacture a range of solar cells from different polymers, testing the influence of thicknesses, and post treatment processes. It was used to fabricate tandem solar cells with several thousand cells manufactured in the process for creating a recipe that would allow a wet processed layer on layer coating to function without having penetration and dissolution through the up to 12 separately printed layers.

Testing and analysis of a nanoparticle based method with water used as the transport agent for the active layer inks in solar cells was conducted, with a primary focus on testing the morphology of the nanoparticles. This type of ink could allow a more environmentally friendly production of solar cells, due to a lower use of organic solvents, while further allowing a new level of control for the active layer morphology.

Besides solar cells, the lab scale coating method was applied to both electrochromic devices and light emitting electrochemical cells. In these cases relatively large devices could be manufactured, without the use of protective atmospheres and without using evaporated electrode materials. The performance of the devices was lower than the state of the art, however this was to be expected due to the proof of concept manufacturing.

Finally a section has been included on the use of an open source electronic platform with a dedicated sourcemeter board developed to test solar cell devices without the need of expensive multipurpose source meters. This also shows the potential for stand-alone test, especially relevant for the various outdoor test conducted around the world and for the logging of various high-impact parameters, such as temperature, humidity and solar insolation.

Resume

Organisk elektronik er et stort og hurtigt udviklende forskningsområde, med mange forskellige anvendelser foreslået siden opdagelsen af halvledende polymerer i 1991.

Præmissen for denne afhandling har været at finde mere effektive måder at fremstille billig organisk elektronik og muliggøre en kortere vej fra laboratoriet til produktionsskala. Dette er forsøgt ved nedskalering af metoderne der bruges i fuldskala rulle til rulle (R2R) coating teknikken, til laboratoriebrug. Brugen af lignende teknikker i både laboratoriet og produktionen tillader optimeringer i laboratoriet bliver overført direkte til produktionen, i modsætning til den nuværende spin-coating teknik, hvor optimeringer er stort set umulige at overføre til stor skala produktion.

En mini laboratorieskala rulle coater (MRC) blev derfor udviklet, med henblik på fabrikation af laboratorieskala organisk elektronik ved brug af teknikkerne fra de større R2R maskiner.

Den rapporterede laboratorie slot-die rulle coating teknik tillader udover en hurtigere rute fra laboratoriet til produktion også et mindre materiale forbrug. Mængden af opløsning som er påkrævet ved brug af spin-coating til at fremstille en enkelt 1 cm^2 sol celle, rækker ved brug af mini rulle coateren (MRC) til at coate et 100 cm^2 areal, hvilket resulterer i 60 1cm^2 sol celler ved brug af the nuværende maskedesign. Med de relativt dyre polymerer betyder dette at der opnås en stor besparelse for udførelse af samme mængde forsøg, både i tid og penge ved fremstilling af sol cellerne.

Laboratorieskala rulle coateren er blevet brugt til at fremstille en række solceller ved brug af forskellige polymerer, hvor indflydelsen fra tykkelser og efterbehandlingsprocesser blev undersøgt. Den er blevet brugt til at fremstille tandem solceller, med fremstilling af flere tusind solceller fremstillet undervejs, for at finde en opskrift der tillod våd processering af lag på lag coatings uden at der opstod gennemtrængning eller opløsning af de optil 12 separat printede lag.

En test og analyse af en metode baseret på nanopartikler, med brug af vand som transportmiddel for aktivt lag blækket blev udført, med et primært fokus på test af morfologien af nanopartiklerne. Denne blæktype kan muliggøre en mere miljø venlig fremstilling af solceller, grundet et lavere forbrug af organiske solventer, mens et nyt niveau af kontrol med morfologien af det aktive lag kan opnås.

Udover solceller, er laboratorieskala coate metoden brugt til både at fremstille elektrokrome enheder og lys emitterende elektrokemiske celler. I begge tilfælde kunne relativt store enheder fremstilles, uden brug af en beskyttende atmosfære og uden brug af pådampede elektrode materialer. Enhedernes ydelse var noget lavere end førende eksempler, hvilket dog også var forventet grundet proof-of-concepts fremstillingen.

Endelig er der inkluderet en sektion om brugen af en open source elektronik platform med et dedikeret source meter printkort udviklet til test af solceller uden brugen af dyre multifunktions source metre. Dette afsnit viser også potentialet for selvdrevne tests, hvilket er specielt relevant for forskellige udendørs tests gennemført rundt omkring i verden, og for registrering af forskellige betydningsfulde parametre, såsom temperaturen, luftfugtigheden og sol indstrålingen på solcellen.

Content

1. Introduction

Organic electronics has been heralded as one of the largest revolutions within electronics[1], with its possibilities of being immensely cheaper and easier to fabricate than inorganic based types of electronics [2,3] and with a much lower environmental impact [4]. Furthermore, the research into making computers with transistors made of molecules and screens made with organic light emitting diodes has spanned a high level market, were the use of organics is a question of increasing the performance, more so than reducing the price. However the to date largest use of organic electronics is still accounted for by the low-cost high-volume RFID market [5]

One of the most sought after objects within organic electronics, are ways to manufacture them on a large scale. So far the success of large scale manufacturing has been limited. The up scaling has for the most part also shown to be considerably more difficult than what was initially expected.

1.1 Conjugated Polymers

The basis for most of the organic electronics is conjugated polymers. These are polymers where an overlap of one p_z-orbital with another across a sigma bond exists, illustrated in Figure 1.1. This overlap of two p_z-orbitals creates a π bond, which together with a sigma bond is what is referred to as double bonds. In other words the conjugated polymers have a portions of its electrons loosely bound to the polymer, via the π bonds . These electrons can therefore travel more freely in the polymer and are at the highest occupied energy state (HOMO) of the polymer chain from which they can be exited to the lowest unoccupied states (LUMO) level of the polymer.

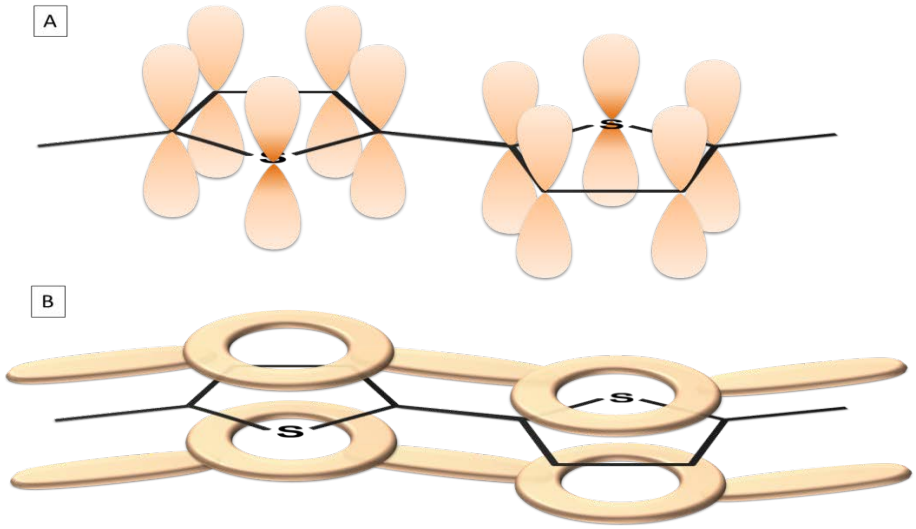

Figure 1.1: The conjugated electron system of a (poly)-thiophene system. A) The p_z orbitals contribute an electron giving rise to a π or anti-π bond between the orbitals. B) The π bond is a delocalization of the p_z orbitals in the system across the polymer.

The move of an electron from the HOMO level to the LUMO level is a change of the bonding state of the electron from a π state to the higher energy anti-bonding π* state. This can happen by the absorption of light. The distance between the π and π* state is also referred to as the band gap of the material. A photon with an energy above the band gap will therefore be able to be absorbed in the polymer by the transfer of its energy to a π state electron, exciting it to a π* state. Reversely, an electron in the π* state can disperse of some of its energy, dropping to the π state by the emission of a photon.

1.1.1 PEDOT:PSS

One of the most often used polymers within organic electronics is PEDOT:PSS. poly(3,4-ethylenedioxythiophene) (PEDOT) and poly(styrenesulfonate) (PSS) is a polymer mixture of two ionomers. The sodium polystyrene sulfonate is a sulfonated polystyrene and carry a negative charge. PEDOT is a conjugated polymer and carries positive charges. These charged macromolecules together form a macromolecular salt. [6]

It is used as a transparent conductive polymer in a variety of different applications. One of the largest uses previously has been for coating of photographic films as an an-

tistatic agent to prevent electrostatic discharges during production and normal film use, independent of humidity conditions [7].

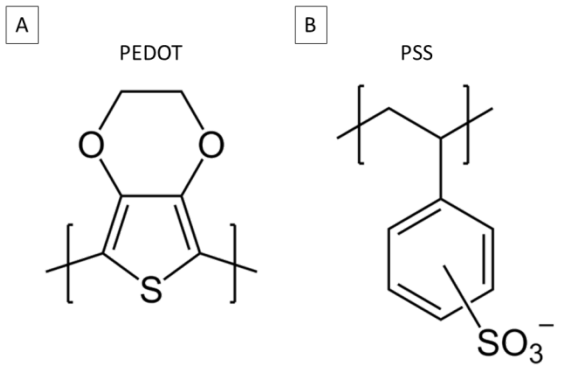

Figure 1.2: One of the most commonly used conducted polymers in organic electronics. The conductive / hole-selective polymer PEDOT:PSS.

A new use for PEDOT:PSS is as a transparent conductor for light emitting devices and for solar cells. High conductivities, up to 3000 S/cm , can be reached by threating PEDOT:PSS with sulfuric acid [8], and previously ethylene glycol, dimethyl sulfoxide (DMSO) has also shown increased conductivities. The current transparent conductor benchmark has been indium tin oxide, however due to the scarcity of indium and increasing prices [9], the quest for a substitute has been ongoing.

1.2 Solar cells

The ever-increasing world energy demand, causing a depletion of non-renewable energy resources and disruptive climate changes due to the greenhouse gases has raised an increased interest in alternative renewable energy sources. Solar energy is one of the best available alternatives, with its abundance and cleanness.

Since the discovery of the photovoltaic effect in silicon (Si) diodes in 1954, by Chapin et. al. [10], which started the evolution of modern solid state photovoltaic (PV) technology. Since then Si solar cells have evolved, into the by far most mature photovoltaic technology and represent over 90% of the present day photovoltaic market worldwide [11].

1.2.1 Types of solar cells

Solar cells are used to convert the incoming energy from the sun into electricity in a very direct way and with efficiencies up to 40% [12,13] with the most advanced systems and roughly 10-20% for the commonly used systems [11,12].

Solar cells have traditionally been divided into three generations. The first generation of solar cells is crystalline silicon cells. Crystalline silicon is the defacto standard for solar cell production and mounting to this day, with the basic principle of the solar cell not seeing much change in buildup. They have seen a gradual increase in efficiencies due to anti-reflective surface coatings and better fabrication techniques. The efficiencies of the single crystalline silicon solar cells have increased to a level of 25% in research cells and general production cells and modules with efficiencies above 18% and 16% respectively [14]. Multi crystalline silicon cells are also considered as a first generation technique and shows slightly lower efficiencies, however with some panel manufactures also reaching the 16 % mark for the multi crystalline modules.

The Second generation of solar cells was defined as the a group of cells based on cheaper substrates and thin film technologies. These include amorphous silicon solar cells, polycrystalline silicon solar cells on glass or metal substrates and the thin film Cadmium Telluride (CdTe) and Copper Indium (Gallium) diSelenide (CI(G)S) solar cells.

Organic solar cells are considered part of the 3rd generation solar cells. The 3rd generation refers to several techniques with very different types of solar cells included. It spans the ground from very advanced multi cell tandem devices produced from III-V semiconductors used for satellites and concentrator systems, to nanoparticles and quantum dots which shows promise as strong absorbers with very small material use, to the organic solar cells which are simple and extremely cheap to produce with the future idea of solar cells produced with methods close to newspaper printing [15].

The performance marks during the last 30 years are presented in Figure 1.3, with several variations of the above mentioned technologies indicated.

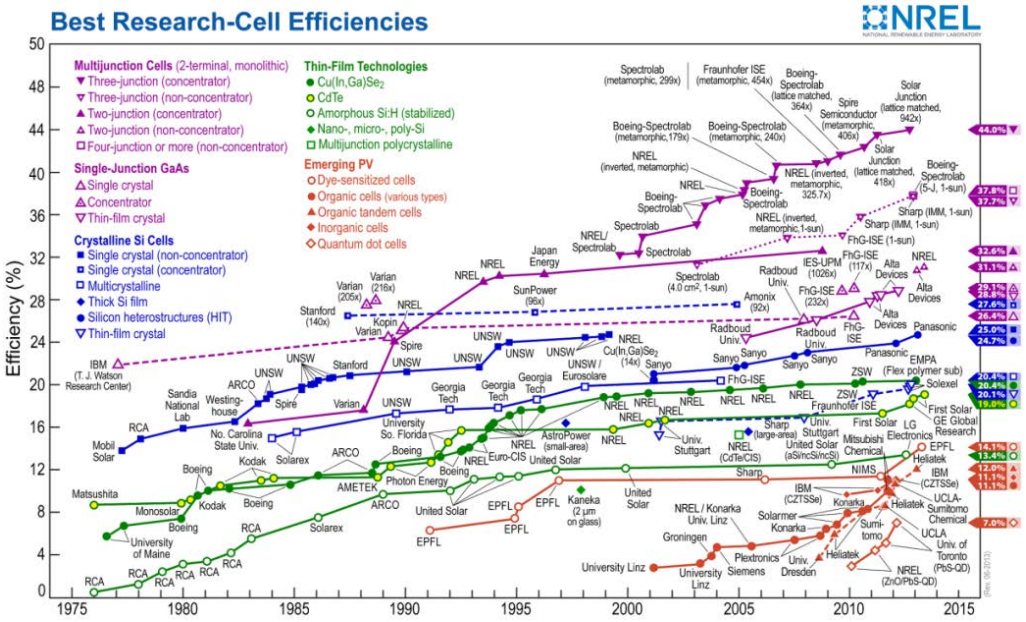

Figure 1.3: The highest performing solar cell of different types during the last 40 years. The clime in efficiency for OPV has been very fast during the last ten years. NREL Research-Cell Efficiency chart Reproduced from [16]

The performance of most of the 2nd and 3rd generation technologies lies below the 1st generation silicon technologies, the exception being the multijunction cells, concentrator cells and IIIV semiconductor cells. The performance of the emerging PV technologies, however, shows a fast increase in the maximum efficiency of research scale solar cells.

1.2.2 Solar cell market

The PV market has been increasing at a rate of 64% in the period from 2006 to 2011. [11,17], however flattened in 2012, as seen in Figure 1.4, and are expected to increase only slightly in 2013.

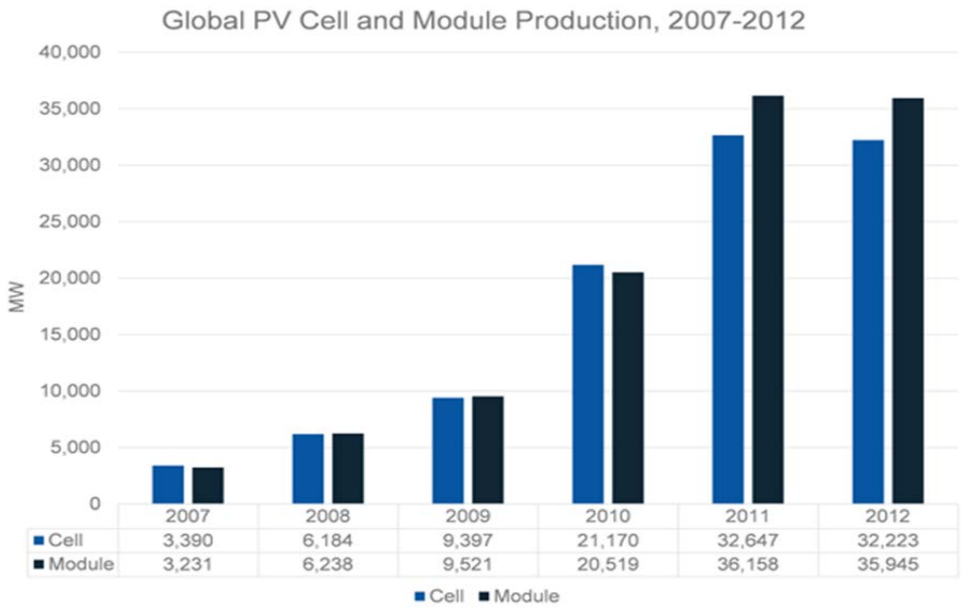

Figure 1.4: Global production of solar cells in the period from 2007-2012. Reproduced from GTM Research [4]

Of the total solar cells and modules produced in 2012 63 % and 64 % respectively were made in mainland China, which is a marginal increase over 2011 (62 % and 59 %). In total, Asia made up 86 % of global module production, and showed an even higher dominance in cell production, with an estimated 95 % of cells being produced in Asia in 2012 [11].

1.2.3 Making a competitive organic solar cell

For the organic solar cells or any of the solar cell technologies to have a chance on the market terms, it needs to not only show a high power conversion efficiency, but also do so at a competitive cost level and with a guaranteed lifetime long enough to back the initial investment. For this to be fulfilled, one has to make solar cells that abides to all three of these points (Figure 1.5), having an adequate efficiency at a low cost with a significant lifetime.

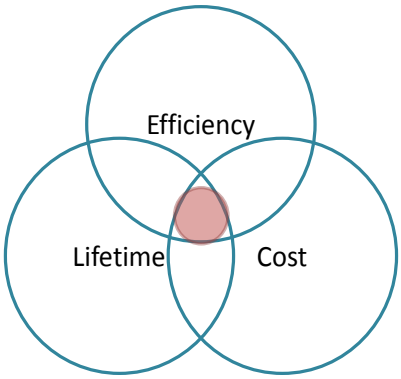

Figure 1.5: Venn diagram with the three most important parameters for an organic device. The red circle pinpoints the overlap between the key parameters – the place where the solar cell will have to be to be competitive.

Going deeper into the unification of the three key parameters for solar cells, the range of the circles and their overlap is hugely different depending on the technology. For organic photovoltaics the cost in both energy and money is significantly lower pr. area solar cell, compared to crystalline silicon, amorphous silicon, and III-V devices. Thin film devices are lower than the aforementioned, but still not as low as OPV devices are projected to be. At present however, the price of manufacturing an organic solar cells has been quite high due to the less than industrialized processing methods and the material price points, which at the relatively small scales used has a significantly higher price level than what should be obtainable in large scale productions. Studies of the prices of organic solar cell, and potential market shares were completed by Nielsen et. al. [18] and Azzopardi et. al. [19].

Furthermore, one of the large issues with the OPV manufacturing has been to not only increase the efficiency of the solar cells, but to do so in a fashion which can be up scaled and, with the lower level of efficiency that it is currently at, at a cost significantly below the ever present silicon technology. So far the primary method for producing the research scale solar cells has been by spin coating in protective atmosphere. Both spin coating and using protective atmospheres, are not technologies well suited for up scaling device sizes, and especially not at an attractive cost. This is especially clear when comparing the maximum efficiencies of the OPV in Figure 1.3, with the few large cell and module OPV devices reported. Efficiencies of 1 % to 3 % for larger areas [20–

23] compared to the promising 10 % for lab scale devices shows a significant gap to be filled for a widespread adoption of OPV.

1.3 Substrates

For roll coating there is an added issue to the substrate requirements in comparison to spin coating and many other production techniques. It needs to be flexible.

When roll coating, the substrate will pass several rollers going through the coating machine and will have to bend over these rollers. For this reason a bendable substrate is needed for roll coating, and for devices such as the herein presented electrically active devices an extra complication of having bendable electrodes also arises.

For most of the experimental world working with organic electronic devices the lab scale experiments are spin coating of glass slides, and for solar cells, OLED's and other devices that requires transmissive electrodes, the use of indium tin oxide (ITO) covered glass slides is normal. The development of new electrodes to substitute ITO is ongoing and important, since Indium is a scarce resource which has seen a high price increase during the last decade due to the use of ITO in popular products such as touch screens, flat-screen televisions and mobile phone displays.

Examples of possible electrode substitutes are materials such as grid based structures, were a metal grid array, nanowires from metals, or carbon based materials such as carbon nanotubes [24–26], graphite [27] or graphene [28–33] are used. Other possibilities are to use high-conductivity PEDOT:PSS materials, either alone or as hybrids with metal grids or nano-wire/tubes [34–38]. In comparison to ITO based materials, and of special importance for the flexible substrates, many of these alternatives show better bending abilities than ITO, which is a brittle material that handles bending poorly [39,40].

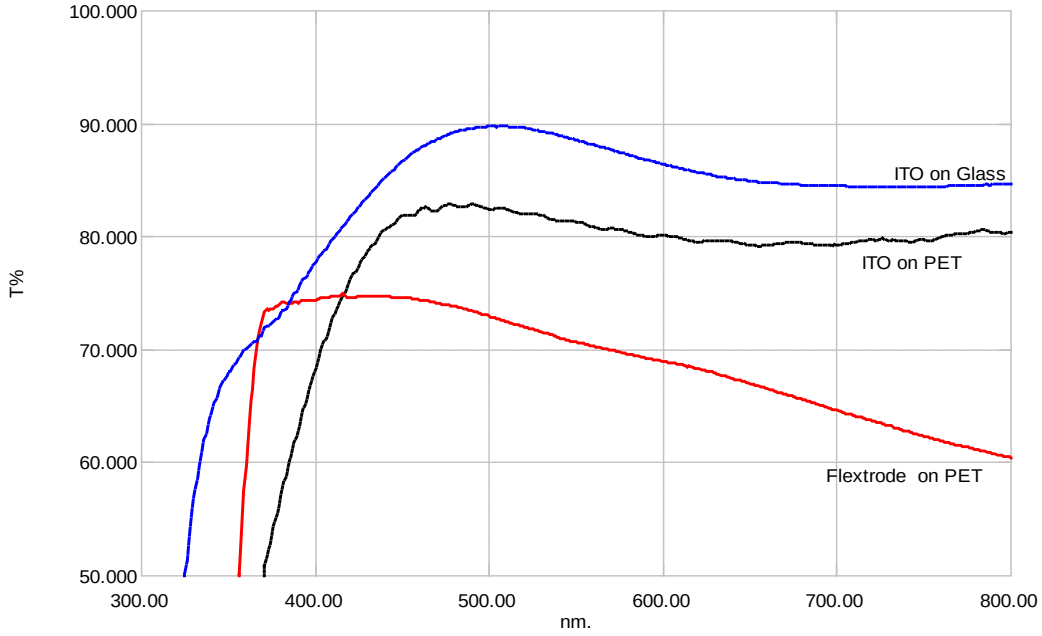

Figure 1.6: Comparison of the transmission through glass and PET electrodes with an ITO layer or a PEDOT:PSS- metal grid electrode.

Figure 1.6 shows the transparency of three different electrode materials. ITO on glass which has a very high transparency (blue). ITO on PET which is less transparent, but due to the brittleness of the ITO is also less conductive (black). Flextrode which is a PEDOT:PSS-Ag grid electrode on PET which has a lower transparency, but a high conductivity and handles bending well.

The devices manufactured and presented in this work has primarily been based on roll coating and are therefore made using either pre-patterned ITO on PET or the Flextrode PEDOT:PSS-silver grid substrates.

1.4 Encapsulation

When considering substrates for the manufacture of organic devices, it is a necessity to consider the possibility of encapsulation of the fabricated device, since most of the organic electronics are very susceptible to degradation caused by air or water vapor[41–44]. For this reason several different barriers are used, both in this report and in general [45].

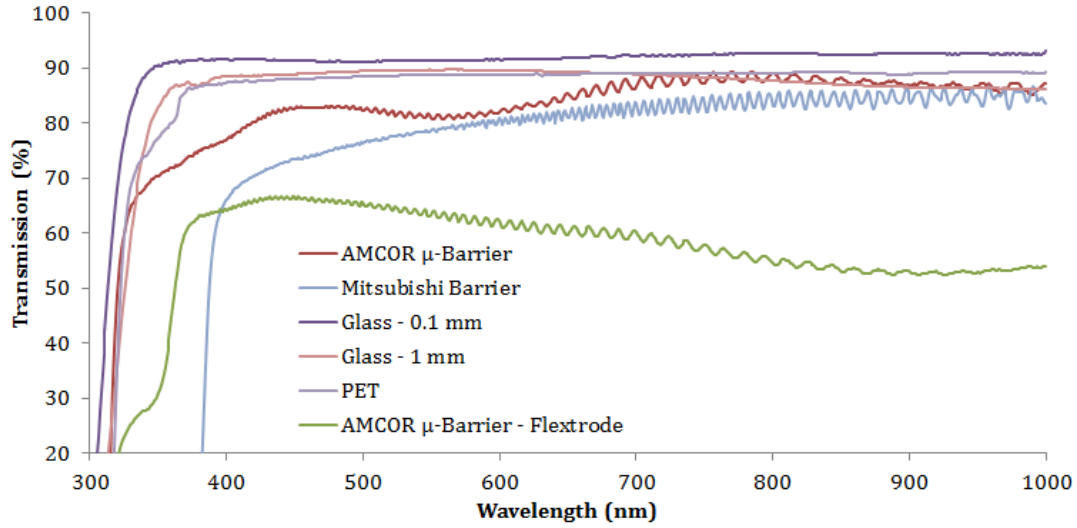

Figure 1.7: Transmission of light through different barriers. The Mitsubishi barrier is with a UV filter, cutting away radiation below 390 nm. For comparison, the transmission of the flextrode electrode coating directly on the barrier foil is also included.

The transmission of these barrier materials does however also contribute to the reduction of light absorbed or transmitted by the organic device. In Figure 1.7 the transmission of different barrier materials are presented, ranging from low-cost barriers such as AMCOR µ-Barrier and Mitsubishi barrier materials [43,46], which are roll 2 roll compatible, to glass slides which are not roll 2 roll compatible with regular PET shown for reference. A second option is to use the barrier material directly as a substrate, eliminating the cost of the PET substrate and inherent transmission losses[47].

1.5 Description of chapter contents

The somewhat widespread number of subjects which has been treated within the three years of this Ph.D. has been divided into the following chapters.

Chapter 2:

Description of the roll coating technique used for most of the devices produced and presented in this thesis. The chapter is meant to illustrate the issues and concerns, which makes slot-die coating and roll coating in general a difficult area to master.

Chapter 3:

Presentation of the organic polymer solar cell. The inner workings of this type of junction and the different cells with variation of active materials, electrode materials and blocking layers. The efficiency of several different polymers will be presented in a slot-die coated device structure and with quantum efficiencies included. The chapter will describe single junctions only.

Chapter 4:

Description of the use of nanoparticle based inks made from polymer and acceptor materials, and the analysis of these using both x-ray technology and electron microscopy. The nanoparticle approach is shown as an example of a way to reduce the solvent amount used and giving a benefit of a possibly higher degree of morphological control of the active layer mixing.

Chapter 5:

Organic tandem solar cells are described in this chapter, with fully roll coated cells. The initial devices were manufactured as thick homo junction cells to allow optimization and partial optical separation of the two cells. Later cells have been focused on using the obtained intermediate layer stack to increase the performance of the cells by applying thinner layers and more optimized polymers.

Chapter 6:

Having described primarily solar cells in the precious chapters, chapter 6 will present the result of another type of organic electronic device. This is the electrochromic device. A device consisting of two polymer layers and an electrolytic layer sandwiched between two electrodes. The polymers changes their absorbance on application of an electric pulse, causing a reduction and oxidation of the two polymers respectively. Roll coated devices was manufactured and these are presented with performance numbers.

Chapter 7:

The chapter will describe a light emitting device, the light emitting electrochemical cell (LEC), which is an OLED like device, but with the benefit of being significantly easier to manufacture and with the possibility of a higher efficiency than the OLED. Devices were manufactured in air and only using roll coating methods.

Chapter 8:

The final chapter describes a solar cell tester developed based on the open source Arduino electronics platform, for the use for solar cell testing in labs and offsite life-time studies.

1.6 Summary

This chapter is written as an introduction to the world of organic electronics, with a description of some of the common denominators for the various devices presented in this thesis. Emphasis has also been put on describing the solar cell market and the various technologies that any organic solar cell will have to compete against.

References

[1] A.C. Arias, J.D. MacKenzie, I. McCulloch, J. Rivnay, A. Salleo, Materials and applications for large area electronics: solution-based approaches, *Chem. Rev.* 110 (2010), 3–24.

[2] M. Berggren, D. Nilsson, N.D. Robinson, Organic materials for printed electronics, *Nat. Mater.* 6 (2007), 3–5.

[3] H.E. Katz, Recent Advances in Semiconductor Performance and Printing Processes for Organic Transistor-Based Electronics, *Chem. Mater.* 16 (2004), 4748–4756.

[4] L. Frazer, Organic electronics: a cleaner substitute for silicon., *Environ. Health Perspect.* 111 (2003), A288–A291.

[5] D.J. Gundlach, Organic electronics: Low power, high impact, *Nat. Mater.* 6 (2007), 173–174.

[6] L. Groenendaal, F. Jonas, D. Freitag, H. Pielartzik, J.R. Reynolds, Poly(3,4-ethylenedioxythiophene) and Its Derivatives: Past, Present, and Future, *Adv. Mater.* 12 (2000), 481–494.

[7] C.C. Anderson, M.D. DeLaura, D. Majumdar, Photographic element containing an electrically-conductive layer, U.S. Patent 6,440,654, 2002.

[8] Y. Xia, K. Sun, J. Ouyang, Solution-Processed Metallic Conducting Polymer Films as Transparent Electrode of Optoelectronic Devices, *Adv. Mater.* 24 (2012), 2436–2440.

[9] M.A. Green, Estimates of te and in prices from direct mining of known ores, *Prog. Photovoltaics Res. Appl.* 17 (2009), 347–359.

[10] D.M. Chapin, C.S. Fuller, G.L. Pearson, A new silicon p-n junction photocell for converting solar radiation into electrical power, *J. Appl. Phys.* 25 (1954), 676–677.

[11] Andrew Krulewitz, Paul Maycock, PV News, *Pv News*. 31 (2012), 1–28.

[12] M.A. Green, K. Emery, Y. Hishikawa, W. Warta, E.D. Dunlop, Solar cell efficiency tables (version 39), *Prog. Photovoltaics Res. Appl.* 20 (2012), 12–20.

[13] M. Yamaguchi, T. Takamoto, K. Araki, Super high-efficiency multi-junction and concentrator solar cells, *Sol. Energy Mater. Sol. Cells*. 90 (2006), 3068–3077.

[14] Canadian Solar, Alex Solar, Astronergy, Yingli, JA Solar, Trina Solar, Suntech, http://www.solar-facts.com/panels/panel-manufacturers.php, (n.d.),.

[15] B.A. Gregg, M.C. Hanna, Comparing organic to inorganic photovoltaic cells: Theory, experiment, and simulation, *J. Appl. Phys.* 93 (2003), 3605–3614.

[16] L.L. Kazmerski, NREL Best Research-Cell Efficiencies, *Wikipedia Free Encycl.* (2013),.

[17] S. Sista, Z. Hong, L.-M. Chen, Y. Yang, Tandem polymer photovoltaic cells—current status, challenges and future outlook, *Energy Environ. Sci.* 4 (2011), 1606.

[18] T.D. Nielsen, C. Cruickshank, S. Foged, J. Thorsen, F.C. Krebs, Business, market and intellectual property analysis of polymer solar cells, *Sol. Energy Mater. Sol. Cells*. 94 (2010), 1553–1571.

[19] B. Azzopardi, C.J.M. Emmott, A. Urbina, F.C. Krebs, J. Mutale, J. Nelson, Economic assessment of solar electricity production from organic-based photovoltaic modules in a domestic environment, *Energy Environ. Sci.* 4 (2011), 3741–3753.

[20] R. Tipnis, J. Bernkopf, S. Jia, J. Krieg, S. Li, M. Storch, et al., Large-area organic photovoltaic module—Fabrication and performance, *Sol. Energy Mater. Sol. Cells*. 93 (2009), 442–446.

[21] R. Tipnis, J. Bernkopf, S. Jia, J. Krieg, S. Li, M. Storch, et al., Erratum to: “Large-area organic photovoltaic module—Fabrication and performance” [Sol. Energy Mater. Sol. Cells 93 (2009) 442–446], *Sol. Energy Mater. Sol. Cells*. 93 (2009), 1457.

[22] M. Jørgensen, J.E. Carlé, R.R. Søndergaard, M. Lauritzen, N.A. Dagnæs-Hansen, S.L. Byskov, et al., The state of organic solar cells—A meta analysis, *Sol. Energy Mater. Sol. Cells*. (n.d.),.

[23] Y. Galagan, D.J.D. Moet, D.C. Hermes, P.W.M. Blom, R. Andriessen, Large area ITO-free organic solar cells on steel substrate, *Org. Electron.* 13 (2012), 3310–3314.

[24] K. Al-Shamery, H.-G. Rubahn, H. Sitter, eds., Organic Nanostructures for Next Generation Devices, Springer Berlin Heidelberg, Berlin, Heidelberg, 2008.

[25] T.M. Barnes, X. Wu, J. Zhou, A. Duda, J. van de Lagemaat, T.J. Coutts, et al., Single-wall carbon nanotube networks as a transparent back contact in CdTe solar cells, *Appl. Phys. Lett.* 90 (2007), 243503.

[26] T.M. Barnes, J.D. Bergeson, R.C. Tenent, B.A. Larsen, G. Teeter, K.M. Jones, et al., Carbon nanotube network electrodes enabling efficient organic solar cells without a hole transport layer, *Appl. Phys. Lett.* 96 (2010), 243309.

[27] N. Espinosa, M. Hösel, D. Angmo, F.C. Krebs, Solar cells with one-day energy payback for the factories of the future, *Energy Environ. Sci.* 5 (2012), 5117–5132.

[28] S. Bae, H. Kim, Y. Lee, X. Xu, J.-S. Park, Y. Zheng, et al., Roll-to-roll production of 30-inch graphene films for transparent electrodes, *Nat. Nanotechnol.* 5 (2010), 574–578.

[29] J. Chen, Chen, J., Ishigami, M., Jang, C., Hines, D. R., Fuhrer, M. S., and Williams, E. D., Printed graphene circuits., *Adv. Mater.* 19 (2007), 3623–3627.

[30] Z. Liu, J. Li, F. Yan, Package-Free Flexible Organic Solar Cells with Graphene top Electrodes, *Adv. Mater.* (2013), n/a–n/a.

[31] H. Park, J.A. Rowehl, K.K. Kim, V. Bulovic, J. Kong, Doped graphene electrodes for organic solar cells, *Nanotechnology*. 21 (2010), 505204.

[32] X. Wan, G. Long, L. Huang, Y. Chen, Graphene - A Promising Material for Organic Photovoltaic Cells, *Adv. Mater.* (2011), n/a–n/a.

[33] Y. et al. Wang, Wang, Yu et al.'', Large area, continuous, few-layered graphene as anodes in organic photovoltaic devices, *Appl. Phys. Lett.* 95 (2009), 063302.

[34] C. Celle, C. Mayousse, E. Moreau, H. Basti, A. Carella, J.-P. Simonato, Highly flexible transparent film heaters based on random networks of silver nanowires, *Nano Res.* 5 (2012), 427–433.

[35] J. Jiu, M. Nogi, T. Sugahara, T. Tokuno, T. Araki, N. Komoda, et al., Strongly adhesive and flexible transparent silver nanowire conductive films fabricated with a high-intensity pulsed light technique, *J. Mater. Chem.* 22 (2012), 23561–23567.

[36] A.R. Madaria, A. Kumar, C. Zhou, Large scale, highly conductive and patterned transparent films of silver nanowires on arbitrary substrates and their application in touch screens, *Nanotechnology*. 22 (2011), 245201.

[37] T. Tokuno, M. Nogi, M. Karakawa, J. Jiu, T.T. Nge, Y. Aso, et al., Fabrication of silver nanowire transparent electrodes at room temperature, *Nano Res.* 4 (2011), 1215–1222.

[38] R. Zhu, C.-H. Chung, K.C. Cha, W. Yang, Y.B. Zheng, H. Zhou, et al., Fused silver nanowires with metal oxide nanoparticles and organic polymers for highly transparent conductors, *Acs Nano*. 5 (2011), 9877–9882.

[39] S.R. Dupont, M. Oliver, F.C. Krebs, R.H. Dauskardt, S.R. Dupont, M. Oliver, et al., Interlayer adhesion in roll-to-roll processed flexible inverted polymer solar cells, in: Sol. Energy Mater. Sol. Cells, Elsevier BV North-Holland, 2012: pp. 171–175.

[40] S.-I. Na, S.-S. Kim, J. Jo, D.-Y. Kim, Efficient and Flexible ITO-Free Organic Solar Cells Using Highly Conductive Polymer Anodes, *Adv. Mater.* 20 (2008), 4061–4067.

[41] A. Asadpoordarvish, A. Sandström, S. Tang, J. Granström, L. Edman, Encapsulating light-emitting electrochemical cells for improved performance, *Appl. Phys. Lett.* 100 (2012), 193508.

[42] A. Morlier, S. Cros, J.-P. Garandet, N. Alberola, Gas barrier properties of solution processed composite multilayer structures for organic solar cells encapsulation, *Sol. Energy Mater. Sol. Cells*. 115 (2013), 93–99.

[43] D.M. Tanenbaum, H.F. Dam, R. Rösch, M. Jørgensen, H. Hoppe, F.C. Krebs, Edge sealing for low cost stability enhancement of roll-to-roll processed flexible polymer solar cell modules, *Sol. Energy Mater. Sol. Cells*. 97 (2012), 157–163.

[44] R. Rösch, D.M. Tanenbaum, M. Jørgensen, M. Seeland, M. Bärenklau, M. Hermenau, et al., Investigation of the degradation mechanisms of a variety of organic photovoltaic devices by combination of imaging techniques—the ISOS-3 inter-laboratory collaboration, *Energy Environ. Sci.* 5 (2012), 6521–6540.

[45] J.-S. Park, H. Chae, H.K. Chung, S.I. Lee, Thin film encapsulation for flexible AM-OLED: a review, *Semicond. Sci. Technol.* 26 (2011), 034001.

[46] S.A. Gevorgyan, A.J. Medford, E. Bundgaard, S.B. Sapkota, H.-F. Schleiermacher, B. Zimmermann, et al., An inter-laboratory stability study of roll-to-roll coated flexible polymer solar modules, *Sol. Energy Mater. Sol. Cells*. 95 (2011), 1398–1416.

[47] M. Hösel, R.R. Søndergaard, M. Jørgensen, F.C. Krebs, Fast Inline Roll-to-Roll Printing for Indium-Tin-Oxide-Free Polymer Solar Cells Using Automatic Registration, *Energy Technol.* 1 (2013), 102–107.

2. Roll Coating

Roll coating of polymer devices is the holy grail for many of the devices which are discussed in this thesis. A large issue with roll coating however, is the difficulty in moving from small scale production methods to the inherent large scale roll-to-roll processing. Most of the laboratory development of new materials, structures and devices are done by using spin coating; a technique that has shown its value for the many generation of wafer scale processing in the semiconductor industry. The issue arising with the spin coating technique is that, however well working it is for producing thin and very uniform films on small glass slides or wafers, the trouble arising when scaling from small to large the advantages quickly disappears with impossible demands on machinery, ink formulation and substrate uniformity.

Furthermore, the scaling of foil speed for different coating techniques often also have very large influence on the obtained film quality and patterns in the coatings. A coating technique such as flexographic printing can for less viscous solutions require coating speeds of more than 15 m/min before it becomes possible to produce uniform films.

Roll coating as a technology is mainly used for very high volume applications. The use of speeds of >100 meter/min and widths for polymer and paper substrates up to 1 m for wet coating [1,2] and 2.5 meters for evaporation techniques [3].

2.1 Laboratory roll 2 roll coater

The issue with working on full size roll-to-roll coating equipment is that the entrance level for this technology lies with a considerable minimum cost, as can be expected when the minimum amount of material for one device in a spin-coating setting would be a substrate of 10 x 10 mm^2, while in roll-coating the substrate comes in a width of 305 mm or larger . A typical machine requires more than 5 m of foil to get from the unwinder roll to the pickup roll. An example of one of the roll 2 roll coating

systems used at DTU Energyconversion is shown in Figure 2.1. This system is still considered a small scale system despite the 305 mm rollers with a 20 m/min max speed.

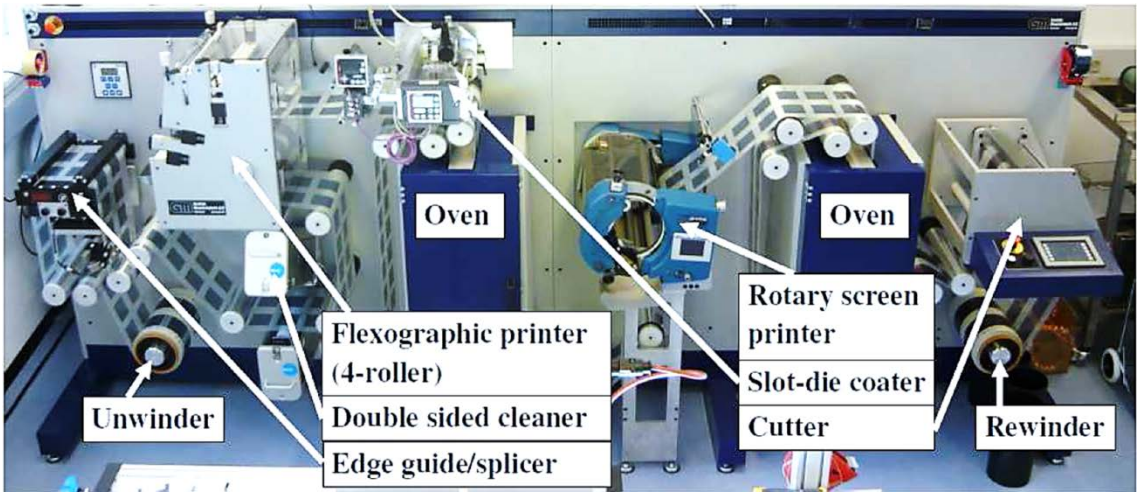

Figure 2.1: Roll to roll coater as found at DTU Energyconversion. The machine is a full size roll 2 roll coater and allows running coatings of 305 mm width at up to 20 meter/min.

The throughput of this machine peaks at a maximum of just below 40 m^2 per hour.

The roll to roll coater pictured does however offer the option making available several different coating techniques on one machine.

2.2 Development of mini roll coater

Following from the high entry point of roll coating and the many lab scale experiments being conducted with spin coating, the process of developing a laboratory scale mini roll coater was initiated. The principle of which was to make a system that allowed an easier and faster, not to mention cheaper method for testing new polymers, electrode materials and transport layers for coated electronics. Optimizations on the MRC would then be possible to transfer to the larger scale roll 2 roll coaters, instead of having optimized the processing of a new polymer in a spin coating situation, later to find that the transfer to roll coating required the optimization to be carried out once again for this technique. Furthermore the use of the roll coating, with a slot-die head and a flexographic printed head enables the use of a single machine for manufacturing of a complete solar cell.

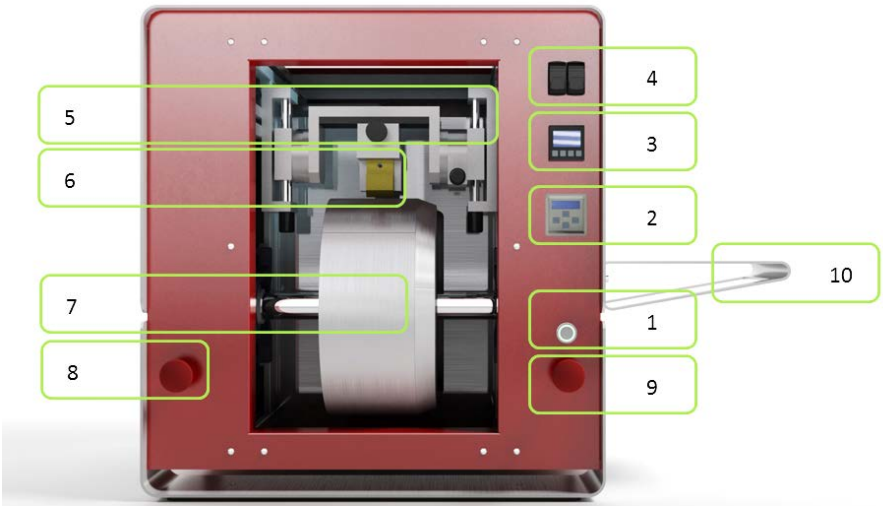

Figure 2.2: The mini roll coater (MRC) as first illustrated. The indicated parts are (1) start button, (2) motor controller, (3) heating controller, (4) breakers for motor and heat controller, (5) translation stage for adjusting the position of the coating head in horizontal and vertical position. (6) shows the slot-die coating head. (7) shows the central axel for the rotation of the drum, and (8) and (9) are the emergency stops. (10) is a shelf for holding the ink supplying pump.

The principle buildup of the coater came to be a 320 mm diameter solid aluminum drum with build in heating elements and a temperature sensor mounted on a transversal axel. The heaters are adjusted via a PID temperature controller and a temperature range of room-temperature to 190 °C has been tested, however since most coatings are performed on PET plastics, normal working temperature lies between 30 °C to 140 °C.

The drum rotational speed is adjusted via a frequency motor speed controller, which allows a speed between 0 and 2 m/min, with an option of changing the gearing to allow up to 5 m/min. Speeds of over 2 m/min, however has the disadvantage of very short experiment times, with a complete rotation in 30 seconds at 2 m/min resulting in the need of an experienced operator to adjust the head height and lateral position with respect to any previously coated layer(s).

To adjust the position of the coating head translation stages were used with a vertical stage in both sides of the coater giving the possibility of also adjusting the head to the correct angle with respect to the substrate. A horizontal translation stage was

mounted to adjust the head position with respect to the coating of individual stripes on the substrate and to offset one coating with respect to the next layer coating.

2.3 Slot-die head design

The slot-die head design developed at the former Risø National Laboratory, now DTU, consists of a slot-die head with a steel foil meniscus guide acting to control the width of the coating line. The head is divided into three distinct parts: The meniscus guide (Figure 2.3A), which is a metal foil center piece serving to define the width of the coating. A front part (Figure 2.3B) with a milled grove, which is the channel, where the liquid flow from a top inlet down to the outlet and out onto the meniscus guide. The back part (Figure 2.3C) is a solid piece which holds the screw mount and has a flat backing for the meniscus guide and front piece.

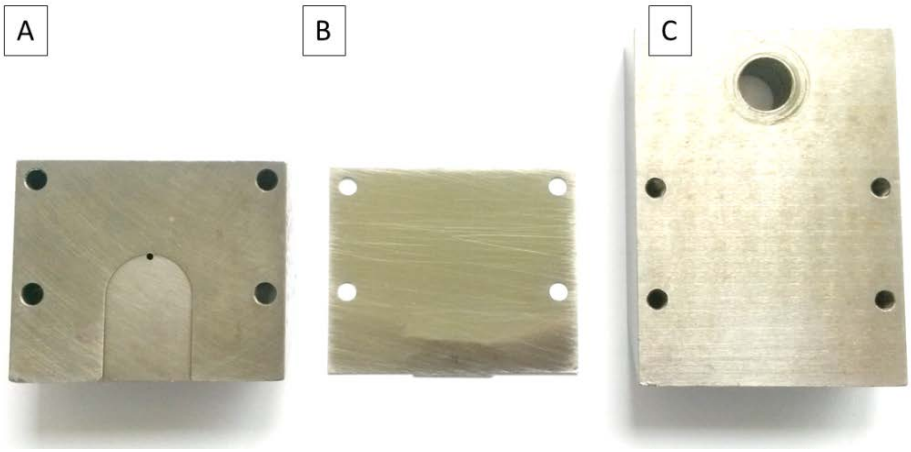

Figure 2.3: Example of a 3 piece 13 mm width coating head. A) The front part of the head with the milled groove. B) The meniscus guide insert directing the flow at the head outlet. C) The slot-die head back piece.

The use of a meniscus guide offsets this technique somewhat from the conventional slot-die coating technique, where the coating head only consists of the front and back piece, with the groove outlet defining the coating width. The advantage of using the meniscus guide technique lies in an easier change of the coating pattern and a slightly different meniscus formation.

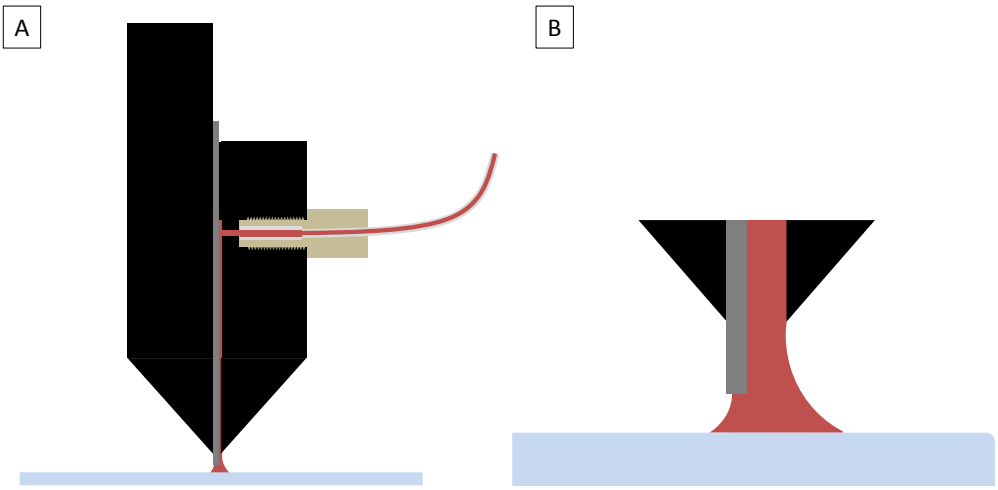

Figure 2.4: Illustration of a slot-die coating head with a meniscus guide and meniscus. A) shows the entire coating head, while B) is an illustration of the ink flow around the meniscus guide and tip of coating head. Meniscus size and shape is illustrative only.

2.3.1 Meniscus guides and slot-die head sizes.

The initial head size used for the MRC was made with a 13 mm coating width and with two optional head sizes of 25 mm and 50 mm. The use of a 13 mm wide coating width, comes from the compromise between alignment width, number of possible cells on a full width 305 mm substrate and the necessity for a high aspect ratio in a solar cell to reduce the series resistance of the cells.

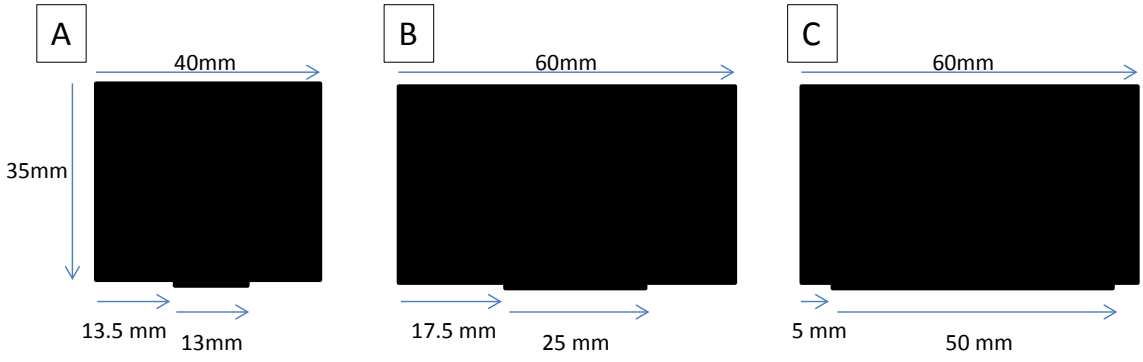

Figure 2.5: Foil inserts for the MRC standard coating heads. A) Foil insert for making a 13 mm wide slot-die coating. This is the stripe width used in many of the modules produced at DTU and the width used in the pre-patterned electrodes.

13 mm head

A COMSOL simulation of the flow through the 13 mm wide head was completed to check the variation of the flow exiting the bottom of the groove, as a function of the distance from the center of the groove. The simulation of the flow showed the flow rate across the exit slit to vary less than 1 % over the width of the outlet. The simulation was completed with a groove size of 13 mm width, 0.2 mm depth and a 25 mm

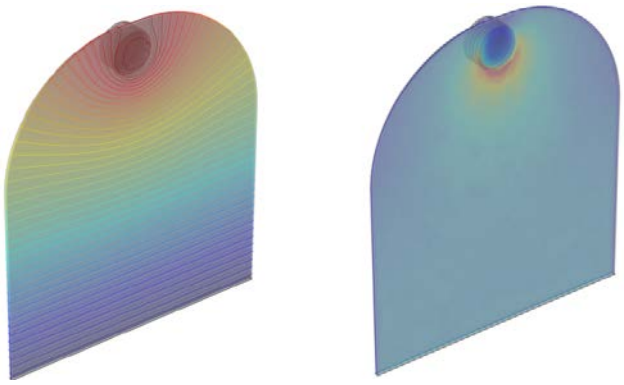

Figure 2.7: COMSOL simulation of the coater head groove in a 13 mm wide head. A) Pressure field through the groove and B) flow rate through the groove. The size of the simulated groove is 13 mm wide, 25 mm high and 0.2 mm deep.

height, corresponding to the coating heads used in the slot die coater. The liquid simulated was water.

The creeping flow standard physics module was chosen for the simulation due to

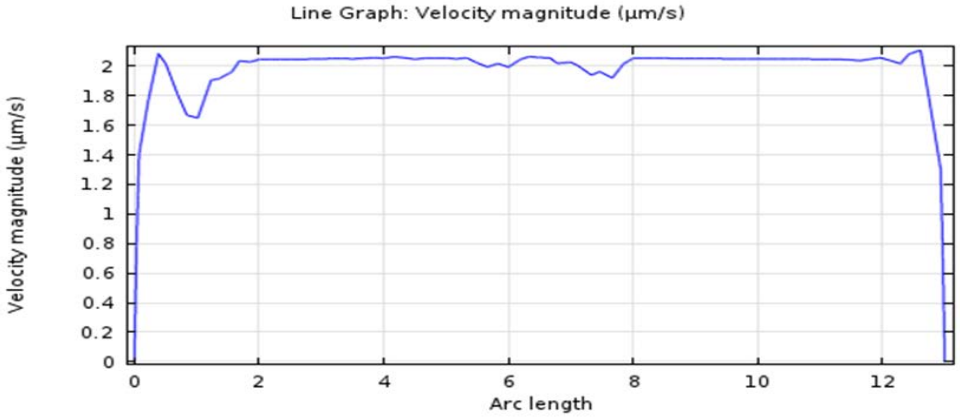

Figure 2.6: Variation in flow rate across the centerline of the bottom outlet from the slot-die head. The variation is small and does not indicate a tendency for a depletion of the ink flow towards the outer edges of the outlet.

the low Reynolds numbers in most of the flow region.

25 mm head

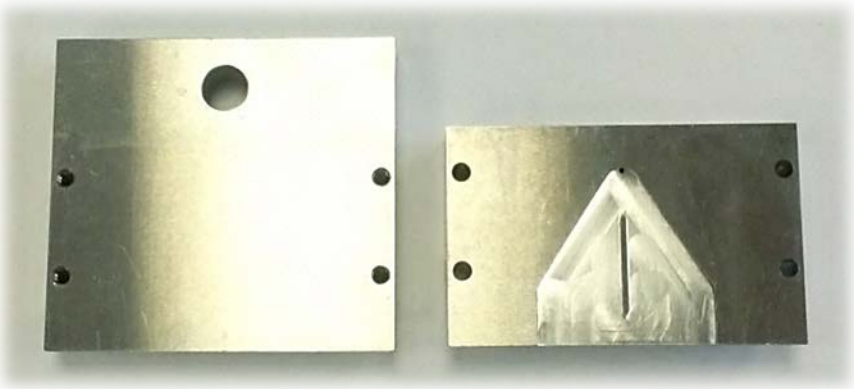

Figure 2.8: 25 mm head design. The curved edges are to reduce the head dead volume, while keeping a uniform flow profile. The center line acts as a support beam for the foil insert.

The optional 25 mm coating head was made using a different design than the 13 mm head. The groove in the head top part was made as a triangular shape to reduce the dead volume in contrast to the founded shape used in the 13 mm head. In the center of the head a support beam for the foil insert was made to ensure that the foil insert would not bend into the groove and thereby reduce the depth of ink channel. An image of the head front and rear piece is shown in Figure 2.8.

50 mm head

For the largest head used, the 50 mm width head, three iterations was completed be-

Figure 2.9: 50 mm head design. At the inlet a pressure distribution channel has been milled into the head to even out the pressure across the width of the bottom outlet. This head also has a support beam in the center similar to the 25 mm head.

fore a design which could produce a uniform coating was reached. The final design is shown in Figure 2.11. The initial design was made based on the 13 mm head with the only difference being an enlargement of the heads coating width. However, a problem with the variation of the pressure at the outlet during coating was seen, resulting in an issue with the flow rate at the edges being significantly reduced when coating layers of viscous fluids such as some of the PEDOT:PSS solutions. As shown in the COMSOL simulation for the 13 mm head with water used as medium. The issue was traced to two separate issues. One being the width of the groove with respect to the foil insert. The second being the width of the groove in respect to the hydraulic flow resistance. The second iteration of the head included a support beam, as was also used on the 25 mm head, to ensure the correct distance between the foil insert and the groove wall. A third iteration included the support beam and added the pressure equalling reservoir channel which significantly improved the flow rate uniformity at the outlet, due to a more uniform hydraulic resistance from the inlet to the outlet. .

2.3.2 Reduced coating width: 10 mm

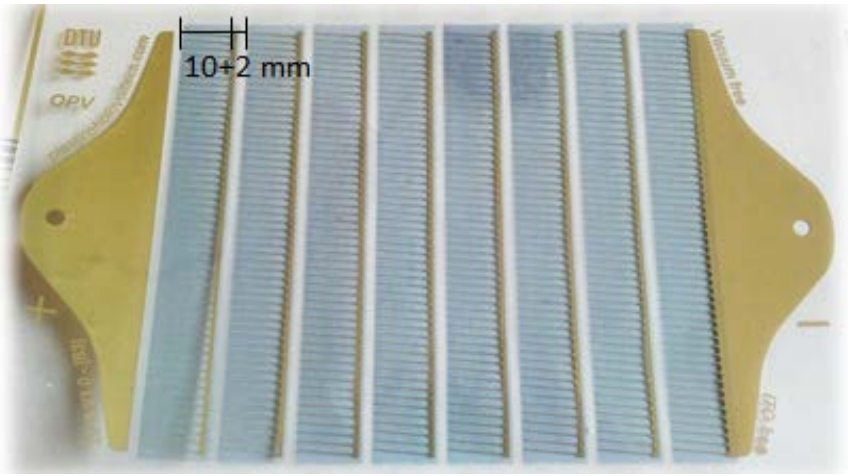

Figure 2.10: FreeOPV electrode design. Made for production of modules consisting of 8 cells in series, with two modules side-by-side on a 305 mm wide substrate.

A new design was developed to allow fitment of two modules on a 305 mm coating width. The new design is made for manufacturing of the FreeOPV modules [4], with 8

stripes of 10 mm width. An example of a FreeOPV Flextrode substrate is shown in Figure 2.10.

A new set of foil inserts were designed for use with existing heads and the FreeOPV substrate, with a meniscus guide width of 10 mm. The design of the three different meniscus guides seen in Figure 2.11, was done to allow both the coating of single cells and modules. Modules could be produced with a single meniscus guide type foil insert, however using the multiple meniscus guide foils allows a full 8 stripe module to be manufactured on the MRC with only two parallel coatings of each layer and without having to worry about alignment of the extra stripes.

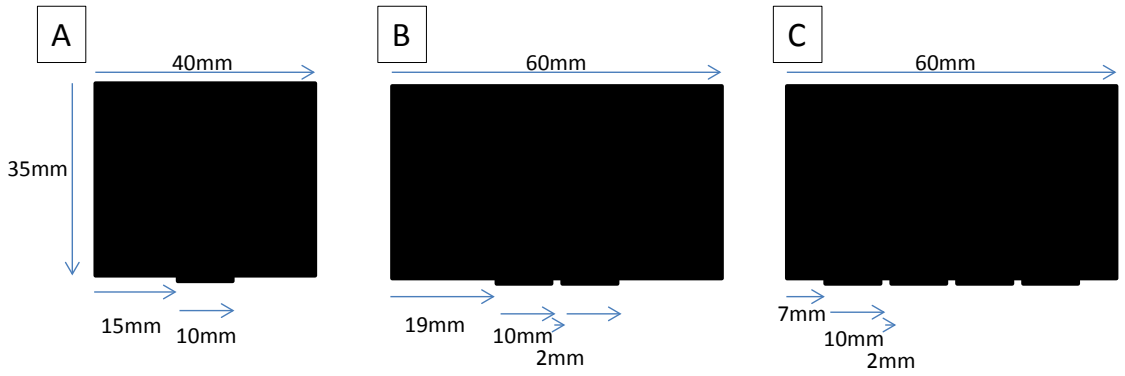

Figure 2.11: Meniscus guides for use with the free OPV design. A) Single 10 mm wide guide. B) Double 10 mm wide guides with a 2 mm spacing and C) a 4 line guide with 4x10 mm guides and a 12 mm pitch for making complete FreeOPV substrate based modules on the MRC.

The foil inserts were made with the single meniscus guide foil insert fitting the 13 mm head design, the dual meniscus guide insert fitting the 25 mm head and the quatro meniscus guide insert fitting the 50 mm head design.

2.4 Screen printed top electrodes

Initially the top electrodes were screen printed on a flatbed screen printer. This was done in a similar fashion to the technique used in Krebs et. al [5], where a roll 2 roll screen printer was used. However, the use of a screen printer for making the top silver electrode necessitated an extra machine for doing the screen printing.

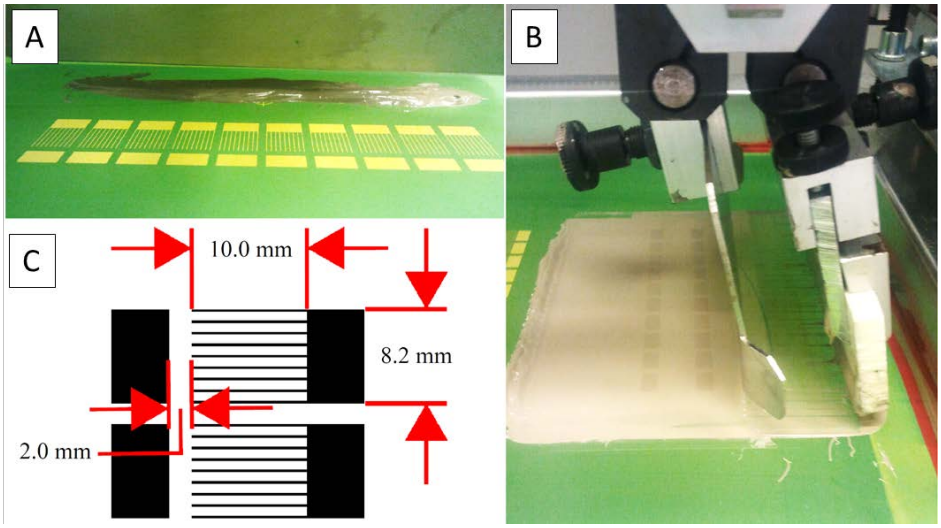

Figure 2.12: Screen printing of top electrodes using Dupont PV410 silver paste on an Alraum Screen printer. The screen is for printing of 10 cells of 1 cm^2 each on a 13 mm wide stripe pattern. A) View from in front of the squeegy before the first print. B) Side view after the first print. C) The electrode mask design.

2.5 Flexographic printing head

A flexographic printing head was developed as a solution to enable full processing of a solar cell on the mini roll coater, without the need of any other equipment for the fabrication of any of the layers.

The flexo printing head consists of a mounting block with a horizontal axel on which two beams are attached carrying a 100 mm diameter coating roller. The roller can be fitted with a range of different patterned rubber flexo-rollers enabling the printing of a 2D patterned top electrode. Two different versions were developed with a change in the width of the roller, to enable the use of either a 30 mm wide roller enabling a wider movement range on the horizontal translation stage and a 60 mm wide roller which enabled compatibility with the patterns used in the SameSUN solar tester system and cell size and electrode layouts identical to the patterns used on the laboratory glass-ITO slides.

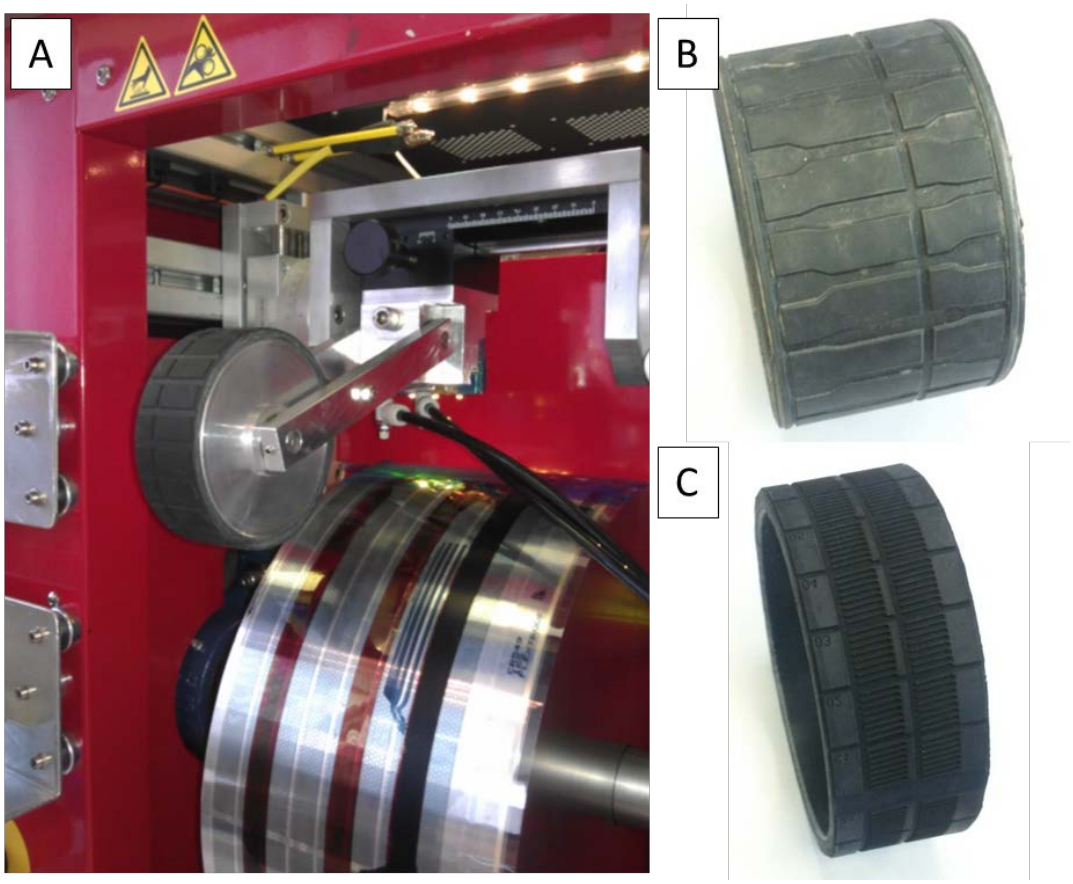

Figure 2.13: Flexographic rollers for printing the top electrode. Currently the ink used with these rollers is the silver particle ink PV410. A) Flexographic printhead mounted on the MRC machine. This version has a 30 mm flexoroller and a pneumatic piston to apply pressure against the printing surface. B) Shows a roller for the manufacture of 1 cm2 cells compatible with the SameSUN system. C) A grid electrode for creating a series connected two cell module, with a 5 degree slanted finger electrode.

To supply a uniform pressure during the coating of silver the mounting block was fitted with a pneumatic piston and a two-way valve with a regulator, to supply constant force on the flexo-roller during the printing of the silver and increase the reproducibility of the cells produced on the machine.

2.6 Ink supply system

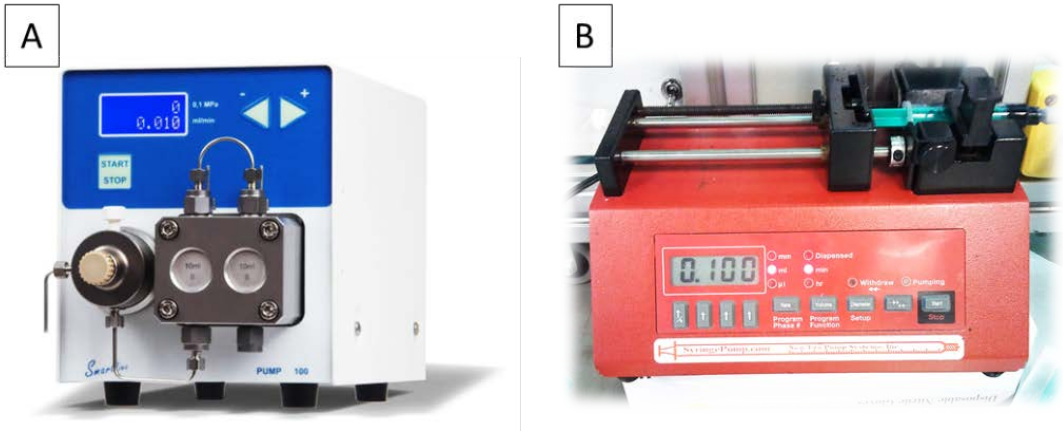

Figure 2.14: A) Knaur Smart Pump 100 HPLC pump initially used on the roll coater, however the cleaing and removal of air in the pump made it less suitable B) Aladdin NE-1000X syringe pump used for the coating of solutions on the coaters. The use of syringe pumps gives a wide range of flow rates with a choice of syringe diameter and with the use of disposable syringes enables a quick change of solution and cleaning.

Supplying the ink to the slot-die coating head was initially done using Knaur Smartline Pump 100 HPLC pumps (see Figure 2.14A), however the cleaning when changing between inks and the associated removal of air bubbles in tubing and pump reservoirs made it less suitable. Instead of the HPLC pumps an Aladdin NE-1000X syringe pump

Table 2.1: Calculated thicknesses for coatings on the MRC with estimated dry thicknesses for a P3HT:PCBM 1:1 mixture ink. Numbers are for a 13 mm head width. Dry film densities for the materials was assumed to be: ρ(P3HT) = 1.10 g/cm^3 and ρ(PCBM) = 1.50 g/cm^3. Dry numbers corresponds to the use of a 15:15 mg/ml or 20:20 mg/ml solution respectively.

Speed	Flow Rate	Thickness		
m/min	ml/min	Wet	Dry (15:15)	Dry (20:20)
0.40	0.050	9.6 µm	227 nm	303 nm
0.50	0.050	7.7 µm	182 nm	242 nm
0.60	0.100	12.8 µm	303 nm	404 nm
0.80	0.100	9.6 µm	227 nm	303 nm
1.00	0.100	7.7 µm	182 nm	242 nm
1.50	0.100	5.1 µm	121 nm	162 nm
2.00	0.200	7.7 µm	182 nm	242 nm

system (see Figure 2.14B) was bought for use with the coater, which helped to reduce the amount of cleaning needed between coating of different materials, with the pump reservoir now being reduced to an disposable syringe. Air bubbles are also much less of an issue in the syringe pumps, due to the lack of any counter-moving valves.

2.6.1 Gradient pumping system

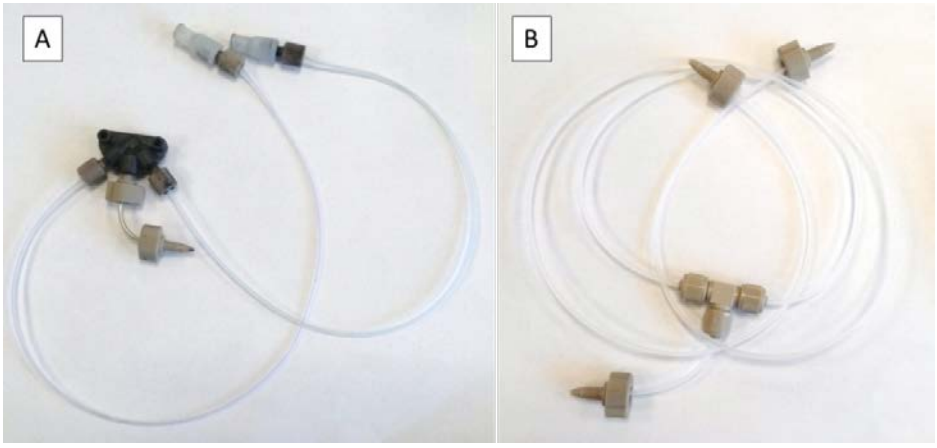

Figure 2.15: Mixers for making gradient pumping experiments. A) Upchurch Scientific U-466 mixing tee with connectors for attachment of Luer Lock syringes on ends and slot-die mount. B) Upchurch Scientific M-540 micro static mixing tee.

For the purpose of enabling variation along the coating line for an experiment, a dual ink supply system was developed allowing mixing of two components during a coating, for instance for varying the concentration ratio between donor and acceptor in the coated film or for reducing the concentration of a ink by having a ink supply and a solvent supply line. This technique can give similar experimental possibilities to what was previously described in Alstrup et. al. [6] and [7] in both cases using a full scale roll 2 roll coater.

To allow coating with two pumps and two different solutions a mixing tee was used. However, depending on the coating width used and flow rate used, the use of two different mixers were required. In Figure 2.15A a mixer for high flow rates is shown, which is used when the flowrate is higher than 0.3ml/min, while in Figure 2.15B a smaller channel mixer is shown, which enables efficient mixing at lower flowrates.

Together with the mixing tees two syringe pumps were used to supply the ink/solvent flow for precise mixing during a coating run. This was further assisted by an in-house developed pump control program, which enables setup of a time controlled rate experiment for a coating. The graphical user interface of the program is shown in Figure 2.16.

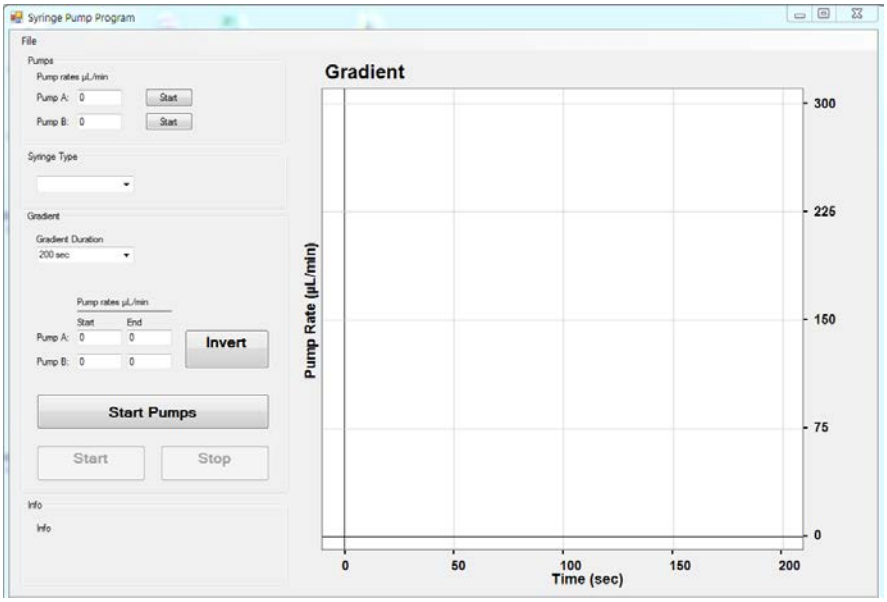

Figure 2.16: Screenshot of the gradient pumping control program. The program enables use of a two-pump system with individual ramping up/down of both pumps over a step ramp period.

2.6.2 Pressure driven pump for high viscosity

Due to the high viscosity of the PEDOT:PSS inks used as top electrodes, the use of the Knaur pumps was not possible, due to issues with clogging and incurred stopping of the flow. Instead a pressure driven pump was used on the large roll 2 roll coating system. To keep the similarities and the transferability between the two systems, a similar pressure driven pump was made for the MRC. This is shown in Figure 2.17. The pump is run of the compressed air lines in the lab with a regulator to adjust the coating pressure depending on the ink viscosity and flow rate needed.

Figure 2.17: Pressure driven pump for supplying viscous PEDOT:PSS top layer ink. Pump is driven from the laboratory compressed air system with a 1.5 bar to 2 bar pressure.

2.7 Development of Micro roll 2 roll coater for X-ray analysis purposes

A further evolvement of the small scale coating equipment has been the development of a micro roll 2 roll coater (MR2C). The MR2C is a true R2R coating machine, in contrast to the MRC. The advantage of this is the possibility of running at higher foil speeds and having a longer stretch of foil to vary coating parameters.

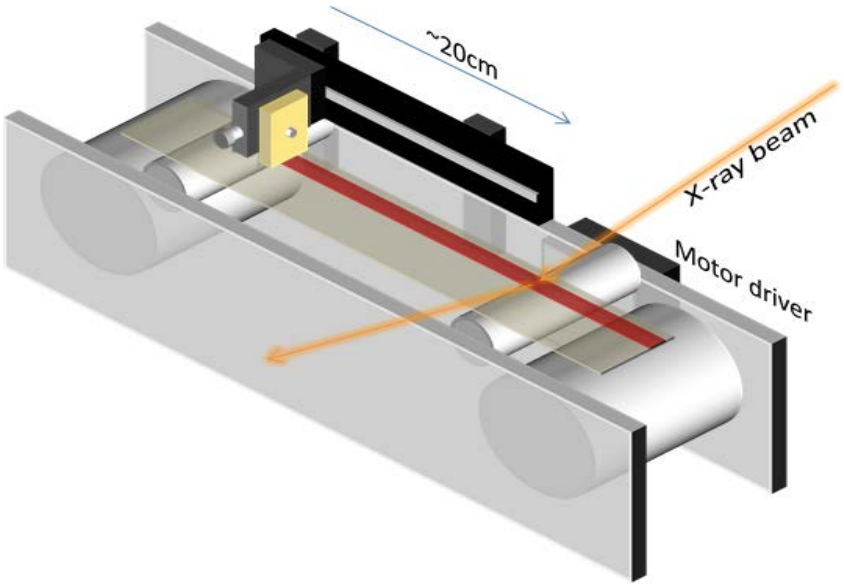

Figure 2.18: Micro Roll 2 Roll Coater (MR2C) constructed with the purpose of analyzing film morphology while drying by the use of X-rays.

The primary aim of this setup is to have a way of characterizing morphology. The machine is made with compatibility to grazing angle x-ray scattering experiments in mind. Using this technique a variation in the morphology as a function of changes in parameters, for instance thickness, speed and temperature is possible. Furthermore the movement of the coating head with respect to the characterization spot enables characterization of these parameters during the drying process of the film.

The system comprises two rollers mounted on bearings with the receiving roller being driven by a computer controlled stepper motor and the unwinding roller keeping tension by a Teflon screw providing friction. Two glides are mounted higher to assure a constant height of the foil as it is unrolled from the rear roller and onto the front roller. The film width is a maximum of 25 mm enabling coating of a complete 13 stripe based complete cell with the same offset as on the larger machines.

A translation unit is used for mounting of the slot-die head, enabling a variation of the distance from the coating head to the impinging x-ray beam from 2 cm – 20 cm.

2.8 Flatbed slot-die coater

Figure 2.19: An Erichson draw bar coater converted to a flatbed slot die coater. The purpose of the coater is to allow coating by slot die on glass substrates for analysis and calibration purposes.

One of the disadvantages of working on flexible substrates or soft substrates is the incurred difficulty in finding layer thicknesses of coated layers. The typically used method of measuring with a profilometer by scratching a sample and measuring the depth of the scratch can only rarely be used, due to the ever present risk of making scratches that are not only in the film which is to be measured, but also going into the underlying substrate. Measuring a thickness of a film at the edge of a coated film is possible, but rarely gives a correct value due to the edge effect of the coating method. Long scans over the edge and across a film will only give localized film variations, since getting the substrate to lie flat on a surface to within the accuracy wanted when measuring a 100 nm film is nearly impossible.

A solution to this problem have been to make a coater, which applied the same slot-die coating technique as the MRC, while doing so on a planar surface, enabling the use of glass substrates, which are much more scratch resistant and planar over longer ranges.

For this purpose an Erichson draw-bar coater was used, with a replacement of the draw bar with a positioning stage and slot-die head mount as seen in Figure 2.19. An Aluminum plate with heater elements was added as a substrate holder enabling use of elevated temperatures for the drying of the coating.

2.9 Summary

This chapter has described the process of roll coating in a roll 2 roll setting and, more importantly in this context, in a lab scale setting as a substitute for spin coating. The use of roll coating techniques in the lab could allow a quicker development of new materials, due to possibilities of testing and transferring in settings similar to the full scale production.

References

[1] N. Alleborn, Einführung und Überblick über industrielle Verfahren zum Auftrag dünner flüssiger Filme,, *Proceedings of Fundamentals and Methods in Coating*. LSTM Erlangen 2005 (n.d.), 1.

[2] P.M. Schweizer, Verfahren zur gleichzeitigen Mehrfachbeschichtung, *Proceedings of Fundamentals and Methods in Coating*. LSTM Erlangen 2005 (n.d.), 15.

[3] A.A. Tracton, in: Coatings Technology Handbook, CRC, Taylor & Francis, Boca Raton [u.a., 2006: pp. 31.1–31.30.

[4] F.C. Krebs, M. Hösel, M. Corazza, B. Roth, M.V. Madsen, S.A. Gevorgyan, et al., Freely available OPV—The fast way to progress, *Energy Technology*. (2013), n/a–n/a.

[5] F.C. Krebs, T. Tromholt, M. Jørgensen, Upscaling of polymer solar cell fabrication using full roll-to-roll processing, *Nanoscale*. 2 (2010), 873.

[6] J. Alstrup, M. Jørgensen, A.J. Medford, F.C. Krebs, Ultra Fast and Parsimonious Materials Screening for Polymer Solar Cells Using Differentially Pumped Slot-Die Coating, *ACS Applied Materials & Interfaces*. 2 (2010), 2819–2827.

[7] N. Espinosa, H.F. Dam, D.M. Tanenbaum, J.W. Andreasen, M. Jørgensen, F.C. Krebs, Roll-to-Roll Processing of Inverted Polymer Solar Cells using Hydrated Vanadium(V)Oxide as a PEDOT:PSS Replacement, *Materials*. 4 (2011), 169–182.

3. Organic Single Junction Solar Cells

During the last three years a vast array of different solar cells has been produced with variations in active layer materials, transport layers electrodes and geometries. Here a selected few are presented, which represents part of the range of materials worked on and part of the range of techniques used.

The results in this chapter will be based on previously unpublished results, with sections based on the papers Espinosa et. al [1] and Dam et. al [2] attached as appendix A2 and A1.

This chapter will however be started with an introduction to what the principles for the polymer solar cell are and which considerations to take.

3.1 Principle of the polymer organic solar cell

As conjugated polymers have their overlapping p-orbitals and the associated loosely bound π electron, the interesting thing for the use of the conjugated polymer is how to absorb the energy in the polymer by exciting the π electron to its antibonding state, π*, the high energy one, and then dissociate it from the polymer [3,4].

Having a π* electron is also described as an exciton together with its corresponding hole, both still bonded to the polymer.

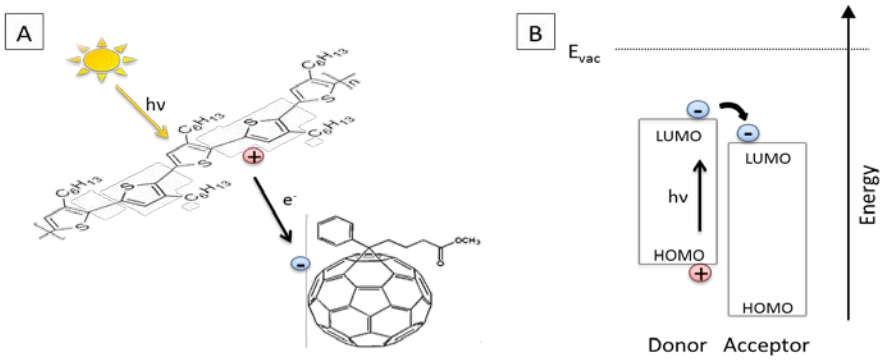

Figure 3.1: Process of light absorption in an organic polymer with the associated breakage of the exciton bond between the hole and electron by at the donor-acceptor interface and transfer of the electron to the acceptor.

The breaking of this exciton and dissociation from the polymers occurs by the introduction of an acceptor material, which has a lower LUMO level than the polymer. By transferring the excited electron from the LUMO level of the polymer (donor) to the LUMO level of the acceptor material the charges are separated and can pass through the respective material, donor/acceptor, to the corresponding electrode.

When fabricating organic solar cells the junction between the donor acceptor species needs to be close to the materials, since the exciton diffusion length within the donors are generally less than 20 nm. There have typically been two different approaches two achieving this: The use of either a bilayer heterojunction or a bulk heterojunction. The bilayer junction is made by producing cells with two separate layers

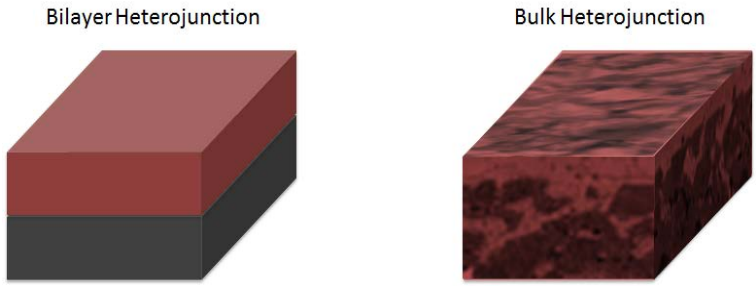

Figure 3.2: The two types of junctions used in the organic solar cells, both based on the heterojunction principle of donors and acceptors.

for the donor and acceptor materials, while the more commonly used bulk heterojunction is manufactured with a single mixed layer of donor acceptor material. The advantage of the bulk heterojunction lies in the short distance between acceptors and donors, increasing the change of exciton dissociation.

3.1.1 Donors

The donors for which results are presented in this thesis are shown in Figure 3.3. The most typically used of these is the P3HT donor, which was also shown in Figure 3.1A as an example of light absorption and charge transfer process. The usefulness of P3HT lies not only with the LUMO-HOMO level, but also with the relative simplicity of the polymer, the high mobility and the solubility and mixing with acceptors. The absorption of

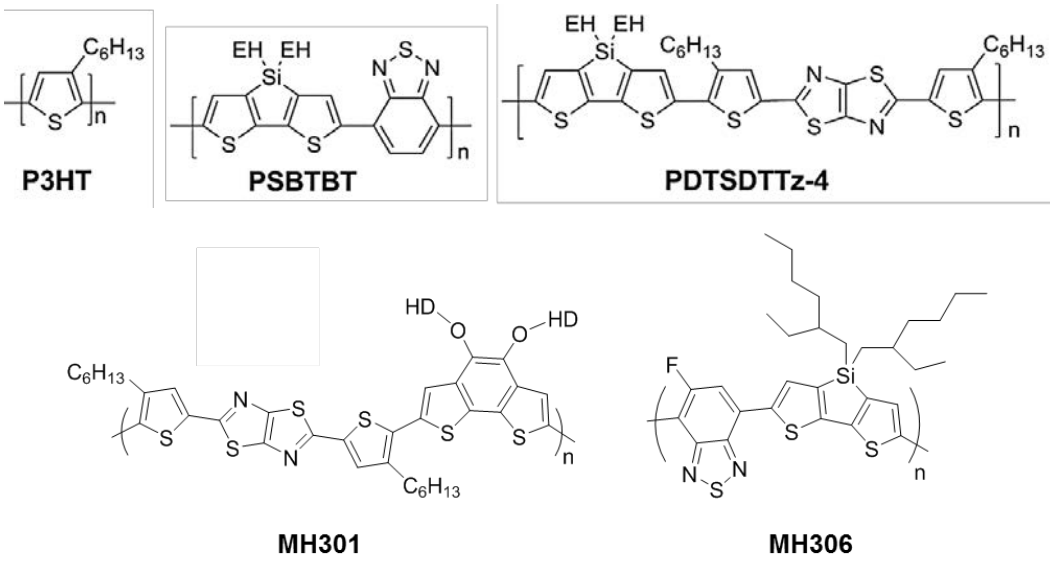

Figure 3.3: Examples of polymers used in polymer solar cells. The P3HT polymer has been around for the last decade, while PSBTBT [7] **is a low bandgap polymer and PDTSDTTz-4** [8] **is a polymer with better alignment to the donors resulting in a higher voltage output. MH301 and MH306 are similar in absorption to P3HT and PSBTBT respectively.**

P3HT is relatively high, however the bandgap of approximately 2 eV results in the polymer not absorbing any light with a wavelength longer than ≈620 nm.

Several polymers have later been synthesized with the aim of increasing the absorption range of the polymer by lowering the bandgap and thereby increasing the efficiency of the solar cells, as shown by Bundgaard et. al. [5]. The absorption limit for the

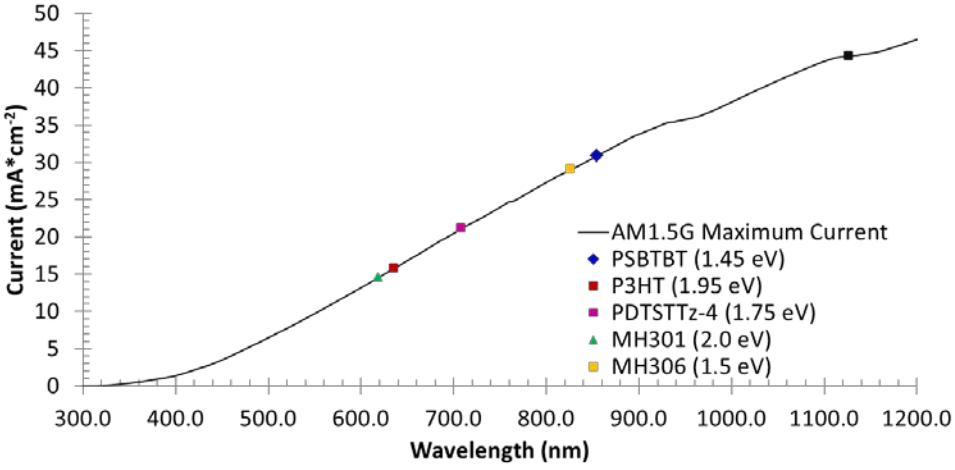

Figure 3.4: The maximum current which can be extracted from the incoming sun light under the assumption of 100% absorption, 100% photon to electron-hole pair conversion and 100% extraction.

polymers presented in Figure 3.3 are shown in Figure 3.4 plotted on a scale of maximum current, which can be extracted at that limit, assuming absorption of all the photons with energies higher than the bandgap.

Low bandgap polymer with an absorption out to 1000 nm (bandgap of 1.1 eV) [6] have been developed and polymers such as PSBTBT also shown in Figure **3.3** shows absorption out to 850 nm, however it is difficult to make a polymer which absorbs all the photons with an energy higher than the polymers bandgap.

3.1.2 Acceptors

A selection of commonly used acceptor molecules are shown in Figure 3.5. In this work only PCBM have been used due to its lower cost, however by the use of other acceptors such as $PC_{71}BM$ or ICBA, the efficiency of the organic solar cells has shown to improve. Using $PC_{71}BM$, the efficiency of the solar cells are increased both due to a lower bandgap in $PC_{71}BM$ resulting in an absorption in the visible range within the acceptor molecule and an excellent miscibility with the donors, increasing the chances of exciton separation [7,8]. The use of ICBA as an acceptor has shown to be favorable with P3HT due to a higher LUMO level of the ICBA acceptor molecule, which results in a higher voltage of the solar cell output.

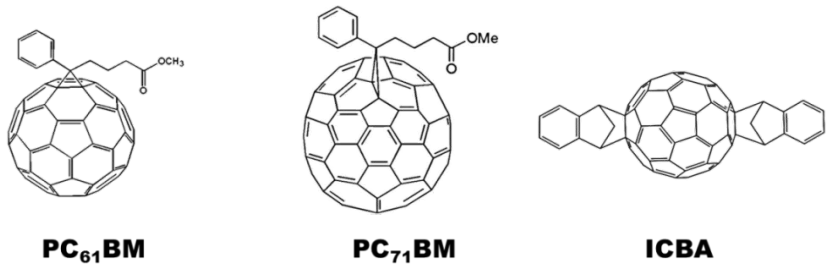

Figure 3.5: Typically used acceptors in organic solar cells. A) $PC_{60}BM$ is the cheapest and most often used acceptor. B) $PC_{71}BM$; The C_{70} variant of the PCBM molecule is much more expensive but offers a higher absorption and tends to give higher performance. C) ICBA; This acceptor is often used due to its better energy alignment with the typically used P3HT polymer. It gives a higher voltage compared to the other to, with up to 1 V for P3HT under concentrated light conditions

The higher voltage which can be obtained by use of ICBA is caused by the alignment of the donors bandgap to the bandgap of the acceptor[9], and together with the in-

herent losses in the cells defines the solar cell open circuit voltage. The maximal voltage which can be obtained has been found to be,

$$V_{oc} = (1/e)\left(\left|E_{HOMO}^{Donor}\right| - \left|E_{\mathrm{LUMO}}^{Acceptor}\right|\right) - 0.3\ \mathrm{V}$$

where the 0.3 V is an empirical constant which refers to the internal losses [9–11].

3.2 Structure of a typical organic polymer solar cell

The commonly used polymer and acceptor in organic solar cells has for a long time been P3HT and PCBM, not due to an incredibly high performance, but more due to their reasonable performance, with a high tolerance to different processing conditions and a much better stability than many other polymer acceptor mixes. At the same time the P3HT polymer is one of the cheapest and easiest polymers to buy / produce.

The electrical structure of the solar cells in the two most often used geometries are as shown in Figure 3.6. Both structures are based on the light entering through the transparent ITO front electrode. Figure 3.6A shows the energy levels of the materials used in a normal geometry solar cell, where the electrons goes through the Aluminum back electrode and the holes through the front ITO electrode. In the case of a normal geometry OPV solar cell, a PEDOT:PSS layer is used for band alignment and electron blocking between the ITO electrode and active layer, while an optional Lithium Fluoride layer is sometimes used at the Aluminum back electrode.

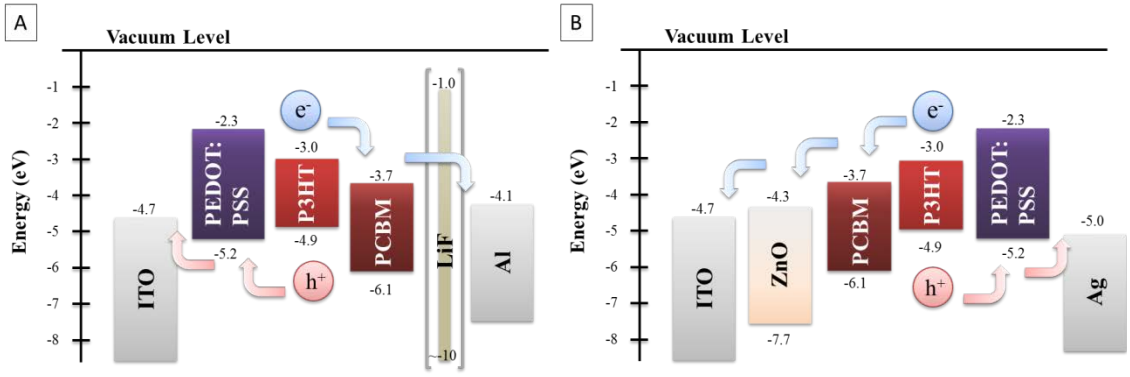

Figure 3.6: Energy diagram of a A) Normal geometry solar cell and B) Inverted geometry solar cell. The LiF layer in the normal geometry is not always used. In both types the P3HT:PCBM material is in a mixed layer creating a bulk hetero junction (BHJ).

Figure 3.6B shows the energy levels of the materials of an inverted geometry OPV solar cell. In the inverted geometry, the inversion lies in the direction of transport of the charge carriers. This type of device uses the ITO electrode to transport the electrons and a silver back electrode to transport the holes. To direct the charges a Zinc Oxide layer is used between the ITO layer and active layer, which only transports the electrons, while a PEDOT:PSS layer is used between the active layer and the silver back electrode.

3.3 Electrical characteristics of an organic solar cell

Since the total power which can be extracted is the product of the current and voltage, bad alignment of the energy levels of the acceptor, donor and buffer layers will reduce the operating voltage and thereby the power output of the solar cell. An example of the electrical characteristics of a solar cell is shown in Figure 3.7. The main characteris-

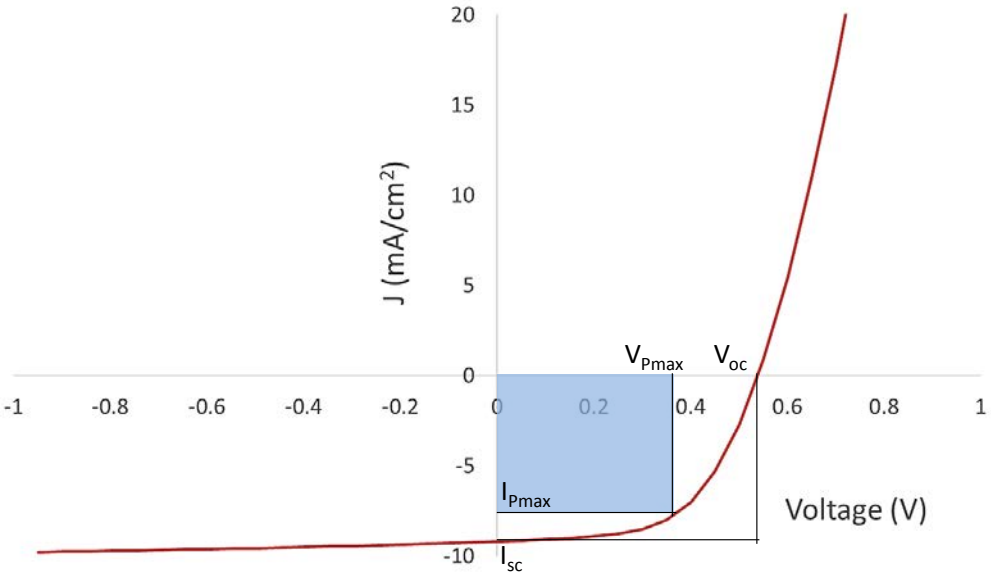

Figure 3.7: Illustration of the Current-Voltage characteristics of a solar cell. Important parameters, such as the open circuit voltage, V_{oc}, and short circuit current, I_{sc}, are shown, together with an illustration of the Maximum power point Current and Voltage, and the fill factor, FF, being the ratio between the area described by $\{I,V\}_{Pmax}$ and V_{oc},I_{sc}.

tics are the short circuit current, I_{SC}, and the open circuit voltage, V_{OC}. The maximum power point for a solar cell is defined as the point of the highest power output, and re-

lates to the open circuit voltage, V_{oc}, and short circuit current, I_{sc}, with a quantity described as the fill factor, *FF*.

$$FF = \frac{P_{max}}{V_{oc} I_{sc}}$$

3.4 Spin and roll coated cell with varying Vanadium or PEDOT:PSS hole transport layers

The purpose of these cells were to test the possibility of using Vanadium Oxide as a substitute for PEDOT:PSS as a Hole Transport Layer (HTL) in an inverted geometry organic solar cell. Vanadium oxide has previously been tested by others in normal geometry cells or hybrids [12] and often by use of evaporative techniques as a hole transport layer [13–15]

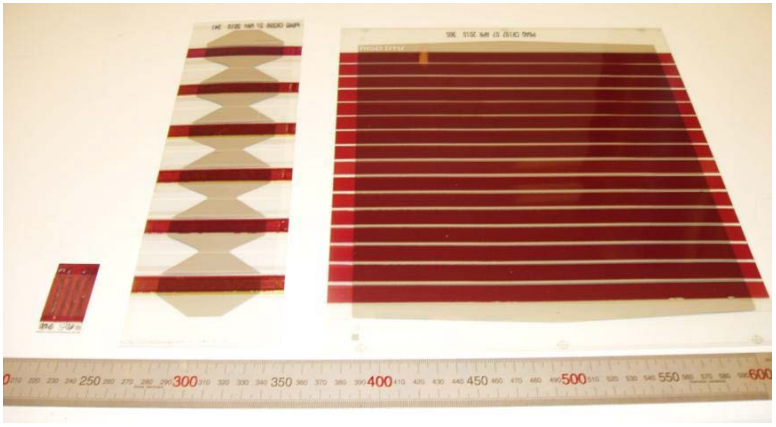

Figure 3.8: Three type of VTIP devices. To the left a spin coated cell on ITO-glass slides, in the middle roll coated individual cells on ITO-PET substrate and to the right a full module with 16 serially connected stripes. Reproduced with permission from MDPI [1].

The cells produced and tested are divided in to three distinct steps, however all made in the inverted geometry. Initial tests were completed on spin coated glass-ITO substrates, as seen as the outer left cell in Figure 3.8. After testing on glass, the second set was PET with ITO fully roll coated single cells, with an area of 4.2 cm^2. Finally a set of full size modules consisting of 16 stripes connected in series with a total area of 360 cm^2 were made.

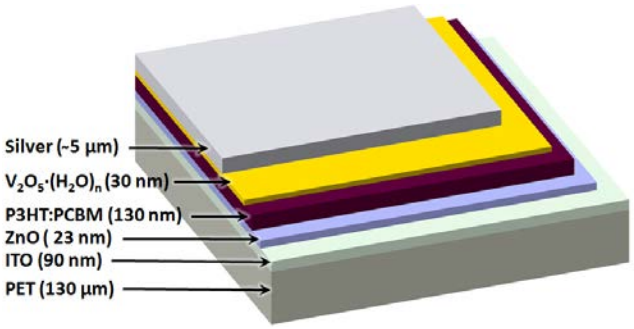

Figure 3.9: The structure of the cells. Devices were produced in an inverted structure with an ITO bottom electrode, a ZnO ETL layer, a P3HT:PCBM active layer, a Vanadium Oxide HTL layer and a screen-printed full silver top electrode. Reproduced with permission from MDPI [1].

3.4.1 Spin coated cell optimizations

Different concentrations of VTIP in isopropanol (3.5, 6.5, 12.5, 25, 50 and 100 mg/mL) was used as a HTL in the cells, and different numbers of layers were fabricated. The results of the best cells are shown in Figure 3.10. These were achieved with one or two layers of 12.5 mg/mL of VTIP. The efficiency of the VTIP based cells was roughly 0.4%.

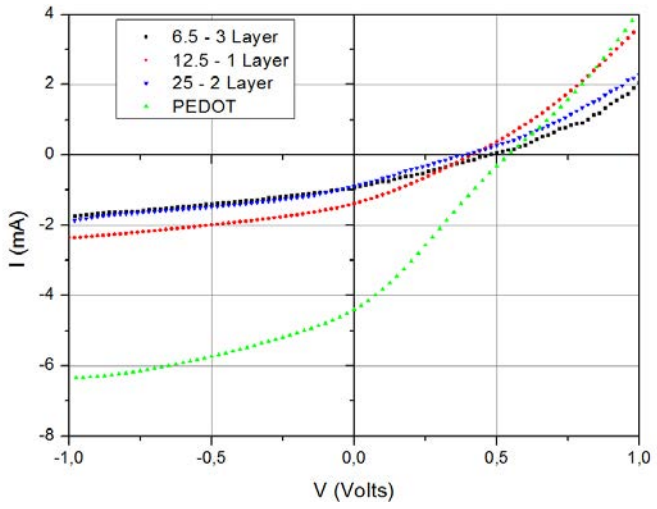

Figure 3.10: Spin coated devices on ITO glass slides with an area of 0.5 cm^2. Devices reported are coated with 1, 2 or 3 layers of varying concentration of VTIP. Reproduced with permission from MDPI [1].

Comparing the efficiency of the Vanadium based cells to the PEDOT based cells, the vanadium oxide cells are limited by the conductivity of the cells resulting in both low current and a low fill factor.

3.4.2 Analysis of an annealed Vanadium Oxide film

Hydrated vanadium(V)oxide films were prepared on glass, silicon, and PET substrates and characterized by optical spectroscopy, ellipsometry, profilometry, scanning electron microscopy (SEM), energy dispersive X-ray spectroscopy (EDX), and grazing incidence wide angle X-ray scattering (GIWAXS). Measurements with GIWAXS on silicon substrates combined with the structural model of $(H_2O)_n$ [16], indicated the films to be largely low-crystalline hydrated vanadium pentoxide $V_2O_5{\cdot}(H_2O)_{0.3}$ with an interlayer spacing of 1.11 nm, as seen in the measurements shown in Figure 3.11. The hydrated vanadium pentoxide is always of low crystallinity, typically characterized as nanocrystalline, and the locally ordered structure was therefore determined by pair distribution function analysis [16]. EDX data confirmed the relative vanadium and oxygen concentrations. A SEM image of a cleaved cross section through a 15 nm-thick film is shown in Figure 3.12. The low conductivity of the hydrated vanadium(V)oxide films is a limiting factor in the devices, which is a major difference between this study and pre-

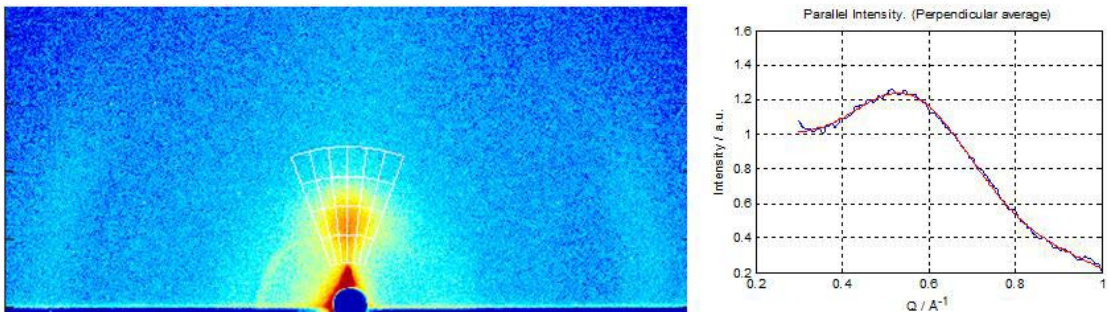

Figure 3.11: Left side shows the GIWAXS data as measured, with a logarithmic colour scale representing intensities. The strongest scattering feature near the center of the image corresponds to the 001 reflection, whereas the weaker scattering at the edges of the image, correspond to the 110 and 11-1 reflections [16], showing that the crystallites are preferentially oriented with the ab-plane parallel to the substrate surface. Right: Integration over 001 peak, assuming sample to detector distance of 121 mm, yields a d-spacing of 11.1 Å. Reproduced with permission from MDPI [1].

Figure 3.12: SEM cross section (tilted 17°) of 15 nm-thick cleaved $V_2O_5·(H_2O)_{0.3}$ film on a crystal silicon substrate showing film thickness and uniform morphology on the film surface.

vious studies where vanadium oxide films were prepared by different methods [12,13].

It has been reported that for hydrated vanadium(V)oxide films the conductivity in thicker films increases with the annealing temperature as long as the film retains the layered slab structure with a bilayer of vanadium oxide stacked between layers of water molecules. However, annealing at higher temperatures transforms the hydrated oxide to crystalline V_2O_5 with much lower conductivity, presumably because of the formation of grain boundaries [17]. Compared to the previously reported measurements on vanadium(V)oxide xerogel films which were cast from gel solutions [17,18], our VTIP cast films are extremely thin, with a much higher surface to volume ratio. This makes dehydration effective at lower temperatures, so that our 120–140 °C anneal results in n values of ~0.3, comparable to much higher temperature annealing processes on the gel based films where similar n values required annealing at above 250 °C.

The thickness of the roll coated films on PET substrates was calculated using a dry film density based on the GIWAXS results and the speed, coating width and flow rate used for the coating process, according to a formula

$$t = \frac{f \times \rho_{\mathrm{w}} \times M_{\mathrm{V2O5}}}{2 \times S \times W \times \rho_{\mathrm{d}} \times M_{\mathrm{VTIP}}}$$

where f is volumetric flow, ρ_{w} and ρ_{d} are the densities of the VTIP solution and the dry $V_2O_5·(H_2O)_{0.3}$ film, M_{V2O5} and M_{VTIP} are molecular weights, and S and W are the coating speed and width of the stripe. For a PET sample coated with 15 mg/mL, a profilometer measurement of the dry film thickness showed a range with an average of 34 ± 9 nm, in agreement with the 27 nm predicted by our model.

3.4.3 Variation of the Vanadium concentration in an in-situ experiment

To test the parameter space for the thickness of the vanadium oxide layer in a roll coating setting, an in-situ thickness variation experiment was completed. The experiment was done using the technique previously shown in work by Alstrup et. al. [19] and also described in the roll coating chapter of this thesis for use on the mini roll coater.

The technique involves a gradual change of the dilution of the coated solution by the use of a dual pump setup, where one pump is pumping a solution of the VTIP precursor in the maximal concentration which one wants to coat, and the other pump is pumping the pure solvent used to create the gradual change of concentration.

The result of the experiment is seen in Figure 3.13, where three separate dilution runs are shown. Two runs with a dilution using isopropanol shows the need of a 5 mg/ml concentration corresponding to a 10 nm dry thickness to be needed for the solar cells to work. A second experiment where butanol was used to dilute the VTIP stock solution shows a twice as thick layer to be needed for the cells to work, however the use of butanol also showed cells with an overall lower efficiency.

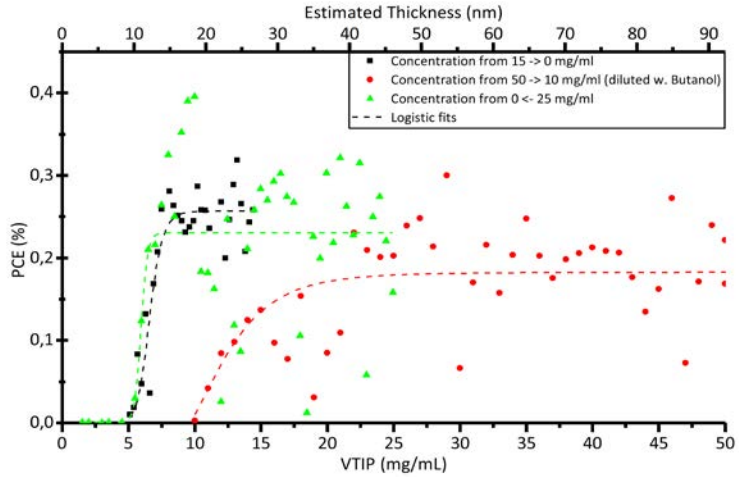

Figure 3.13: Variation of the concentration of the VTIP solution in the coating process. A two pump system similar to that described in the Roll coating chapter of the thesis was used. Reproduced with permission from MDPI [1].

Table 3.1: Performance of 360 cm^2 modules in outdoor measurements.

Measurement	PCE (%)	Voc (V)	Isc (mA)	FF (%)
Outdoor	0.12 ± 0.06	6.0 ± 2.0	−25.4 ± 4.8	26.8 ± 1.1

3.4.4 Full size modules

Based on the gradient experiment, a VTIP concentration of 15 mg/ml in isopropanol was chosen for production of the full size modules shown on the right in Figure 3.8. The modules consisted of 16 stripes connected in series with a total module area of 360 cm^2. The performance of the modules is shown in Table 3.1

Although the performance of the large modules was not very high, a degradation study on the modules was completed to compare the lifetime of a module made with Vanadium oxide and a reference module made with PEDOT. The cells were mounted on an outdoor solar tracker and the dose, to which the modules were exposed was registered using a bolometer. Unfortunately, the aging of the modules showed a degradation to D80 of ≈50MJ/m^2 for the vanadium based cells, and a D80 of >150MJ/m^2 for the PEDOT based modules, where D80 is the dose at which the module had dropped to 80% of its initial performance.

3.4.5 Summary of vanadium experiments

The performance of both the cells and modules made with vanadium oxide indicates that the use of vanadium oxide as a substitute for PEDOT in the solar cells not to be a viable solution with the ProcessOne [20] method used in these experiments.

3.5 Roll coated cells produced on the MRC

One of the initial uses of the MRC presented in chapter 2 was for manufacturing of solar cells on a 13 mm wide ITO substrate with the three solvents chlorobenzene, 1,2-dichlorobenzene and 1,2,4-trichlorobenzene. The result of which was published and is attached as appendix A1. The goal of the experiments conducted was to test for variation of performance on the basis of different solvents and coating at different temperatures. An example of the J-V curves for a subset of the cells are presented in Figure 3.14, together with an example of the newer ITO-free cells based on the flextrode sub-

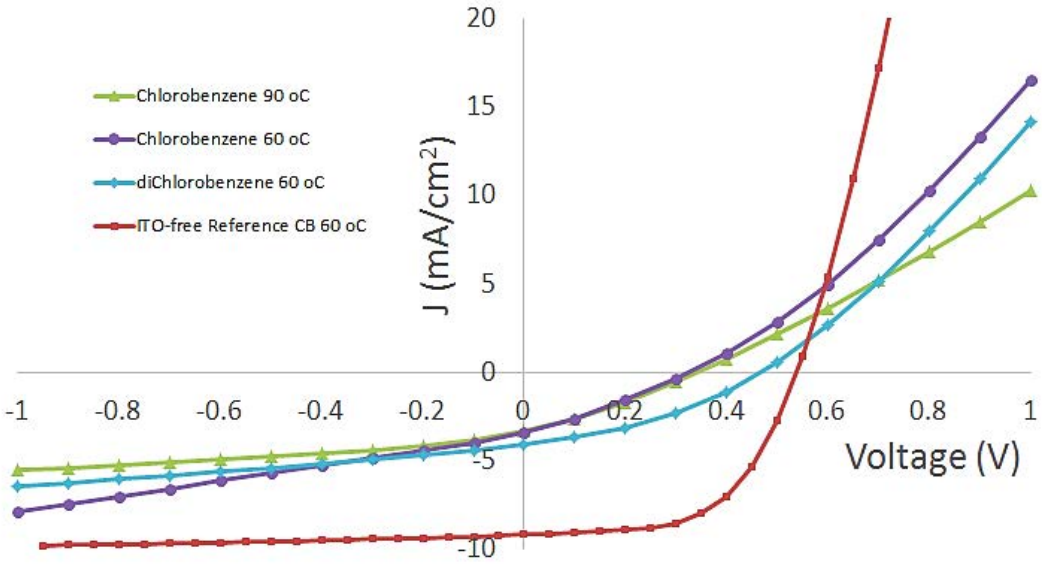

Figure 3.14: Comparison of solar cells manufactured at different parameters. The use of different solvents and temperatures shows a difference, however the ITO-free cells shows much better performance compared to the PET-ITO based cells.

strate. Much of the reason for the large discrepancy between the ITO based cells and the ITO free cells lies with the use of ITO substrates with a high resistance. The nominal resistance of the ITO substrate used was 100 Ω/□, while the resistance of the Flextrode design is a combination of a ≈200 Ω/□ PEDOT:PSS layer and 0.1 Ω/□ silver fingers.

A further issue with the ITO flexible substrates is the high risk of cracking of the ITO layer upon bending. The ITO handles bending badly due to its brittleness. Examples of sheet resistivities ranging from the nominal 100 Ω/□, up to was 1.5 kΩ/□, was measured with the batch of ITO substrate used for the production of these cells, indicating that the efficiencies would be lower than for non-flexible or higher quality ITO substrates.

3.6 ITO-free solar cells

The switch to ITO free solar cells has been completed, as a way to avoid the issues with the ITO substrates. The use of ITO substrates comes at a high cost. The Indium in ITO is a scarce material and prices of it is increasing, with the evaporative methods used to

manufacture it and the patterning process needed to define the electrode patterns being further cost intensive processes. It has been so, that both cost and energy wise the ITO substrate made up approximately half of the total cost of the solar cell [21–23]. Combined with the issues of flexibility and the high resistances for ITO on PET com-

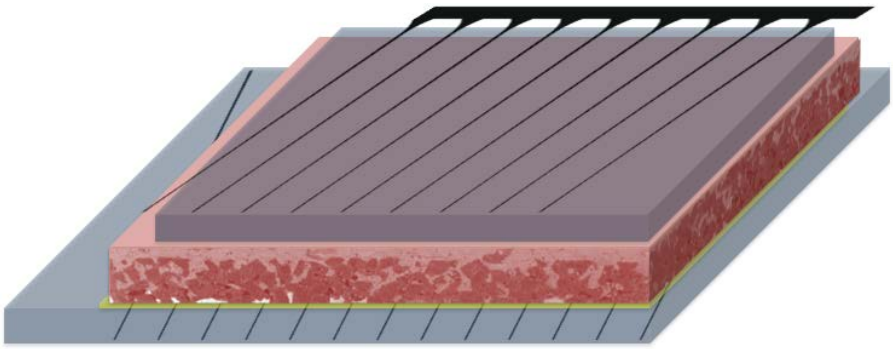

Figure 3.15: Structure of a -ITO free solar cell with a PEDOT:PSS Ag grid electrode. The flextrode bottom electrode is illustrated as a black grid with a blue PEDOT:PSS layer. A yellow layer indicates the ZnO layer. The red layer is the active material layer with a dark and light part indicating the bulk heterojunction of donor and accepter materials. A top electrode consists of three separate PEDOT:PSS layers and a silver grid electrode.

pared to ITO on glass substrates, the development of a different electrode was done. The electrode design that has replaced the previously used ITO-PET substrates, is a PET foil, which is flexoprinted with a finger or honeycomb silver grid and further flexoprinted with a full area highly conductive PEDOT:PSS layer. For the use in an inverted geometry the electrode is further slot-die coated with an Aluminum doped Zink Oxide

Table 3.2: The coating parameters used for the developed coating stack as shown in Figure 3.15

Layer	Material	Concentration	Temp	Speed	Flow	T_{wet}
			°C	m/min	mL/min	µm
Substrate	Flextrode					
1st active layer	Active Polymer	20:20 mg/ml	60	1.0	0.20	15
Compatibilizer	PEDOT F010:IPA	1:4 vol/vol	60	1.0	0.10	8
HTL	PEDOT 4083:IPA	1:2 vol/vol	60	1.0	0.30	23
Conducting Layer	PEDOT F10:IPA	1:1 vol/vol	60	1.0	0.40	31
Top Electrode	Ag PV410		60	1.2		

layer. An illustration of the electrode structure is shown in Figure 3.15, with an active layer and a semitransparent top electrode. The parameters for the typical cell on flextrode with the PEDOT:PSS silver grid top electrode is shown in Table 3.2. The top PEDOT layer is actually a combination of three separate PEDOT layers; a thin diluted PEDOT (F010) layer to aid in adhesion, a second PEDOT layer (Clevios 4083) to give hole selectivity and a top layer of high conductivity F010 PEDOT.

Table 3.3: Performance of different polymers coated on the MRC with the Flextrode substrate.

Active layer	**Ratio**	**Solvent**	**V_{OC}**	**J_{SC}**	**FF**	**PCE**
			V	mA cm^{-2}	%	%
P3HT:PCBM	1:1	CB	0.54	-9.20	57.8	2.85
PSBTBT:PCBM	2:3	$CHCl_3$	0.56	-5.66	41.7	1.33
PDTSTTz-4:PCBM	2:3	CB	0.68	-7.15	37.3	1.81
MH301:PCBM	1:2	CB	0.83	-4.67	54.1	2.09
MH306:PCBM	2:3	CB	0.63	-5,57	41.4	1.33

Using the flextrode substrate and the 3-PEDOT top electrode structure, a range of polymers were made on the MRC with performance numbers for the various polymers presented in Table 3.3. The highest performance cells have still been P3HT:PCBM cells, however this is also the material for which the process has originally been optimized. Variation of the solvents, additives and temperatures together with optimization of thicknesses can improve on the performance of the polymers.

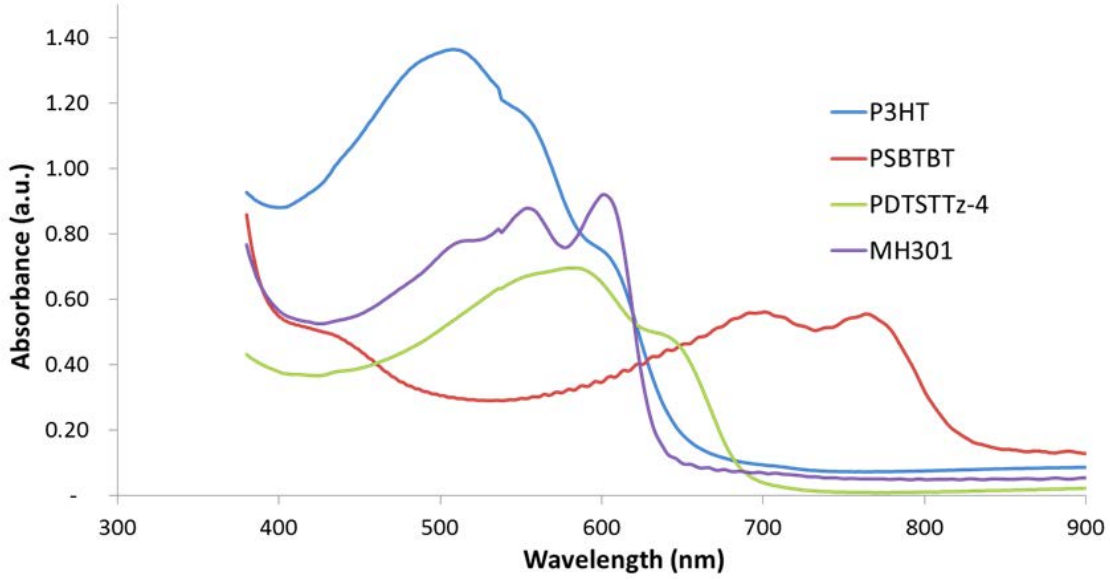

Figure 3.16: Absorbance of coated films of four of the tested polymers. The MH306 polymer was unfortunately not tested, however the absorption is very similar to PSBTBT.

The low bandgap polymers are somewhat low in performance, which to a certain degree can be blamed on the absorption of the bottom electrode PEDOT, which has a decreasing transmission at longer wavelengths, as shown in chapter 1. Considering the light available after the passage of the substrate and bottom electrode also shows some of the reason as to why the flexible solar cells shows a lower performance. The maximum current that can be extracted from the different substrates, under the assumption of a 100% EQE after passage of the substrate and bottom electrode are shown in Table 3.4. The drop in maximum attainable current when using the flextrode substrate compared to a ITO glass substrate is >20%.

Table 3.4: Maximum current which is achievable by the use of the flextrode depending on the substrate used. Numbers are an integration of the AM1.5G spectrum over the shown wavelengths. ITO M-type is a ITO glass reference substrate.

Substrate	350-800 nm	350-650 nm	650-800 nm
Melinex Flextrode	18.5	11.8	6.7
Mitsubishi flex	15.3	9.5	5.8
Amcor flex	16.6	10.5	6.1
ITO M-type	23.3	14.4	8.9

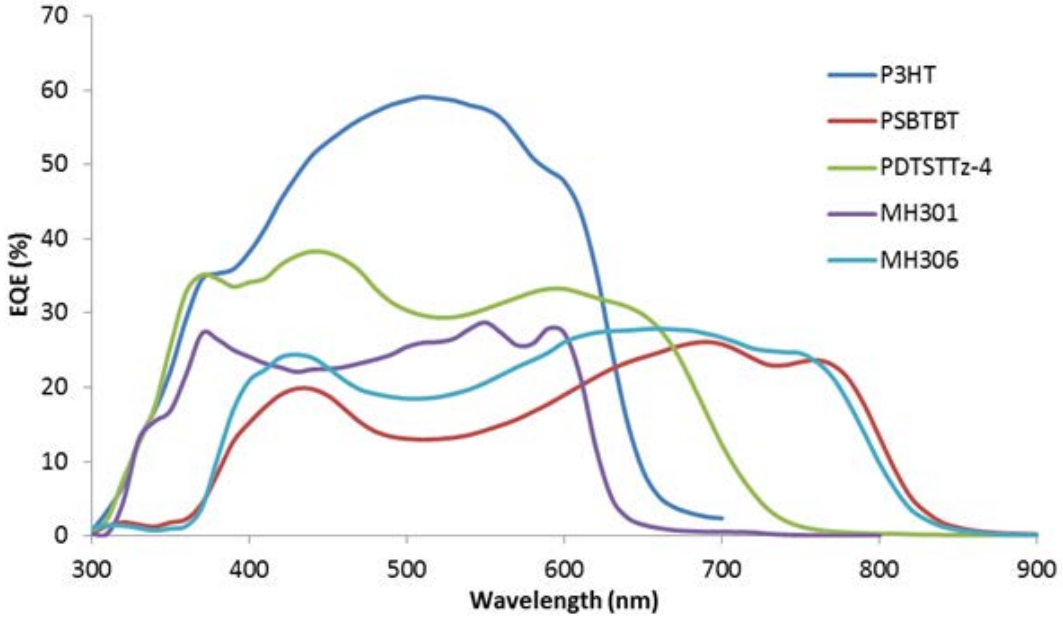

Figure 3.17: EQE measurements of different polymers manufactured using the Flextrode substrate and a F10 PEDOT:PSS and silver grid top electrode.

External quantum efficiency (EQE) measurements on the cells, as shown in Figure 3.17, indicates the absorption and charge extraction of the P3HT cells to be substantially higher than for the other polymers, but simultaneously follows the trends of the absorption curves in Figure 3.16, with the offset of the PEDOT absorption showing as the EQE values relative to the Absorbance numbers are higher at the lower wavelengths.

The use of other polymers than P3HT shows potential to increase efficiencies further compared to the present level, however as also shown some optimizations has to be completed for the solar cells.

3.7 Summary

This chapter has been a description of a large range of different solar cells produced with a range of techniques and with several variations in the materials used. From spin coating and full roll-2-roll production of solar cells with vanadium oxide hole transport layers to ITO based flexible devices based on the ProcessOne methods completed on a lab scale roll coater, to ITO-free devices with a range of different polymers used.

References

[1] N. Espinosa, H.F. Dam, D.M. Tanenbaum, J.W. Andreasen, M. Jørgensen, F.C. Krebs, Roll-to-Roll Processing of Inverted Polymer Solar Cells using Hydrated Vanadium(V)Oxide as a PEDOT:PSS Replacement, *Materials*. 4 (2011), 169–182.

[2] H.F. Dam, F.C. Krebs, Simple roll coater with variable coating and temperature control for printed polymer solar cells, *Sol. Energy Mater. Sol. Cells*. 97 (2012), 191–196.

[3] B.A. Gregg, M.C. Hanna, Comparing organic to inorganic photovoltaic cells: Theory, experiment, and simulation, *J. Appl. Phys.* 93 (2003), 3605–3614.

[4] B.A. Gregg, Excitonic solar cells, *J. Phys. Chem. B*. 107 (2003), 4688–4698.

[5] E. Bundgaard, F.C. Krebs, Low band gap polymers for organic photovoltaics, *Sol. Energy Mater. Sol. Cells*. 91 (2007), 954–985.

[6] E. Zhou, J. Cong, K. Hashimoto, K. Tajima, Introduction of a conjugated side chain as an effective approach to improving donor–acceptor photovoltaic polymers, *Energy Environ. Sci.* 5 (2012), 9756–9759.

[7] M.M. Wienk, J.M. Kroon, W.J.H. Verhees, J. Knol, J.C. Hummelen, P.A. van Hal, et al., Efficient Methano[70]fullerene/MDMO-PPV Bulk Heterojunction Photovoltaic Cells, *Angew. Chem. Int. Ed.* 42 (2003), 3371–3375.

[8] Y. Yao, C. Shi, G. Li, V. Shrotriya, Q. Pei, Y. Yang, Effects of C70 derivative in low band gap polymer photovoltaic devices: Spectral complementation and morphology optimization, *Appl. Phys. Lett.* 89 (2006), 153507–153507–3.

[9] M.C. Scharber, D. Mühlbacher, M. Koppe, P. Denk, C. Waldauf, A.J. Heeger, et al., Design Rules for Donors in Bulk-Heterojunction Solar Cells—Towards 10 % Energy-Conversion Efficiency, *Adv. Mater.* 18 (2006), 789–794.

[10] C.J. Brabec, A. Cravino, D. Meissner, N.S. Sariciftci, T. Fromherz, M.T. Rispens, et al., Origin of the Open Circuit Voltage of Plastic Solar Cells, *Adv. Funct. Mater.* 11 (2001), 374–380.

[11] A. Cravino, Origin of the open circuit voltage of donor-acceptor solar cells: Do polaronic energy levels play a role?, *Appl. Phys. Lett.* 91 (2007), 243502.

[12] J.-S. Huang, C.-H. Wu, C.-Y. Chou, M.-Y. Liu, W.-H. Lin, Y.-H. Lin, et al., Solution-processed vanadium oxide interlayer for improving the performance of polymer/ZnO nanorod hybrid solar cells, in: 2009 34th IEEE Photovolt. Spec. Conf. PVSC, 2009: pp. 000554–000556.

[13] V. Shrotriya, G. Li, Y. Yao, C.-W. Chu, Y. Yang, Transition metal oxides as the buffer layer for polymer photovoltaic cells, *Appl. Phys. Lett.* 88 (2006), 073508–073508–3.

[14] J. Wu, J. Hou, Y. Cheng, Z. Xie, L. Wang, Efficient top-emitting organic light-emitting diodes with a V2O5 modified silver anode, *Semicond. Sci. Technol.* 22 (2007), 824.

[15] G. Li, C.-W. Chu, V. Shrotriya, J. Huang, Y. Yang, Efficient inverted polymer solar cells, *Appl. Phys. Lett.* 88 (2006), 253503–253503–3.

[16] V. Petkov, P.N. Trikalitis, E.S. Bozin, S.J.L. Billinge, T. Vogt, M.G. Kanatzidis, Structure of $V_2O_5 \cdot nH_2O$ Xerogel Solved by the Atomic Pair Distribution Function Technique, *J. Am. Chem. Soc.* 124 (2002), 10157–10162.

[17] G.N. Barbosa, C.F.O. Graeff, H.P. Oliveira, Thermal annealing effects on vanadium pentoxide xerogel films, *Eclética Quím.* 30 (2005), 7–15.

[18] Y. Wang, G. Cao, Synthesis and Enhanced Intercalation Properties of Nanostructured Vanadium Oxides, *Chem. Mater.* 18 (2006), 2787–2804.

[19] J. Alstrup, M. Jørgensen, A.J. Medford, F.C. Krebs, Ultra Fast and Parsimonious Materials Screening for Polymer Solar Cells Using Differentially Pumped Slot-Die Coating, *ACS Appl. Mater. Interfaces*. 2 (2010), 2819–2827.

[20] F.C. Krebs, S.A. Gevorgyan, J. Alstrup, A roll-to-roll process to flexible polymer solar cells: model studies, manufacture and operational stability studies, *J. Mater. Chem.* 19 (2009), 5442.

[21] N. Espinosa, R. García-Valverde, A. Urbina, F.C. Krebs, A life cycle analysis of polymer solar cell modules prepared using roll-to-roll methods under ambient conditions, *Sol. Energy Mater. Sol. Cells*. 95 (2011), 1293–1302.

[22] N. Espinosa, R. García-Valverde, F.C. Krebs, Life-cycle analysis of product integrated polymer solar cells, *Energy Environ. Sci.* 4 (2011), 1547.

[23] B. Azzopardi, C.J.M. Emmott, A. Urbina, F.C. Krebs, J. Mutale, J. Nelson, Economic assessment of solar electricity production from organic-based photovoltaic modules in a domestic environment, *Energy Environ. Sci.* 4 (2011), 3741–3753.

4. X-ray and TEM morphology characterization of nanoparticle based solar cells

Making an organic photovoltaic (OPV) from nanoparticles instead of the traditional use of solvent based inks is one of the ways to reduce the use of solvents for solar cell manufacturing and thereby making the OPV production both more environmental friendly and cheaper in both terms of embodied energy and traditional economic cost [1]. However, when manufacturing the solar cells from nanoparticles instead of solvents, the traditional bulk heterojunction is not obtained [2], but a more complicated structure of packed nanoparticles with an internal morphology and an external packaging morphology [3,4].

One of the ways to characterize the morphology of nanoparticle based polymer solar cells is by using x-ray characterization. A Near-Edge X-ray Absorption Fine Structure (NEXAFS) spectrum is taken to find the absorption peaks for the materials inside the particles. The most significant components are chosen to do a scanning transmission x-ray microscopy (STXM) image of the sample with the chosen energies and a following de-convolution of the amount of each component in each pixel. This chapter will show results based on both x-ray and electron microscopy of the morphology of the nanoparticle structure.

The P3HT polymer system has been previously described in [5], however no analysis of particles based on chlorobenzene as the initial solvent has been completed. The low-band gap polymer PSBTBT has previously been studied by Morana et. al. [6] who did morphology studies on the PSBTBT polymer, while Schmith et. al. did in-situ X-ray scattering to estimate the crystallinity during the drying process [7]. However, no previous experiments have been completed on nanoparticles of the PSBTBT polymer.

4.1 Preparation of nanoparticles

The aqueous inks were prepared according to the procedure presented by Landfester et al. [8], with minor variations as described in Andersen et. al. [9]. PSBTBT and PCBM

was dissolved in chloroform while P3HT and PCBM was dissolved in Chlorobenzene, after which an aqueous solution of sodium dodecyl sulfate (SDS) was added and allowed to form a macro-emulsion for 1 hour while vigorously stirring in both. The macro-emulsion was subjected to ultrasound energy to form a micro-emulsion, which was heated at 75 °C for 3 hours to evaporate away the chloroform/chlorobenzene, resulting in an organic nanoparticle dispersion in water. The dispersion was dialyzed against demineralized water to remove excess SDS. The remaining dispersion was concentrated by centrifugation in a dialysis centrifugation tube to approximately 55-60 mg/mL. Specification of the two batches can be seen in Table 4.1.

Table 4.1: Specifications of the nanoparticles used for the experiments. Two different batches were made for devices and STXM sample of each of the polymers

Batch	Solid (mg)	Solvent (mL)	SDS conc. (g/L)	SDS (mL)	Ultra-sound	Size (nm) SAXS
Device	740	17.5	30	50	6.5 min, 900 W	32 (10)
STXM	100	5.3	0.357	9.3	5.0 min, 650 W	-

4.2 Near-Edge X-ray Absorption Fine Structure

To calibrate the intensities of X-ray absorption a scan over the X-ray energy range is completed initially on a pristine sample consisting of a thin film spin coated from a solvent based solution of the respective component.

4.2.1 Preparation of pristine samples for NEXAFS

Pristine samples were prepared by spin coating on small glass slides. A 1 x 1 cm^2 glass slide was pre-treated with standard cleaning process and a 10 min ozone treatment. The substrates were then spin coated with a thin layer of Clevios 4083 PEDOT:PSS, to allow a lift off of the spin coated films. The PEDOT:PSS layer was air dried for 2 min after which the solvent based solutions were spin coated.

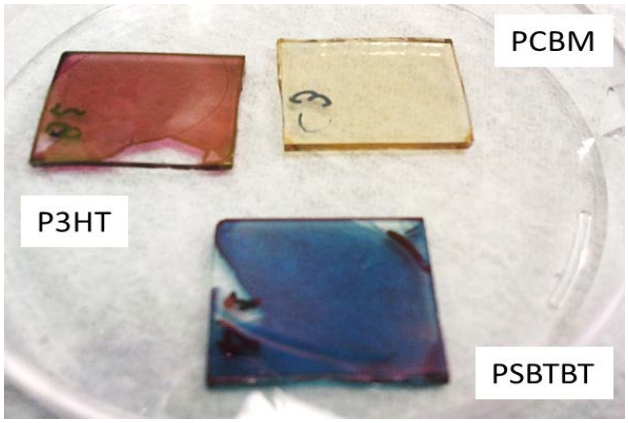

Figure 4.1: Pristine films of the P3HT, PSBTBT and PCBM materials, spin coated from solution. The films were spin coated to obtain a thickness of ~100 nm.

A thickness of the spin coated reference samples of ~100 nm was aimed for, to obtain the best contrast in the NEXAFS measurements. The thicknesses of the spin coated samples are listed in Table 4.2.

Table 4.2: Thicknesses and spin parameters for the P3HT, PSBTBT and PCBM reference samples.

	P3HT	**PSBTBT**	**PCBM**
Thickness	117 (5) nm	115 (10) nm	85 (8) nm
Spin parameters	1300 rpm, 1min	1800 rpm, 1 min	500 rpm, 1min

For the lift off the films were scratched in squares of roughly 2 x 2 mm^2 and slowly slid into a beaker of water, with the film floated onto the water surface. The films were then transferred to TEM cobber grids enabling analysis in the X-ray beam line. Images of the TEM grids with the pristine films are shown in Figure 4.2

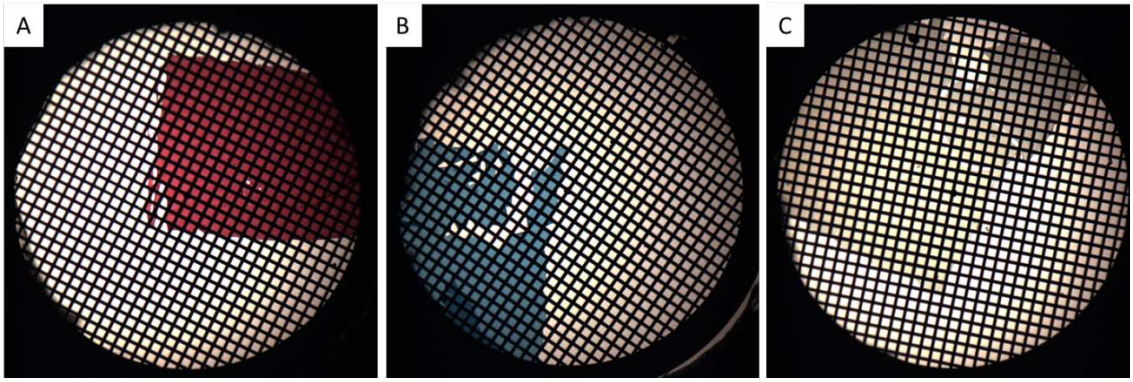

Figure 4.2: Pristine samples floated onto TEM cobber grids. Microscopy images of the P3HT (A), PSBTBT (B) and PCBM (C) pristine films.

4.2.2 Near edge absorption fine structure spectra

After making a NEXAFS line scan across one of the edges of the floated off pristine samples, the intensities were normalized to account for the background. The spectra were further normalized to a calculated absorption spectra for each of the polymers, obtained from the online solid x-ray filter tables [10,11].

The normalized spectra for P3HT and PSBTBT are plotted in Figure 4.3 A and B together with the normalized absorption spectra for PCBM. From the two spectra suitable energies for distinguishing between polymer and PCBM was chosen. These, for both polymers, were chosen at 284.5 eV, 287.4 eV, and 288.2 eV.

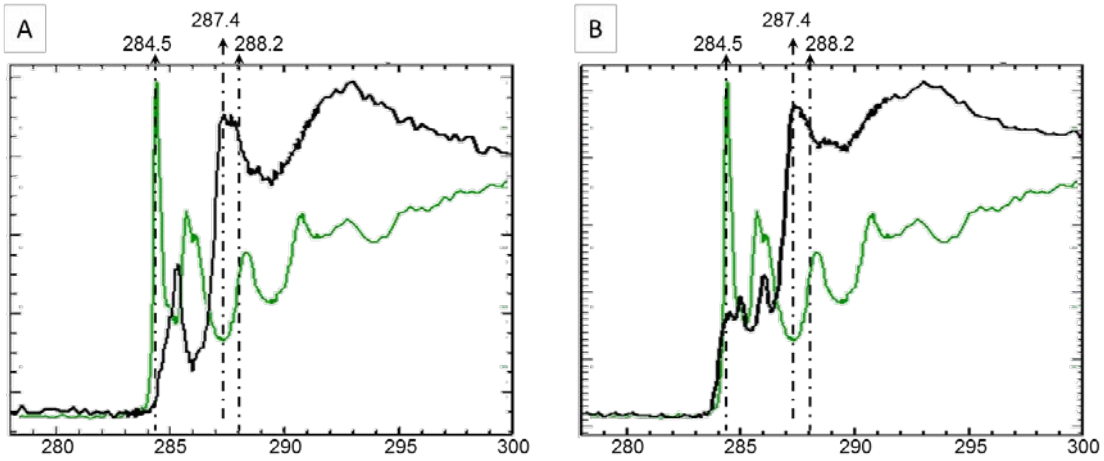

Figure 4.3. Normalized absorption spectra for the reference samples prepared and the three selected energies used for the STXM scan. Black is the P3HT reference (A), the PSBTBT reference (B) and green is the PCBM reference in both A and B.

4.3 Scanning transmission x-ray microscopy

With the chosen energies from the NEXAFS spectrums scanning transmission x-ray microscopy maps could be obtained. These were done by setting the energy of the beam line constant, and doing a scan over the sample area after which the second and third energies were set and another scan completed for each of these. This will be refered to as a stack. A stack consists of the three STXM images completed at the three selected energies.

The analysis of the STXM stacks was completed using the techniques as described by Burke et. al. [3]. Singular value decomposition was used to fit a sum of the pristine spectra to the measured blend spectrum, at each pixel in the STXM images. Image analysis was performed with the aXis2000 software package developed by Hitchcock et. al. [12]. The intensity maps presented in this chapter shows the relative mass composition for the PSBTBT, P3HT and PCBM, respectively, in relation to the total mass in the scanned areas.

4.3.1 Preparation of nanoparticle samples for STXM

The polymer-PCBM nanoparticles were spin coated onto a silicon substrate with a 250 x 250 µm silicon nitride window. The Si substrate was attached with double-sided tape to a glass slide during the spin coating. Images of the initial drop casting of the solutions can be seen in Figure 4.4.

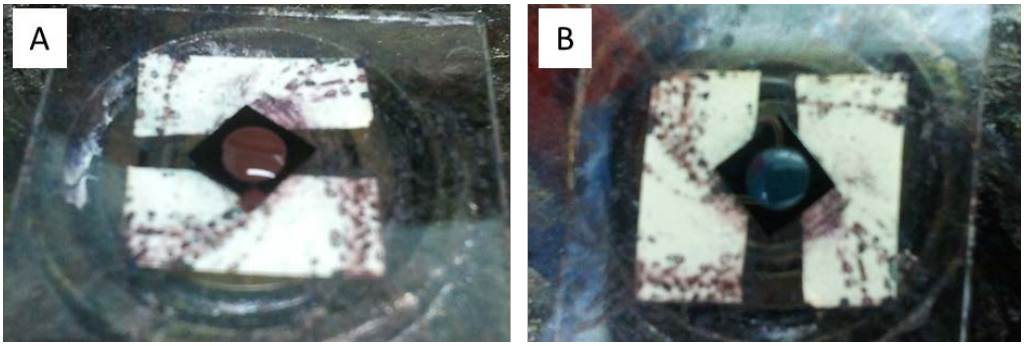

Figure 4.4: Spin coating of Silicon substrates with a 250 x 250 µm SiN window. Dispersions of P3HT:PCBM nanoparticles (A) or PSBTBT:PCBM nanoparticles (B) are spin coated. The Si substrate was attached with double-sided tape to a glass slide during the spin coating.

After having spun the solutions and dried, visual light microscopy images of the samples were acquired, to ensure an adequate coverage of the Silicon Nitride window and help in the location of suitable sections on the windows for doing the STXM scans. These images for the two samples are shown in Figure 4.5 A and B with a red square to indicate the area in which the STXM scans reported here were completed.

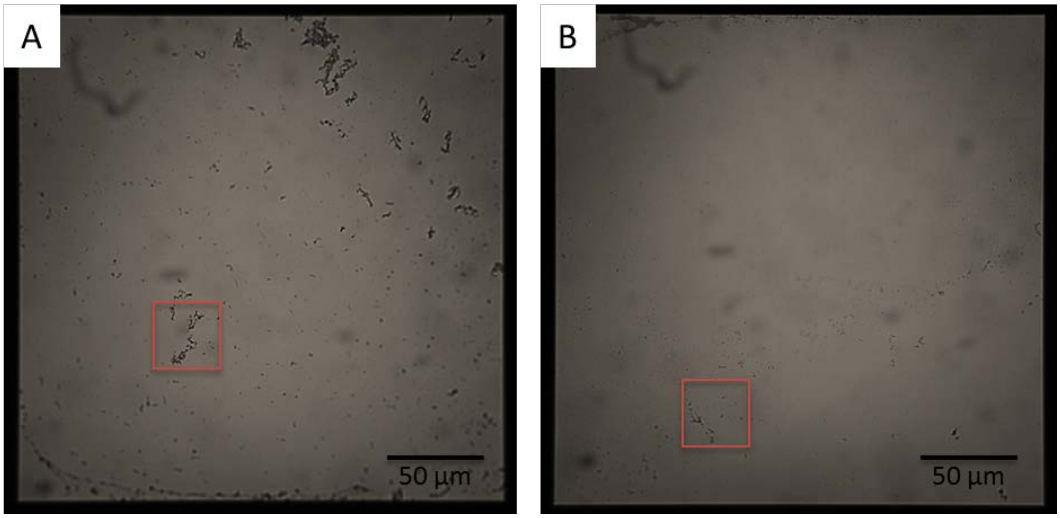

Figure 4.5: Visual light microscope images of the spin coated SiN windows. A) P3HT nanoparticle sample window. B) PSBTBT nanoparticle sample window. The red square marks the area in which the STXM scans were completed.

4.4 Composition and structure of nanoparticles

Several different types of nanoparticle composition has been suggested for the polymer:fullerene system, with core-shell-, Janus- or heterogeneous-particles as the main possibilities. A fourth type of particles is the homo particles, which are made from separate batches ensuring no mixing.

The objective of these investigations has been to find whether the nanoparticles showed any signs of a predominant type of phase-separation.

4.4.1 P3HT:PCBM nanoparticles

In the following, two separate x-ray stacks are presented. Both are from the red square, marking a large cluster of nanoparticles in Figure 4.5A.

Section 1 shows a cluster with relatively few evenly sized large particles and few small particles surrounding. The P3HT and PCBM relative mass contents shown in Figure 4.6A and Figure 4.6B, respectively, shows clear signs of a higher concentration of P3HT in the shell of the particles, with the PCBM concentration primarily in the core of the particles.

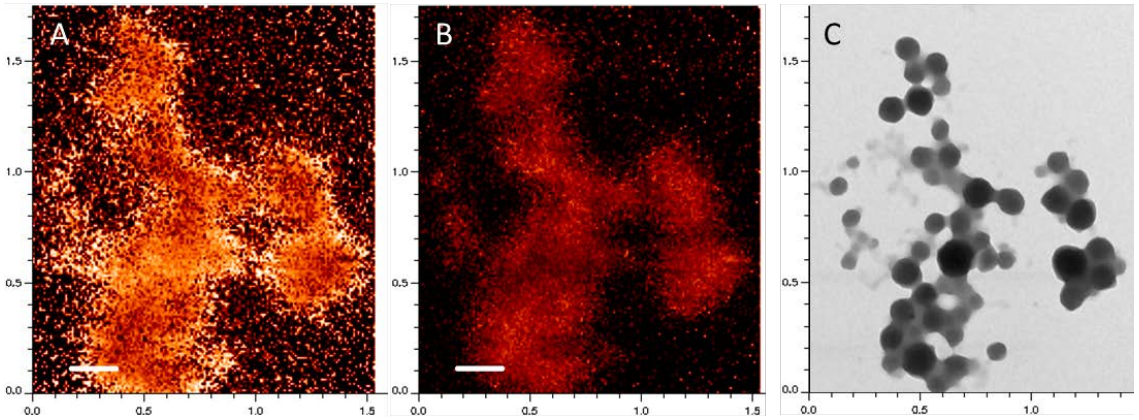

Figure 4.6: Section 1: Composition of P3HT:PC_{60}BM nanoparticles from STXM. A) Relative mass composition of P3HT to total mass. B) Relative mass composition of PCBM to total mass. C) TEM image of nanoparticle cluster taken after STXM imaging. Mass composition plots are shown on a black to white color scale.

The TEM image captured of the section shows the particles to be somewhat fused together, which is not as evident from the X-ray images due to the lower resolution.

The second section shows a larger view of another part of the nanoparticle sample, with a larger size range of the particles than in the first section.

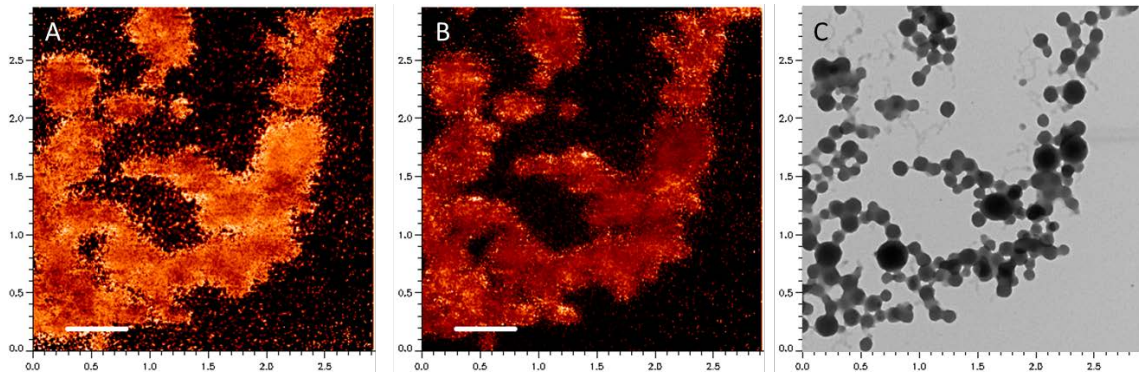

Figure 4.7: Section 2: Composition of P3HT:PC_{60}BM nanoparticles from STXM. A) Relative mass composition of P3HT to total mass. B) Relative mass composition of PCBM to total mass. C) TEM image of nanoparticle cluster taken after STXM imaging. Mass composition plots are shown on a black to white color scale.

The bonding between many of the particles is quite pronounced as indicated by the TEM image in Figure 4.7C. This shows in the relative density mass of both P3HT and PCBM as more of a smearing of the structures, with only few particles showing as core-shell structures.

4.4.2 PSBTBT:PCBM nanoparticles

The relative mass densities for the PSBTBT polymer and PCBM are presented in the following three figures, which are the result of three distinct stacks. All three stacks are from within the area marked by the red square in Figure 4.5B.

In contrast to the P3HT:PCBM nanoparticles the PSBTBT:PCBM nanoparticles shows less agglomeration together with more well defined single particle.

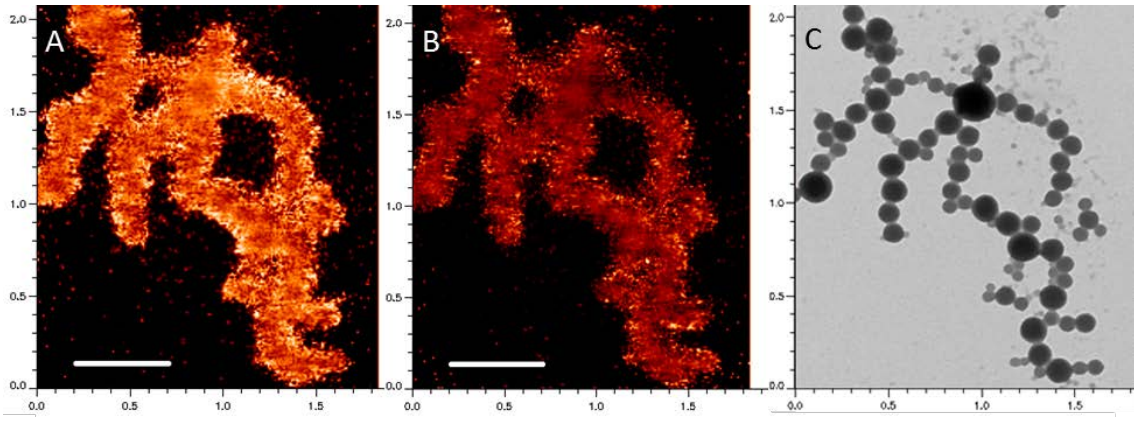

Figure 4.8. Section 1: Composition of PSBTBT:$PC_{60}BM$ nanoparticles from STXM. A) Relative mass composition of PSBTBT to total mass. B) Relative mass composition of PCBM to total mass. C) TEM image of nanoparticle cluster taken after STXM imaging. Mass composition plots are shown on a black to white color scale.

Section 1 shows a section of the sample with a clear indication of a core-shell structure, as seen by the bright high-intensities in the rim of the particles in Figure 4.8A and the smaller areas of intensity in Figure 4.8B, indicating the high concentration of PSBTBT in the shell of the particles and high concentration of PCBM in the centre of the particles.

In Figure 4.9, the second section of PSBTBT:PCBM nanoparticles, the STXM resolution of the particles is a little better than for section one. The core-shell structure seen in the previous figure is therefore also more noticeable here, with the larger centre particle, with a diameter of ≈250 nm and the smaller particles down to 100 nm showing a P3HT rich outer shell and PCBM rich core.

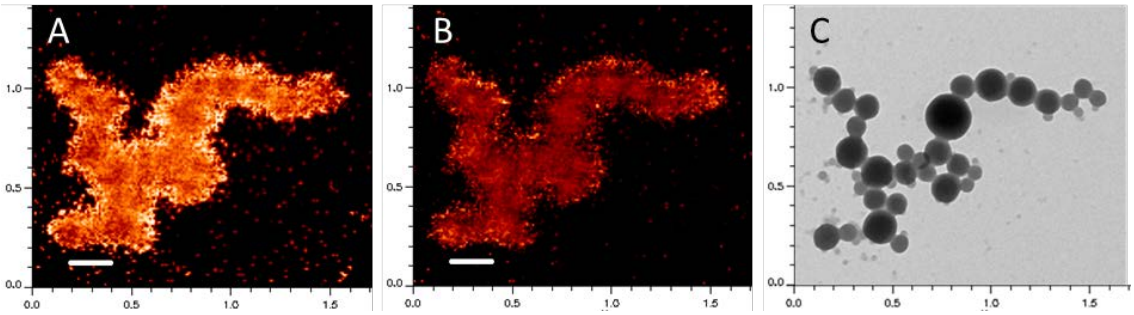

Figure 4.9: Section 2: Composition of PSBTBT:$PC_{60}BM$ nanoparticles from STXM. A) Relative mass composition of PSBTBT to total mass. B) Relative mass composition of PCBM to total mass. C) TEM image of nanoparticle cluster taken after STXM imaging. Mass composition plots are shown on a black to white color scale.

Finally, in the third section, the particles ware resolved with almost all the particles in the imaged area showing a clear core-shell structure. Especially the PCBM image shows more clearly the separation between the particles.

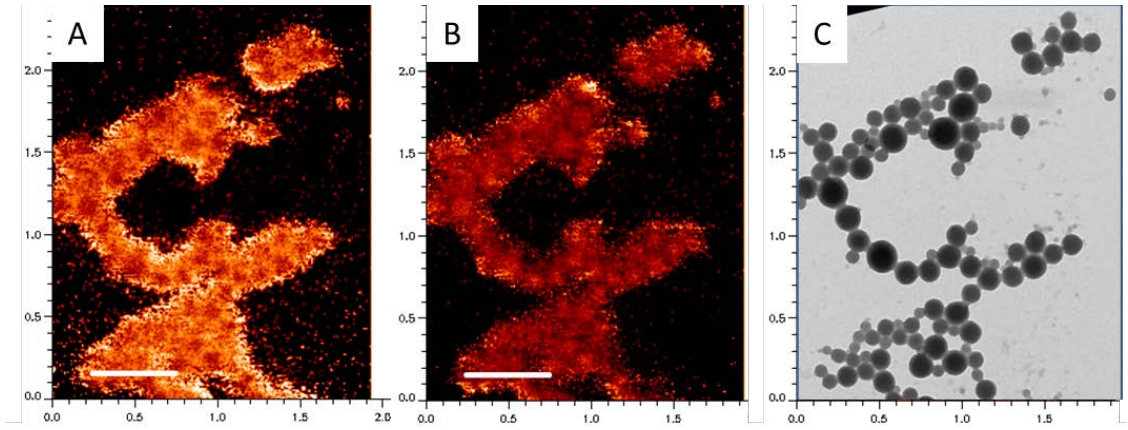

Figure 4.10: Section 3: Composition of PSBTBT:$PC_{60}BM$ nanoparticles from STXM. A) Relative mass composition of PSBTBT to total mass. B) Relative mass composition of PCBM to total mass. C) TEM image of nanoparticle cluster taken after STXM imaging. Mass composition plots are shown on a black to white color scale.

4.4.3 TEM images of nanoparticles which has not been X-rayed

A set of reference nanoparticle samples were imaged with TEM before going to the synchrotron, to ensure that the particle coverage and size distributions were adequate for using the samples in the beam line experiments. A further reason for doing TEM on these samples was to have a reference for the particle agglomeration and shape for

nanoparticles that had not been exposed with x-rays. The use of both x-rays and electron imaging techniques, such as TEM, could incur radiation damage to the particles.

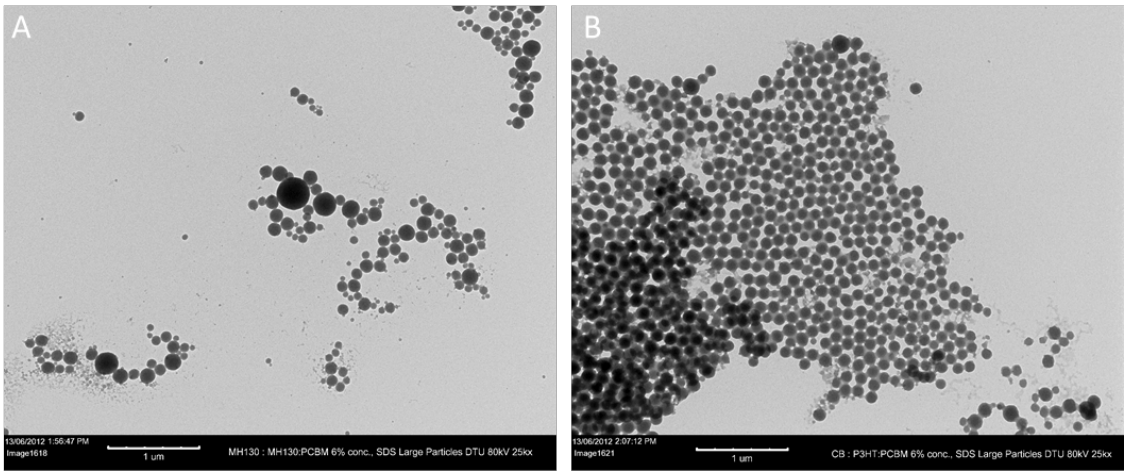

Figure 4.11: TEM images of nanoparticles of PSBTBT:PCBM (A) and P3HT:PCBM (B). These samples have not been used for x-ray experiments.

This has however not been observed in these particles as the shape and type of agglomeration of the particles in the un exposed TEM images seen in Figure 4.11 show a similar structure of the nanoparticles to the nanoparticles in the TEM images of Figure 4.6, Figure 4.7, Figure 4.8,Figure 4.9 and Figure 4.10. The larger amount of particles in Figure 4.11B, shows the very nice packaging of an area with a large concentration of particles.

4.5 Performance of solar cells produced from nanoparticles

Solar cells have been fabricated from the PSBTBT:PCBM nanoparticles, with numbers for their efficiency given in the following section, however due to difficulties in coating the P3HT:PCBM nanoparticles manufactured from Chlorobenzene, there is not presented any data for the P3HT:PCBM system.

4.5.1 Efficiency of PSBTBT cells

The efficiency of the OPV devices produced from PSBTBT:PCBM nanoparticles gave a, for nanoparticle based OPV, promising result of 1.29% best efficiency. In comparison to

what has previously been reported [5], this is among the highest efficiencies recorded for water based OPV production. The efficiency of the cells were primarily low due to the 33% fill factor, which might be blamed on an inefficient transport of the charges from the nanoparticles to the electrodes. The current density versus voltage curve for a typical device is shown in Figure 4.12.

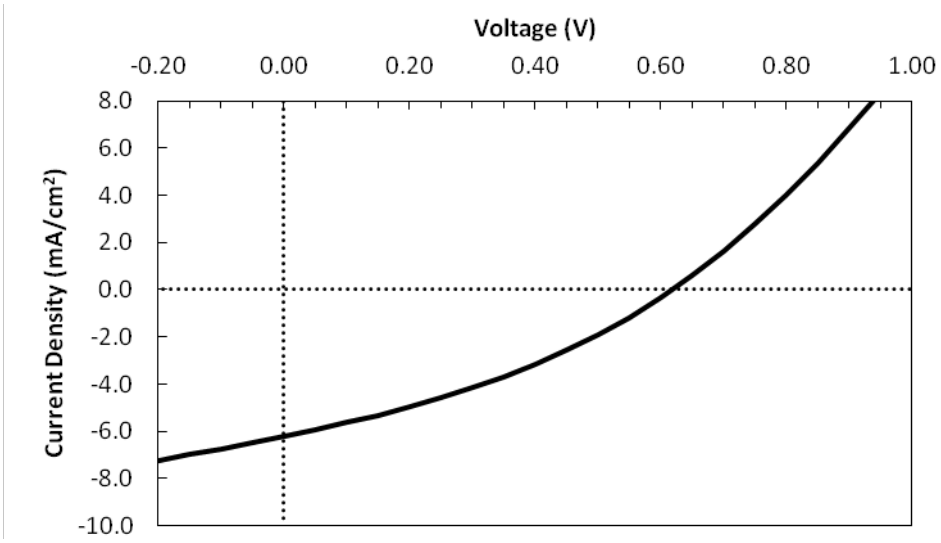

Figure 4.12. Current Density versus Voltage curve for a typical PSBTBT NP device. The device showed a short circuit current density (J_{sc}) of 6.21 mA/cm^2, an open circuit voltage (V_{oc}) of 0.62 V and a fill-factor of 33 %. The efficiency of the device (η) is 1.29 %. The device area was 5x5 mm^2.

The short-circuit current density of the device is 6.21 mA/cm^2 and the open circuit voltage is 0.62 V. This compares quite well to other nanoparticle based polymer solar cells, but is however not fully at the level of solar cells based on the PSBTBT polymer processed from solution, where a current density of 12mA/cm^2 was originally reported Hou et. al. [13].

4.5.2 IPCE of PSBTBT:PCBM nanoparticle based cells.

Internal photon conversion efficiency (IPCE) data for the cells produced from the nanoparticle system was completed, however not until three days after the cells were manufactured. The IPCE of the cells after the three days in a non-protective atmosphere is shown in Figure 4.13. The current density of the cell has dropped from the 6.21 mA/cm^2 measured initially, to 3.56 mA/cm^2 after the storage in air. The IPCE of

the cell also matches the absorption pattern of the PSBTBT polymer, as shown in Chapter 3.

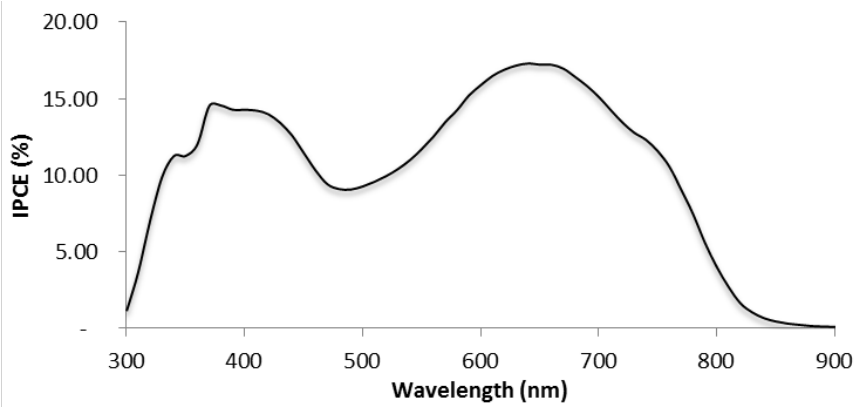

Figure 4.13: IPCE measurement of the cell presented in Figure 4.12. The IPCE measurement was not completed until three days after fabrication of the cell. The integrated current density from the IPCE is 3.56 mA/cm^2.

4.6 Summary

This chapter has described the production of nanoparticles for use on organic solar cells coated from water and the morphology of the as produced nanoparticles internal morphology. It has been shown that the nanoparticles produced from the chloroform and the PSBTBT polymer gives spherical particles with a core-shell structure, while the chlorobenzene based P3HT based particles gives a similar core-shell structure, but with a tendency towards a less spherical shape and a larger degree of agglomeration. The performance of the PSBTBT:PCBM nanoparticles was evaluated and found to lie below the record for the polymer, but with a, for a nanoparticle based system relatively high 1.3% efficiency.

References

[1] A.M. Ruder, Potential Health Effects of Occupational Chlorinated Solvent Exposure, *Ann. N. Y. Acad. Sci.* 1076 (2006), 207–227.

[2] Y. Kim, S.A. Choulis, J. Nelson, D.D.C. Bradley, S. Cook, J.R. Durrant, Composition and annealing effects in polythiophene/fullerene solar cells, *J. Mater. Sci.* 40 (2005), 1371–1376.

[3] K.B. Burke, A.J. Stapleton, B. Vaughan, X. Zhou, A.L.D. Kilcoyne, W.J. Belcher, et al., Scanning transmission x-ray microscopy of polymer nanoparticles: probing morphology on sub-10 nm length scales, *Nanotechnology*. 22 (2011), 265710.

[4] Y. Lee, S.H. Lee, K. Kim, J.W. Lee, K.-Y. Han, J. Kim, et al., Single nanoparticle of organic p-type and n-type hybrid materials: nanoscale phase separation and photovoltaic effect, *J. Mater. Chem.* 22 (2012), 2485–2490.

[5] S. Ulum, N. Holmes, D. Darwis, K. Burke, A.L. David Kilcoyne, X. Zhou, et al., Determining the structural motif of P3HT:PCBM nanoparticulate organic photovoltaic devices, *Sol. Energy Mater. Sol. Cells*. 110 (2013), 43–48.

[6] M. Morana, H. Azimi, G. Dennler, H.-J. Egelhaaf, M. Scharber, K. Forberich, et al., Nanomorphology and Charge Generation in Bulk Heterojunctions Based on Low-Bandgap Dithiophene Polymers with Different Bridging Atoms, *Adv. Funct. Mater.* 20 (2010), 1180–1188.

[7] B. Schmidt-Hansberg, M.F.G. Klein, M. Sanyal, F. Buss, G.Q.G. de Medeiros, C. Munuera, et al., Structure Formation in Low-Bandgap Polymer:Fullerene Solar Cell Blends in the Course of Solvent Evaporation, *Macromolecules*. 45 (2012), 7948–7955.

[8] K. Landfester, R. Montenegro, U. Scherf, R. Güntner, U. Asawapirom, S. Patil, et al., Semiconducting Polymer Nanospheres in Aqueous Dispersion Prepared by a Miniemulsion Process, *Adv. Mater.* 14 (2002), 651–655.

[9] T.R. Andersen, T.T. Larsen-Olsen, B. Andreasen, A.P. Bottiger, J.E. Carlé, M. Helgesen, et al., Aqueous processing of low-band-gap polymer solar cells using roll-to-roll methods, *Acs Nano*. 5 (2011), 4188.

[10] B.L. Henke, Filter Transmission - X-ray transmission of a solid., *Http://henke.lbl.gov/optical_constants/filter2.html*. (n.d.),.

[11] B.L. Henke, E.M. Gullikson, J.C. Davis, X-Ray Interactions: Photoabsorption, Scattering, Transmission, and Reflection at E = 50-30,000 eV, Z = 1-92, *At. Data Nucl. Data Tables*. 54 (1993), 181–342.

[12] Adam Hitchcock, Chris Jacobsen, Peter Hitchcock, Carl Zimba, Billy Loo, Eli Rotenberg, et al., aXis 2000 - Analysis of X-ray Images and Spectra Software Package, *http://unicorn.mcmaster.ca/aXis2000.html*. (n.d.),.

[13] J. Hou, H.Y. Chen, S. Zhang, G. Li, Y. Yang, Synthesis, characterization, and photovoltaic properties of a low band gap polymer based on silole-containing polythiophenes and 2, 1, 3-benzothiadiazole, *J. Am. Chem. Soc.* 130 (2008), 16144–16145.

5. Tandem Solar Cells

The quest for the fabrication of tandem solar cells has been recently started for organic photovoltaics with few occurrences of tandem cells previously, but recently with efficiencies overcoming the efficiencies of the individual cells.

The results presented in this chapter are based on results from the paper attached by Andersen et. al. [1] as appendix A5, together with examples of single sided illumination solar cells not previously published.

5.1 A traditional tandem solar cell

The traditional tandem solar cells are based on III-V crystalline materials with the added benefits of the multijunctions being the possibility of absorbing the incoming photons in a range of cells, which are each better matched to convert the energy of the photons to an electron with an energy as close as possible to the energy of the incoming photon. This is in contrast to the single cell junctions, where the energy of the photon higher than what is needed for exciting an electron across the materials band gap is dissipated as heat in the material.

These tandem solar cells are however performing significantly better than organic solar cells, with efficiencies in the >40 % range [2,3]. The performance of these is also further increased by the use of concentrator lenses to increase the intensity upon the cells and reduce the size of the cells required to cover a given area. Using concentrator systems for this type of cells is also a necessity from an economical viewpoint, however concentrators requires accurate tracking of the sun for the focusing of the light onto the solar cell area. A further issue with this solution in countries, such as Denmark, is the low amount of the sun light which comes in as direct sunlight in comparison to the diffuse component of the incoming irradiation.

5.2 Organic tandem solar cells

In organic solar cells, the implementation of a tandem structure was realized as early as 1986 with the 2-cell tandem cell structure by Tang et al. [4]. The efficiency increase in the single cells and the complications in making tandem cells have however kept high efficiency organic tandem cells from reaching a performance level similar to the organic based single cells. It is not until recently that organic tandem cells have begun to show a competitive performance to the single cells. Evaporated small molecule cells by Heliatek have been certified with a 12% conversion efficiency for a 1.1 cm^2 tandem cell [5], while the polymer tandem cell have been reported with efficiencies just above 10% by You et. al. [6,7], however with device areas of a somewhat smaller 0.1cm^2.

The reason for increasing the complexity of the organic solar cells by the use of a tandem cell structure lies with the possibility of tailoring the individual cells in the device towards a specific wavelength range. This is similar to the argument of making inorganic tandem cells, however in the organic tandem solar cells, the difficulty in making a material with a wide absorption is larger. As shown in Figure 5.2, the low bandgap polymers tend to absorb less at the shorter wavelengths. Furthermore, due

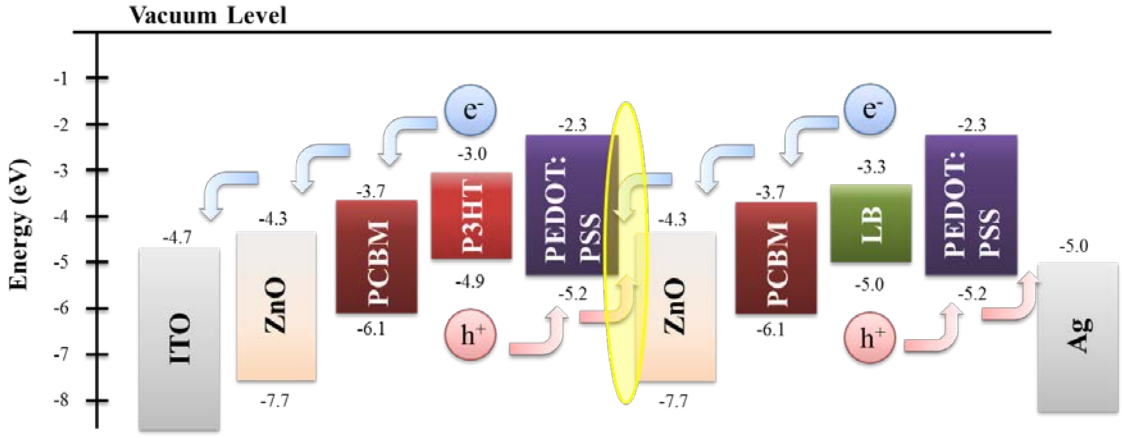

Figure 5.1: Energy level diagram of the materials in an inverted geometry OPV tandem solar cell, with the materials aligned according to their position in the cell. A recombination layer consisting of a PEDOT:PSS-ZnO layer has holes from the front cell recombining with electrons from the back cell. The front cell based on P3HT only absorbed the light out to 650 nm while the back cell consisting of a low-bandgap polymer such as PSBTBT absorbed the light out to 850 nm.

to the much lower mobilities, it is not possible to make the active layers very thick, resulting in a somewhat transparent layer.

An example structure of an inverted structure organic tandem solar cells is shown in Figure 5.1, being in essence a stack consisting of two solar cells coated on top of each other, however with the top electrode of the first cell replaced by a transparent recombination layer, which the long wavelength light haves to pass before being absorbed in the second cell.

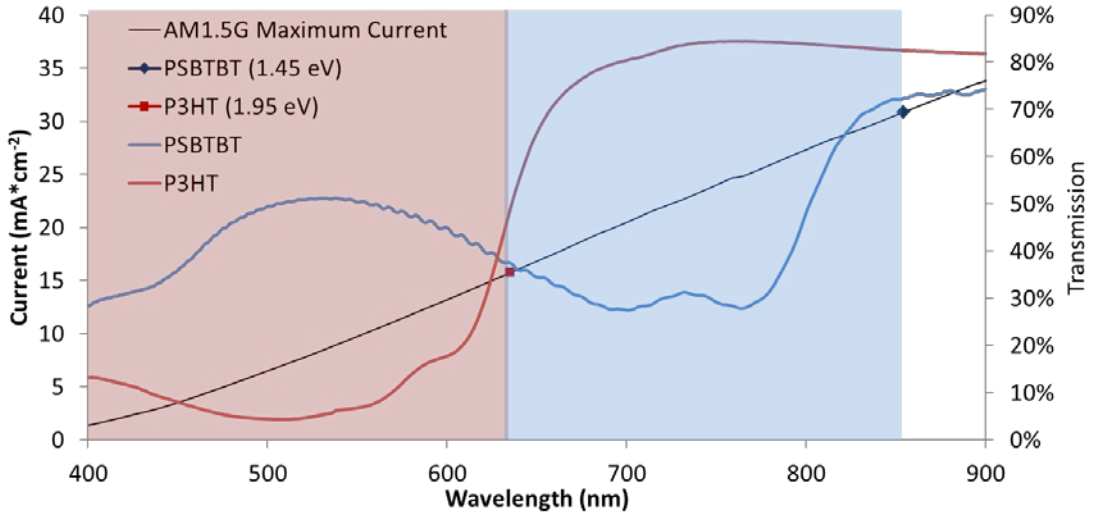

Figure 5.2: Splitting the incoming solar radiation between two active layers consisting of P3HT and PSBTBT for example would allow a significant increase in the efficiency of the solar cell, here illustrated with the red highlight showing the absorption area of the P3HT layer and the blue highlight the absorption area of the PSBTBT polymer.

The principle of the two different polymers absorbing the light is shown in Figure 5.2, where the part of the solar spectrum marked with red will be absorbed in the front P3HT:PCBM cell while the part of the solar spectrum marked with blue will be absorbed in the PSBTBT:PCBM back cell. This type of cell, with these two polymers was demonstrated by Sista et. al in 2009 [8] showing an efficiency of >5 %.

5.3 Tandem cells by wet processing

However simple these results shows the processing of tandem cells to be, the use of only wet processing complicates the process slightly, since the coated layers need to withstand coating of several extra layers on top. Therefore the intermediate layer of the tandem cells becomes indeed the most essential part of creating the polymer organic solar cell. Tandem cells have been shown previously, manufactured using doctor blading techniques [9] or spin coating and with the use of thin evaporated metal layers in the intermediate layer [8]. The tandem cells presented herein however are made using wet processing for the entire 12 layer stack.

5.4 Testing of devices

Since one of the concerns for the tandem solar cells made by wet processing is the separation of the individually coated layers, the idea of using a two sided illumination and two thick P3HT:PCBM active layers evolved. This allowed a semi-separation of the performance of the two active layers, since the thick P3HT:PCBM layers allow very little of the light to pass through to the other active layer, and thereby a possibility of di-

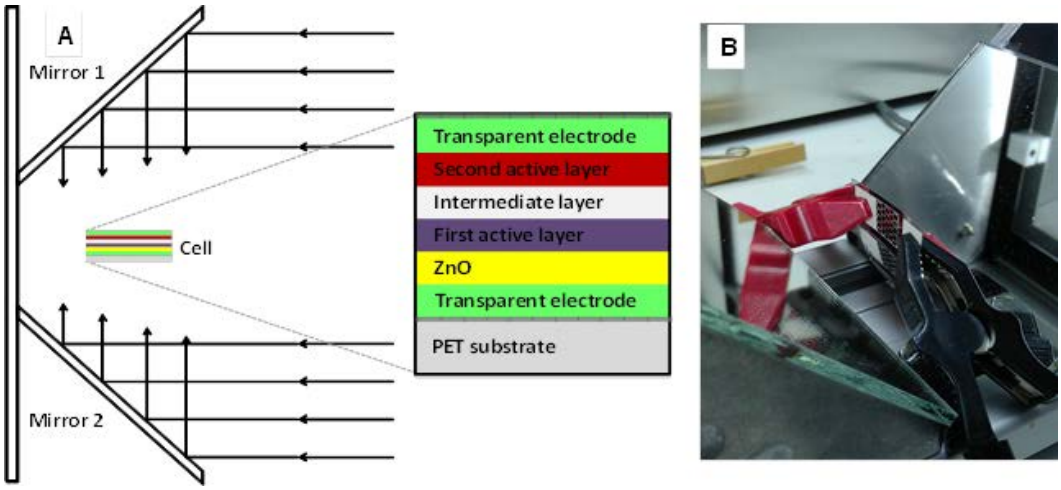

Figure 5.3: Illustration of the double sided illumination test setup. Two mirrors angled at 45 degrees with the solar cell mounted between them allowed a two sided illumination of the solar cell with equal intensity on both sides using a single solar simulator. Reproduced with permission from Elsevier [1]

agnosing which of the two cells in the tandem device was the limiting cell.

A test stand with two mirrors angled at 45 degrees with a mount for the solar cell between them was made. The advantage of this setup was the uniform intensity too both sides of the solar cell with the use of a single solar simulator. The intensity used with this setup was 700 W/m^2 for each side.

5.5 Intermediate layer

One of the biggest issues when making a tandem solar cell using wet processing methods is the added complexity in keeping the individual layers separated.

During the fabrication of these tandem solar cells, it was found that the largest difficulty was making the intermediate layer solvent resistant. This issue arose by the top active layer solvent penetrated through the intermediate layer and dissolved the bottom active layer, thereby resulting in a blend of the two active layers and a partially covering intermediate layer. The performance of these cells were abysmal, with performance numbers of less than one fifth of what is the norm for the single junction roll coated cells and with voltages of roughly 0.5 V.

To find the culprit of this solvent penetration several different intermediate layer combinations was tried and tested for both solvent penetration and coatability. Initially making cells with a Clevios 4083 PEDOT:PSS layer and ZnO layer was tried, however the Clevios 4083 layer could not be coated on the P3HT:PCBM active layer, due to dewetting.

A solution to this was tried with the use of VTIP as a substitute for the PEDOT layer, however the coating of the VTIP solution on the mini roll coater gave very non-uniform films, as seen in Figure 5.5. The VTIP dried into small islands of Vanadium Oxide crystals, with the size of the particles highly dependent on the amount of VTIP material.
Even with a 60 nm thick Vanadium Oxide layer with a 80 nm thick ZnO layer the solvent test proved that the intermediate layer was not solvent resistant, as shown in the last microscope image of Figure 5.5.

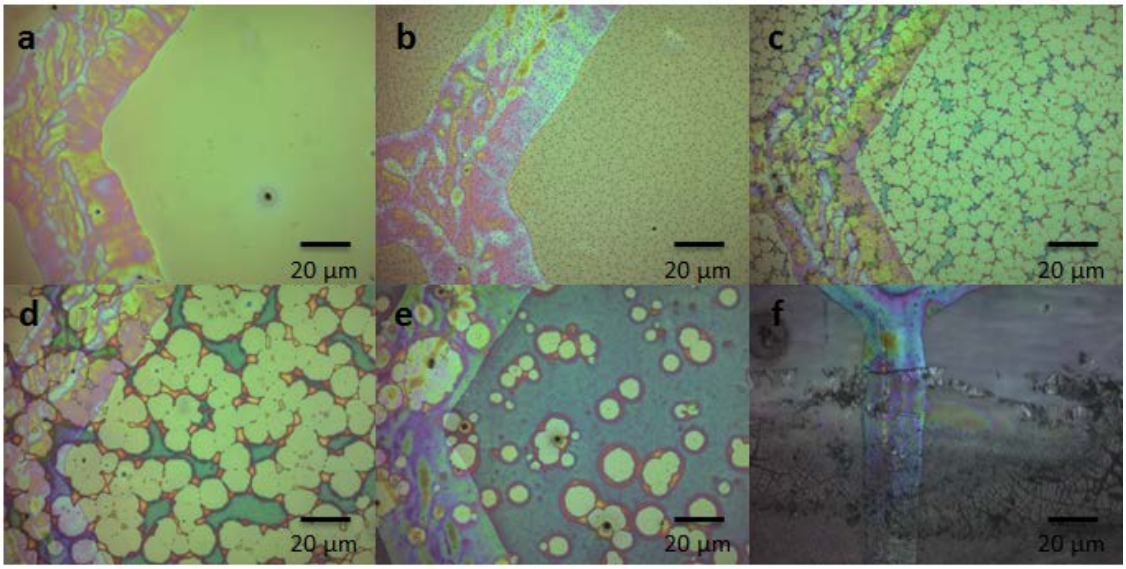

Figure 5.5: Coating of a Vanadium Oxide layer from a VTIP precursor. The microscope images shows a Flextrode substrate coated with a P3HT layer and varying amounts of VTIP solution. (a) is the bare P3HT layer, (b) is 7.5 nm of VTIP, (c) is 15 nm, (d) is 30 nm and (e) is 60 nm. (f) shows dissolution of the complete coated V_2O_5 ZnO intermediate layer on solvent penetration testing.

Switching to using MoO_x as the hole conducting layer in the intermediate layer stack showed nicer coating properties towards uniformity compared to the Vanadium layer, however, as seen in Figure 5.4A, the resulting intermediate layer stack showed crack

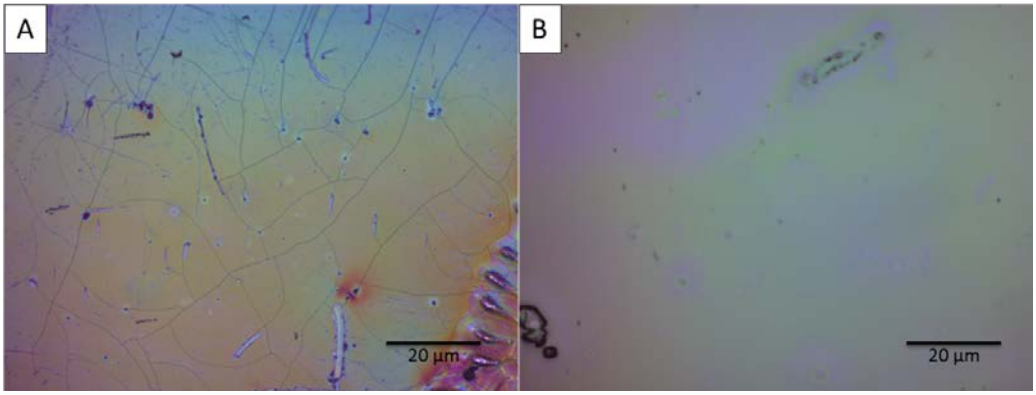

Figure 5.4: Variations of the intermediate layer to stop solvent penetration. Microscope images of roll coated sample cells coated to and including the top active layer. A) An intermediate layer consisting of a MoOx HTL layer and a ZnO ETL layer with P3HT coating on top. Image shows significant crack formations. B) Intermediate layer with MoOx, PEDOT:PSS 4083 and ZnO with P3HT coated on top. No cracks is seen in the layer when using a PEDOT:PSS 4083 layer as a HTL and solvent blocking layer. Re-produced with permission from Elsevier [1]

formations after the coating of the 2nd active layer material.

We did however find, that with an intermediate layer with MoO_x, PEDOT:PSS and ZnO, the cracks does not form, as seen in Figure 5.4B, and that the films underneath does not dissolve upon application of a solvent onto of the intermediate layer.

A further complication to the process of finding a suitable material combination for the intermediate layer lied with the Flextrode electrode used. As shown in Figure 5.6, spikes caused by the flexographic printing of the bottom silver electrode in some cases as high as 0.6 µm, caused the solvent resistance of the intermediate layer to be ineffective. This was shown to be an issue with some batches of the flextrode electrode, where tandem cells could simply not be fabricated. The issue was eventually solved with an improvement of the silver printing reducing the amount of spikes.

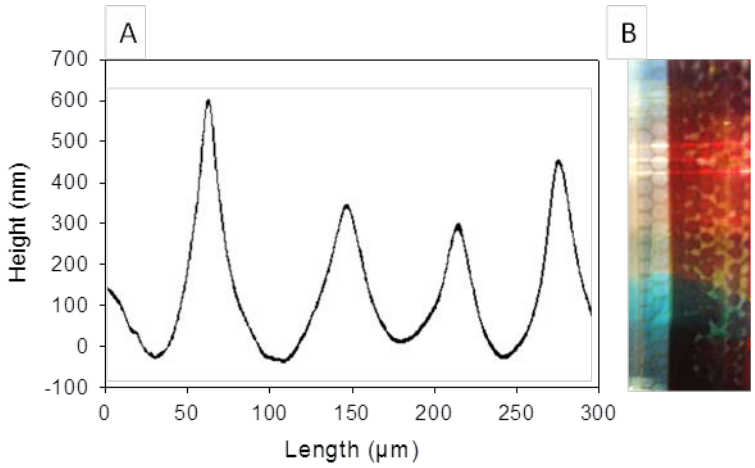

Figure 5.6: One added difficulty for the production of tandem cells on the Flextrode substrate is the inherent spikes in the flexographic printed silver bus bars. As seen in (A), the height of the spikes in the print is up to 0.6 µm for the flextrode substrate. Solvent penetration through the intermediate layer is shown in (B). Reproduced with permission from Elsevier [1]

5.6 Absorbance of the extra layers of the tandem cell

Making the intermediate layer solvent resistant is a necessity for the manufacture of the tandem cells as described in the previous section, however the solvent resistance has to be done, without increasing the absorbance of the intermediate layer to a level where it can no longer be used in single side illumination tandem solar cells. An ab-

sorbance test of the individual layer materials of the cell coated by roll coating on bare substrate was completed. The absorbance of the materials of the tandem cell can be seen in Figure 5.7. The absorbance of the intermediate layer components is very small. The variation of the measurement of the absorbance of the substrate is negligible for both VTIP and ZnO layers, while there is a slight absorbance of less than 0.05 in the Pedot 4083, primarily at higher wavelengths.

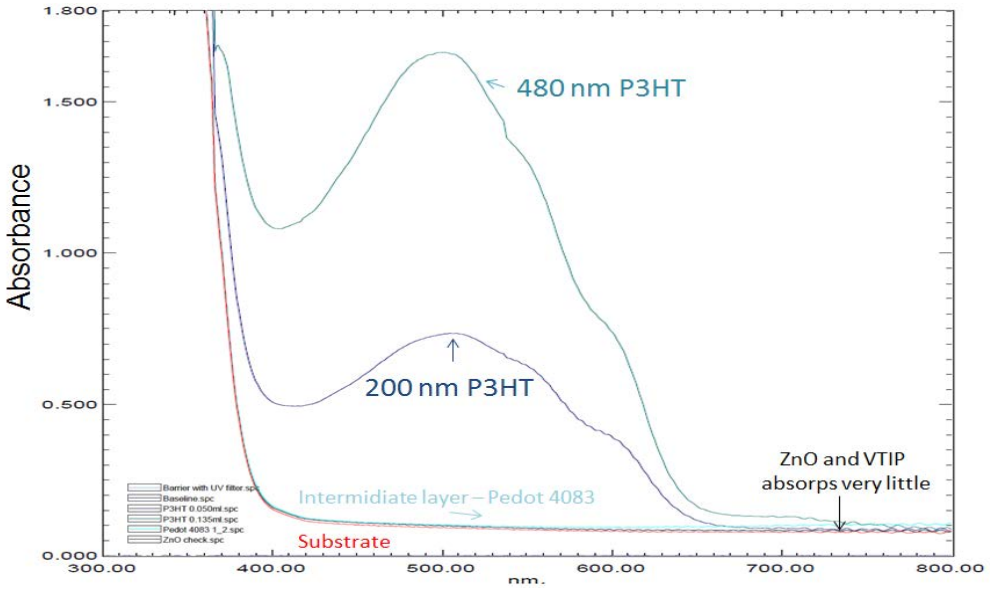

Figure 5.7: The absorption of the layers of the tandem solar cell. All absorbance measurements are conducted with an air reference, so the PET substrate is included in all the measurements. The absorbance of the layers in the intermediate layers can be seen to very small.

5.7 Illustration of the tandem cell stack

The optimized stack found to work in a complete wet processed procedure is shown in Figure 5.8, with the materials and other of these similar to those shown in Figure 5.1. The stack consists of two identical polymer layers sandwiched with a ZnO and PEDOT layer on each side of them. The use of the three layer PEDOT structure in both intermediate layer and top layer, shows the further potential for the stacking of more than two cells onto each other, however this would require a careful choice of suitable polymers and absorber layer thicknesses.

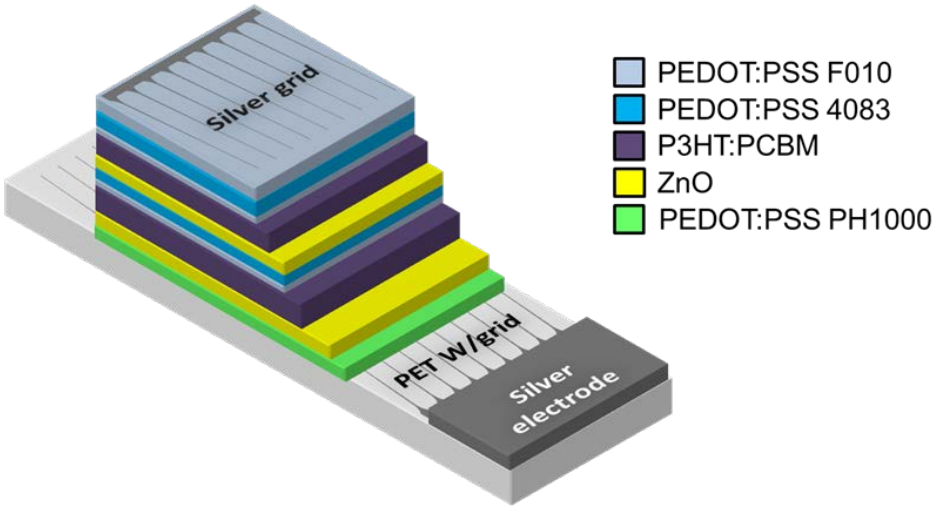

Figure 5.8: The stack of an optimized tandem solar cell using a PEDOT:PSS and ZnO intermediate re-combination layer. Reproduced with permission from Elsevier [1]

5.8 Manufacturing Parameters for a tandem cell

For the fabrication of the final design of the two layer P3HT:PCBM; tandem cells the parameters described in Table 5.1 were used. The parameters are based on the optimizations carried out, while some are chosen due to convenience. A temperature of 60°C for instance, was chosen to allow an efficient drying of the layers, while not being too high causing defects while coating ZnO. Coating speeds has been kept at 1.0 m/min, due to this offering a good compromise allowing corrections during coating

Table 5.1: The coating parameters used for the developed coating stack as shown in Figure 5.8

Layer	Material	Concentration	Temp	Speed	Flow	T_{wet}
			°C	m/min	mL/min	µm
Substrate	Flextrode					
1st active layer	P3HT:PCBM	20:20 mg/ml	60	1.0	0.20	15
Compatibilizer	PEDOT F010:IPA	1:4 vol/vol	60	1.0	0.10	8
HTL	PEDOT 4083:IPA	1:2 vol/vol	60	1.0	0.30	23
ETL	ZnO	39 mg/ml	60	2.0	0.10	3.8
2nd active layer	P3HT:PCBM	20:20 mg/ml	60	1.0	0.08	6
Compatibilizer	PEDOT F010:IPA	1:4 vol/vol	60	1.0	0.10	8
HTL	PEDOT 4083:IPA	1:2 vol/vol	60	1.0	0.30	23
Conducting Layer	PEDOT F10:IPA	1:1 vol/vol	60	1.0	0.40	31
Top Electrode	Ag PV410		60	1.2		

and still offering a high throughput.

Concentrations of the different solutions were based on what have generally been used in the lab in the case of ZnO and active materials and with dilutions of PEDOT:PSS solutions to allow an easier coating process.

5.9 Encapsulation

Encapsulation of the tandem solar cell was needed to allow the cell to open at positive bias. As seen in Figure 5.10, the opening of the diode does not occur before the device has been encapsulated. This is believed to be a question of the humidity and oxygen content in the top PEDOT:PSS layer.

The encapsulation was done in two different ways. For the typical cells encapsulation was done with two microscope cover slides of 18 x 18 mm^2, with DELO LP-655 UV curable epoxy. This encapsulation means that the cells are no longer flexible and the technique is therefore not roll 2 roll compatible, however for the testing of cells, the cheapness and the pre-cut size of the cover glass made this an ideal solution. The second type of encapsulation was done using an AMCOR µ-barrier foil and the LP-655 epoxy. These cells are flexible and the encapsulation method is the same as presently used on the roll 2 roll produced cells.

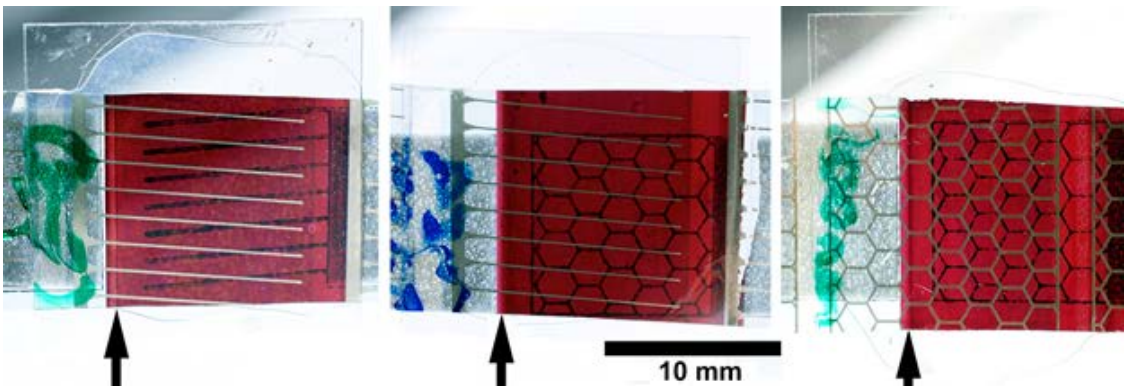

Figure 5.9: Images of encapsulated tandem cells with different electrode patterns. All are encapsulated in 18 x 18 mm^2 0.1 mm thickness glass with DELO epoxy glue.

5.10 Post treatment

After completing the solar cell, a series of post treatment steps has to be performed to allow the full performance of the solar cell. First, any shunts present in the solar cell is burned, with the use of a negative bias between 14 V and 20 V. This enables a non-resistor J-V characteristic, as shown with the first curve in Figure 5.10. Secondly the cells is heat-annealed, which is supposed to improve the morphology of the active layers and dissipating moisture from the PEDOT:PSS layers. The result of this is shown in the second curve, with a higher short circuit current. The third step is to encapsulate the solar cell, which due to the type of PEDOT:PSS is required to show a diode characteristic. The use of a UV-curable adhesive also enables a doping of the ZnO layers in the cell, which increases the conductivity of the cell in the forward bias direction. Final steps of applying a negative voltage, heating and soaking shows the highest efficiency of the device, with an improvement in voltage, current and fill factor.

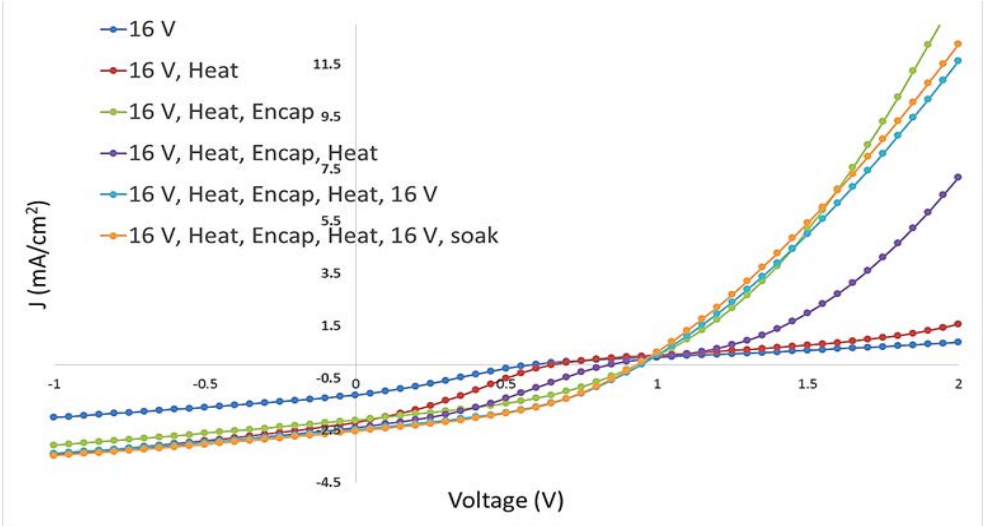

Figure 5.10: Post treatment of the tandem solar cells. For the solar cells to perform, the post treatment is crucial for these wet processed tandem cells. Post treatment consists of high voltage shunt burning, heat annealing, encapsulation and light soaking.

5.11 Variation of second active layer thickness

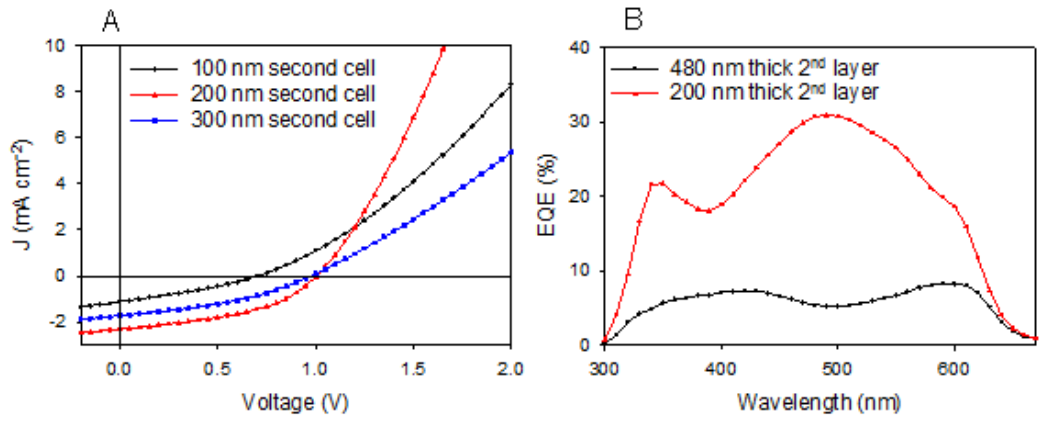

Figure 5.11: Variation of the thickness of the second coated active layer. A) J-V curves for 2nd layer active curves of 100 nm, 200 nm and 300 nm. B) EQE measurement corresponding to thick and thin 2nd active layers. Curves are completed with light biasing of the 1st cell. Reproduced with permission from Elsevier [1]

The use of two identical cells was the initial idea for testing the cell stack, however after completing external quantum efficiency (EQE) measurements on the two sides of the cell, the efficiency of the top cell was found to be very low. The shape of the EQE of the thick top cell, as shown in Figure 5.11B, shows an EQE value of less than 10% with a significant dip where the peak of the P3HT absorption lies. This was concluded to be caused by a high percentage of the light being absorbed in the first part of the second active layer film, causing the electrons to travel across a long distance before reaching the recombination layer and thereby increasing the risk of recombination within the active layer. A test of the effect of using thinner cells was therefore completed with thicknesses of 100 nm, 200 nm and 300 nm for the 2nd cell active layer. The J-V curves shown in Figure 5.11A shows the use of a 200 nm active layer to give the highest performing cell, with a better matching of the current from the top and bottom cell and a better conductivity through the cell, while the 100 nm cell is too thin to absorb enough light and the 300 nm cell shows a similar transport problem to the full thickness cell. The EQE of the 200 nm 2nd active layer cell (Figure 5.11B), shows the clear improvement from the full thickness 2nd layer. The previously observed drop in

EQE where P3HT absorbs the most has been effectively removed by reducing the layer thickness. As expected there is a minor peak in EQE around 340 nm, which is due to the illumination through the top electrode and thereby the light does not get absorbed in the ZnO layer.

5.12 Comparison of a single P3HT cell and a P3HT:P3HT tandem cell

Comparing the performance of a typical single cell P3HT cell to the two layer P3HT tandem cells, shows the tandem cell to perform worse. The voltage is 1.9 times higher than the single cell, the current is 44 % of the single junction and the fill factor is down from 44.4 % to 35.8 %. The lower performance of the tandem cell is expected when using a material such as P3HT, where most of the light is absorbed in the active layer for this thickness and the transport properties of the active layer is not a problem.

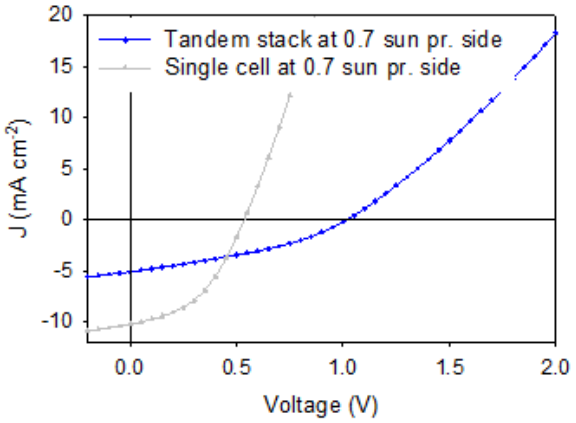

	Tandem■	Single■
V_{oc}	1.02 V	0.54 V
J_{sc}	5.11 mA cm^{-2}	11.4 mA cm^{-2}
FF	35.8 %	44.4 %
PCE	1.33 %	1.94 %

■Measured at 0.7 sun pr. side

Figure 5.12: Comparison of the J-V curve for a single junction solar cell and a tandem solar cell in the two side illumination setup. The V_{oc} of the tandem cell is almost two times the V_{oc} of the single junction, while the current and fill factor of the single cell are higher than for the tandem cell. Reproduced with permission from Elsevier [1]

5.13 Use of PDTSTTz-4 versus P3HT

As a test for the use of other polymers, a batch of tandem cells based on different combinations of the P3HT and PDTSTTz-4 polymers were made. The PDTSTTz-4 poly-

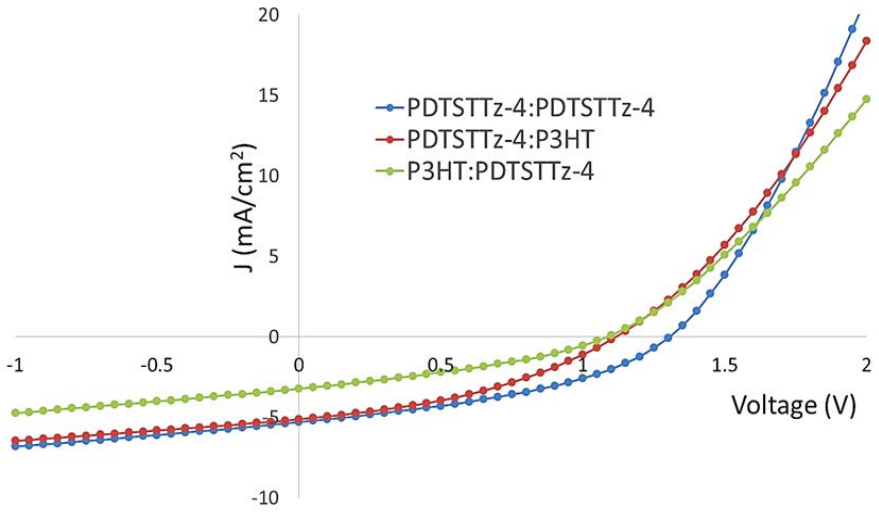

Figure 5.13: Example of tandem cells with the P3HT and PDTSTTz-4 polymers. The PDTSTTz-4 polymer gives a higher voltage than the P3HT polymer, due to a better alignment with the PCBM acceptor.

mer is similar in its absorption spectrum, however due to lower energy levels, the voltage of single cells based on this polymer is higher than for P3HT. This also applies for the tandem cells based on the polymer. By using a combination of P3HT and PDTSTTz-4 in the tandem solar cell, the V_{oc} of the solar cell is increased from 1.02 V to 1.09 V with the P3HT as the first layer and 1.12 V with P3HT as the second layer. By using PDTSTTz-4 in both active layers the V_{oc} was raised to 1.30 V. The increased voltage with similar current levels resulted in a power conversion efficiency of 1.8 % under two sided illumination. The high voltages proves the intermediate layer to be a very efficient recombination layer

Table 5.2: Performance of double sided illuminated tandem solar cells based on PDTSTTz-4 and P3HT polymers. Numbers measured at 0.7 suns pr. side

	PDTSTTz-4: PDTSTTz-4	PDTSTTz-4: P3HT	P3HT: PDTSTTz-4
V_{oc}	1.30 V	1.12 V	1.09 V
J_{sc}	4.82 mA cm^{-2}	4.66 mA cm^{-2}	2.93 mA cm^{-2}
FF	39.9 %	38.0 %	33.9 %
PCE	1.79 %	1.41 %	0.77 %

5.14 Single sided illumination with the developed intermediate layer

With the use of the developed intermediate layer solution of F10 PEDOT, 4083 PEDOT and ZnO the progress onto single sided illumination was completed. Solar cells based on the two polymers PDTSTTz-4 [10]and PSBTBT [11] both mixed with PCBM was completed.

Table 5.3: Coating parameters used for a single sided illumination tandem solar cell.

Layer	Material	Concentration	Temp	Speed	Flow	T_{wet}
Substrate	Flextrode		°C	m/min	mL/min	µm
1st active layer	PDTSTTz-4:PCBM	16:24 mg/ml	60	1.0	0.20	15
Compatibilizer	PEDOT F010:IPA	1:4 vol/vol	60	1.0	0.10	8
HTL	PEDOT 4083:IPA	1:2 vol/vol	60	1.0	0.30	23
ETL	ZnO	39 mg/ml	60	2.0	0.10	3.8
2nd active layer	PSBTBT:PCBM	20:20 mg/ml	60	1.0	0.08	6
Compatibilizer	PEDOT F010:IPA	1:4 vol/vol	60	1.0	0.10	8
HTL	PEDOT 4083:IPA	1:2 vol/vol	60	1.0	0.30	23
Conducting Layer	PEDOT F10:IPA	1:1 vol/vol	60	1.0	0.40	31
Top Electrode	Ag PV410		60	1.2		

The cells were manufactured according to the parameters presented in Table 5.3 with a variation of the PSBTBT active layer thickness with three stripes coated at 0.12 ml/min, 0.10 ml/min and 0.08 ml/min respectively. Representative J-V curves of the cells are presented in Figure 5.15. The best performing cells showed efficiencies of approximately 1.1% under 1000W/m^2 AM1.5G illumination. These were cells with the thinner second active layer. The lower efficiency of the thicker active layer suggests possible issues with recombination in the layer.

Comparing the efficiency of the single sided illuminated cells to the double sided illuminated cells shown in Figure 5.13, shows a drastic reduction in the short-circuit current extracted from the cells. However the lower efficiency of the single cell PSBTBT solar cell compared to a single cell P3HT solar cell is clearly part of the reason, while matching of the band gaps of the two polymers would also be beneficial to move a bit since the use of the flextrode substrate allows less light to pass through in the region from 600 nm to 850 nm, where the PSBTBT cell is primarily working, than what passes

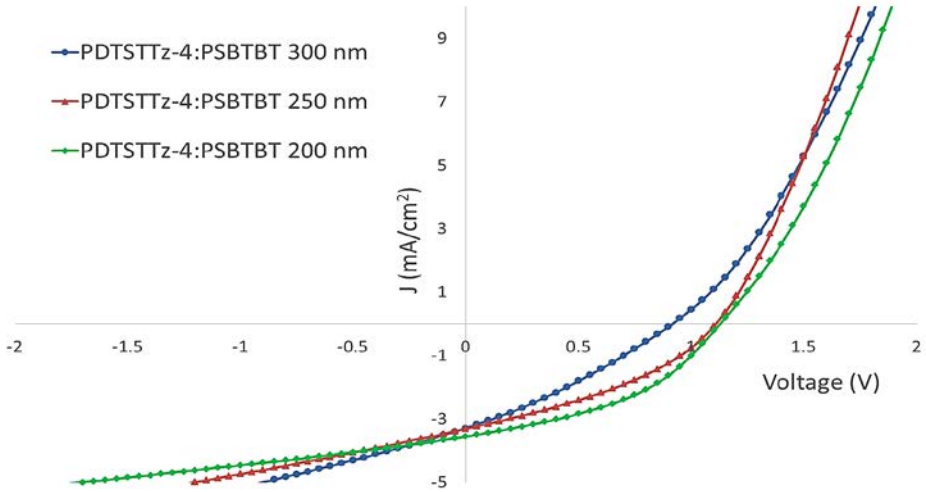

Figure 5.15: Tandem cells made with the PDTSTTz-4 polymer and the PSBTBT low band gap polymer. The low band gap polymer was coated in three different thicknesses, ~300 nm, ~250 nm and ~200 nm.

through an ITO based substrate as used in the previous reports of this polymer combination.

A picture of one of the coated tandem cells is shown in Figure 5.14. The image shows the tandem solar cells to be pseudo-transparent, which is another limiting factor. A reflective back electrode could help to reflect back light through the active layers, increasing the absorption in the active material and help to reduce the need for as thick active layers.

Figure 5.14: Semi-transparent tandem solar cell consisting of the 12 layer stack with active layers of PDTSTTz-4:PCBM and PSBTBT:PBCM.

5.15 Bending Test

The added complexity of coating more layers also means that there are more interfaces between these layers and thereby a larger risk of having issues with delamination or cracking of the films during exposure to mechanical strain.

Doing bending tests can help to show how the solar cells responds to mechanical strain and how well the solar cells can withstand handling. In the case of roll to roll coating the production of the solar cells is the first step on the path of mechanical straining of the materials, since the roll to roll machines runs the foil through going over a number of rollers, most of which have diameters from 90 mm and upwards. Bending tests on dedicated compression testing machinery with smaller bending diameters and repetitive bending can help to show if any drop in performance happens during repetitive bending or if there is a critical bending angle above which the devices dies immediately or simply dies faster.

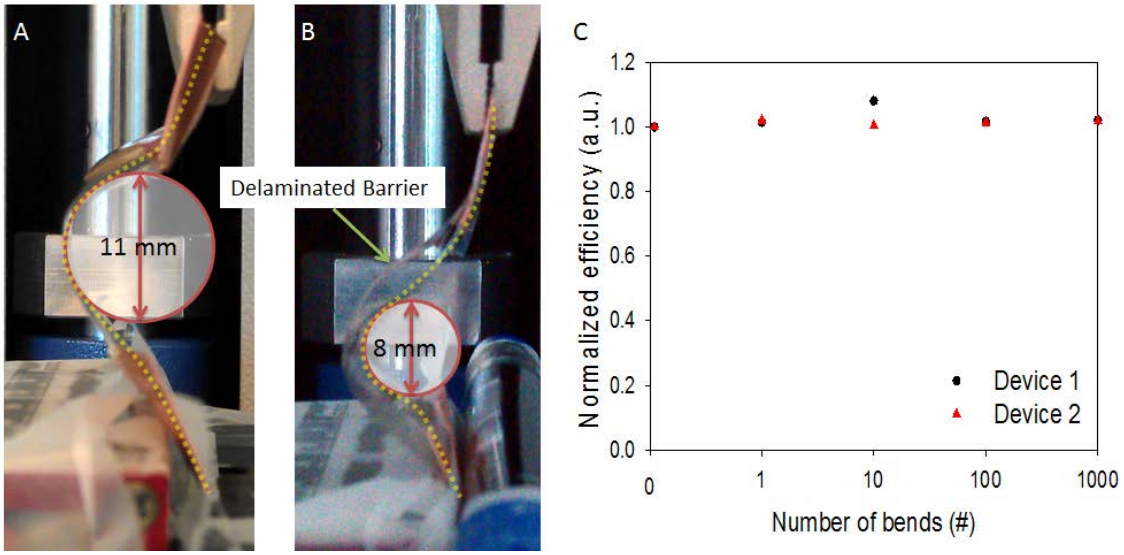

Figure 5.16: Bending tests performed on Tandem solar cells coated on Amcor Flextrode substrate with an encapsulation of DELO LP-655 and AMCOR barrier foils. A) shows device 1 with a bending radius of 11 mm while B) shows device 2 under a bending radius of 8 mm. Both cells were bend for 1, 10, 100 and 1000 times with IV-curves being captured at each of the aforementioned numbers. C) Normalized efficiencies of the cells, with practically identical performance. Both cells also showed the delamination as seen in B). The dashed yellow line indicates the position of the solar cell.

Two tandem cells were taken from a P3HT:P3HT tandem batch, and encapsulated in AMCOR barrier foil using DELO LP-655 epoxy glue. The silver top contacts were contacted using conductive cobber tape and expanded to enable contacting of the cell, while keeping the area of the cell under bending without too much variation in flexibility. Both cells were bend for 1, 10, 100 and 1000 times with IV-curves being captured at each of the aforementioned numbers. The performance of the cells after each of the bending cycles showed to be very constant, as shown in Figure 5.16C, with only an outlier at 10 bends for device 1, due to slightly higher lamp intensity during that measurement.

Both cells showed a delamination of the encapsulation, which was caused by a weak adhesion between an UV-barrier glued to the substrate and the substrate itself. Images of the two cells under bending are seen in Figure 5.16. The dashed yellow line on the images indicates the position of the solar cell.

5.16 Summary

This chapter has shown the possibility of making tandem solar cells with a solvent resistant intermediate layer using only wet processing technologies and with the mini roll coater (MRC) used as the only machine necessary for the fabrication.

Two sided illumination of tandem cells were manufactured using the scheme for testing the efficiency of the intermediate layer as recombination layer, showing voltages on the level of two individual cells, when using either P3HT or PDTSTTz-4 polymers. A single sided illumination tandem cell was made using the PDTSTTz-4 and PSBTBT polymers, showing an efficiencies 1.1 % due to a current limitation caused by the PSBTBT polymer.

References

[1] T.R. Andersen, H.F. Dam, B. Andreasen, M. Hösel, M.V. Madsen, S.A. Gevorgyan, et al., A rational method for developing and testing stable flexible indium- and vacuum-free roll processed tandem polymer solar cells, *Sol. Energy Mater. Sol. Cells*. (n.d.),.

[2] L.L. Kazmerski, NREL Best Research-Cell Efficiencies, *Wikipedia Free Encycl.* (2013),.

[3] M.A. Green, K. Emery, Y. Hishikawa, W. Warta, E.D. Dunlop, Solar cell efficiency tables (version 39), *Prog. Photovoltaics Res. Appl.* 20 (2012), 12–20.

[4] C.W. Tang, Two-layer organic photovoltaic cell, *Appl. Phys. Lett.* 48 (1986), 183–185.

[5] Heliatek consolidates its technology leadership by establishing a new world record for organic solar technology with a cell efficiency of 12% - http://www.heliatek.com, *Heliatek*. (n.d.),.

[6] J. You, C.-C. Chen, Z. Hong, K. Yoshimura, K. Ohya, R. Xu, et al., 10.2% Power Conversion Efficiency Polymer Tandem Solar Cells Consisting of Two Identical Sub-Cells, *Adv. Mater.* (2013), n/a–n/a.

[7] J. You, L. Dou, K. Yoshimura, T. Kato, K. Ohya, T. Moriarty, et al., A polymer tandem solar cell with 10.6% power conversion efficiency, *Nat. Commun.* 4 (2013), 1446.

[8] S. Sista, M.H. Park, Z. Hong, Y. Wu, J. Hou, W.L. Kwan, et al., Highly efficient tandem polymer photovoltaic cells, *Adv. Mater.* 22 (2009), 380–383.

[9] N. Li, D. Baran, K. Forberich, M. Turbiez, T. Ameri, F.C. Krebs, et al., An Efficient Solution-Processed Intermediate Layer for Facilitating Fabrication of Organic Multi-Junction Solar Cells, *Adv. Energy Mater.* (2013), n/a–n/a.

[10] Z.-G. Zhang, J. Min, S. Zhang, J. Zhang, M. Zhang, Y. Li, Alkyl chain engineering on a dithieno[3,2-b:2',3'-d]silole-alt-dithienylthiazolo[5,4-d]thiazole copolymer toward high performance bulk heterojunction solar cells, *Chem. Commun.* 47 (2011), 9474–9476.

[11] J. Hou, H.Y. Chen, S. Zhang, G. Li, Y. Yang, Synthesis, characterization, and photovoltaic properties of a low band gap polymer based on silole-containing polythiophenes and 2, 1, 3-benzothiadiazole, *J. Am. Chem. Soc.* 130 (2008), 16144–16145.

6. Electrochromic Devices

Electrochromic are materials which changes their color or color intensity when an electric field is applied to them. For polymer based electrochromics this occurs by a reduction or oxidation of the polymer.

In the work described by Jensen et. al. [1], attached as appendix A6 roll-coated electrochromic devices (ECDs) were fabricated and tested with success, showing the possibility of making organic based electrochromic devices such as windows and displays on a cheap in-air slot-die coating process.

6.1 Working Principle

The majority of ECDs consists of one polymer which changes color when switched between the reduced and oxidized state and a counter polymer, which is necessary to balance the redox reaction. Preferably the charge balancing polymer should lend minimal absorption to the device in both redox states. Between the two polymers is an electrolyte layer, which is electrically insulating, but ionically conducting. The change in color is caused by the application of an electric field across the two electrodes causing

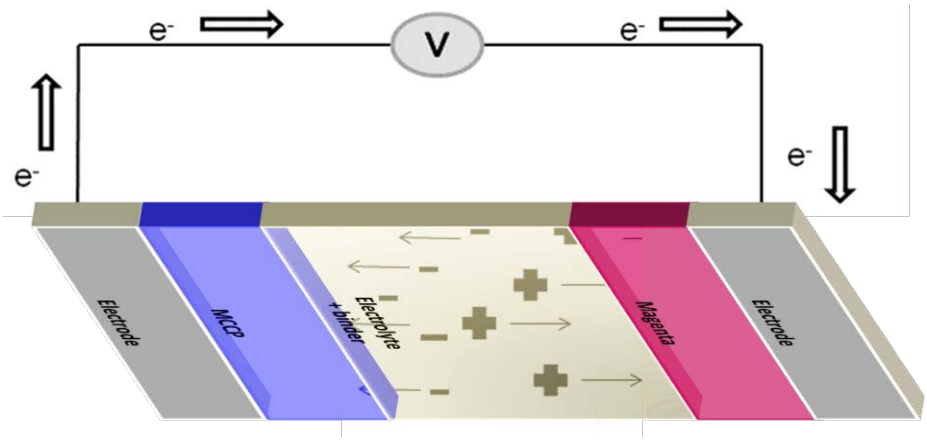

Figure 6.1: Principle of an electrochromic device. The connection of the electrodes to a voltage supply respectively oxidizes and reduces the polymers and to compensate the charge build up the mobile ions in the electrolyte moves to screen the charges.

an oxidation and reduction of the respective polymers. The effect is reversible, so the polymer can be repeatedly switched between its two states.

Compared to light emitting devices and liquid crystal displays, the principle of the electrochromic device is similar to that of a capacitor, where power only needs to be applied when changing the color of the device. The device will remain in one of the two redox states until the polarity is reversed or slowly discharge the built in potential until the ground state is reached.

6.2 Considerations in manufacturing an electrochromics display

In general, there are several challenges for electrochromic technology as presented in Figure 6.2 which has to be considered. These have been broken down into three main points: materials, addressability, and device manufacture. Previous work has addressed the challenges in regards to color availability and processing, allowing for a full color palette of solution processable polymers [2,3]. However, less effort has focused on utilizing these different materials in full device manufacture, on flexible substrates

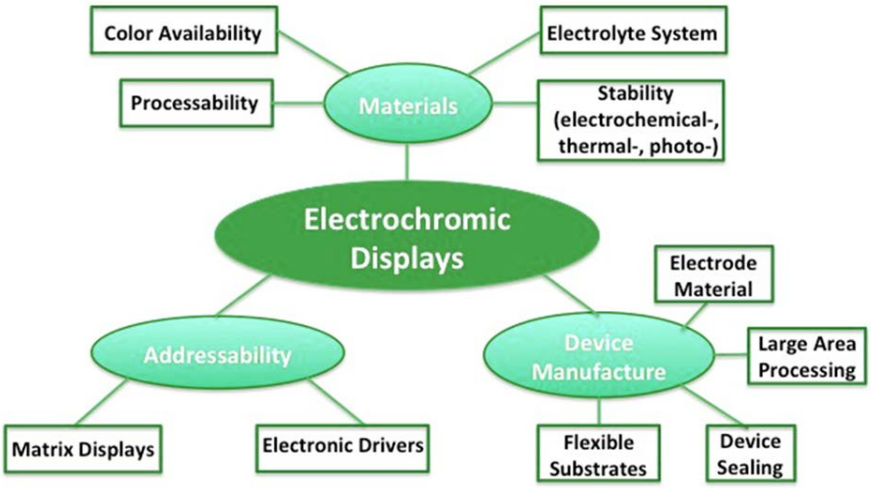

Figure 6.2: Chart of the considerations which has to be applied for manufacturing relevant electrochromic devices.

utilizing large area processing, let alone addressability of matrix displays and integration of electronics drivers [4]. As effort towards use of EC materials in commercial applications, such as currently available in auto mirrors, the development process for

ECDs is at a stage where further progress has to centre on efficient production methods combining high output, reliability and low cost. To realize these important parameters, where conjugated polymers are concerned, the employment of roll coating onto flexible substrates emerges as the technique of choice. The success of using these techniques in polymer photovoltaics manufacture has stimulated the use of similar techniques in electrochromic devices, addressing several of the points illustrated in Figure 6.2.

6.3 Materials

All chemicals and solvents were used as received unless otherwise noted.

The polymers used for the devices was the magenta polymer (ECP-Magenta), poly((2,2-bis(2-ethylhexyloxymethyl)-propylene-1,3-dioxy)-3,4-thiophene-2,5-diyl) and the minimally changing polymer (MCCP), poly(N-octadecyl-(propylene-1,3-dioxy)-3,4-pyrrole-2,5-diyl), previously reported in Reeves et. al. [5] The schematic of both polymers can be seen in Figure 6.3.

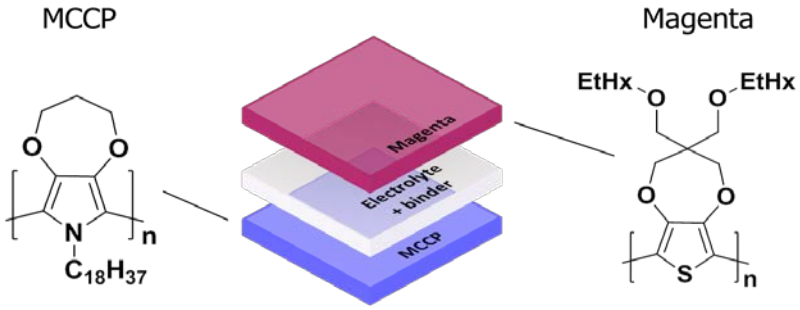

Figure 6.3: Materials used in an organic electrochromic device. A Minimally Colour Changing Polymer (MCCP), an electrolyte+binder layer and a Radiantly Colour Changing Polymer (RCCP) consisting of the Magenta polymer.

The polymer inks used for the poly(methylmethacrylate) (PMMA)/propylene carbonate (PC) devices had an electrolyte content equivalent to that of the electrolyte-binder layer (w/w) to avoid cracking in the polymer film. Chloroform was used as solvent because of the solubility of both polymer and salt, while having a reasonably low

vapor pressure making it suitable for roll coating. The ElectroChromic Polymer (ECP)-Magenta had a M_n of 76 kDa and the MCCP had a Mn of 56 kDa. The concentrations of inks were varied according to coating method. Solutions of 5 mg/mL were used in the spray coating experiments. In the spin coating experiments 20 mg/mL concentration of polymer was used, whereas the concentration used for slot-die coating varied from 20 to 40 mg/mL in $CHCl_3$.

The ionic liquid electrolyte solution was made according to Susan et. al [6] with a slight modification. Methylmethacrylate (MMA) and the crosslinking agent ethyleneglycol-dimethacrylate was purified by distillation and degassed before use. Benzoylperoxide was recrystallized from chloroform/methanol before use. MMA (0.02 mol), the crosslinker ethylenedimethacrylate (2 mol %) and 1-ethyl-2-methyl-imidazolium-bis(triflouromethane sulfonyl)imide (0.02 mol) were mixed in a round-bottomed flask and benzoyl peroxide (BPO) (0.5 mol %) was added. A condenser was added and the solution stirred at 85 °C for 4 hours, after which 10 mL of acetonitrile was added. Further stirring for 12 hours at 85 °C yielded a slightly yellow viscous solution that was used without further purification.

6.4 Fabrication of a electrochromic device

The polymer is coated on a substrate with a transparent conducting electrode. Examples of coatings of Magenta and MCCP on the MRC can be seen in Figure 6.4. On top of the polymer the electrolyte layer is coated, which supply the ions necessary to ensure charge balance when the polymer is reduced or oxidized.

The electrochromic devices reported here were produced by either slot die coating or spray coating, the advantage of the slot-dye coating process being a higher uniformity and one dimensional pattern control.

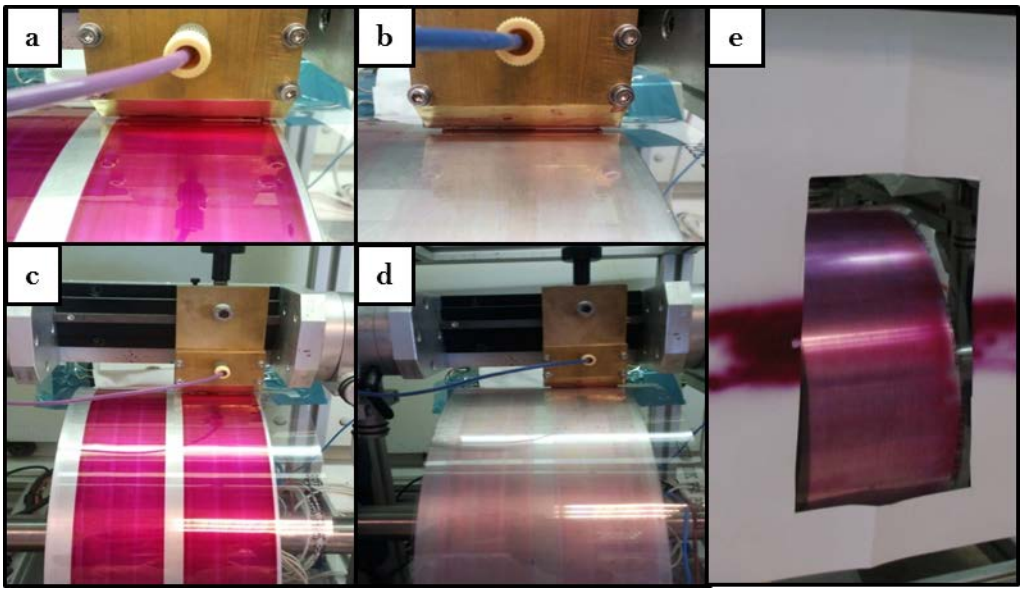

Figure 6.4: Roll coating of (a and c) ECP-Magenta from a 20 mg/mL solution and (b and d) MCCP from a 20 mg/mL solution. (e) A spray-coated substrate coated with 20 mg/mL ECP-Magenta. Reproduced with permission from Wiley [1].

Roll coating was performed on the mini roll coater [7,8], as presented in Chapter 2, using PET foil substrates pre-coated with a 175 nm sputtered ITO layer. The ITO came pre-etched into stripes of 4 mm or 13 mm width. The ITO electrode layer had a nominal sheet resistivity of 100 Ω/□. Lengths of 1 m were coated at a time with a coating width of 50 mm, thereby covering three or eight of the pre-patterned ITO stripes, respectively. ECP-Magenta, MCCP, and electrolyte were coated on the machine with a high degree of uniformity, as seen in the color uniformity of the coating in Figure 6.4.

6.4.1 EC Assembly

The ECDs were assembled manually due to the adhesiveness of the electrolyte. The ITO covered PET substrate was cleaned with isopropanol prior to coating. After coating of the various layers, 1 cm of ITO was carefully cleaned for electrical contact by removing the polymer and electrolyte layer with isopropanol.

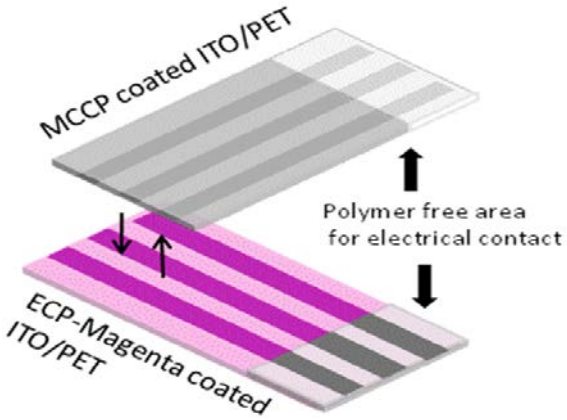

Figure 6.5: Assembly of the ECD. The foils consist of PET with ITO stripes or solid ITO. MCCP (top) and ECP-Magenta (bottom) is coated onto the foils followed by a layer of electrolyte. The foils are placed on top of each other with the ITO stripes perpendicular. An area of 1 cm on each foil is cleaned of polymer for connection to an external power source. Reproduced with permission from Wiley [1].

The two films were assembled perpendicular to each other, as shown in Figure 6.5. After assembly, the device was run through a laminator effectively forming a single united electrolyte- binder layer.

6.5 Pixelated devices

An example of the pixelated devices with a 4 x 4 mm^2 pixel size is shown in Figure 6.6. The pixelated devices can be switched between the reduced and oxidized states independently for each pixel, however showing a little crosstalk between pixels.

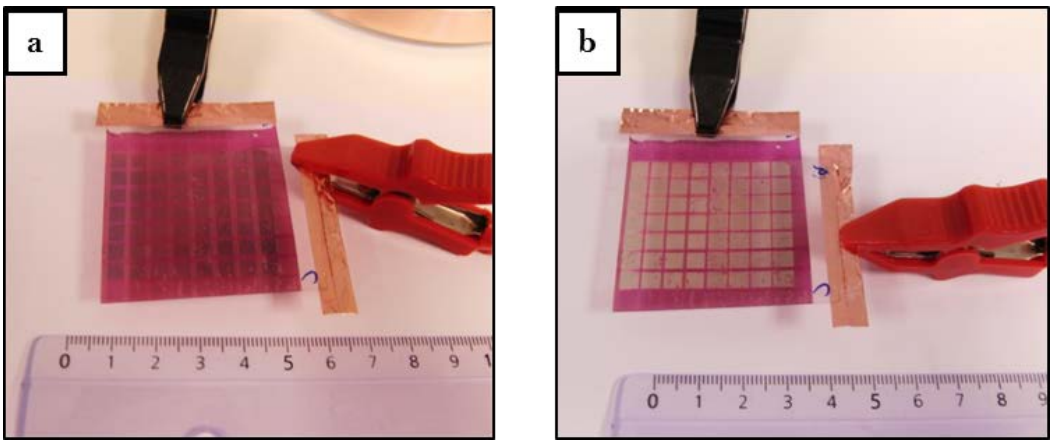

Figure 6.6 Example of pixelated device in the reduced (a) and oxidized state. The device is a roll coated multi pixel device using an eight striped 4 mm wide ITO patterned substrate.

6.6 Switching the device

The electrochromic device is operated by the application of a positive or negative voltage to its two electrodes to either reduce or oxidize the colored polymer.

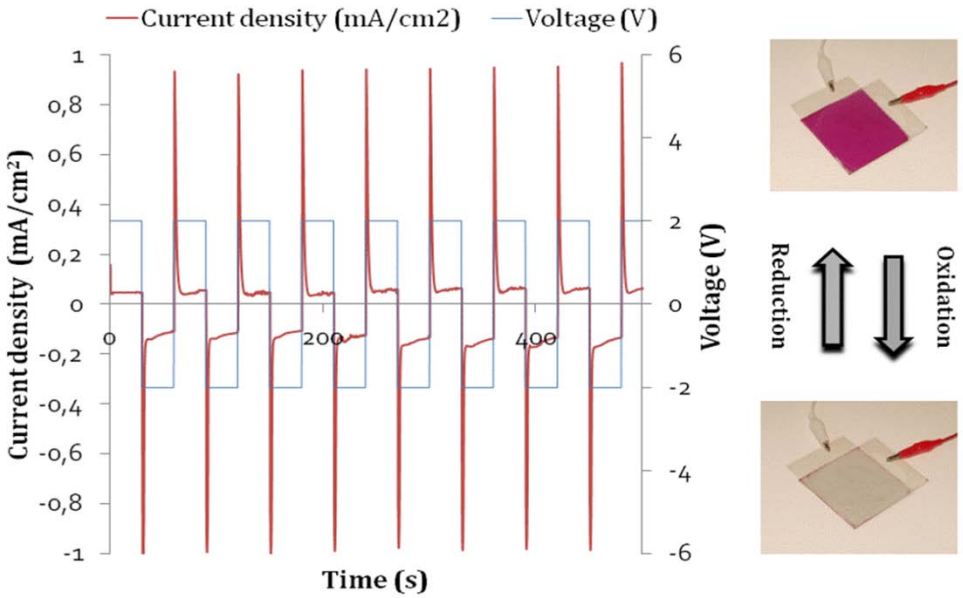

Figure 6.7: Current (left axis)/voltage (right axis) switching of a 10 cm^2 device, when switched between -2 and 2 V. The colored (reduced ECP-magenta) and bleached (oxidized ECP-Magenta) states for a device are shown in the photographs to the right. Reproduced with permission from Wiley [1].

Switching of the manufactured devices was completed with a symmetric square wave pulse switching between ±2 V. The current response to the switching voltage is seen in Figure 6.7. It can be seen that the response to the voltage is not symmetric with a clearly faster switching from the reduced to the oxidized state.

6.7 Period of color stability

The stable state for the ECD is the colored (reduced) state. The hold time of the oxidized state is however important. During a time period of 4 hours without current after having switched the device to its transparent state, the device switches back to the magenta reduced (stable) state, as shown in Figure 6.8. This is caused by the movement

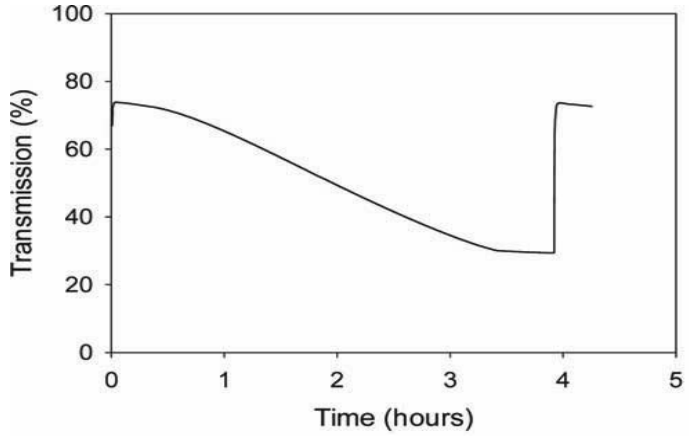

Figure 6.8: The hold time of a roll coated device. During a time period of 4 hours without current after having switched the device to its transparent state, the device switches back to the magenta oxidized state. Reproduced with permission from Wiley [1].

of the ions in the electrolyte. They will not completely screen the potential of the charged polymer, so while some of the polymer chains changes back to the neutral state the screening ions will move in the electrolyte, since the small screening field is no longer there and thereby increase the risk of another unit to go to its reduced state. This is of importance for large area applications as a short hold time would result in a need for applying a switching/holding voltage at more regular intervals, thereby increasing the power consumption.

Based on this result, it would seem that these ECDs have a large potential for display and shading applications with very low power consumption either through self-powering using a solar cell as demonstrated in [1,9] or through brief updates of the color state every 30 min.

6.8 Device degradation

Degradation of the electrochromic devices was investigated by several different tests. First of the change in transmission as a result of repeated switching of the device was tested, with an automated switching test of the transmission of the device before, after and during a switch of the device under the ±2 V potential previously used.

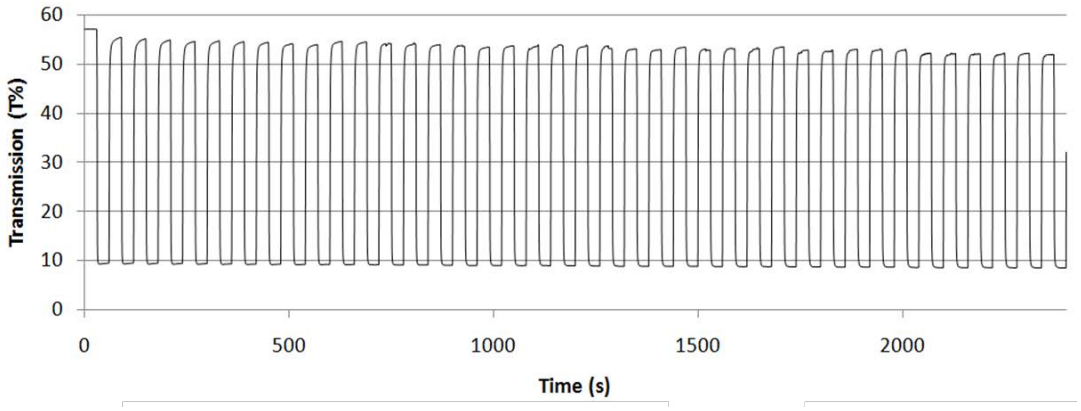

Figure 6.10: Transmission of a device at 550 nm while switching from 2 to -2 V for 30 s at each potential. For a 45-min period (90 switches) a slight decrease in DT is observed.

In Figure 6.10 the transmission of the device is shown. A slight drop in transmission of the oxidized (clear) state can be seen after 90 switches. The degradation can be minimized by the use of a lower switching potential, however also resulting in a longer switching time. The switching times of the device has been extrapolated from the trial for the interval from 600 seconds to 750 seconds, as shown in Figure 6.9, showing a 90% switch to occur in 2.3 seconds and 3.9 seconds for the colour-to-bleach and bleach-to-colour, respectively.

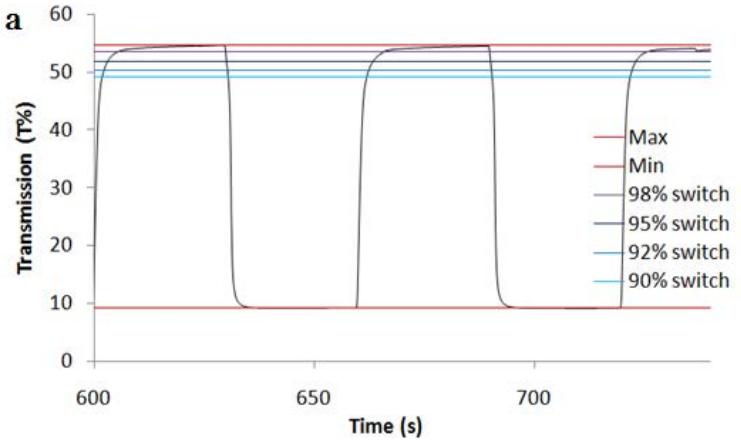

b

	Colour to bleach		Bleach to colour	
% of full switch	% T	t (sec)	%T	t (sec)
100% switch	54.6	10	9.2	9.8
98% switch	53.7	6.2	10.1	6.8
95% switch	52.3	3.8	11.4	4.8
92% switch	51.0	2.7	12.8	4.2
90% switch	50.1	2.3	13.7	3.9

Figure 6.9: Transmission of a device at 550 nm while switching from 2 to -2 V for 30 s at each potential. Response times for the 600–750-s interval. The colors represent various degrees of switching. (b) Table showing response times corresponding to the lines in (a). Reproduced with permission from Wiley [1].

The devices prepared here were not encapsulated in a barrier to oxygen and water and in spite of this showed a reasonable stability both towards shelf lifetime and under light illumination. We illuminated an operational device with a solar simulator (AM1.5G, 1000 W/m2, 45 C) for 100 h continuously and found that the degree of photo bleaching was limited.

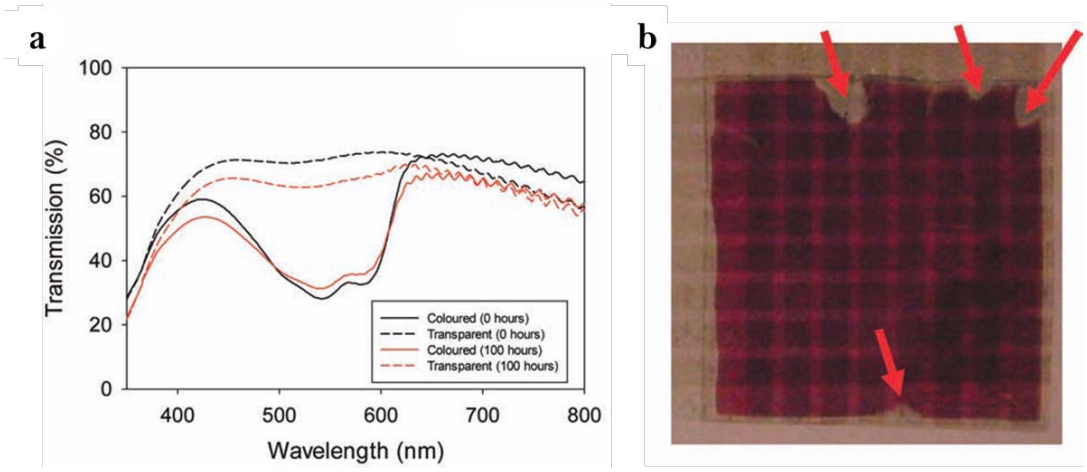

Figure 6.11: Degradation of the electrochromic device due to photo bleaching. A complete device underwent continuous illumination (AM1.5G, 1000 W/m^2, 45 °C) for 100 h. The loss in switching capacity as a consequence of the 100-h illumination condition was 25% (see a). The effect of photo bleaching is shown in the photograph (b) of the photo bleached device. Red arrow marks an observed ingress all around the edges.

The device lost 20% in absorbance and when switching about 25% of the transmission change was lost, as seen in (Fig. 11). The photo bleaching was just visible to the eye and most significant in areas around the edges where slight delamination had occurred allowing for ingress of water and oxygen. This is a convincing result and it is estimated that operation for many years is possible provided that water and oxygen are excluded from the ECD through a suitable barrier material. The shelf life is encouragingly long for practical development and use. It was not possible to detect any decrease in absorbance or performance for devices stored or cycled in the dark for 4 months.

6.9 Summary

Demonstration of fully roll coated devices of various sizes, up to 4 x 4 cm^2, are demonstrated with pixelated devices containing pixel sizes of 4 x 4 mm^2 or 13 x 13 mm^2. The transmission contrast exhibited by the devices, when switched between the fully bleached and fully colored state was 58 % at a visible wavelength of 550 nm and the devices exhibited switching times of <10seconds, with 95% switching within 5 seconds.

References

[1] J. Jensen, H.F. Dam, J.R. Reynolds, A.L. Dyer, F.C. Krebs, Manufacture and demonstration of organic photovoltaic-powered electrochromic displays using roll coating methods and printable electrolytes, *J. Polym. Sci. Part B Polym. Phys.* 50 (2012), 536–545.

[2] A.L. Dyer, E.J. Thompson, J.R. Reynolds, Completing the color palette with spray-processable polymer electrochromics, *Acs Appl. Mater. Interfaces*. 3 (2011), 1787–1795.

[3] C.M. Amb, A.L. Dyer, J.R. Reynolds, Navigating the Color Palette of Solution-Processable Electrochromic Polymers†, *Chem. Mater.* 23 (2011), 397–415.

[4] P. Andersson, R. Forchheimer, P. Tehrani, M. Berggren, Printable All-Organic Electrochromic Active-Matrix Displays, *Adv. Funct. Mater.* 17 (2007), 3074–3082.

[5] B.D. Reeves, C.R.G. Grenier, A.A. Argun, A. Cirpan, T.D. McCarley, J.R. Reynolds, Spray Coatable Electrochromic Dioxythiophene Polymers with High Coloration Efficiencies, *Macromolecules*. 37 (2004), 7559–7569.

[6] M.A.B.H. Susan, T. Kaneko, A. Noda, M. Watanabe, Ion Gels Prepared by in Situ Radical Polymerization of Vinyl Monomers in an Ionic Liquid and Their Characterization as Polymer Electrolytes, *J. Am. Chem. Soc.* 127 (2005), 4976–4983.

[7] H.F. Dam, F.C. Krebs, Simple roll coater with variable coating and temperature control for printed polymer solar cells, *Sol. Energy Mater. Sol. Cells*. 97 (2012), 191–196.

[8] J.E. Carlé, T.R. Andersen, M. Helgesen, E. Bundgaard, M. Jørgensen, F.C. Krebs, A laboratory scale approach to polymer solar cells using one coating/printing machine, flexible substrates, no ITO, no vacuum and no spincoating, *Sol. Energy Mater. Sol. Cells*. 108 (2013), 126–128.

[9] C.M. Lampert, Large-area smart glass and integrated photovoltaics, *Sol. Energy Mater. Sol. Cells*. 76 (2003), 489–499.

7. Light Emitting Electrochemical Cell (LEC)

Light emitting electrochemical cells (LEC) [1] are a competitive and somewhat complementary technique to the more well-known OLED. However there are some inherent advantages in the LEC compared to the OLED and of course also some drawbacks. The main selling point of LEC devices is a prospect for better efficiency than OLEDs and easier processing conditions.

In Figure 7.1 examples of operating roll coated LEC devices are shown. The two images are of a fabricated LEC device with light emission from the back (a) and front (b) while operated at 7 V. The emitting area is ~300 mm^2

In the work described in the article Sandström et. al. [2], attached as appendix A7 roll-coated LEC devices were fabricated and tested with success, showing the possibility of making large scale displays on a cheap in-air slot-die coating process. This chapter is based on the paper with some added data which was not presented in the paper.

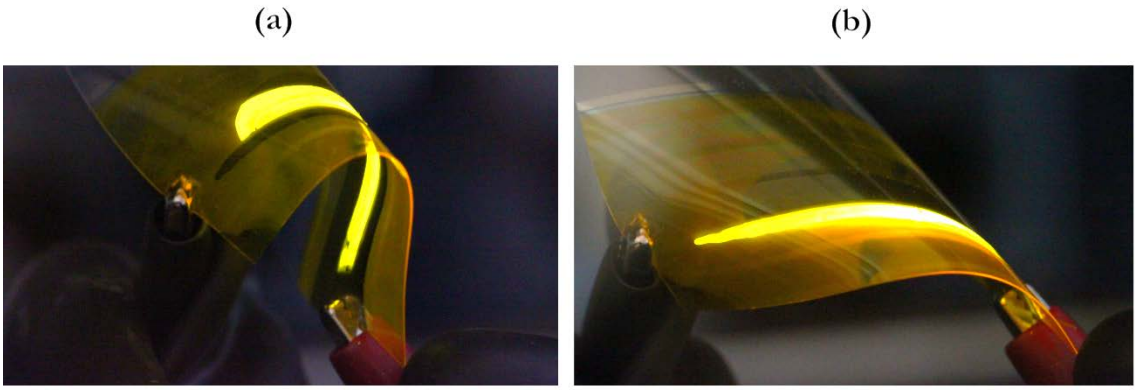

Figure 7.1: (a, b) Photographs of the light emission from two slot-die coated LEC devices driven at V = 7 V illustrating the bi-directional light emission and the device conformability. Reproduced with permission from Nature Publishing Group [2]

7.1 Principle of a LEC device

LEC's works by the principle of radiative recombination. The active material is a conjugated polymer (in this case Merck, Superyellow , no. PDY-132) which has a strong yellow colored light emission when electrons and holes recombine in the polymer. This

makes it an ideal candidate in both OLED and LEC devices. For it to work in a LEC device the SY layer is mixed with an electrolyte to enable a doping of the polymer.

This means that upon turning on the voltage for the device an injection of electrons and holes from each of the corresponding electrodes will cause a doping of the polymer with the injection of electrons increasing the amount of free carriers in the LUMO level, while the charging occurring being offset by the positive ions in the electrolyte. From the hole injection side the number of carriers in the HOMO level will increase and the charging will be offset by the negative ions in the electrolyte, in total causing a cancelation of the charge concentration associated to the polymer. The resulting P-N junction will emit light from the PN-boundary layer, when charges from each of the doped sides of the polymer meet.

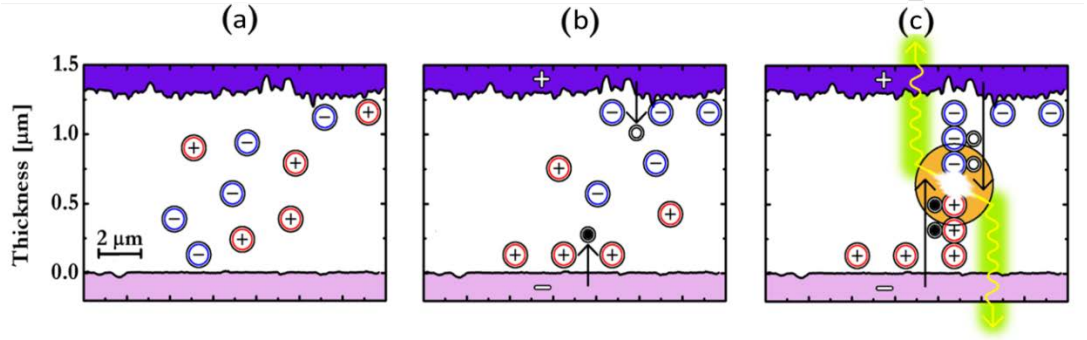

Figure 7.2: Working principle of a light-emitting electrochemical cell. a) schematic structure of a pristine LEC device indicating the existence of mobile ions, b) the electric double-layer formation and initial electronic charge injection within the same device following application of a voltage bias, c) and the light-emission from the in-situ formed p-n junction at steady-state.

The advantage of this principle in contrast to OLED devices is that the dependency on making uniform layers of active material to get uniform light emission is no longer required. In the OLED a variation of the layer thickness will cause a change in the strength of the electric field and places with a thin active layer will therefore see a higher field than areas with thicker layers. Being a diode a higher electric field will result in a higher current and thereby a higher light intensity.

This is also in stark contrast to the organic solar cells, where a thickness variation doesn't cause issues since the principle of the solar cells is closer to the principle of the

LEC than the OLED, with a heterojunction in the solar cell consisting of two materials that in the interface between them make up the PN-junction.

The disadvantage on the other hand for a LEC in comparison to an OLED is the slower turn on time, due to the doping process. This makes LEC devices great for slow changing lights, such as commercial signs, road signs and other slow changing lighted displays, while fast changing and high resolutions displays is much better suited to be produced by the OLED technique.

7.2 Fabrication of LEC devices

The LEC devices were fabricated by slot-ide coating on the MRC coater described in the roll-coating chapter of this thesis. The devices were coated on a PET substrate with pre-patterned ITO in either a 4 mm or 13 mm wide stripe pattern. The coated however was performed in a 13 mm stripe pattern regardless of the underlying substrate pattern. In principle is seen in Figure 7.3(a) and in Figure 7.3(b) a picture of the coated devices on the prototype mini roll coater described in the roll coating chapter.

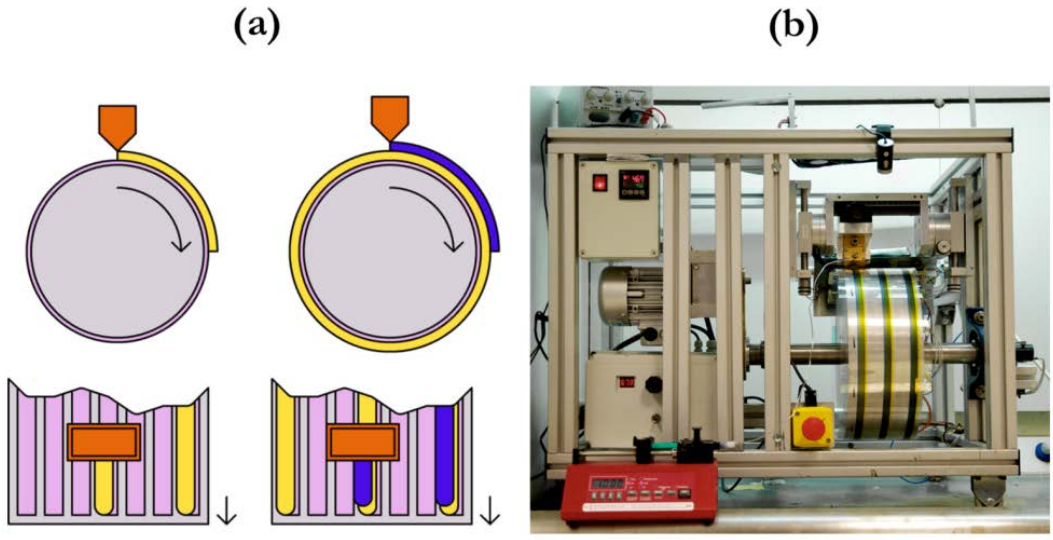

Figure 7.3: (a) Schematic view of the slot-die roll coating of the (yellow) active layer and the (blue) semi-transparent anode, (b) photograph of the roll coater during the deposition of the active layer. Reproduced with permission from Nature Publishing Group [2]

Devices both with and without ZnO between the ITO and Active layer was fabricated, however only devices with ZnO are reported here. The device stack consisted of the pre-patterned substrate, which was coated with a thick layer of the light emissive layer consisting of the Superyellow polymer and a KCF_3SO_3 salt in a poly(ethylene oxide) PEO polymer matrix. A layer consisting of conductive PEDOT:PSS was coated on top of the active layer as a top electrode (see schematic in Figure 7.5b). The coating of both the active layer and the PEDOT:PSS was completed at a speed of 0.6 m/min and a substrate temperature of 40°C. To dry the PEDOT:PSS fully it was degassed in a vacuum oven to avoid exposure of the devices to the higher temperatures used in the coating of solar cells.

An inherent issue with the coating of these materials used the slot-die coating technique is the roughness of the coated film. AFM scans of the layers in the device are shown in Figure 7.4 with an overlay of the individual layers in Figure 7.4(a) showing the substantial thickness of these films and in Figure 7.4(b) a separate plot of the rougher interfaces of the cathode and anode interface layers. The root mean squared value of the surface roughness of the cathode and anode layers were 4.5 nm and 20 nm, respectively.

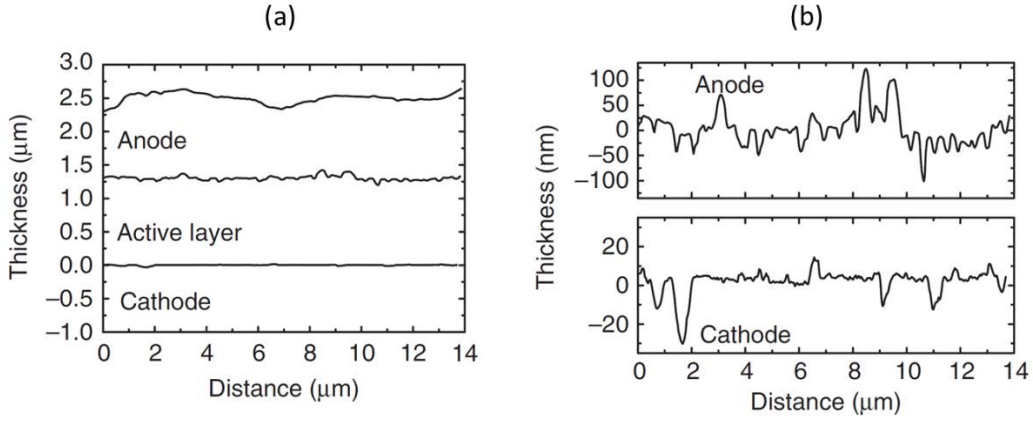

Figure 7.4 Thickness of the layers manufactured with the slot-die technique. A) An overlay of the three layers of the LEC, with AFM scans conducted on each layer. B) The roughness of each of the interfaces for the Anode-active layer and cathode-active layer respectively.

The reason as to why the LEC devices still works even with roughness's on this order of magnitude is due to the thick films, which it is possible to use in a LEC. In the OLED the film thickness is limited by the conductivity of the small molecule or polymer used and therefore most devices are made with film thicknesses of 30 nm to 100 nm [3,4]. In the LEC, the combination of materials in the active layer creates a doping of the polymer spreading from the electrode interfaces until they meet, illustrated in Figure 7.5(c). This in-situ created interface is where the light emission happens and due to this interface being created, the uniformity of the light emission is much less dependent on the electrodes, since the distance to the electrode no longer directly defines the electric field across the active layer.

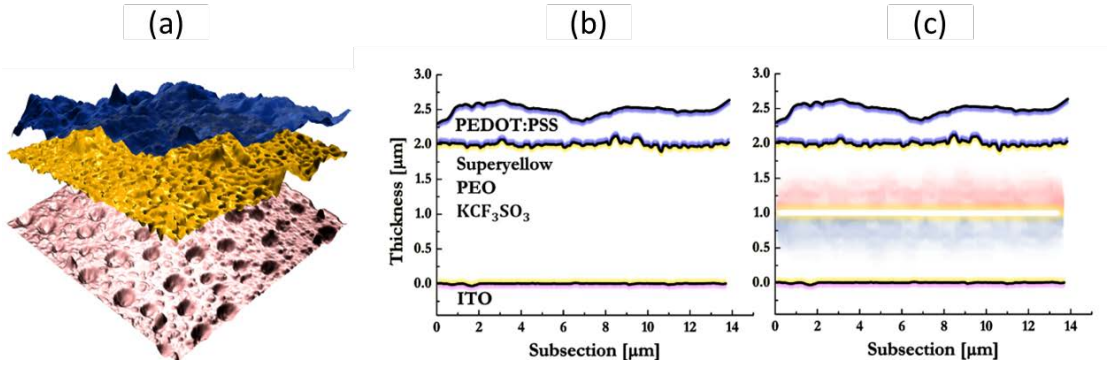

Figure 7.5: The figure shows: a) An exploded view of atomic force microscopy (AFM) height maps of the 10x10 µm^2 PEDOT-PSS anode (top), the active layer (middle), and the ZnO cathode (bottom). (b) The layer structure of the device, with the ITO bottom electrode, the Superyellow, PEO, KCF_3SO_3 active layer mix, and PEDOT:PSS top electrode, (c) Coloring indicated the doping of the polymer during operation, with a blue haze indicating a p-type doping of the polymer and red indicating a n-type doping. Light emission is marked by the yellow center lines.

7.3 Performance of a roll fabricated LEC device

The performance of the LEC devices produced are shown in Figure 7.6a, where optoelectronic data was recorded during a voltage sweep at 0.1 V/s, during which the brightness reached 150 cd/m^2 at a voltage of 10 V. The turn-on voltage at which the device began to emit visible light (B > 1 cd/m^2) was 3.7 V. This is close to the theoreti-

cal limit, as dictated by the band-gap potential of Superyellow, with a band gap of 2.4 V as described by Becker et. al. [5] and Sandström et. al. [6].

The time required is another essential part of the LEC device puzzle. While the OLED turns on instantly, in the LEC the doping of the polymer has to occur for the cell to reach its full brightness and efficiency. The turn-on time has been defined as the time to reach a brightness of B > 10 cd/m^2 for a pristine device: The turn on time was found to be roughly 2 s at a current of 770 A/m^2.

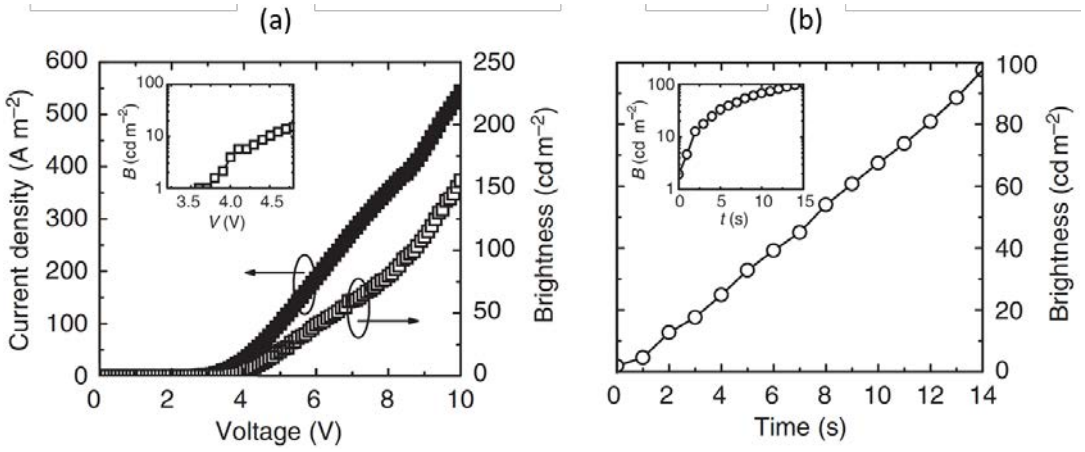

Figure 7.6: (a) Optoelectronic data recorded on a roll-coated PET / Indium-tin-oxide / ZnO / {SY+PEO+KCF$_3$SO$_3$} / PEDOT:PSS device during a voltage sweep at 0.1 V/s. Inset: the brightness data plotted on a logarithmic scale. (b) The turn-on time for a nominally identical device driven in galvanostatic mode at j = 770 A/m^2. Inset: the data plotted on a logarithmic scale. Reproduced with permission from Nature Publishing Group [2]

The fabrication yield of the roll-coated LECs was found to be satisfying, which could primarily be contributed to the fault-tolerant device geometry with a very thick active layer and some semi-air-stable materials. All tested devices, which were not mistreated during transportation and contacting, were functional and emitted light.

7.4 Stability of light emitting electrochemical cells

The operational stability of a roll-coated LEC can be quantified by the time for it to reach half-maximum brightness [7,8], which was found to be roughly 8 hours at a drive current density of 77 A/m^2, for these devices. The latter results were attained on de-

vices that had been stored in a glove box for more than 6 months. The highest recorded current efficacy is 0.6 cd/A at a brightness of 50 cd/m^2.

A study on the effect of using an encapsulation for improving the lifetime has been studied by Asadpoorvish et. al. [9] , where the barrier keeps the device protected from O_2 and H_2O vapor.

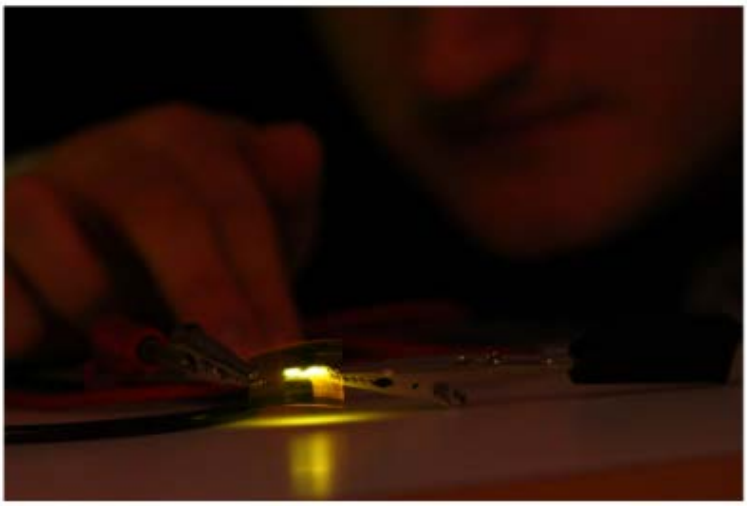

Figure 7.7: Photograph of an encapsulated roll-coated device operating at V = 7 V under ambient conditions. Note that the device had been stored under ambient air for 3 days before the voltage was applied.

The mentioned devices, from a performance context, were fabricated from a less than optimal ink, since the ink was made with the primary intent of making the coating as easy as possible. An example of the little optimization of the ink towards performance or stability is the high electrolyte content, which has proven to be detrimental for the attainment of both high efficiencies and long-term stability [10]. One could therefore also expect a significantly improved performance and stability with further optimization of the constituent processes and the utilization of lower-electrolyte-content active materials, resulting in closer to the state-of-the art efficiency and operational stability numbers for polymer LECs. These are at present efficiencies of roughly 10 cd/A and several 1,000 hours stability, which can be attained also for roll-coated LEC devices [11–14].

The ink formulation and coating processes, as presented herein, were conveniently executed solely under ambient conditions, but during light emission the active material in LECs (and in OLEDs) must be free from oxygen and water vapour to enable a satisfying performance. This challenge should, however, be addressable in a manner compatible with ambient processing by including an efficient drying stage at an elevated temperature to drive out remnants of O_2/H_2O/solvents followed by an immediately subsequent encapsulation stage, where a flexible barrier material is attached to the device with, for example, pressure-sensitive adhesive or a heat or UV-curable epoxy. A photograph of such an encapsulated roll-coated LEC device during operation at a voltage of 7 V and working under ambient conditions, is shown in Figure 7.7. The device could be operated without any signs of deterioration in performance following 3 days of ambient storage, despite the fact that the encapsulation material exhibits rather limited barrier properties with respect to water and oxygen permeability (see ref. [15]). Considering the current cost for high-performance barrier materials [16], the possibility of using a low-cost barrier material together with a material-conservative and time-efficient fabrication process could thus be an indicative step towards conformable emissive devices for low-end applications, at a cost that could be accepted by the market.

7.5 Summary

In summary, a demonstration of a full manufacturing of emissive LEC sheets, including the initial preparation of inks, to the coating of the constituent layers, to the final encapsulation in flexible substrates, can be carried out in air. This was done using slot-die coating, directly compatible with high-speed and low-cost roll-to-roll fabrication.

The fabricated devices are robust and fault-tolerant by the utilization of air-stable materials and a micrometer-thick emissive layer.

References

[1] Q. Pei, G. Yu, C. Zhang, Y. Yang, A.J. Heeger, Polymer light-emitting electrochemical cells, *Science*. 269 (1995), 1086.

[2] A. Sandström, H.F. Dam, F.C. Krebs, L. Edman, Ambient fabrication of flexible and large-area organic light-emitting devices using slot-die coating, *Nat. Commun.* 3 (2012), 1002.

[3] C.W. Tang, S.A. VanSlyke, Organic electroluminescent diodes, *Appl. Phys. Lett.* 51 (1987), 913–915.

[4] H. Youn, M. Yang, Solution processed polymer light-emitting diodes utilizing a ZnO/organic ionic interlayer with Al cathode, *Appl. Phys. Lett.* 97 (2010), 243302.

[5] H. Becker, H. Spreitzer, W. Kreuder, E. Kluge, H. Schenk, I. Parker, et al., Soluble PPVs with enhanced performance—a mechanistic approach, *Adv. Mater.* 12 (2000), 42–48.

[6] A. Sandström, P. Matyba, L. Edman, Yellow-green light-emitting electrochemical cells with long lifetime and high efficiency, *Appl. Phys. Lett.* 96 (2010), 053303.

[7] R.D. Costa, E. Ortí, H.J. Bolink, S. Graber, C.E. Housecroft, E.C. Constable, Intramolecular π-stacking in a phenylpyrazole-based iridium complex and its use in light-emitting electrochemical cells, *J. Am. Chem. Soc.* 132 (2010), 5978–5980.

[8] Y. Cao, G. Yu, A.J. Heeger, C.Y. Yang, Efficient, fast response light-emitting electrochemical cells: Electroluminescent and solid electrolyte polymers with interpenetrating network morphology, *Appl. Phys. Lett.* 68 (1996), 3218–3220.

[9] A. Asadpoordarvish, A. Sandström, S. Tang, J. Granström, L. Edman, Encapsulating light-emitting electrochemical cells for improved performance, *Appl. Phys. Lett.* 100 (2012), 193508.

[10] J. Fang, P. Matyba, L. Edman, The Design and Realization of Flexible, Long-Lived Light-Emitting Electrochemical Cells, *Adv. Funct. Mater.* 19 (2009), 2671–2676.

[11] S. Tang, L. Edman, Quest for an appropriate electrolyte for high-performance light-emitting electrochemical cells, *J. Phys. Chem. Lett.* 1 (2010), 2727–2732.

[12] Y. Shao, G.C. Bazan, A.J. Heeger, Long-Lifetime Polymer Light-Emitting Electrochemical Cells, *Adv. Mater.* 19 (2007), 365–370.

[13] Z. Yu, M. Wang, G. Lei, J. Liu, L. Li, Q. Pei, Stabilizing the Dynamic p- i- n Junction in Polymer Light-Emitting Electrochemical Cells, *J. Phys. Chem. Lett.* 2 (2011), 367–372.

[14] Y. Yang, Q. Pei, Efficient blue-green and white light-emitting electrochemical cells based on poly [9, 9-bis (3, 6-dioxaheptyl)-fluorene-2, 7-diyl], *J. Appl. Phys.* 81 (1997), 3294–3298.

[15] F.C. Krebs, S.A. Gevorgyan, B. Gholamkhass, S. Holdcroft, C. Schlenker, M.E. Thompson, et al., A round robin study of flexible large-area roll-to-roll processed polymer solar cell modules, *Sol. Energy Mater. Sol. Cells*. 93 (2009), 1968–1977.

[16] J.-S. Park, H. Chae, H.K. Chung, S.I. Lee, Thin film encapsulation for flexible AM-OLED: a review, *Semicond. Sci. Technol.* 26 (2011), 034001.

8. Solar Cell Test Platform and Systematic Data Logging

8.1 Testing of and issues with testing of solar cells

Testing of organic solar cells are done by tracing a IV curve of the cell under test with most often a Keithley 2400 sourcemeter or similar. Most of the solar cells produced around the world in different labs are solar cells of a size of 0.04 mm^2 to 1 cm^2. With efficiency maximums of roughly 10 % and current densities up to 20 mA/cm^2 combined with highest voltages for tandem cells under 2 V, the measurement range required for testing a solar cell is quite small. The use of an instrument such as a Keithley 2400, which has become the defacto source measure unit, to some degree validates the result, however this can only be said to be true when used correctly. The range of the Keithley supports voltages up to ±21 V at a current level of ± 1 A. One of the troubles with this is that if the instrument range is set incorrectly or with a too high range, for instance testing a 0.1 cm^2 solar cell with a short-circuit current density J_{sc} of 10 mA/cm^2, the current would be I_{sc}=1 mA and if the range of the Keithley is set at 1 A the incurred offset of the instrument will give an extra ≈0.02 mA current. Furthermore with a cost of roughly 10 k$ the Keithley comes at a premium compared to what the cost of the components needed to supply and measure the more limited range of the smaller area organic solar cells.

8.2 Arduino – open source electronics

The Arduino platform is an open source hardware and software platform. Much like open source software, where the source code is available, the open source hardware and software platform has both a reference hardware design, but at the same time makes available the schematics and knowledge of the design enabling redesigns and changes of the original design to be made.

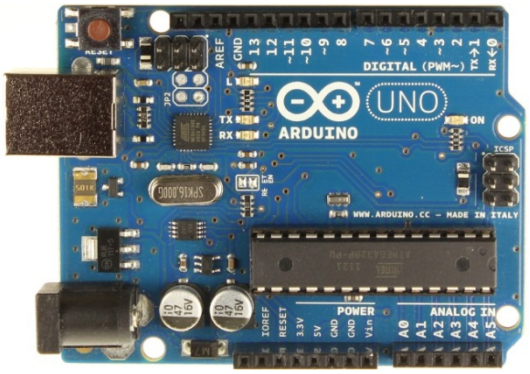

Figure 8.1: Example of Arduino board. The Arduino Leonardo board. The board features a 53 x 73 mm layout size with a header layout defined for mounted shields which adds components or functions to the board. Courtesy of the Arduino homepage [1]

The Arduino platform itself is based on a C-like programming language with its own Integrated Development Environment (IDE), a range of board reference designs and bootloaders that allows an easy access to microcontrollers and using these in small scale development projects.

8.3 Building a sourcemeter for solar cell tests

The principle of any sourcemeter is to have the possibility to source a voltage to a device and measure the current through the device while doing so. For solar cell testing the range of test methods goes from a multimeter based measurement of the short-circuit current and the open circuit voltage, which is basically the unloaded and maximally loaded solar cell, via a resistor array based measurement, where different valued resistors are used as loads for the solar cell giving a sampling of the solar cell behavior under different loads, with the voltage and current still measured in each point. Following this, the use of the source meter, which in contrast to the previously mentioned is an active measurement method, where the supply of current makes it possible to, not only measure in the 4th quadrant of the IV-diagram, but also in the other three quadrants.

A blog post from the PV group at MIT showed an example of how to build a solar cell tester based on the Arduino platform [2], which has also been the basis for this sourcemeter.

8.4 Components

To make a source meter the components needed are a digital to analog converter (DAC), which will take a digital input and set a voltage on an output channel. This output needs an operational amplifier (OPAMP) to buffer the output voltage of the DAC, since the output terminals of a DAC are not made for supplying current. A unity gain OPAMP is therefore used to supply the current needed to apply the voltage set on the DAC on the solar cell. The

The components needed for the board is therefore;
A 2 channel DAC
A 2 channel OPAMP
A 2 channel ADC
A shunt resistor
Two resistors for voltage division

Since single solar cells have not reached voltages higher than 2V in short circuit current a voltage range of +-2 volt should be sufficient, however to enable test of small serially connected modules a higher voltage could also be considered. For the current range, the current output of some of the best organic solar cells are up to 20 mA/cm^2, with many of the cells being tested around laboratories being down to 0.01 cm^2. The roll coated devices however tend to be bigger devices with sizes up to 10 cm^2 per. cell. Therefore, a current range of roughly 100 mA was chosen. The use of the Arduino form factor and the goal of keeping number of components low also mean that the power will be limited by the USB supply to the Arduino board, if powered only by the USB port. This combined with the microprocessors running at 3.3 V or 5 V, resulted in a

choice of components that could operate at both 3.3 V and 5 V. For communication with the chips the I2C bus was chosen, due to it having only two data lines connected to the components with build in addressability, reducing the need for input/output pins, compared to the SPI bus.

The following components were chosen based on the requirements above.

8.4.1 MCP4728 4 channel digital to analog converter (DAC)

The MCP4728 [3] is a 12-bit 4 channel DAC which can be driven from a supply between 2.7 to 5.5 V. It has an integrated 2.048V reference with a 1x/2x programmable gain amplifier (PGA) and is controlled by an I2C interface. All channels are buffered by a unity buffer capable of supplying 20 mA and sinking approximately 10 mA.

The use of this circuit means the external OPAMP is not required for small cells were the current does not get beyond 10 mA.

8.4.2 TLV4113 2 channel operation amplifier (OPAMP)

A high powered OPAMP capable of supplying up to 200 mA with a rail-to-rail output and a 2.5 V to 6 V power requirements was chosen. This Texas Instrument TLV4113 dual-channel amplifier was used to enable a high enough power output to test large cells with a high current output. The further advantage of this unit is its power down mode, enabling the shutdown of the amplifier to reduce both power consumption and heat.

8.4.3 MCP3424 4 channel analog to digital converter (ADC)

The most important component on the board is the ADC, which measured both the current and voltage values of the cell. A MCP3424 ADC [4] was chosen. This was due to its, 4 channels, 18 bit resolution combined with a 2.048 V internal reference and a 1x / 2x /8x PGA. The integrated PGA means the need of an OPAMP to amplify the voltage drop over the Shunt resistor could be excluded.

8.4.4 Shunt resistor

The shunt resistor for the board was chosen to be a 0.1 Ohm or 1 Ohm resistor depending on the internal resistance of the solar cells to test. For cells with a lower current and a high internal resistance the use of higher valued shunt resistor would give a higher resolution.

8.4.5 Voltage divider

Due to the 2.048V reference of the ADC, a voltage divider was applied to enable use of voltages higher than this. First version uses an equal resistor 2-1 divider with two 20 kOhm resistors in parallel.

8.4.6 Resulting parameters

The resulting range for the current measurement would be a 0.256 V range, with a 2 µV resolution, which for a 1 Ohm Shunt resistor gives a 0.256 A range with 2 µA resolution. The voltage measurement could be completed with a resolution of 18 bits also, giving a resolution down to 30 µV. The control of the device by the I2C bus means the number of pins required from a microcontroller is reduced to 2 data pins, a ground (GND) and a positive supply of either 3.3 V or 5 V regulated DC.

8.5 Board design and layout of components

Design of the PCB was done using the freeware version of Cadsoft EAGLE 6.3, which is limited to a maximum board size of 10 x 10 cm^2. The board was laid out in a Arduino form factor of 53 x 73 mm2 size with the full pin header set mountable (2 x 8pins on upper side and 2 x 6 pins on lower side). Three HST 2 mm connectors were laid out for connection of 1) a solar cell 2) Current measurement 3) Voltage measurement, enabling use of all four channels of the ADC. The ADC was put on the upper half of the board, with the voltage divider and the current channel shunt resistor. The DAC was placed at the center part of the board and the OPAMP at the bottom part of the board closest to the solar cell connector. These parts, which handle measurements, were all

offset towards the (right) rear edge of the board. On the left side the layout was complemented with an optional real time clock (RTC) circuit and a microSD socket (although the microSD socket would only be useful when running on a 3.3 V supply). A switch for selecting the measurement board supply voltage was put in near the supply pins, made by putting a surface jumper, which can be closed by bridging with a dap of solder.

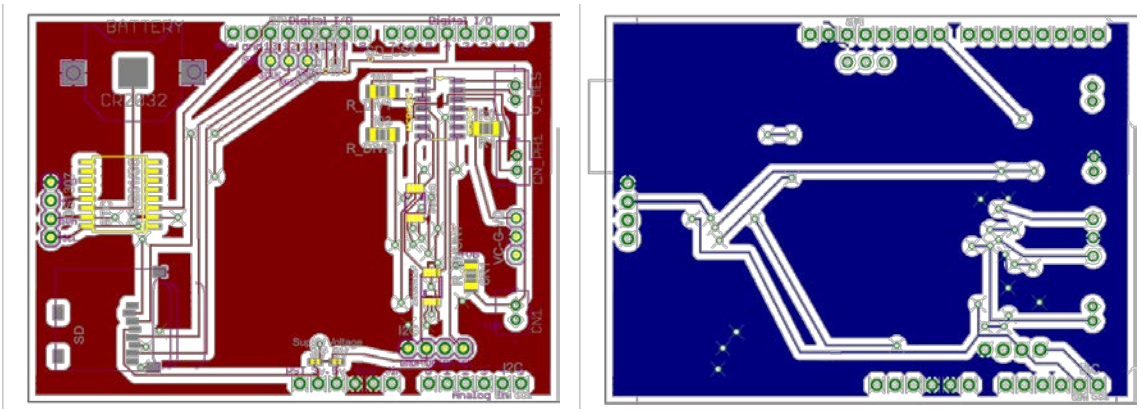

Figure 8.2: First generation measurement board. Left is the board top layer layout and right is the bottom side layout. The layout is based on an Arduino shield form factor (size 53x73 mm2). It contains a DAC circuit with a 4.096 V range and a 200 mA buffer amplifier for sourcing, while a 4 channel ADC with 18 bit resolution handles data collection.

Routing of the signals was done using the auto-router function and afterwards corrected for a more appropriate layout. Headers were put in to allow connection to the I2C bus on two locations on the board and the Arduino SPI terminals on one location.

8.6 Enabling data logging

An alternative to the use of the shield and Arduino as a computer controlled sourcemeter, the Arduino can be fitted with a SD card, or an Arduino compatible board such as the Seeedstudio Stalker can be used for a self-contained measurement board, which can be mounted at remote locations.

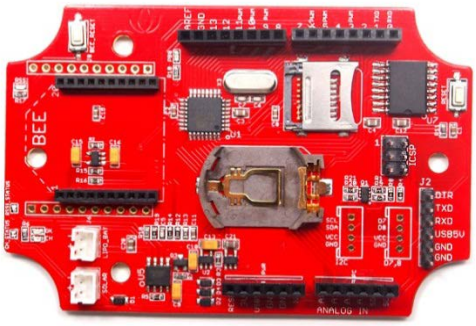

Figure 8.3: Seeeduino Stalker board. An Arduino compatible board, with a build in microSD socket, temperature sensor, RTC clock, lithium polymer battery connector and solar cell connector with charge controller.

The board can be setup to log the temperature and time and take an IV curve for the connected cell and store the information on the microSD card. The board will be driven from a solar cell and a lithium-polymer battery through the built in lithium battery charge controller. This is of relevance for remote test studies such as the round robin experiments [5,6] and for cases with multiple cell tests [7]. In these cases the associated cost and complexity of a standard source measure units for each test stand becomes too high.

8.6.1 Sensors

For solar cell testing the use of other sensors, than only the tracing of the solar cells IV curve can be quite beneficial. Factors such as the temperature, both of the surroundings and of the solar cell, the humidity level around the solar cell and the intensity of the illumination used is very important for judging the solar cells performance.

Examples of sensors which can be used together with the boards are such as below:

Light intensity: Registration of the intensity of incoming light can be done by several methods. The most accurate and often used is calibration via a pyranometer, which registers the heating caused by the incoming radiation and outputs a voltage signal as a function of the incoming intensity. Another approach is the use of a small solar cell or

a photodiode, where the measurement of the short circuit current will be approximately proportional to the incoming irradiation. A third option is the use of a light sensitive resistor, which is what is most often used together with Arduino electronics, however not due to its accuracy but due to the easy measurement of a change in resistance with the Arduino.

Temperature sensor: The temperature can also be measured with a variety of sensors, were for many situations KT100 or similar sensors are used, which will give a small voltage difference with the change of temperature due to the work function of a junction between to metals. For embedded electronics the Dallas DS18 one wire digital temperature sensors can be used, which is a digital temperature sensor which can be daisy-chained together allowing many sensors to be connected without using many inputs on the board.

Humidity sensor: Measuring the humidity with an Arduino can be done with a DHT11 or DHT22 temperature and humidity sensor. The sensor was a library already written for it for acquiring data.

8.7 Manufacturing of board and soldering of components

The choice of manufacturing technology was done on the base of having a board with a minimum of components which needed to be mounted and with all components being surface-mount devices (SMD) type devices. The printed circuit boards were manufactured out of house, due to a cost of 30 $ for the manufacture of 10 test board PCBs.

Soldering of the components was done with a Nordson EFD SolderPlus Sn96.3Ag3.7 solder paste, which was applied to the solder pads with a 0.6 mm syringe needle. The melting temperature of the solder paste is 221 °C and reflow temperature is suggested to be between 25 °C to 50 °C above the melting point. The components were mounted in the solder paste and the print baked out on a hotplate set at 280 °C for 2 min. This melts the solder paste and the solder paste helps to draw the components to the cor-

rect position due to the wetting of the solder paste occurring only on the solder pads of the PCB.

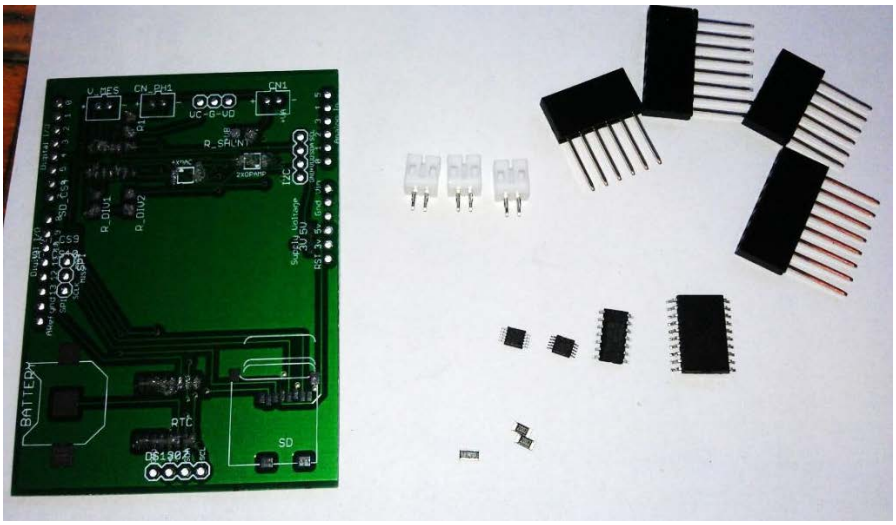

Figure 8.4: The finalized board design with the 2-layer PCB (left), test connectors (white, middle), board headers (top right) and the microchips and resisters (lower middle).

8.8 Programming of the microcontroller and defining the interface.

Using the DAC and ADC together with the Arduino board, was vastly simplified by the availability of open source libraries for both components. A library for the DAC was made available on the Arduino forum [8] and a library for the ADC was made available on the Adafruit forum [9] .

The interface for making the Arduino do a measurement and report values back to the user, was completed in an initial version that was compatible with the IVy Processing application, which was used in the MIT DIY solar cell tester [2]. This allowed an easy way to get a graphical interface with control and plotting capabilities.

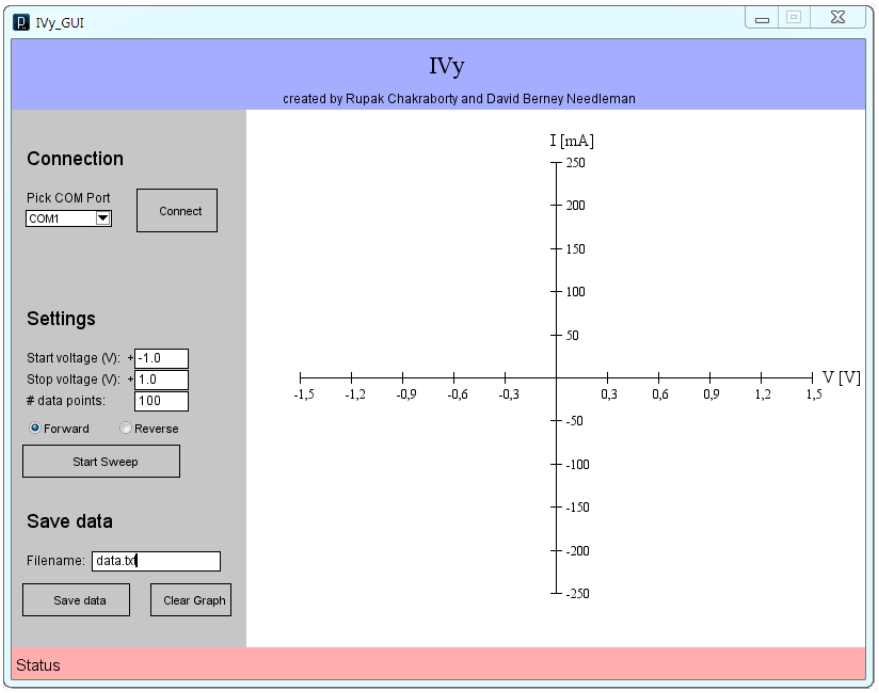

Figure 8.5: Ivy GUI for solar cell measurement. Applet was made by the MIT pv-solar test lab. [2]

The interface was then changed to allow use with an in-house developed IV-test program, originally developed for taking data with the Keithley 2400. The GPIB command for device id, "*IDN?" was implemented, enabling automation of choosing the COM port. The board is connected by sending a "C" over the serial port, and a measurement is started by sending a "S" for starting the measurement, with the standard start voltage, end voltage and number of steps. For setting these parameters separately a command of the form "S V_start V_end Steps" is used to start the measurement.

8.9 A demonstrator suitcase for showcasing tandem and single solar cells

The simultaneous work completed on tandem solar cells was to be presented at an EU project meeting, of which a demonstrator suitcase was made. The suitcase was to help present the produced double side illumination tandem cells, with the higher voltage.

Figure 8.6: Double sided illumination tandem solar cell demonstration. A rugged case with two LED torches, a multimeter, wires, crocodile clips and an Arduino with the measurement board attached. The case was developed to help demonstrate what and how the roll coated solar cells look and perform.

For the measurement a set of wires, a multimeter two LED flashlights an Arduino and the testboard was put in the suitcase. Two cases with single cell devices in one and tandem devices in the other was also added. Connecting a cell, shining light with the two torches on the cell and doing an IV sweep with the testboard and an attached computer showed the desired voltage difference between the tandem and single cells.

8.10 An Advantage of open source building blocks

Since the test board is based on the Arduino form factor, Arduino compatible shields can be used with the board and Arduino to add extra functionality. Two examples of such extra functionality are shown in this chapter with using a Bluetooth serial shield as the first example and a network shield as the second example.

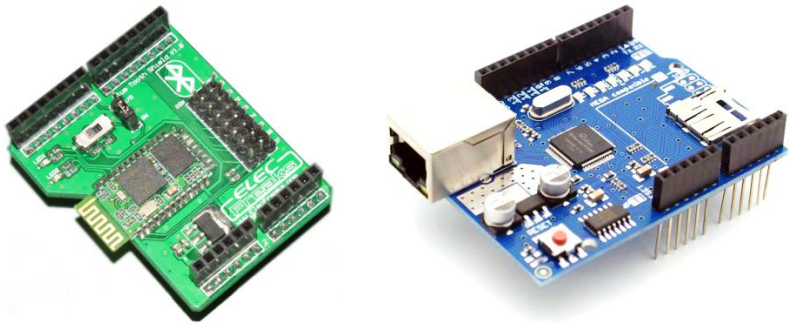

Figure 8.7: Example of compatible shields. Left is a Bluetooth shield for serial to Bluetooth conversion and right is an Ethernet shield.

8.10.1 Bluetooth Shield

Adding Bluetooth to the tester setup gives the possibility of using the board from a separate power supply, such as an USB phone charger or 7 V to 20 V DC, instead of a pc and with the interface to the measurement being a phone or tablet. This would enable the use of an inexpensive tablet with a graphical app as the only extra needed instead of a bulky laptop. The use of a smart phone would allow the possibility of doing data collecting in remote locations with the phones build in modem sending data of for central collection, all at a significant easier fashion than what would be possible with a laptop, laptop supply and network connections.

An example of running the testboard and Arduino from a terminal on an android phone can be seen in Figure 8.8

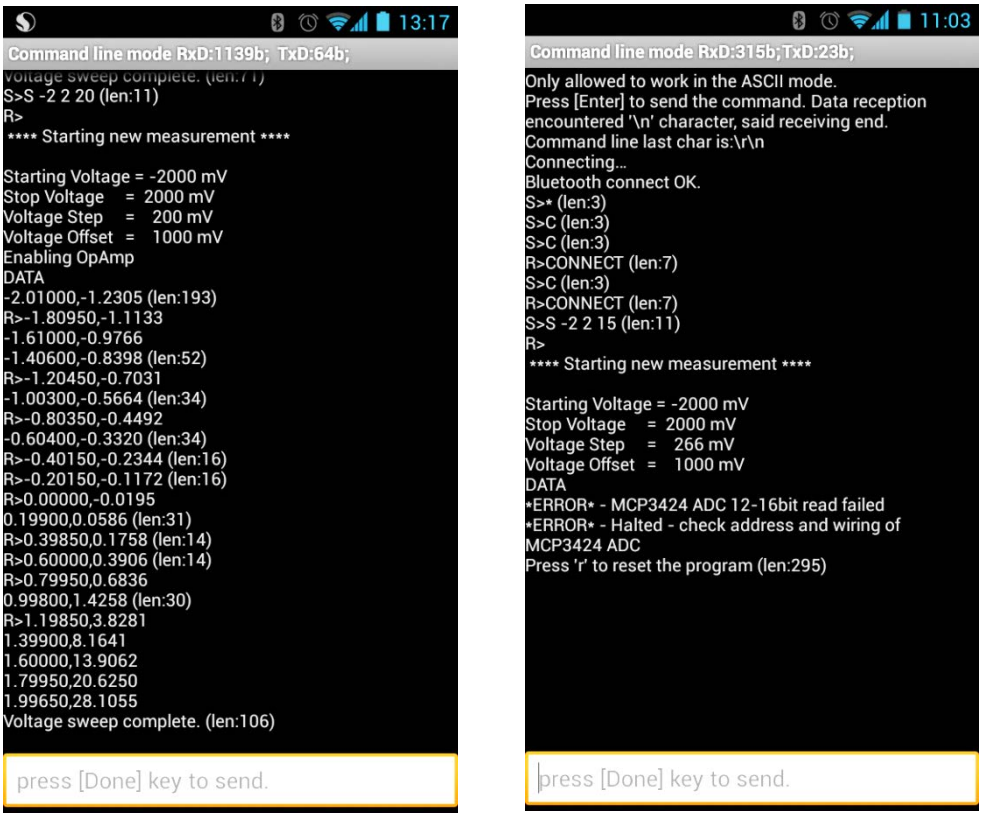

Figure 8.8: Serial terminal on an android phone connected to the measurement board via Bluetooth. The left screenshot shows a dark measurement of a 1cm2 solar cell. The right screenshot shows an example of the error reporting of the Arduino libraries. An error message is thrown due to the ADC not responding (the test board was not actually connected for the test, only the Arduino)

8.10.2 Ethernet Shield

An Ethernet shield can be added to the setup to allow uploading of data to a server. The Ethernet shields can be had with Power-over-Ethernet (POE) requiring a single cable for connecting the tester to its surroundings.

8.11 Example of measurement

A measurement completed with the board with the OPAMP circumvented is shown in Figure 8.9, with a comparison between the measurement of a roll-coated normal geometry solar cell with an area of 1cm^2 under 1000W/m^2 AM1.5G illumination completed with the Arduino based sourcemeter and a Keithley 2440 sourcemeter. The meas-

urement shows the Arduino to trace the same measurement curve as the Keithley with a slight deviation at the higher currents where the build-in buffer amplifier of the DAC has issues in with sinking the current.

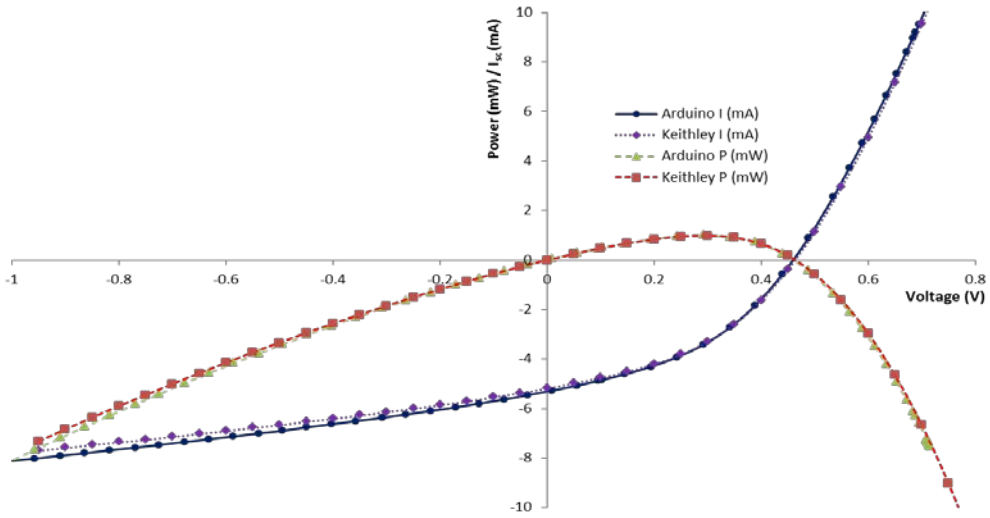

Figure 8.9: Measurement of 1 cm^2 solar cell under 1000W/m^2 AM1.5G illumination with both the Arduino based sourcemeter and a Keithley 2440 sourcemeter.

Measurements done with the version of the board with the integrated amplifier enabled allows the full 200mA. An example of a measurement of a dark curve measurement of a tandem solar cell is shown in Figure 8.10.

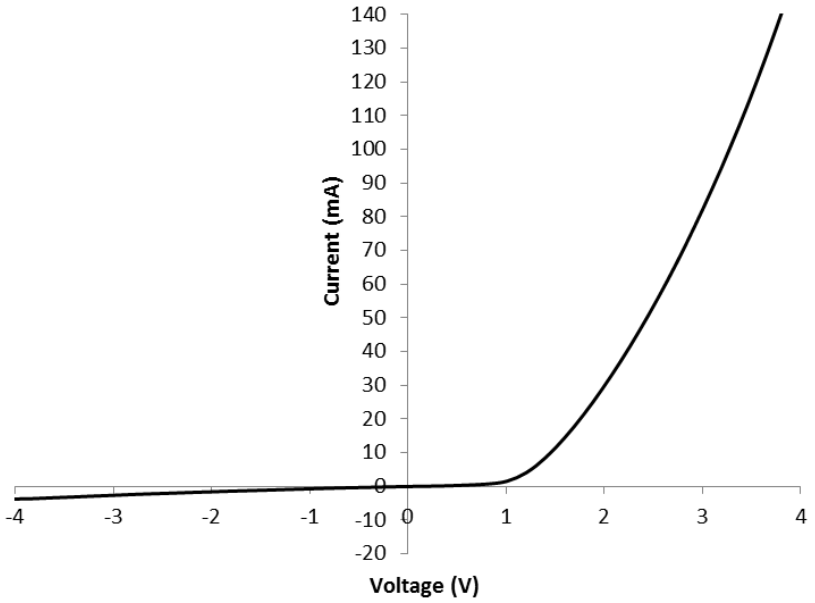

Figure 8.10: Dark measurement of tandem solar cell from -4 V to 4 V.

8.12 Summary

The construction of an alternative measurement solution for testing of solar cells was completed and showed the possibility of replacing the standard test equipment used by most OPV research groups around the world with a significantly cheaper test unit, which has the added benefit of enabling several other measurements, such as temperature, humidity and light intensity to be collected simultaneous and even running autonomously with reporting to SD card s or directly to a central network service. This work implemented a initial version of the test board and microprocessor firmware, with option of running from a windows GUI software or standard serial terminal.

References

[1]Arduino Homepage, (n.d.),.

[2] D.B. Needleman, R. Chakraborty, DIY IV Tester - Build Your Own Sourcemeter, *MIT Photovoltaic Research Laboratory*. (n.d.),.

[3]MCP4728 Datasheet (10/05/2010): Quad 12-bit voltage output Digital-to-Analog Convertor (DAC), (n.d.),.

[4]MCP3424 Datasheet (01/27/2010) : Four channel low-noise, high accuracy delta-sigma A/D converter with differential inputs and up to 18 bits of resolution, (n.d.),.

[5] F.C. Krebs, S.A. Gevorgyan, B. Gholamkhass, S. Holdcroft, C. Schlenker, M.E. Thompson, et al., A round robin study of flexible large-area roll-to-roll processed polymer solar cell modules, *Solar Energy Materials and Solar Cells*. 93 (2009), 1968–1977.

[6] S.A. Gevorgyan, A.J. Medford, E. Bundgaard, S.B. Sapkota, H.-F. Schleiermacher, B. Zimmermann, et al., An inter-laboratory stability study of roll-to-roll coated flexible polymer solar modules, *Solar Energy Materials and Solar Cells*. 95 (2011), 1398–1416.

[7] M.O. Reese, S.A. Gevorgyan, M. Jørgensen, E. Bundgaard, S.R. Kurtz, D.S. Ginley, et al., Consensus stability testing protocols for organic photovoltaic materials and devices, *Solar Energy Materials and Solar Cells*. 95 (2011), 1253–1267.

[8] Neurostar, Quad 12-bit DAC MCP4728 libary - http://forum.arduino.cc/index.php/topic,51842.0.html, *Arduino Forum*. (n.d.),.

[9] fat16lib, adafruit, Great 18-bit ADC for GPS and Proto Shield sensor logging - http://www.adafruit.com/forums/viewtopic.php?f=31&t=12269&start=30, *Adafruit Forum*. (n.d.),.

9. Conclusion and Outlook

Through this thesis the focus has been on the improvement of manufacturing by the development of the mini roll coater machine, which through the previous chapters of this thesis has proven to allow optimization of slot-die coated solar cells, electrochromics and light emitting electrochemical cells in a lab scale setting, while using a minimal amount of materials and time. Furthermore, the advantage of using the slot-die technique in the lab setting is the more direct transfer of optimizations from the lab scale to the production scale setting.

Water based nanoparticle inks have been investigated, with characterization of the nanoparticle morphology using both X-ray and TEM methods to find the shape of the particles and estimate the chemical distribution of the polymer and acceptor species.

It has been shown that fully wet processed solar cells can be manufactured using a single machine and even tandem solar cells with a wet processing of 12 separate layers can be completed in this fashion. Performance of tandem solar cells produced by this technique has shown the series connection of two solar cells through wet processing to output a voltage just below that of two separate cells, indicating the effectiveness of the technique. However, performance levels of the herein developed tandem solar cells have not yet reached the state of the single cells, due to lower extracted currents.

Lastly, a test setup was completed which allows a smaller and easier method of doing testing of solar cells in an outdoors setting or for demonstrating efficiencies or current voltage characteristics of the solar cells.

A future use of the lab scale roll coating technique presented herein is expected to make the path towards finding new polymers suitable for roll coating and essentially finding the best conditions for roll coating polymers to make efficient solar cells, which has so far been far from an easy task. The development of better performing tandem solar cells, which might even lead to a fully wet processed tandem solar cell with a better performance than that of the single solar cells, is expected to be performed. Further investigations of nanoparticle based inks could lead the way towards less solvent

intensive production, however the morphology shown from water processed films is apparently not yet sufficient enough to match the efficiencies attained by solvent processing methods. This however will be an area where the combination of different inks and testing of a large range of roll coating parameters might show the possibilities and further support the hope of a controlled solar cell morphology.

The test platform which was developed is hopefully going to help in completing outdoor tests and in replacing expensive research scale equipment where possible. A key in this being the further development of the testboard and software, to enable registration of cell temperatures, humidity levels etc. in an automated way, allowing a more thorough investigation of the direct causes of failure of solar cell devices.

10. Appendix

The published articles are attached without supporting information. The material is available free of charge via the Internet or by contacting the author.

10.1 List of Publications

A1.

Simple roll coater with variable coating and temperature control for printed polymer solar cells

H. F. Dam and F. C. Krebs, Solar Energy Materials and Solar Cells, vol. 97, no. 0, pp. 191–196, Feb. 2012.

A2.

Roll-to-Roll Processing of Inverted Polymer Solar Cells using Hydrated Vanadium(V)Oxide as a PEDOT:PSS Replacement

N. Espinosa, H. F. Dam, D. M. Tanenbaum, J. W. Andreasen, M. Jørgensen, and F. C. Krebs, Materials, vol. 4, no. 12, pp. 169–182, Jan. 2011.

A3.

Edge sealing for low cost stability enhancement of roll-to-roll processed flexible polymer solar cell modules

D. M. Tanenbaum, H. F. Dam, R. Rösch, M. Jørgensen, H. Hoppe, and F. C. Krebs, Solar Energy Materials and Solar Cells, vol. 97, pp. 157–163, 2012.

A4.

Morphological study of low band gap polymer:PCBM nanoparticles for organic photovoltaics (OPVs)

H. F. Dam, N. P. Holmes, T. R. Andersen, T. T. Larsen-Olsen, F. C. Krebs, P. C. Dastoor, 2013, RSC Nanoscale, *abstract – in draft*

A5.

A rational method for developing and testing stable flexible indium- and vacuum-free roll processed tandem polymer solar cells, ***in press***

T. R. Andersen, H. F. Dam, B. Andreasen, M. Hösel, M. V. Madsen, S. A. Gevorgyan, R. R. Søndergaard, M. Jørgensen, and F. C. Krebs, Solar Energy Materials & Solar Cells.,

A6.

Manufacture and demonstration of organic photovoltaic-powered electrochromic displays using roll coating methods and printable electrolytes

J. Jensen, H. F. Dam, J. R. Reynolds, A. L. Dyer, and F. C. Krebs, Journal of Polymer Science Part B: Polymer Physics, vol. 50, no. 8, pp. 536–545, 2012.

A7.

Ambient fabrication of flexible and large-area organic light-emitting devices using slot-die coating

A. Sandström, H. F. Dam, F. C. Krebs, and L. Edman, Nat Commun, vol. 3, p. 1002, Aug. 2012.

Popular Science

A8.

Polymersolceller

T. R. Andersen, H. F. Dam, B. Andreasen, T. Tromholt, F. C. Krebs, 2012, in *Aspekter af dansk kemi i det 20. og 21. århundrede*., KemiForlaget.

Not included in thesis - ISOS-3 studies

The ISOS-3 inter-laboratory collaboration focused on the stability of a variety of organic photovoltaic devices

D. M. Tanenbaum, M. Hermenau, E. Voroshazi, M. T. Lloyd, Y. Galagan, B. Zimmermann, M. Hösel, H. F. Dam, M. Jørgensen, and S. A. Gevorgyan, ..., K. Norrman, and F. C. Krebs , RSC Advances, vol. 2, no. 3, pp. 882–893, 2012.

Investigation of the degradation mechanisms of a variety of organic photovoltaic devices by combination of imaging techniques—the ISOS-3 inter-laboratory collaboration
R. Rösch, D. M. Tanenbaum, M. Jørgensen, M. Seeland, M. Bärenklau, M. Hermenau, E. Voroshazi, M. T. Lloyd, Y. Galagan, B. Zimmermann, ..., H. Hoppe and F. C. Krebs, Energy & Environmental Science, vol. 5, no. 4, pp. 6521–6540, 2012.

On the stability of a variety of organic photovoltaic devices by IPCE and in situ IPCE analyses–the ISOS-3 inter-laboratory collaboration
G. Teran-Escobar, D. M. Tanenbaum, E. Voroshazi, M. Hermenau, K. Norrman, M. T. Lloyd, Y. Galagan, B. Zimmermann, M. Hösel, H. F. Dam,... , F. C. Krebs and M. Lira-Cantu, Physical Chemistry Chemical Physics, vol. 14, no. 33, pp. 11824–11845, 2012.

TOF-SIMS investigation of degradation pathways occurring in a variety of organic photovoltaic devices–the ISOS-3 inter-laboratory collaboration
B. Andreasen, D. M. Tanenbaum, M. Hermenau, E. Voroshazi, M. T. Lloyd, Y. Galagan, B. Zimmernann, S. Kudret, W. Maes, L. Lutsen, ..., F. C. Krebs and K. Norrman, Physical Chemistry Chemical Physics, vol. 14, no. 33, pp. 11780–11799, 2012.

Solar Energy Materials & Solar Cells 97 (2012) 191–196

Contents lists available at SciVerse ScienceDirect

Solar Energy Materials & Solar Cells

journal homepage: www.elsevier.com/locate/solmat

Simple roll coater with variable coating and temperature control for printed polymer solar cells

Henrik F. Dam, Frederik C. Krebs *

Risø National Laboratory for Sustainable Energy, Technical University of Denmark, Frederiksborgvej 399, DK-4000 Roskilde, Denmark

ARTICLE INFO

Available online 29 September 2011

Keywords:
Organic photovoltaic
Roll coating
Low cost
Prototyping
Low ink usage

ABSTRACT

A simple and low cost thin film solution processing system comprising a single roll coating machine has been developed to allow direct investigation of variable parameter effects in roll-to-roll processing. We present roll coating of the active layers in polymer solar cells and validate the instrument by reinvestigating the well known effect of solvent on performance. We obtained a maximum power conversion efficiency of 1.6% for the reference cells, which compares well with reported roll-to-roll coated cells according to ProcessOne, with a relative deviation caused by solvent type nearing 40% on roll coated cells, confirming the solvent to have a significant influence on the performance of the finished cell. We further present a slot-die coating head with an ultra low dead volume allowing for the preparation of roll coated polymer solar cells on flexible substrates with nearly no loss of solution, enabling roll coating testing of new polymers where only small amounts are often available. We demonstrate the formation of >50 solar cells (each with an active area of 1 cm^2) with printed metal back electrodes using as little as 0.1 mL of active layer solution. This approach outperforms spin coating with respect to temperature control, ink usage, speed and is directly compatible with industrial processing and upscaling.

1. Introduction

The polymer and organic solar cell (OPV) is a new photovoltaic (PV) technology that potentially solves the problems of scale, speed and materials abundance that most of the current PV technologies are faced with [1,2]. Even though manufacture of OPVs have been demonstrated on a reasonable scale [3] and OPVs have been demonstrated [4,5] and integrated into product prototypes [6], there is a significant amount of development needed before the technology answers well to the environmental concerns. Life cycle analysis (LCA) studies show that the energy payback time (EPBT) is comparable to the current device lifetimes achieved [7] and when integrated into products the EPBTs are significantly longer than the anticipated operational lifetime of the assembly driven by the OPV, which limits the usability of OPV to cases where they can efficiently replace a more environmentally damaging device [8]. While this does comprise usefulness it also limits the scope and applicability of the technology unless the challenges are efficiently addressed. The majority of polymer solar cells reported to date have been prepared by a combination of spin coating and vacuum evaporation of the layers in the device. This approach has proven highly successful on the laboratory scale where device power conversion efficiencies exceeding 8% has been reported by a few companies [9]. The technology in the available form only presents power conversion efficiencies in the range of 1–2% [10,11] as reported by many independent laboratories. One of the possible reasons for this is the fundamental difference between the manner in which a laboratory device is prepared and optimized and the manner in which an industry would approach the manufacture of the OPV technology. The implications of this are that new developments are thus not readily upscaled or easily transferred to an industrial setting and this in part may hold the explanation for the somewhat slow emergence of polymer solar cells as a technology that is integrated in commercial products.

In this work we present a compact roll coater that enable the preparation of polymer solar cells in a directly scalable manner but on a very small scale that is in fact smaller than currently employed spin coating and doctorblading methods. Very small quantities of ink can be applied and a very accurate control of the wet and dry thickness of the coated film is possible, which is in stark contrast to spin coating. In addition the system enable accurate control of the substrate temperature during deposition and is compact enough to fit in an ordinary fume cupboard, a glove box or a cleanroom as no large extraction systems are needed. Toxic materials are also easily encompassed, since the evaporation of solvent or additives can be kept within the fume cupboard. The system is used to test dependence on solvents used

* Corresponding author. Tel.: +45 46 77 47 99.
E-mail address: frkr@risoe.dtu.dk (F.C. Krebs).

0927-0248/$ - see front matter © 2011 Elsevier B.V. All rights reserved.
doi:10.1016/j.solmat.2011.08.027

for the P3HT:PCBM material in a slot-die coating process in contrast to the spin coated test of solvent dependence [12,13].

2. Experimental

2.1. Roll coater

The roll coater (Fig. 1) is constructed to mimic the coating performed on full scale roll-to-roll processing equipment [14,15] making the transition from lab to production faster and enabling optimization of the ink and processing directly at the lab scale prototyping level.

2.1.1. Mechanics

The system is comprised of a single 300 mm diameter roll where to a (PET) foil is attached. A slot-die coating head is mounted at the top of the machine, on a 3-axis movable stage allowing adjustment of height, angle of attack and horizontal position relative to the foil. The roll is driven by a servo motor through exchangeable gear wheels allowing for a large range of web speeds. In these experiments speeds between 0 m/min and 2 m/min were employed. These speeds are comparable to what is used in larger roll-to-roll processing equipment as described earlier [15]. After the slot-die coating head a fan is mounted to further help the drying of the coated material and an optional IR heater is mounted for use at lower coating temperatures. The system allows coating at controlled temperature, with a heated roll on which the PET substrate is attached, meaning that the substrate is kept at a constant controlled temperature while coating and securing a much narrower temperature distribution through the films when drying.

2.1.2. Coating head

The coating head (Fig. 2) is a slot-die coating head with a very small dead volume of less than 50 μL, allowing use of a minute amount of solution for processing. The head is comprised of two brass parts held together by 4 screws. The front side of the head has a 50 μm deep groove milled into it with a width of 13 mm, between the brass parts, a 0.25 mm thick stainless steel foil is placed with a meniscus guide of 13 mm width and protruding 0.5 mm from the bottom of the head. The meniscus guide has been reported earlier in [16].

2.1.3. Pumping systems

For active layer ink delivery a syringe pump was used together with Braun Medical 5 mL two-component syringes. The connection to the slot-die head was done via a 1.0 μm filter, a Luer to HPLC 1/4 in.-28 thread and a 2 mm OD teflon tube or a stainless steel HPLC tube. For PEDOT:PSS coating a purpose built pressure chamber pump was used due to the higher viscosity (viscosity ~270 mPa s) of the PEDOT:PSS ink.

2.2. Materials

The coating was performed on ITO sputtered PET foil with a thickness of 175 μm and a nominal sheet resistivity of 100 $\Omega\,\square^{-1}$. The ITO layer was patterned into stripes of 13 mm width. The foil was precoated with a doped ZnO layer [15]. Foil areas of 1 m × 15 cm were cut out and mounted on the roll coater. P3HT (poly(3-hexylthiophene)) was obtained from BASF as Sepiolid P200 and PCBM ([6,6]-phenyl-C61-butyric acid methyl ester) was obtained from Solenne BV (technical grade). The solvents used were; chlorobenzene (CB), 1,2-o-dichlorobenzene (ODCB) and 1,2,4-trichlorobenzene (TCB). The P3HT:PCBM concentration was kept the same for all solvents at 21 mg/ml P3HT and 18.5 mg/mL PCBM. The PEDOT electrode-buffer layer was based on Orgacon PEDOT EL-P 5010 from Agfa mixed in a 2:1 (w/w) ratio with IPA. The heat curable screen printing silver ink used was PV410 from DuPont.

2.3. Coating procedure

2.3.1. Active layer

The coating of the P3HT:PCBM material was conducted at a speed of 1.5 m/min. The roll was heated to 90 °C to allow a quick and uniform drying of the films. The flow through the head was set to 0.250 mL/min resulting in a wet thickness of 13 μm and an estimated dry thickness of 0.4 μm. The coated stripe was offset 1 mm from the ITO stripe.

2.3.2. PEDOT

The PEDOT layer was coated with a 1 mm offset from the active layer coating and coated with a flow of 1.25 mL/min for a wet thickness of 65 μm. The layer was coated at a 70 °C roll temperature followed by drying for 20 min.

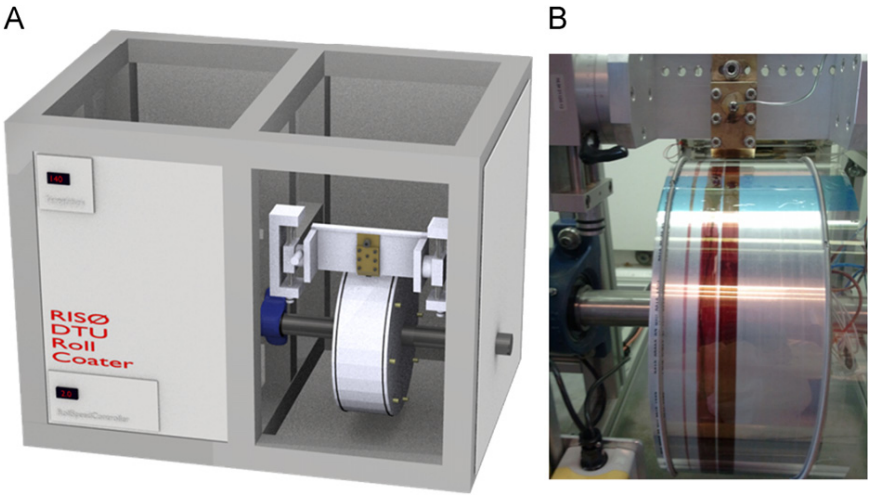

Fig. 1. (**A**) Illustration of the roll coater showing the frame, roll, axis, motor translation stage, pump, heater and slot-die head. (**B**) Picture of the roll with a PET with ITO foil mounted and two stripes coated on the substrate.

Appendix - A1

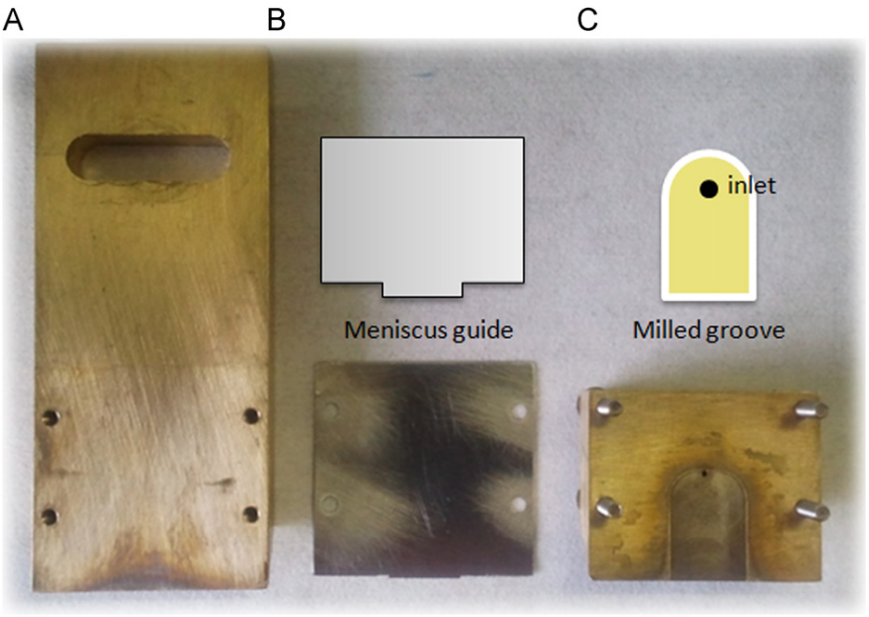

Fig. 2. (**A**) Coating head brass backpiece. (**B**) Illustration of the meniscus guide (top) with the actual steel insert with the 13 mm × 2 mm meniscus guide (bottom). (**C**) Illustration of inlet and liquid groove (top) with the front coating head brass piece, showing the groove for ink passage and the ink inlet (bottom).

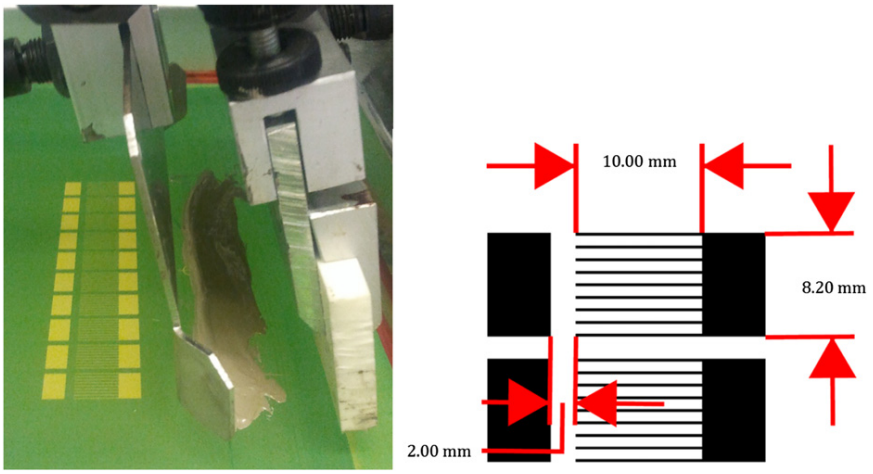

Fig. 3. Screen printing mask for the silver top electrode, which defines the cell area. The pattern was printed across the coated stripe allowing up to ≈90 cells to be produced per coated stripe. The cell area was 1 cm^2.

2.4. Solar cell preparation

Solar cells were prepared from the coated stripes by dividing the 1 m stripe into sections for application of a 1 cm^2 printed top electrode. The pattern for the top electrode is shown in Fig. 3, where 10 cells are fabricated for each screen-print, with a length of foil that is 10 cm. The screen printed solar cells were baked at 140 °C directly after printing, for a period of 2 min, to remove the solvent of the silver ink. Finally the cells were encapsulated using Alcan barrier foil [3,10] and cut out to remove any crosstalk between cells caused by the large ITO and PEDOT:PSS electrode layers.

2.5. Solar cells test and measurement

Solar cells were measured with a Keithley 2400 sourcemeter under a KHS 575 solar simulator with an AM1.5G 1000 W/m^2 output. The produced cells were measured after an initial soak period to stabilize efficiency [10,11]. All cells were put under illumination and measurements were started on the first cells after 40 min of light soaking. The recordings on the last cell were finished after 105 min.

3. Results and discussion

3.1. Coating and simplicity

The coating procedure and the quality of the coated films are very similar to the large scale roll-to-roll coating, while the time involved and amounts of material used are much less. The smaller fabricated cells used here allows for a much denser sampling of parameters with the use of 1cell/cm coated length while in earlier work Alstrup et al. [12], employed a coated length of 8 cm/cell.

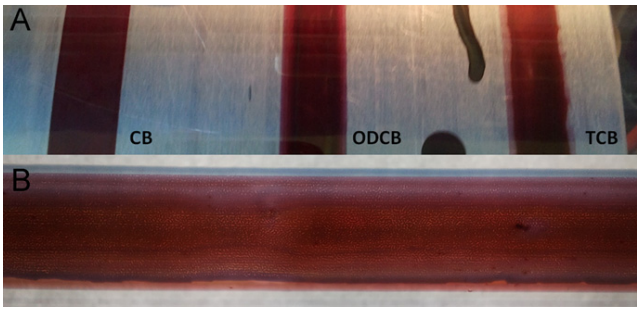

Fig. 4. (A) Film uniformity of as coated P3HT:PCBM before the coating of PEDOT, showing from left to right; CB based material, ODCB based material and TCB based material. (B) PEDOT coated stripe showing a hole-like structure.

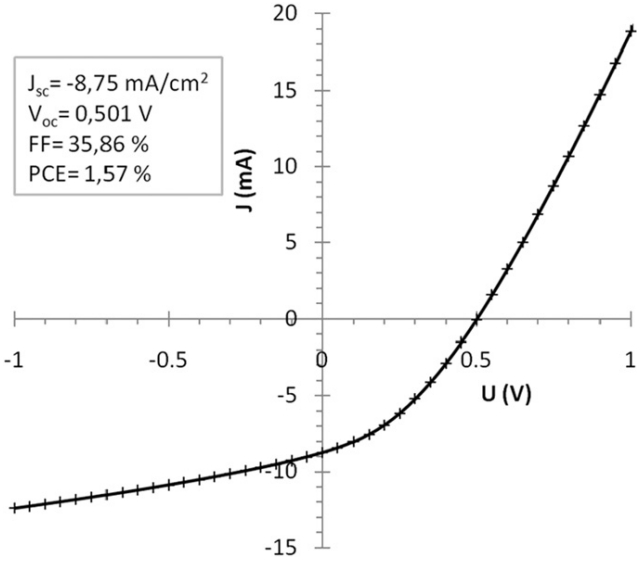

Fig. 5. IV-plot for a reference cell. Scans were conducted from −3 V to 3 V with 100 mV steps (only −1 V to 1 V is shown).

3.2. Quality of films

The film quality from slot-die coating can vary quite significantly with even small changes in parameters, however the coatings performed with the three solvents at a 90 °C temperature showed an even optical film quality, although the uniformity at the edge (picture framing) of the coated stripe was slightly worse for ODCB based films and more so for TCB based films, as seen in Fig. 4A.

The PEDOT:PSS coating showed a tendency to develop holes in the coated film during drying, which lowered the performance of the roll coated cells slightly (Fig. 4B). This can be attributed to the slow drying of the PEDOT:PSS layer at the 70 °C coating temperature used, which due to the heating from below did not allow the PEDOT:PSS to skin, thereby causing the drying defects.

3.3. Performance

The maximum performance of the cells produced was obtained for the spin coated reference sample with a performance of 1.6%, as seen in the IV curve in Fig. 5. The roll coated cell performance was normalized to the maximum performance for the ODCB roll coated cells, with the performance of the cells averaged over modules shown in Fig. 6.

3.4. Effect of solvent

The effect of changing between solvents for the P3HT:PCBM ink showed a distinct difference in the performance of the produced cells. The use of higher boiling point solvents allows a longer drying time and thereby a longer time for the crystallization of the P3HT:PCBM heterojunction. Use of CB as a solvent is often reported for R2R produced solar cells, and resulted in the most even coatings in this study with a reasonable performance. However, the cells coated with ODCB showed a substantial increase in fill factor, open circuit voltage and current (Fig. 7). The even higher boiling point TCB solvent was expected to give a further increase in performance, which was not observed, although this might be attributed to the quality of the coated TCB based films being less uniform than the CB and ODCB films. The drying times of the films at a temperature of 90 °C were

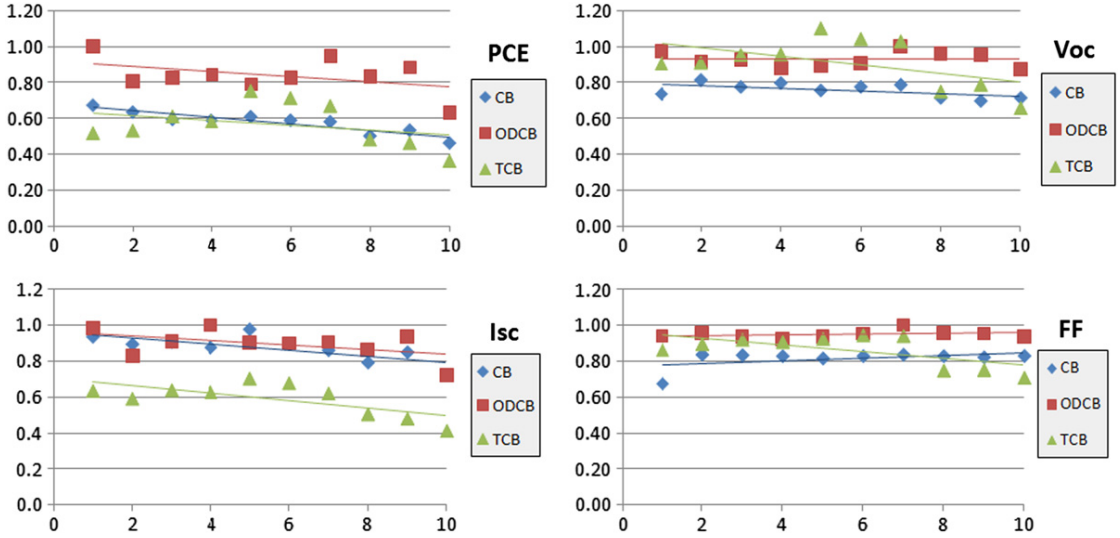

Fig. 6. Plot of the solar cell parameters, including efficiency (PCE), open circuit voltage (V_{oc}), short circuit current (I_{sc}) and fill factor (FF), shows the distribution of the cell performances. All parameters have been normalized to the performance of the ODCB cells.

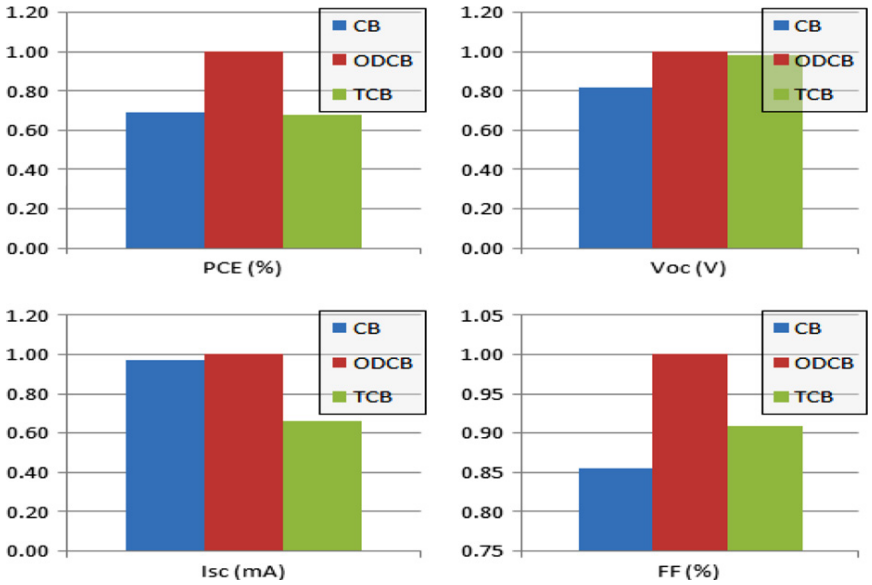

Fig. 7. Average values for the cells produced, showing the ODCB based cells to perform better than the CB and TCB based cells. All parameters have been normalized to the performance of the ODCB cells.

estimated to be 3 s for CB, 6 s for ODCB and about 15 s for TCB. The time the film is subjected to heat is of course longer as the foil is physically attached to the heating element (the roller). The total heating time is then limited by how fast the foil can be removed after coating. Since (in a typical experiment) several stripes were coated using different solvent and this involved cleaning of the pump and coating head the first stripe would be on the heated roll for significantly longer than the lastly coated stripe. The coating of the stripe itself was here carried out at 1.5 m min^{-1} for the active layer implying that the entire coating experiment takes 40 s. After that the foil could be removed in less than 20 s meaning that a single stripe can be coated and removed from the heater within a minute. A typical coating experiment with 4 separate stripes from the same solvent could be completed in less than 5 min. After this of course the film is further heated to 70 °C for 20 min while coating and drying PEDOT:PSS and finally 2 min at 140 °C while curing the printed silver back electrode. The roughness of the films in the even regions away from the edges were in the range of the reported values for slot-die coating (20–40 nm RMS) [3].

4. Conclusions

A novel system for testing roll coating parameters has been developed and the proof of concept experiments completed. The system show great potential to help develop a thorough understanding of the coating factors for ink viscosity, coating speed and general optimization of parameters. The initial experiments even showed a distinct difference between coating with the use of the three different solvents, with a benefit to use ODCB in both V_{oc}, I_{sc} and FF.

Acknowledgments

We would like to thank Kristian Larsen, Jan Alstrup and Torben Kjær for constructing the machine. This work was supported by the Danish Strategic Research Council (DSF 2104-07-0022).

References

[1] T. Markvart, L. Castaner, Solar Cells: Materials Manufacture and Operation, Elsevier Science, 2005, pp. 1–555.
[2] T.D. Nielsen, C. Cruickshank, S. Foged, J. Thorsen, F.C. Krebs, Business, market and intellectual property analysis of polymer solar cells, Solar Energy Materials and Solar Cells 94 (2010) 1553–1571.
[3] F.C. Krebs, T. Tromholt, M. Jørgensen, Upscaling of polymer solar cell fabrication using full roll-to-roll processing, Nanoscale 2 (2010) 873–886.
[4] A.J. Medford, M.R. Lilliedal, M. Jørgensen, D. Aarø, H. Pakalski, J. Fyenbo, F.C. Krebs, Grid-connected polymer solar panels: initial considerations of cost, lifetime, and practicality, Optics Express 18 (S3) (2010) A272–A285.
[5] F.C. Krebs, T.D. Nielsen, J. Fyenbo, M. Wadstrøm, M.S. Pedersen, Manufacture, integration and demonstration of polymer solar cells in a lamp for the Lighting Africa initiative, Energy & Environmental Science 3 (2010) 512–525.
[6] F.C. Krebs, J. Fyenbo, M. Jørgensen, Product integration of compact roll-to-roll processed polymer solar cell modules: methods and manufacture using flexographic printing, slot-die coating and rotary screen printing, Journal of Materials Chemistry 20 (2010) 8994–9001.
[7] N. Espinosa, R. Garcia-Valverde, A. Urbina, F.C. Krebs, A life cycle analysis of polymer solar cell modules prepared using roll-to-roll methods under ambient conditions, Solar Energy Materials and Solar Cells 95 (2011) 1293–1302.
[8] N. Espinosa, R. Garcia-Valverde, F.C. Krebs, Life-cycle analysis of product integrated polymer solar cells, Energy & Environmental Science 4 (2011) 1547–1557.
[9] PCE=8.5% (〈www.Mitsubishi.com〉), PCE=8.3% (〈www.Konarka.com〉), PCE=8.13% (〈www.Solarmer.com〉).
[10] F.C. Krebs, S.A. Gevorgyan, B. Gholamkhass, S. Holdcroft, C. Schlenker, M.E. Thompson, B.C. Thompson, D. Olson, D.S. Ginley, S.E. Shaheen, H.N. Alshareef, J.W. Murphy, W.J. Youngblood, N.C. Heston, J.R. Reynolds, S. Jia, D. Laird, S.M. Tuladhar, J.G.A. Dane, P. Atienzar, J. Nelson, J.M. Kroon, M.M. Wienk, R.A.J. Janssen, K. Tvingstedt, F. Zhang, M. Andersson, O. Inganäs, M. Lira-Cantu, R. de Bettignies, S. Guillerez, T. Aernouts, D. Cheyns, L. Lutsen, B. Zimmermann, U. Würfel, M. Niggemann, H.-F. Schleiermacher, P. Liska, M. Grätzel, P. Lianos, E.A. Katz, W. Lohwasser, B. Jannon, A round robin study of flexible large-area roll-to-roll processed polymer solar cell modules, Solar Energy Materials and Solar Cells 93 (2009) 1968–1977.
[11] S.A. Gevorgyan, A.J. Medford, E. Bundgaard, S.B. Sapkota, H. Schleiermacher, B. Zimmermann, U. Würfel, A. Chafiq, M. Lira-Cantu, T. Swonke, M. Wagner, C.J. Brabec, O. Haillant, E. Voroshazi, T. Aernouts, R. Steim, J.A. Hauch, A. Elschner, M. Pannone, M. Xiao, A. Langzettel, D. Laird, M.T. Lloyd, T. Rath, E. Maier, G. Trimmel, M. Hermenau, T. Menke, K. Leo, R. Rösch, M. Seeland, H. Hoppe, T.J. Nagle, K.B. Burke, C.J. Fell, D. Vak, Th.B. Singh, S.E. Watkins, Y. Galagan, A. Manor, E.A. Katz, T. Kim, K. Kim, P.M. Sommeling, W.J.H. Verhees, S.C. Veenstra, M. Riede, G.M. Christoforo, T. Currier, V. Shrotriya, G. Schwartz, F.C. Krebs, An inter-laboratory stability study of roll-to-roll coated flexible polymer solar modules, Solar Energy Materials and Solar Cells 95 (2011) 1398–1416.
[12] S. Bertho, W.D. Oosterbaan, V. Vrindts, J. D'Haen, T.J. Cleij, L. Lutsen, J. Manca, D. Vanderzande, Controlling the morphology of nanofiber-P3HT:PCBM blends for organic bulk heterojunction solar cells, Organic Electronics 10 (2009) 1248–1251.

Appendix - A1

[13] C.W. Chu, H.C. Yang, W.J. Hou, J.S. Huang, G. Li, Y. Yang, Control of the nanoscale crystallinity and phase separation in polymer solar cells, Applied Physics Letters 92 (2008) 103306-1-4.
[14] N. Espinosa, H.F. Dam, D.M. Tanenbaum, J.W. Andreasen, M. Jørgensen, F.C. Krebs, Roll-to-roll processing of inverted polymer solar cells using hydrated vanadium(V)oxide as a PEDOT:PSS replacement, Materials 4 (2011) 169–182.
[15] J. Alstrup, M. Jørgensen, A.J. Medford, F.C. Krebs, Ultra fast and parsimonious materials screening for polymer solar cells using differentially pumped slot-die coating, ACS Applied Materials & Interfaces 2 (2010) 2819–2827.
[16] F.C. Krebs, Polymer solar cell modules prepared using roll-to-roll methods: knife-over-edge coating, slot-die coating and screen printing, Solar Energy Materials and Solar Cells 93 (2009) 465–475.

Materials **2011**, *4*, 169-182; doi:10.3390/ma4010169

OPEN ACCESS

materials

ISSN 1996-1944

www.mdpi.com/journal/materials

Article

Roll-to-Roll Processing of Inverted Polymer Solar Cells using Hydrated Vanadium(V)Oxide as a PEDOT:PSS Replacement

Nieves Espinosa [1], Henrik Friis Dam [2], David M. Tanenbaum [3], Jens W. Andreasen [2], Mikkel Jørgensen [2] and Frederik C. Krebs [2,*]

[1] Department of Electronics, Computing and projects, Technical University of Cartagena, Campus Muralla del Mar. C/Doctor Fleming s/n, 30202 Cartagena, Spain; E-Mail: nieves.espinosa@upct.es (N.E.)

[2] Risø National Laboratory for Sustainable Energy, Technical University of Denmark, Frederiksborgvej 399, DK-4000 Roskilde, Denmark; E-Mail: hfda@risoe.dtu.dk (H.F.D.); jewa@risoe.dtu.dk (J.W.A.); mijq@risoe.dtu.dk (M.J.)

[3] Department of Physics and Astronomy, Pomona College, Claremont, CA 91711, USA; E-Mail: dtane@risoe.dtu.dk (D.M.T.)

* Author to whom correspondence should be addressed; E-Mail: frkr@risoe.dtu.dk.

Received: 26 November 2010; in revised form: 27 December 2010 / Accepted: 7 January 2011/ Published: 11 January 2011

Abstract: The use of hydrated vanadium(V)oxide as a replacement of the commonly employed hole transporting material PEDOT:PSS was explored in this work. Polymer solar cells were prepared by spin coating on glass. Polymer solar cells and modules comprising 16 serially connected cells were prepared using full roll-to-roll (R2R) processing of all layers. The devices were prepared on flexible polyethyleneterphthalate (PET) and had the structure PET/ITO/ZnO/P3HT:PCBM/$V_2O_5 \cdot (H_2O)_n$/Ag. The ITO and silver electrodes were processed and patterned by use of screen printing. The zinc oxide, P3HT:PCBM and vanadium(V)oxide layers were processed by slot-die coating. The hydrated vanadium(V)oxide layer was slot-die coated using an isopropanol solution of vanadyl-triisopropoxide (VTIP). Coating experiments were carried out to establish the critical thickness of the hydrated vanadium(V)oxide layer by varying the concentration of the VTIP precursor over two orders of magnitude. Hydrated vanadium(V)oxide layers were characterized by profilometry, scanning electron microscopy, energy dispersive X-ray spectroscopy, and grazing incidence wide angle X-ray scattering. The power conversion efficiency (PCE) for completed modules was up to 0.18%, in contrast to single cells where

efficiencies of 0.4% were achieved. Stability tests under indoor and outdoor conditions were accomplished over three weeks on a solar tracker.

Keywords: roll-to-roll printing/coating; polymer solar cells; solution processing; PEDOT:PSS free; hydrated vanadium(V)oxide

1. Introduction

Polymer solar cells [1-3] have seen remarkable progress in recent years and have developed from being a scientific curiosity to an emerging technology that can be manufactured industrially [4-8] and demonstrated in real applications [9-13]. Polymer solar cells have been heralded as the photovoltaic (PV) technology solving all the problems current PV technologies are faced with by providing convincing solutions to problems of cost and abundance of the materials that constitute them. The largest challenges to overcome this far have been the low performance and the short operational lifetime. Today they present power conversion efficiencies in excess of 8% [14] and estimated operational lifetimes in the range of 2–5 years [15]. The typical polymer solar cell is a multilayer structure with typically five layers stacked on top of each other. The active layer responsible for light absorption and generation of free charge carriers is typically the middle layer sandwiched between two charge selective layers, as shown in Figure 1. The two outer layers are highly conducting electrodes for extraction of the generated electrical current. One of those must be transparent. The electron selective layers have been developed recently but have otherwise been limited to the intentional use of low work function metals alone or in combination with very thin wide band gap insulators such as LiF and MgF_2. Relatively recently, a new class of moderately conducting electron selective layers have been explored (ZnO, TiO_2, Nb_2O_5) [16]. The hole selective layer has been limited almost exclusively to various formulations of PEDOT:PSS. The reasons for this are mostly historical and PEDOT:PSS was first employed as an intermediate layer that served to stabilize the work function of ITO and to planarize it, thus enabling formation of nearly defect free thin films on top [17]. PEDOT:PSS has evolved and now exist in various formulations that provide exceptionally high conductivity and transparency. In addition, PEDOT:PSS is highly stable photochemically and is stable towards oxidative conditions.

Figure 1. Schematic of inverted polymer solar cell structure with typical layer thicknesses shown.

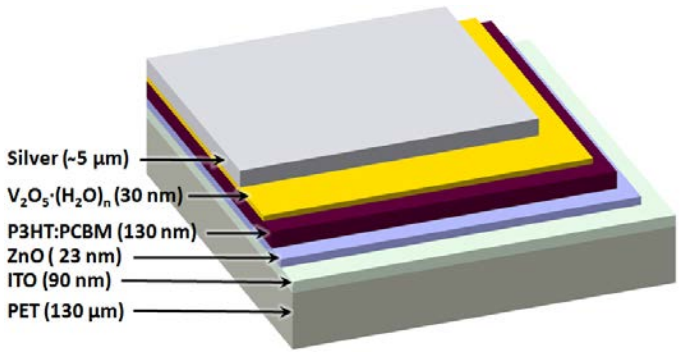

The Achilles heel of PEDOT:PSS, however, is its hygroscopic nature. This problem is normally never encountered under laboratory conditions where experimenters work under relatively dry indoor conditions or in a glovebox environment with nearly no humidity. At higher humidity levels such as those encountered under outdoor conditions (>50% relative humidity) this has been found to be a detrimental and stability limiting factor. This affinity for water also represents a problem when depositing by a roll-to-roll method, due to the high surface tension of the PEDOT:PSS solutions. From this point of view, there are clear incentives to find a humidity stable alternative to PEDOT:PSS. For the purpose of this study, we constructed two different types of polymer solar cell modules: one type that was a standard device with PEDOT:PSS and another type where PEDOT:PSS had been replaced with hydrated vanadium(V)oxide. Global resources are estimated to exceed 63 million tons; making vanadium the 13th most-abundant element in the Earth's crust. The materials employed are shown in Figure 2.

Figure 2. Chemical structures of materials employed in this study: P3HT, PCBM, PEDOT:PSS, and VTIP, R2 = C6H13.

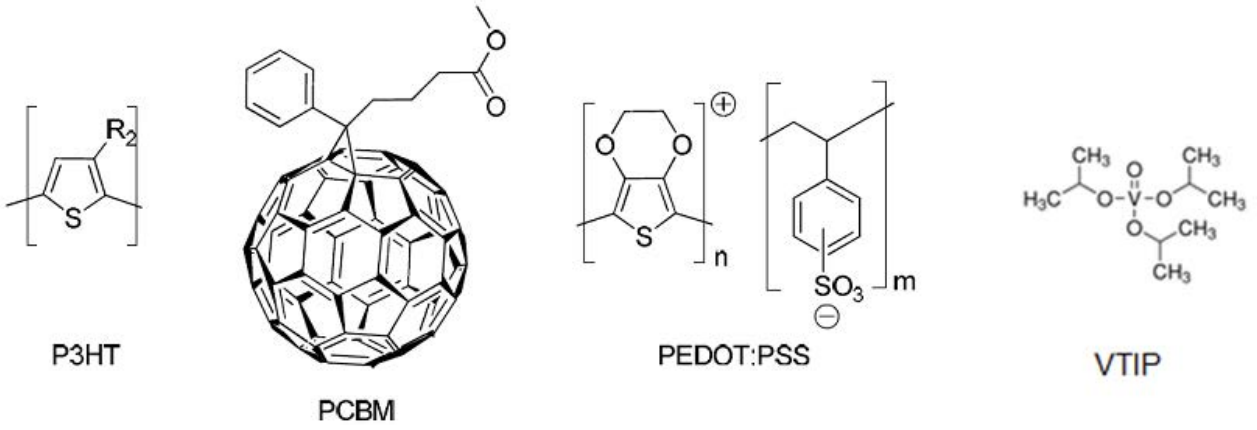

Binary combinations of vanadium and oxygen have a rich phase diagram with a wide range of stable compounds with different valence states for vanadium. In addition, it is common to have xerogels of these compounds with water layered between vanadium oxide sheets [18]. Processing temperatures for films on polyethyleneterphthalate (PET) substrates are limited to 140 °C. In this work, we evaluate hydrated vanadium(V)oxide as a PEDOT:PSS replacement for polymer solar cells prepared under industrially relevant conditions. We employ solutions of vanadyl-triisopropoxide (VTIP) in isopropanol and demonstrate roll-to-roll (R2R) coating of this layer in functional polymer solar cells and modules in contrast to previous OPVs [19] and OLEDs [20] where vanadium oxide films were prepared via thermal evaporation or from a spin casting powder in alcohol [21]. We further test these against a PEDOT:PSS equivalent under accelerated indoor and outdoor conditions. In this study, we have three different classes of devices, as shown in Figure 3, with active areas of 0.5, 4.2, and 360 cm^2 for glass, gradient, and module studies, respectively.

Figure 3. Image of a typical glass cell, gradient cell, and 16 cell module (from left to right) with a mm scale.

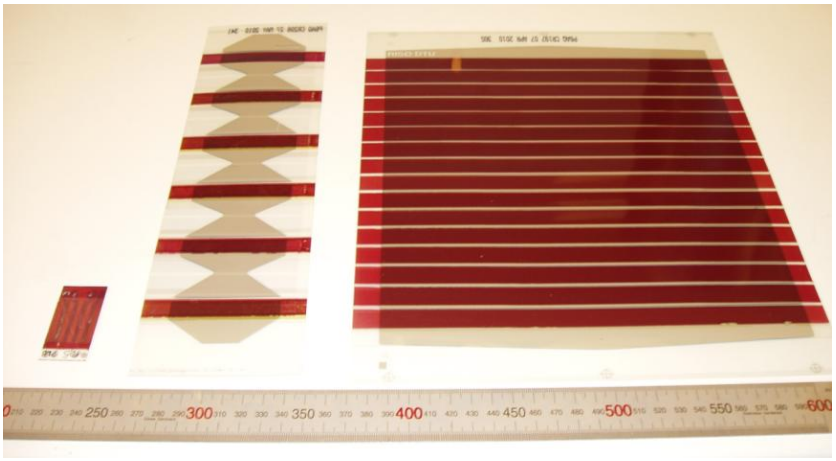

2. Results and Discussion

2.1. Spin Coated Cells on Glass Substrates

Small devices were prepared with a four cell substrate with ITO patterned in stripes giving 0.5 cm^2 active area for each cell. Cells having different concentrations of VTIP in isopropanol (3.5, 6.5, 12.5, 25, 50 and 100 mg/mL), as HTL in the devices, and different numbers of layers were fabricated. Best results, shown in Figure 4, were achieved with one or two layers of 12.5 mg/mL of VTIP, yielding efficiencies around 0.4%.

Figure 4. IV curves on small devices under 1,000 W/m^2 illumination, using several VTIP concentrations, and a similar cell with PEDOT:PSS.

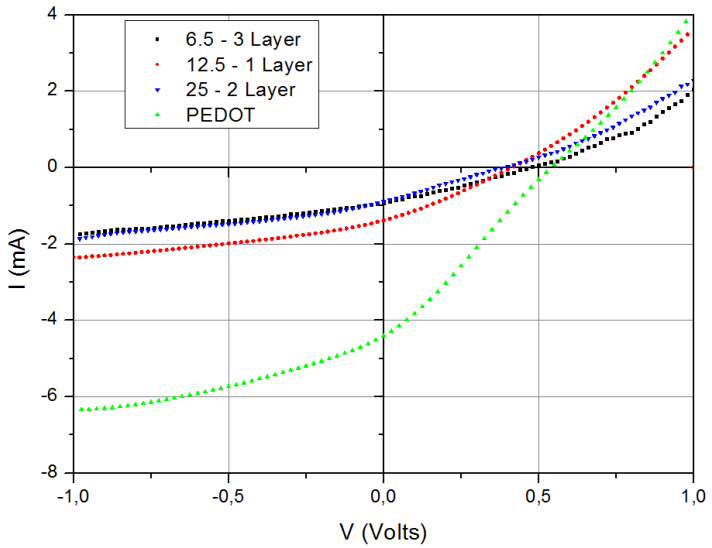

These initial test results indicated that there is a range of concentration between 6.5 and 25 mg/mL for which the cells have an acceptable performance for spin coated films on glass substrates. It is clear

from Figure 4 that the currents supported by the hydrated vanadium oxide films are lower than the PEDOT control sample.

2.2. Gradient Study on R2R PET Cells

One critical aspect when developing new inks for R2R coating is to establish the relationship between the thickness of the dried layer that is to be coated and the coating parameters for the wet film. We have developed a method for variation of the ink properties of any layer during coating enabling identification of the optimal thickness, the critical thickness or the optimal blend ratio between donor and acceptor. In our case, we coated a gradient of the VTIP solution from zero concentration and up to 100 mg/mL. Complete devices without the hydrated vanadium oxide layer are not functional, and once the covering layer is already on top of the others, devices become functional. This is shown in Figure 5 for three series of 50 individual cells with active areas of 4.2 cm^2.

Figure 5. Plot of solar cell efficiency as a function of VTIP concentration in R2R gradient experiments. Estimated film thicknesses are noted on the top axis.

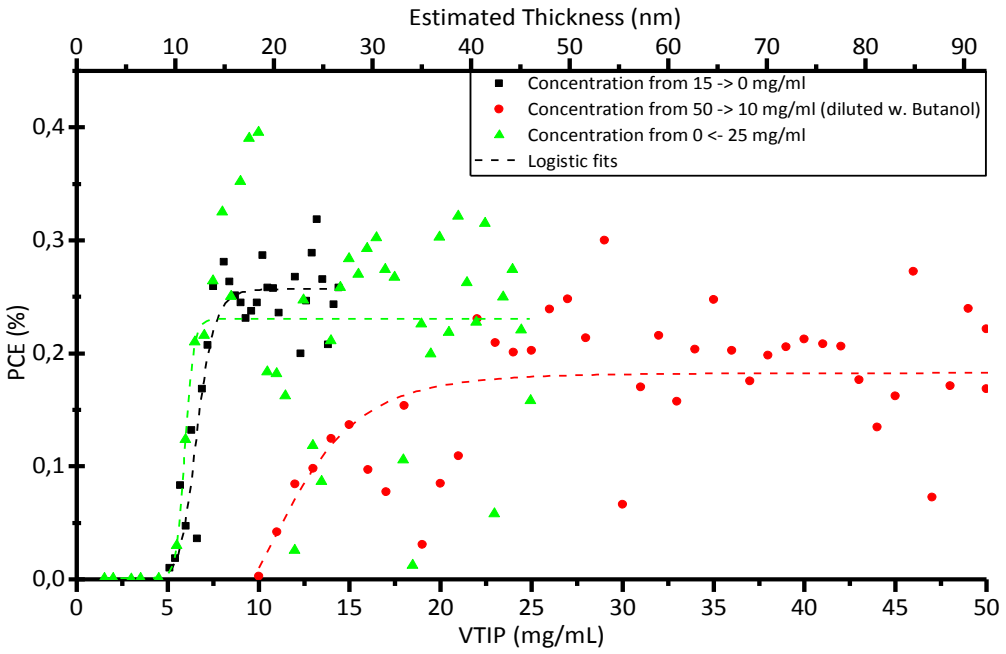

2.3. Characterization of Hydrated Vanadium(V)Oxide

Hydrated vanadium(V)oxide films were prepared on glass, silicon, and PET substrates and characterized by optical spectroscopy, ellipsometry, profilometry, scanning electron microscopy (SEM), energy dispersive X-ray spectroscopy (EDX), and grazing incidence wide angle X-ray scattering (GIWAXS). Measurements with GIWAXS on silicon substrates combined with the structural model of $(H_2O)_n$ [22], indicate that the films in this study are largely low-crystalline hydrated vanadium pentoxide $V_2O_5 \cdot (H_2O)_{0.3}$ with an interlayer spacing of 1.11 nm, as seen in the measurements shown in Figure 6. The hydrated vanadium pentoxide is always of low crystallinity, typically characterized as ―nanocrystalline", and the locally ordered structure was therefore determined by pair distribution function analysis [22]. EDX data confirm the relative vanadium and

oxygen concentrations. A SEM image of a cleaved cross section through a 15 nm-thick film is shown in Figure 7. It is clear that the conductivity of the hydrated vanadium(V)oxide films is a limiting factor in our devices. This is a major difference between this study and previous studies where vanadium oxide films were prepared by different methods [19,21]. It has been reported that for hydrated vanadium(V)oxide films the conductivity in thicker films increases with the annealing temperature as long as the film retains the layered slab structure with a bilayer of vanadium oxide stacked between layers of water molecules. However, annealing at higher temperatures transforms the hydrated oxide to crystalline V_2O_5 with much lower conductivity, presumably because of the formation of grain boundaries [23]. Compared to the previously reported measurements on vanadium(V)oxide xerogel films which were cast from gel solutions [18,23], our VTIP cast films are extremely thin, with a much higher surface to volume ratio. This makes dehydration effective at much lower temperatures, so that our 120–140 °C anneal results in n values of ~0.3, comparable to much higher temperature annealing processes on the gel based films where similar n values required annealing over 250 °C.

Figure 6. Left: The GIWAXS data as measured, with intensities represented on a color log scale. The strongest scattering feature near the center of the image corresponds to the 001 reflection, whereas the weaker scattering at the edges of the image, correspond to the 110 and 11-1 reflections [22], showing that the crystallites are preferentially oriented with the ab-plane parallel to the substrate surface. Right: Integration over 001 peak, assuming sample to detector distance of 121 mm, yields a d-spacing of 11.1 Å.

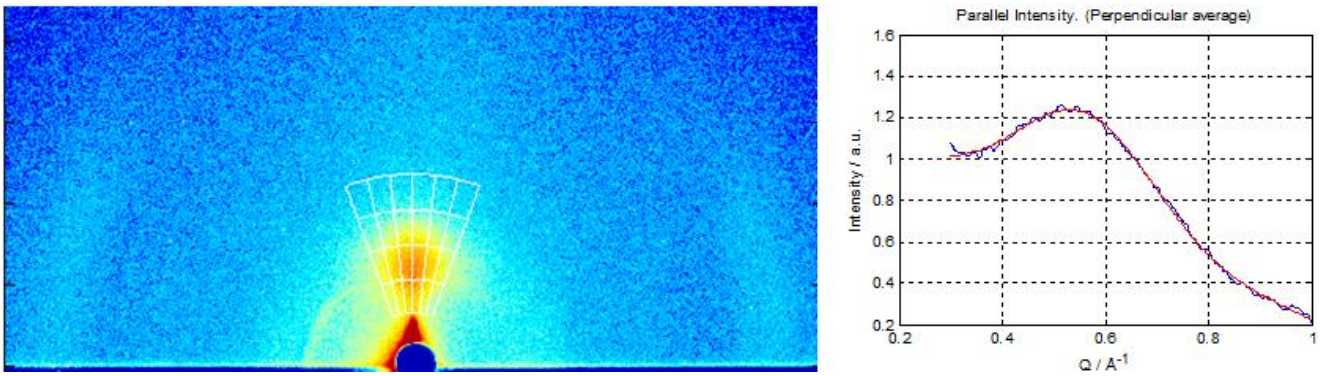

Figure 7. SEM cross section (tilted 17°) of 15 nm-thick cleaved $V_2O_5 \cdot (H_2O)_{0.3}$ film on a crystal silicon substrate showing film thickness and uniform morphology on the film surface.

Thickness of the roll coated films on PET were calculated using a dry film density based on this model and the known parameters of the wet coating process with Equation 1,

$$t = \frac{f \cdot \rho_w \cdot M_{V_2O_5}}{2 \cdot S \cdot W \cdot \rho_d \cdot M_{VTIP}} \quad (1)$$

where f is volumetric flow, ρ_w and ρ_d are the densities of the VTIP solution and the dry $V_2O_5 \cdot (H_2O)_{0.3}$ film, M_{V2O5} and M_{VTIP} are molecular weights, and S and W are the coating speed and width of the stripe.

For a PET sample coated with 15 mg/mL, a profilometer measurement of the dry film thickness showed a range with an average of 34 ± 9 nm, in agreement with the 27 nm predicted by our model.

2.4. Full R2R Fabrication of 16 Cell Modules

A number of A4 size 16 cell modules with an active area of 360 cm^2 were produced with a VTIP concentration of 15 mg/mL on PET substrates in a full R2R process. These 50 modules showed a reasonable yield, as seen in Figure 8, with a few modules around module number 360 that did not function. For the remaining modules the performance varied slightly, as seen in Table 1.

Figure 8. Comparison of the open-circuit voltage, V_{oc}, the short-circuit current, I_{sc}, the fill-factor, *FF*, and the photon conversion efficiency, *PCE*, for R2R modules made with a VTIP concentration of 15 mg/mL. They were measured under two different sun simulators and 5 modules (367–371) were measured in outdoor conditions as well.

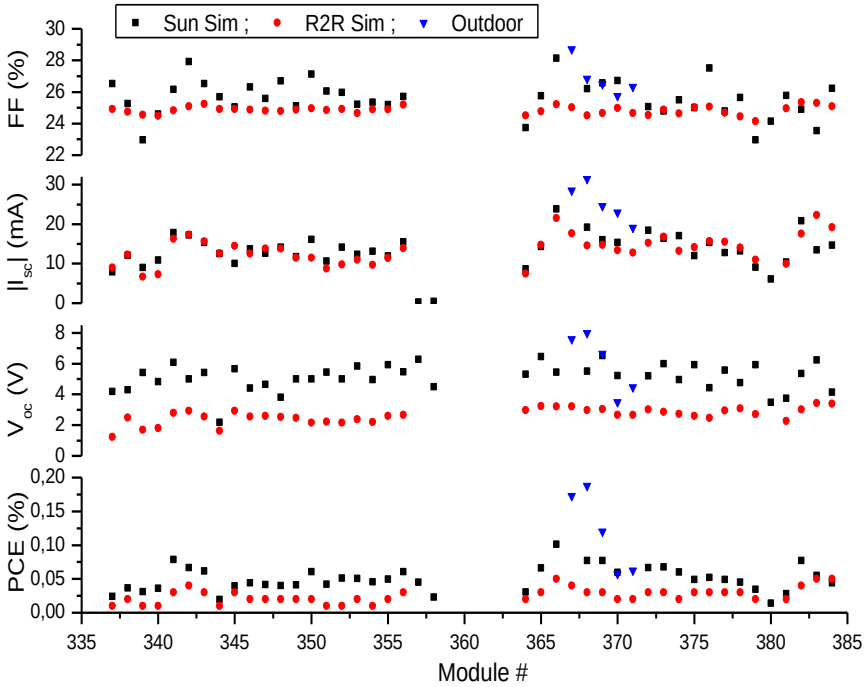

Furthermore, the use of an R2R simulator, an AM1.5G sun simulator and outdoor testing showed a significant difference between the performances of the modules. On the R2R simulator the V_{oc} was generally lower than what was measured later on the stationary sun simulator. Interestingly, the outdoor measurements showed even greater performance with the four outdoor modules showing an increase in PCE to almost double of the indoor measurement for the modules without extra

encapsulation, while the modules encapsulated in polycarbonate (PC) show a performance similar to the indoor measurements.

Table 1. Performance and standard deviations for the 15 mg/mL R2R modules produced and measured. The outdoor test includes both PC and PET encapsulated modules.

Measurement	# of Modules	PCE (%)	V_{oc} (V)	I_{sc} (mA)	FF (%)
R2R Simulator	40	0.025 ± 0.011	2.6 ± 0.5	−13.5±3.6	24.8 ± 0.3
Sun Simulator	40	0.050 ± 0.018	5.1 ± 0.9	−13.8 ± 3.6	25.6 ± 1.2
Outdoor	5	0.12 ± 0.06	6.0 ± 2.0	−25.4 ± 4.8	26.8 ± 1.1

The increased voltage obtained with the sun simulator and the outdoor measurement compared to the R2R simulator is caused by higher contact resistance in the R2R test system and by incomplete photochemical activation of the zinc oxide layer of the initially processed modules. Longer exposure (typically 20 minutes) to a high intensity of UV light in the sun simulator fully activates the zinc oxide and enhances the performance of the cells.

2.5. Stability Measurements

Lifetime studies were carried out under the sun simulator for all types of cells in this study. Spin coated cells on glass showed a degradation of the PCE dominated by loss of current density. The time, *T80,* for a cell to decay to 80% of its initially activated value while under AM1.5G illumination increases with film thickness, up to 18 hours for the thickest films, as shown in Figure 9. The activation of the zinc oxide layer can be seen at the beginning of the study and was similar for all the cells and modules presented here.

Figure 9. Time study over 20 hours on a glass cell with $V_2O_5 \cdot (H_2O)_{0.3}$ (25 mg/mL).

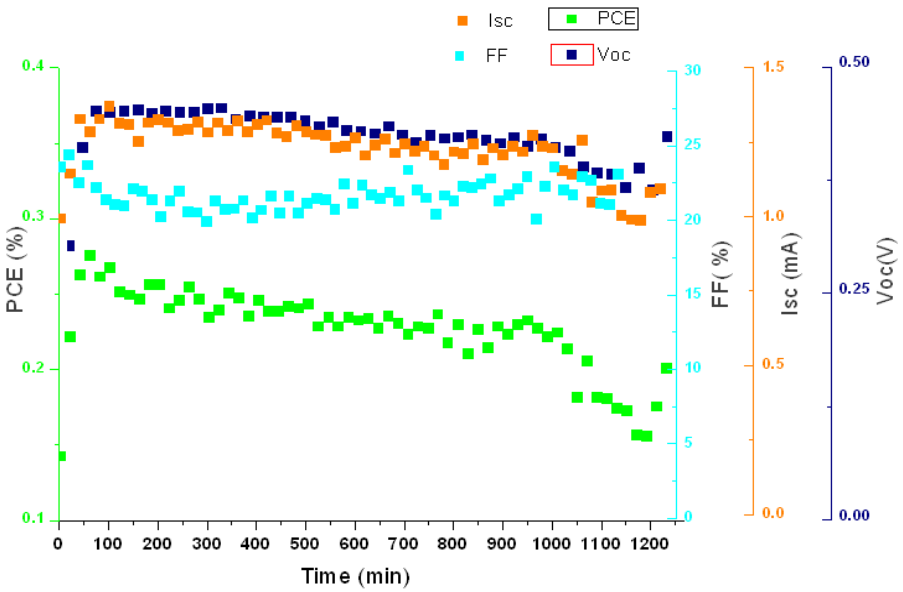

In contrast, cells from the gradient experiments on the R2R process had a *T80* < 30 minutes dominated by a decrease in open circuit voltage. Modules made on the R2R process were observed to

have different *D80* values depending upon their encapsulation, where *D80* is the dose causing a decay to 80% of initial value. The bare PET modules having *D80*~50 MJ/m^2 and *D50* > 300 MJ/m^2, while two polycarbonate clad modules show *D80* > 150 MJ/m^2 and 300 MJ/m^2. It should be noted that modules 369 and 371 were mounted for outdoor measurements without an initial soaking in the solar simulator to photo activate the zinc oxide layer, resulting in an initial increase in performance and enhanced observed stability. Reference PEDOT modules showed minimal degradation, with *D80* > 300 MJ/m^2, with the polycarbonate again showing a reduced efficiency with enhanced stability. The full set of performance characteristics for module 367 can be seen in Figure 10. The J_{sc} has been scaled by the irradiance, and the dominant decay factor for the modules is the decrease in the V_{oc} which clearly tracks the *PCE* data. The 300 MJ outdoor dose corresponds to a 28 day period with a variety of weather conditions. The pyranometer data for this period is shown in Figure 11.

Figure 10. Plots of PCE for all data measured with a solar irradiance above 800 W/m^2 plotted as a function of accumulated irradiance. The upper graph shows reference modules made with Process One using PEDOT. The middle graph shows the modules made with hydrated vanadium oxide. The full characterization, *PCE*, V_{oc}, *FF*, and J_{sc} (scaled by irradiance) plotted *versus* dose for module 367 is shown on the bottom graph. Modules encapsulated in polycarbonate have the prefix PC.

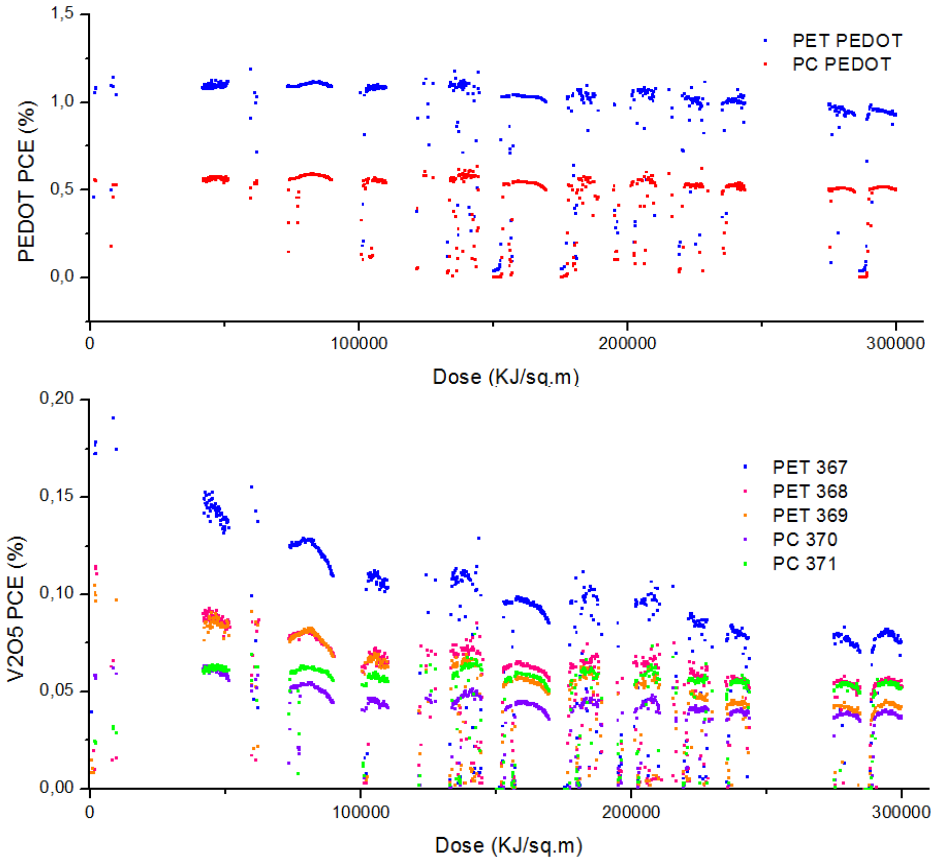

Figure 10. *Cont.*

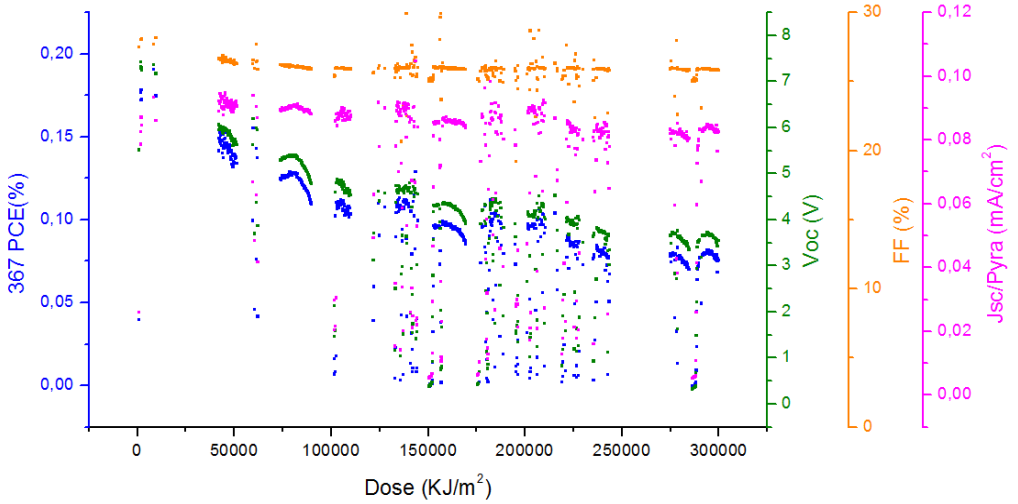

Figure 11. The pyranometer data on the tracking platform for the duration of the outdoor measurements reported in this study.

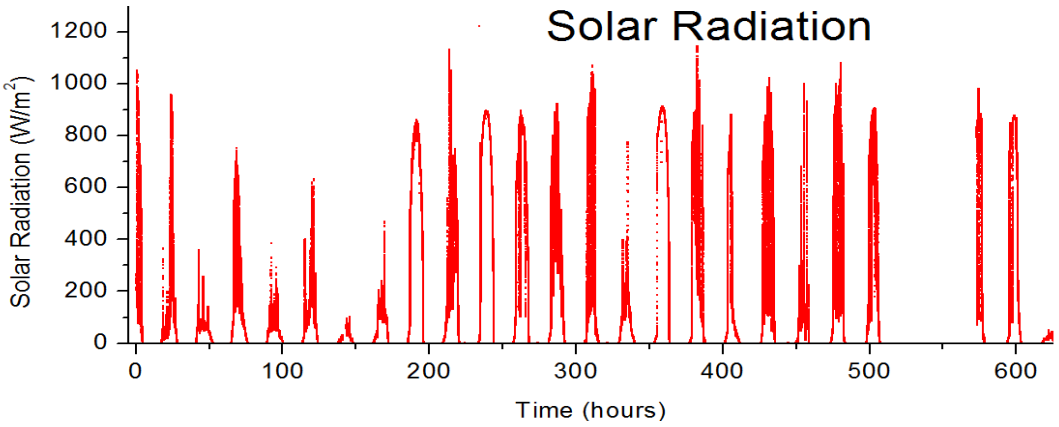

3. Experimental Section

3.1. Materials

A sputtered layer of 90 nm of ITO on PET was used as the anode. ZnO nanoparticles were prepared by caustic hydrolysis of $Zn(OAc)_2 \cdot 2H_2O$ as described previously [4,7,9] and were used for ink formulations using Acetone as solvent. The ZnO ink was filtered through a 0.45 micron filter before coating. The ink for the active layer was prepared by dissolving P3HT (18–24 mg/mL) purchased from BASF (Sepiolid P200), and PCBM (16–22 mg/mL) purchased from Solenne B.V. in half the final volume of 1,2-dichlorobenzene at 120 °C for 3 h, followed by addition of the second half of the final volume of chloroform. The ratio between P3HT and PCBM was typically 10:9. PEDOT:PSS, was purchased as EL-P 5010 from Agfa and was diluted slowly with isopropanol using stirring until a viscosity of 270 mPa s was obtained. The hydrated vanadium(V)oxide layer was prepared by dilution of VTIP purchased from Sigma Aldrich in isopropanol. The silver ink employed, which is screen printable and heat curable was purchased from Dupont (PV 410). The adhesive for encapsulation was

467 MPF from 3M and the barrier material was purchased from Amcar and has a UV filter with a cutoff at 380 nm.

3.2. Grazing Incidence Wide Angle X-ray Scattering

By orienting the substrate surface just below the critical angle for total reflection with respect to the incoming X-ray beam (~0.18°), scattering from the deposited film is maximized with respect to scattering from the substrate. In the wide scattering angle range (>5°), the X-ray scattering is sensitive to crystalline structure. The GIWAXS data were acquired using a camera comprising an evacuated sample chamber with an X-ray photo-sensitive image plate with a rotating Cu-anode operating at 50 kV/200 mA as X-ray source, focused and monochromatized (Cu Kα, λ = 1.5418 Å) by a 1D multilayer [24]. Verification of the crystalline structure was done by simulating the GIWAXS pattern of the published $V_2O_5 \cdot (H_2O)_n$ structure [22] using the simulation software developed by Breiby *et al*. [25].

3.3. Processing Methods

The experiment was performed in a roll-to-roll method, following a procedure previously published and known as ProcessOne [4]. This procedure consists of slot-die coating consecutively on PET covered with ITO, zinc oxide, the active layer, and the VTIP, in a slot-die coater [4,7]. The VTIP layer was deposited in each stripe with a different gradient of concentration, starting from higher to lower, listed in Table 2. Details of the gradient coating technique are outlined in a previous publication [26]. Six gradients with 50 steps were employed in this study, comprising 300 4.2 cm^2 cells. In addition, 50 modules with an active area of 360 cm^2, each consisting of 16 cells in series, were produced with a fixed VTIP dilution of 15 mg/mL in isopropanol. The silver back-electrode contact was printed by means of a roll-to-roll screen printer Alraun, presented in previous publications [9]. Cells and modules were encapsulated in a barrier film with a UV filter with a cut off at 380 nm. Selected modules were further encapsulated in polycarbonate sheets with a polyurethane adhesive with an effective UV cut off at 390 nm.

Table 2. Summary of cells used in this study, each line represents~ 50 devices (400 total).

Substrate	Device	[VTIP] (mg/mL)	Active Area (cm^2)
Glass	Spin Cast Single Cells	0.3–50	0.5
PET	R2R Cells Stripe 1	0–100	4.2
PET	R2R Cells Stripe 2	0–15	4.2
PET	R2R Cells Stripe 3	0–50	4.2
PET	R2R Cells Stripe 4	0–50 (butanol)	4.2
PET	R2R Cells Stripe 5	0–25	4.2
PET	R2R Cells Stripe 6	0–100	4.2
PET	R2R 16 Cell Modules	15	360

3.4. Test Conditions

All cells were measured by collecting IV curves with a Keithley 2400 sourcemeter under illumination from a solar simulator (KHS Solar Constant 1200) calibrated for AM1.5G with an automated roll to roll testing system for an initial screening, followed by an annealing soak (KHS Solar Constant 575, AM1.5G) for 20 minutes with characterization at regular intervals to activate the ZnO layer and maximize the cell performance. Modules both with and without polycarbonate encapsulation were measured outside on a solar tracking platform subjected to rain, frost, temperatures (0–13 °C), and solar radiation up to 1135 W/m^2 at Risø DTU (Latitude: 55°41'42 N, Longitude: 12°4'16 E) Seven modules were characterized over 600 hours at 3 minute intervals throughout October 2010. The modules were open circuit between measurements (90% of the time.) Solar irradiance was recorded at 2 seconds intervals on the same tracker as the modules using a pyranometer (Eppley Lab PSP) Outdoor measurements exceed Level 1 guidelines established at the ISOS workshops [27].

4. Future Perspectives and Conclusion

A major perspective of this work lies in processing. Hydrated vanadium(V)oxide has been employed in the fabrication of inverted PEDOT:PSS free polymer solar cells compatible with all solution processing of all layers. The use of a coating gradient in a R2R system enables a fast and efficient way to vary device parameters. In this case, the concentration of VTIP determines hydrated vanadium(V)oxide layers of varying thickness and enables us to discern the influence this has on device performance. We observe that a minimum critical thickness for the hydrated vanadium(V)oxide layer in our process is 8 nm, beyond which device performance reaches a plateau. Overall, the performance of the devices is limited by the resistance of the hydrated vanadium(V)oxide and interface layers, which reduces the current density in comparison with optimized cells manufactured with PEDOT:PSS. Outdoor stability studies show that modules encapsulated in polycarbonate are superior to PET barrier layer materials alone.

Acknowledgements

The authors thank Søren Fæster Nielsen for his support on the energy dispersive X-ray spectroscopy measurements on the hydrated vanadium oxide films, and Suren Gevorgyan and Jan Alstrup for useful discussions and guidance. This work was supported by the Danish Strategic Research Council (DSF 2104-05-0052 and 2104-07-0022), EUDP (j. nr. 64009-0050), Spanish Ministry of Science and Innovation (Consolider-HOPE CSD2007-00007) and Comunidad Autónoma de la Región de Murcia (CARM-D429-2008). One of the authors (DMT) acknowledges support from the American Scandinavian Foundation.

References

1. Helgesen, M.; Søndergaard, R.; Krebs, F.C. Advanced materials and processes for polymer solar cell devices. *J. Mater. Chem*. **2010**, *20*, 36-60.

2. Nielsen, T.D.; Cruickshank, C.; Foged, S.; Thorsen, J.; Krebs, F.C. Business, market and intellectual property analysis of polymer solar cells. *Sol. Energy Mater. Sol. Cells* **2010**, *94*, 1553-1571.
3. Krebs, F.C. Fabrication and processing of polymer solar cells. A review of printing and coating techniques. *Sol. Energy Mater. Sol. Cells* **2009**, *93*, 394-412.
4. Krebs, F.C.; Gevorgyan, S.A.; Alstrup, J. A roll-to-roll process to flexible polymer solar cells: Model studies, manufacture and operational stability studies. *J. Mater. Chem.* **2009**, *19*, 5442-5451.
5. Krebs F.C. All solution roll-to-roll processed polymer solar cells free from indium-tin-oxide and vacuum coating steps. *Org. Electronics* **2009**, *10*, 761-768.
6. Krebs, F.C.; Tromholt, T.; Jørgensen, M. Upscaling of polymer solar cell fabrication using full roll-to-roll processing. *Nanoscale* **2010**, *2*, 878-886.
7. Krebs, F.C. Polymer solar cell modules prepared using roll-to-roll methods: Knife-over-edge coating, slot-die coating and screen printing. *Sol. Energy Mater. Sol. Cells* **2009**, *93*, 465-475.
8. Krebs, F.C.; Norrman, K. Using light induced thermocleavage in a roll-to-roll process for polymer solar cells. *ACS Appl. Mater. Interfaces* **2010**, *2*, 877-887.
9. Krebs, F.C.; Jørgensen, M.; Norrman, K.; Hagemann, O.; Alstrup, J.; Nielsen, T.D.; Fyenbo, J.; Larsen, K.; Kristensen, J. A complete process for production of flexible large area polymer solar cells entirely using screen printing—First public demonstration, *Sol. Energy Mater. Sol. Cells* **2009**, *93*, 422-441.
10. Krebs, F.C.; Gevorgyan, S.A.; Gholamkhass, B.; Holdcroft, S.; Schlenker, C.; Thompson, M.E.; Thompson, B.C.; Olson, D.; Ginley, D.S.; Shaheen, S.E.; Alshareef, H.N.; Murphy, J.W.; Youngblood, W.J.; Heston, N.C.; Reynolds, J.R.; Jia, S.; Laird, D.; Tuladhar, S.M.; Dane, J.G.A.; Atienzar, P.; Nelson, J.; Kroon, J.M.; Wienk, M.M.; Janssen, R.A.J.; Tvingstedt, K.; Zhang, F.; Andersson, M.; Inganäs, O.; Lira-Cantu, M.; De Bettignies, R.; Guillerez, S.; Aernouts, T.; Cheyns, D.; Lutsen, L.; Zimmermann, B.; Würfel, U.; Niggemann, M.; Schleiermacher, H.-F.; Liska, P.;Grätzel, M.; Lianos, P.; Katz, E.A.; Lohwasser, W.; Jannon, B. A round robin study of flexible large-area roll-to-roll processed polymer solar cell modules. *Sol. Energy Mater. Sol. Cells* **2009**, *93*, 1968-1977.
11. Krebs, F.C.; Nielsen, T.D.; Fyenbo, J.; Wadstrøm, M.; Pedersen, M.S. Manufacture, integration and demonstration of polymer solar cells in a lamp for the ―Lighting Africa" initiative. *Energy. Environ. Sci.* **2010**, *3*, 512-525.
12. Medford, A.J.; Lilliedal, M.R.; Jørgensen, M.; Aarø, D.H.; Pakalski, D.; Fyenbo, J.; Krebs, F.C. Grid-connected polymer solar panels: Initial considerations of cost, lifetime, and practicality, *Optics Express* **2010**, *18*, A272-A285.
13. Krebs, F.C.; Fyenbo, J.; Jørgensen, M. Product integration of compact roll-to-roll processed polymer solar cell modules: Methods and manufacture using flexographic printing, slot-die coating and rotary screen printing. *J. Mater. Chem.* **2010**, *20*, 8994-9001.
14. Solarmer, Inc. Available online: http://www.solarmer.com (accessed on the 10 June 2010).
15. Hauch, J.A.; Schilinsky, P.; Choulis, S.A.; Rajoelson, S.; Brabec, C.J. The impact of water vapor transmission rate on the lifetime of flexible polymer solar cells. *App. Phys. Lett.* **2008**, *93*, 103306-103308.
16. Ameri, T.; Dennler, G.; Lungenschmied, C.; Brabec, C.J. Organic tandem solar cells: A review. *Energy Environ. Sci.* **2009**, *2*, 347-363.

17. Günes, S.; Neugebauer, H.; Sariciftci, N.S. Conjugated polymer-based organic solar cells. *Chem. Rev.* **2007**, *107*, 1324-1338.
18. Wang, Y.; Cao, G. Synthesis and enhanced intercalation properties of nanostructured vanadium oxides. *Chem. Mater.* **2006**, *18*, 2787-2804.
19. Shrotriya, V.; Li, G.; Yao, Y.; Chu, C.; Yang, Y. Transition metal oxides as the buffer layer for polymer photovoltaic cells. *Appl. Phys. Lett.* **2006**, *88*, 073508-073510.
20. Wu, J.; Hou, J.; Cheng, Y.; Xie, Z.; Wang, L. Efficient top-emitting organic light-emitting diodes with a V_2O_5 modified silver anode. *Semicond. Sci. Technol.* **2007**, *22*, 824-826.
21. Huang, J.S.; Wu, C.H.; Chou, C.Y.; Liu, M.Y.; Lin, W.H.; Lin, Y.H.; Lin, C.F. Solution-processed vanadium oxide interlayer for improving the performance of polymer/ZnO nanorod hybrid solar cells. In *Proceedings of Photovoltaic Specialists Conference (PVSC) 2009 34th IEEE*, Philadelphia, PA, USA, 7–12 June 2010; pp. 000554-000556.
22. Petkov, V.; Trikalitis, P.N.; Bozin, E.S.; Billinge, S.J.L.; Vogt, T.; Kanatzidis, M.G. Structure of $V_2O_5{\cdot}nH_2O$ Xerogel Solved by the Atomic Pair Distribution Function Technique, *J. Am. Chem. Soc.* **2002**, *124*, 10157-10162.
23. Barbosa, G.N.; Graeff, C.F.O.; Oliveira, H.P. Thermal annealing effects on vanadium pentoxide xerogel films. *Ecl. Quím.* **2005**, *30*, 7-15.
24. Apitz, D. ; Bertram, R.P.; Benter, N.; Hieringer, W.; Andreasen, J.W.; Nielsen, M.M.; Johansen, P.M.; Buse, K. Investigation of chromophore-chromophore interaction by electro-optic measurements, linear dichroism, X-ray scattering, and density-functional calculations, *Phys. Rev. E* **2005**, *72*, 036610-036619.
25. Breiby, D.W.; Bunk, O.; Andreasen, J.W.; Lemke, H.T.; Nielsen, M.M. Simulating X-ray diffraction of textured films. *J. Appl. Cryst*. **2008**, *41*, 262-271.
26. Alstrup, J; Jørgensen, M.; Medford, A.J.; Krebs, F.C. Ultra fast and parsimonious materials screening for polymer solar cells using differentially pumped slot-die coating. *ACS Appl. Mater. Interfaces* **2010**, *2*, 2819-2827.
27. International Summit on OPV Stability (ISOS-3), Roskilde, Denmark, 21–29 October 2010.

Solar Energy Materials & Solar Cells 97 (2012) 157–163

Contents lists available at SciVerse ScienceDirect

Solar Energy Materials & Solar Cells

journal homepage: www.elsevier.com/locate/solmat

Edge sealing for low cost stability enhancement of roll-to-roll processed flexible polymer solar cell modules

David M. Tanenbaum [a,b,*], Henrik Friis Dam [a], Roland Rösch [c], Mikkel Jørgensen [a], Harald Hoppe [c], Frederik C. Krebs [a]

[a] Solar Energy Programme, Risø National Laboratory for Sustainable Energy, Technical University of Denmark, Frederiksborgvej 399, DK-4000 Roskilde, Denmark
[b] Department of Physics and Astronomy, Pomona College, Claremont, CA 91711, USA
[c] Experimental Physics I, Institute of Physics, Ilmenau University of Technology, Weimarer Street 32, 98693 Ilmenau, Germany

ARTICLE INFO

Available online 20 October 2011

Keywords:
Flexible polymer solar cell
Encapsulation
Stability

ABSTRACT

Fully roll-to-roll processed polymer solar cell modules were prepared, characterized, and laminated. Cell modules were cut from the roll and matched pairs were selected, one module with exposed cut edges, the other laminated again with the same materials and adhesive sealing fully around the cut edges. The edge sealing rim was 10 mm wide. Cell modules were characterized by periodic measurements of IV curves over extended periods in a variety of conditions, as well as by a variety of spatial imaging techniques. Data show significant stability benefits of the edge sealing process. The results of the imaging experiments show that the ingress of atmospheric reactants from the edges leads to degradation. In the case of edge sealed devices the same effects are observed but significantly slowed down. In particular, the fast nonlinear degradation is eliminated.

1. Introduction

Major advances are being made in the field of organic polymer photovoltaics [1]. Cell efficiencies of over 8% have been achieved [2,3] and cell manufacturing techniques have been developed to the level that industrial production of cells and modules is technically feasible with continually decreasing costs [4,5]. Stability of organic photovoltaic (OPV) devices has become a more active area for research as well [6–10]. While progress has been impressive in all three of these areas individually, the next challenge is to bring these research successes together in a single device structure. In this work we focus on two of these three areas, combining economically viable full roll-to-roll fabrication processes with enhanced cell module stability. The stability of polymer solar cells is affected by a complicated mixture of different processes that all result in device degradation. Degradation at interfaces and photochemical degradation are some of the most important mechanisms that involve atmospheric components such as oxygen and water [11]. Methods to improve stability of the polymer solar cells and modules not only include improvement of the inherent stability of the materials and interfaces [12], but also prevention of ingress of atmospheric components through encapsulation [13,14] and reduction of the most reactive part of the electromagnetic spectrum through filtering UV-light [15]. It is of course possible to completely seal the device from the surroundings but the available methods are both tedious and not competitive in terms of cost and processing time. Ideally the encapsulation should be compatible with the manufacture of the solar cells and modules, which is through roll-to-roll processing. In the case of ProcessOne (described below) it is possible to seal the device in a fast roll-to-roll process although the seal is not complete at the edges of the device after it is cut from the roll [7]. In this case a second seal would be needed. In this work we thus aim at establishing the differences between the partially sealed (but easily accessible) device and the edge sealed device (that requires more processing time). Our approach is to look at the established ProcessOne fabrication method, which uses a polyethyleneterephthalate (PET) substrate coated with a transparent front electrode of indium-tin-oxide (ITO), an electron transport layer of ZnO, an active layer comprised of a blend of poly(3-hexylthiophene) (P3HT) as the donor and the phenyl-C61-buytric acid methyl ester (PCBM), a hole transport layer of poly(3,4-ethylenedioxythiophene):poly(styrene–sulfonate) (PEDOT:PSS) and a Ag back electrode all laminated on the roll with a UV filter and barrier film. Modules were prepared with (edge sealed) and without (control) a second level of lamination to form a barrier against diffusion through the cut edges of the devices. We characterize the devices by periodically measuring their IV curves and following their performance under a variety of illumination conditions over time.

* Corresponding author at: Department of Physics and Astronomy, Pomona College, Claremont, CA 91711, USA. Tel.: +909 621 8722.
E-mail addresses: dtanenbaum@pomona.edu, DMT04747@pomona.edu (D.M. Tanenbaum).

0927-0248/$ - see front matter © 2011 Elsevier B.V. All rights reserved.
doi:10.1016/j.solmat.2011.09.064

In addition we image the devices to spatially map their induced photocurrent [16,17], and induced temperature variations under forward and reverse bias [18,19].

2. Material and methods

Polymer solar cell modules were fabricated using ProcessOne by slot die coating in a fully roll-to-roll (R2R) process in an ambient laboratory environment as part of the ISOS-3 workshops held in October 2010 at Risø DTU. Each module consists of 16 individual cells in series. The active area of each module is nominally 35.5 cm^2. Each cell has an inverted architecture consisting of a transparent PET foil substrate coated by a layer stack of ITO/ZnO/P3HT:PCBM/PEDOT:PSS/Ag and laminated with a UV filter and barrier layer. The *inverted* architecture has light entering through the substrate and ITO, which serves as a collector for electrons from the active layer, while the holes are collected through the PEDOT:PSS to the Ag electrode. The advantages of this architecture include the elimination of reactive low work function metals used as the electron collector in the *normal* architecture and enhanced stability in the presence of water vapor. [7] A sputtered layer of 90 nm of ITO on a PET substrate was used as the anode. ZnO nanoparticles were prepared by caustic hydrolysis of $Zn(OAc)_2 \cdot 2H_2O$ as described previously [7,20,21] and were used for ink formulations using Acetone as a solvent. The ZnO ink was filtered through a 0.45 μm filter before coating. The ink for the active layer was prepared by dissolving P3HT (18–24 mg/mL) purchased from BASF (Sepiolid P200), and PCBM (16–22 mg/mL) purchased from Solenne B.V. in half the final volume of chlorobenzene at 120 °C for 3 h, followed by addition of the second half of the final volume of chloroform. The ratio between P3HT and PCBM was typically 10:9. PEDOT:PSS, was purchased as EL-P 5010 from Agfa and was diluted slowly with isopropanol using stirring until a viscosity of 270 mPa s was obtained. The silver ink employed, which is screen printable and UV curable was purchased from Toyo (FS18). Each cell has a full silver back electrode and series connection to adjacent cells, and large silver contacts for the anode and cathode contacts of the module. The adhesive for encapsulation was 467 MPF from 3 M and the barrier material was purchased from Amcor and has a UV filter with a cutoff at 380 nm. The barrier has a water vapor transmission rate $\sim 0.1\ g\ m^{-2}\ day^{-1}$ [38 °C, 90%RH] and an oxygen transmission rate $< 0.01\ cc/g\ m^{-2}\ day^{-1}$ bar [23 °C, 50%RH] as reported by Amcor. The transmission rates for the adhesive are not reported, but are expected to be much higher. After the first level of lamination, modules were cut from the roll leaving open edges on the perimeter of the lamination, ~1 cm from the active cell region. Modules were fully characterized and matched pairs were made with similar performance, typically with a power conversion efficiency, *PCE*, from 1–2%, and pairs were selected with *PCE* values within 0.2%. Cu tape (3 M) was applied to the silver electrodes to extend the electrical contact away from the device region. The edge sealed samples (one from each pair of modules) were then laminated a second time with an adhesive seal ~1 cm wide around the perimeter of any edges. There is no evidence that the edge sealing lamination process changed initial module performance. Metal snap fasteners (#20) are used to pierce the Cu to form the electrical terminals (similar to a 9 V battery) on all the modules.

Electrical characterization was performed by collecting IV curves with a Keithley 2400 sourcemeter under illumination from a metal halide solar simulator (KHS Solar Constant 1200) calibrated for AM1.5G at 1000 W/m^2 with an automated roll-to-roll testing system for an initial screening, followed by an annealing soak (KHS Solar Constant 575) for 40 min to activate the ZnO layer and maximize the module performance. Long term stability was measured under four illumination conditions: full sun (KHS Solar Constant 575, AM1.5G at 1000 W/m^2, $T \sim 55$ °C) halogen lamps (Osram Halopar 64845FL, 250 W/m^2, $T \sim 30$ °C), indoor fluorescent lighting (Osram FQ Lumilux HO, 100 W/m^2, $T \sim 45$ °C), and dark storage ($T \sim 20$ °C). The calibrated irradiance spectra of all three lighting conditions are shown in Fig. 1.

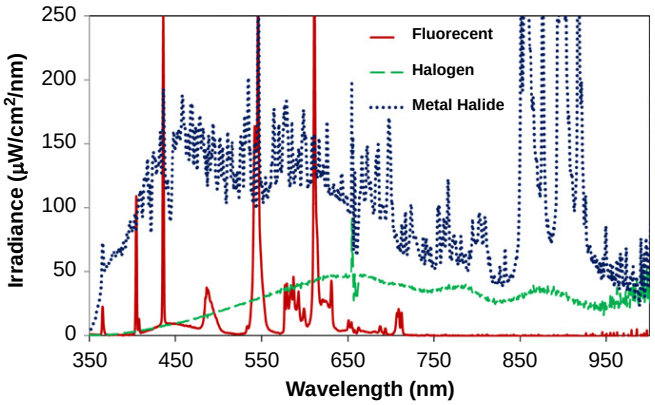

Fig. 1. Calibrated irradiance for the three light sources used in this study: metal halide (KHS Solar Constant 575), halogen lamp (Osram Halopar), and fluorescent lamp (Osram FQ Lumilux HO).

Photocurrent measurements were taken with a novel high speed light beam induced current (LBIC) system developed at Risø DTU. Adjustable gain and offset optimize visualization of patterns within each module image but absolute photocurrent cannot be compared across images. Spatial images of minute thermal fluctuations resulting from dark charge injection into the modules are measured by dark lock-in thermography (DLIT) and highlight ohmic power losses in the cell modules.[19] A high frame rate IR-camera combined with computer controlled charge injection and digital lock-in detection employed at TU Ilmenau enables measurement of thermal variation below 0.1 mK [18].

3. Results

The ZnO nanoparticles in ProcessOne modules require an initial activation, typically by exposure to UV [22]. Fig. 2 shows LBIC and IV characterizations of an edge sealed module before and after an initial 40 min soak to activate the ZnO. (The data is similar for the control module without the edge seal). The activation is not permanent, and is one way to see the effect of the edge sealing on the modules. A module with a full edge seal remained fully activated when stored in the dark for periods over 100 h, while the control module without an edge seal reverts to its initial deactivated state over the same period.

The effect of the edge sealing is most apparent on the samples under full sun illumination. Fig. 3 shows the degradation of a matched pair of modules over 800 h. The red curve represents the edge sealed module with a linear degradation, while the purple curve represents the control module and appears to have an exponential decay. LBIC images are shown at the end of the curves as insets. These modules also display significant visual differences in polymer bleaching and electrode oxidation as they degrade, as seen in Fig. 4, a photo taken after soaking the modules for over 900 h. The left image shows the edge sealed sample is visually unchanged from when it was sealed. There is no bleaching or oxidation apparent. The right image shows significant bleaching of the polymer near the open edges of the control module and along the top cell. A substantial darkening of the printed silver due to oxidation is also present, in marked contrast to its

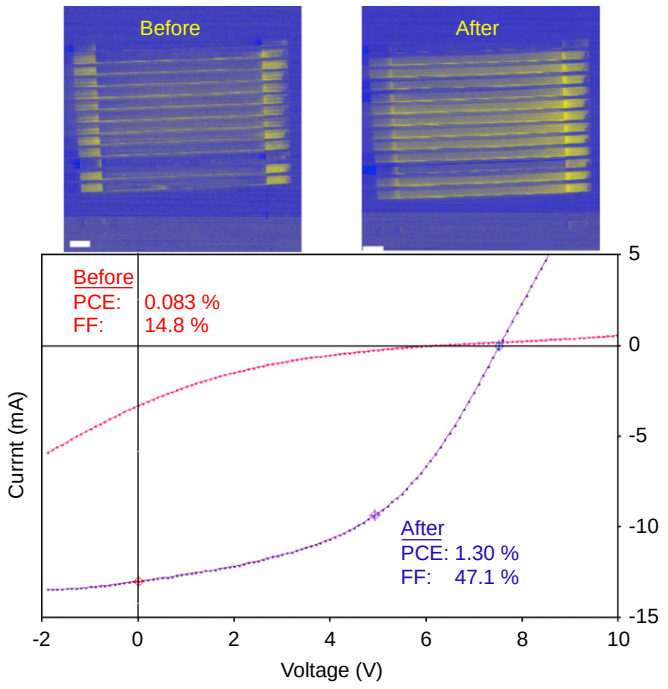

Fig. 2. LBIC (above) and IV characterization curves (below) for an edge sealed module before and after photo-annealing for 40 min under the metal hallide KHS Solar Constant 575, AM1.5G, 1000 W/m^2 to activate the ZnO nanoparticles. The active area is 35.5 cm^2.

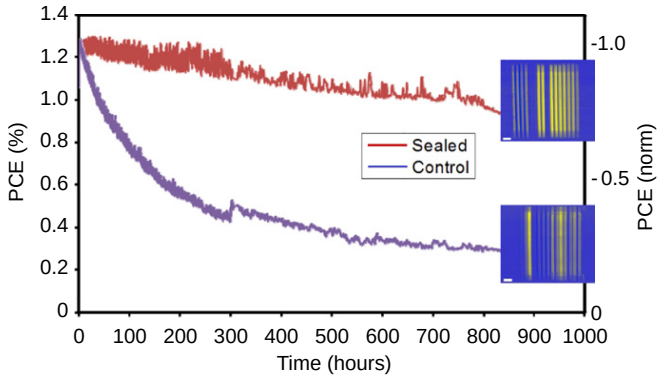

Fig. 3. Power conversion efficiency (*PCE*) over time for an edge sealed (red) and a control (purple) module soaking under a metal halide lamp (KHS Solar Constant 575, AM1.5G, 1000 W/m^2). LBIC images of the sample at the end of the soaking period are shown as insets in the plot. (For interpretation of the references to color in this figure legend, the reader is referred to the web version of this article.)

appearance prior to the soaking. Similar differences in photo-bleaching (albeit to a lesser degree) were seen in the sample pairs soaked under the halogen and fluourescent lamps, although no darkening of the silver was observed in those cases, where the temperatures are lower.

After soaking modules were imaged by both DLIT and LBIC. Fig. 5 shows the data for the modules under the full sun illumination after soaking for over 900 h. The DLIT in reverse bias largely highlights warm shunts in the devices and is not shown, as these shunts appear as a subset of the warm (red) features in the forward bias DLIT images as well. There are many additional warm regions in the forward bias DLIT. The DLIT measurement occurs in the dark with a square wave applied bias from 0–14 V at 10 Hz resulting in rectified AC currents of ~3 and ~4 mA, respectively in the edge sealed and control modules. These

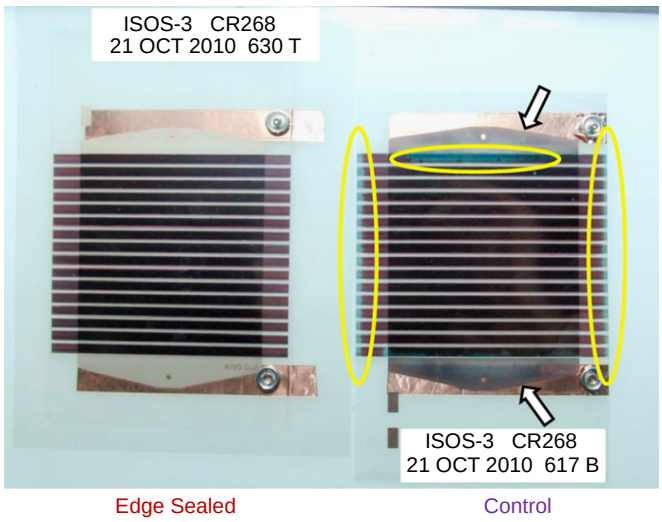

Fig. 4. Photographic images of the same samples measured in Fig. 3 after soaking over 900 h. The ellipses highlight the regions of the control sample where the polymer has been bleached, and the arrows indicate regions where the printed silver electrodes show substantial oxidation.

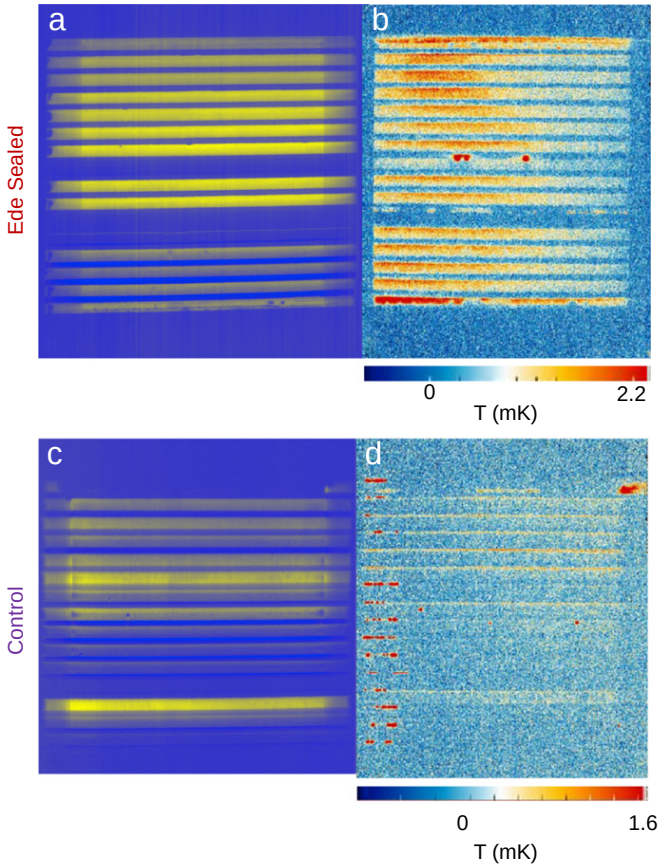

Fig. 5. LBIC (a,c) and DLIT (b,d) images of the same edge sealed samples (a,b) and control samples (c,d) measured in Fig. 3 after soaking over 900 h. It is clear that the LBIC shows a contribution from the active material beyond the printed electrodes, making the LBIC images appear wider than the DLIT images. Localized hot (red) spots in the DLIT represent shorts in the devices and quench the corresponding cells in the LBIC signal. (For interpretation of the references to color in this figure legend, the reader is referred to the web version of this article.)

currents are lower than the currents generated under full sun illumination at the maximum power point, but much larger than the currents induced in the LBIC measurements. In comparing the

DLIT images of the two modules in Fig. 5, it is clear that the edge sealed module has a largely uniform heat distribution across 14 of 16 cells in the module, while the control module is heated dominantly at point like shorts on 13 of 16 cells in the module.

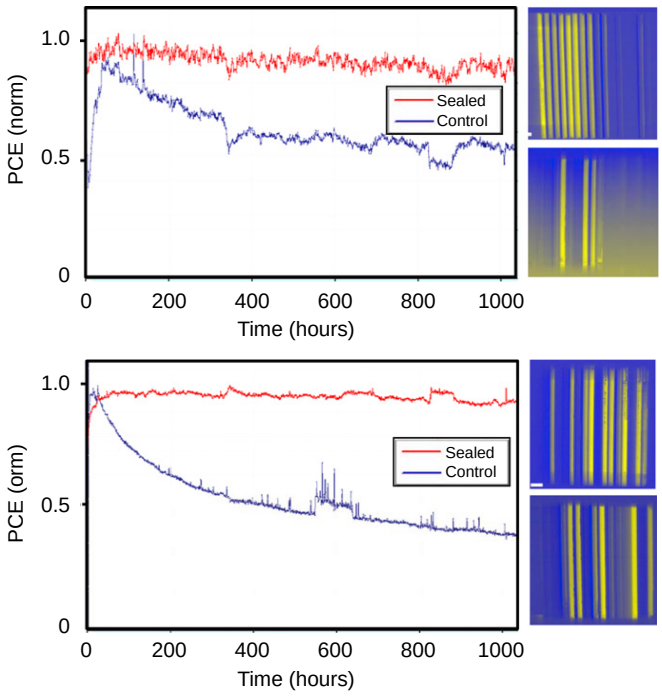

Fig. 6. Normalized *PCE* over time for edge sealed (red) and control (blue) samples under the halogen lamps (upper) and fluorescent lamps (lower), respectively. LBIC data after 1000 h of soaking is shown to the right. (For interpretation of the references to color in this figure legend, the reader is referred to the web version of this article.)

The LBIC data correlate with these images showing the most photocurrent generated in cells that have the most uniform heat distributions. In some cases specific defects can be seen in both the DLIT and LBIC images, but this is not always true and the two techniques complement each other well, characterizing mobile charge transport and mobile charge generation respectively.

Similar results are observed in the samples exposed to the lower intensity halogen and fluorescent lamps for over 1000 h as observed in Fig. 6. In these cases the edge sealed modules appear to show no significant degradation at all. Visual differences are also reduced, although the modules without the edge seal continue to display some polymer bleaching. In contrast the modules stored in the dark showed no significant degradation with or without the edge sealing over more than 3000 h.

In an effort to better understand the changes occurring during the degradation, we have repeated the full sun experiment with LBIC and DLIT imaging both *before* and *after* the degradation of the modules on a matched pair, which had been in dark storage (ambient environment) over 120 days without significant degradation. The modules were placed under a full sun simulator (KHS 1200 AM1.5G 1100 W/m^2) for ~330 h and characterized at 15 min intervals. The degradation in *PCE*, open circuit voltage, V_{oc}, the short circuit current, I_{sc}, and the fill factor, *FF*, were consistent with the initial longer term study and are shown normalized to highlight the changes observed in Fig. 7. Fig. 8 shows the module pair imaged by LBIC and DLIT both *before* and *after* soaking. We have also performed a full complement of experiments with modules fabricated with Plextronics PV2000 for the active layer. The composition of PV2000 is proprietary, but it has a higher V_{oc} (~0.7 V) than P3HT:PCBM blends and an NERL certified *PCE* approaching 6% [23]. In this case the bleaching and oxidation were similar, but while the edge sealed modules did demonstrate higher stability, they still showed some nonlinear degradation under full sun, and overall the effects were less pronounced, in part because the initial currents were very low before the degradation began.

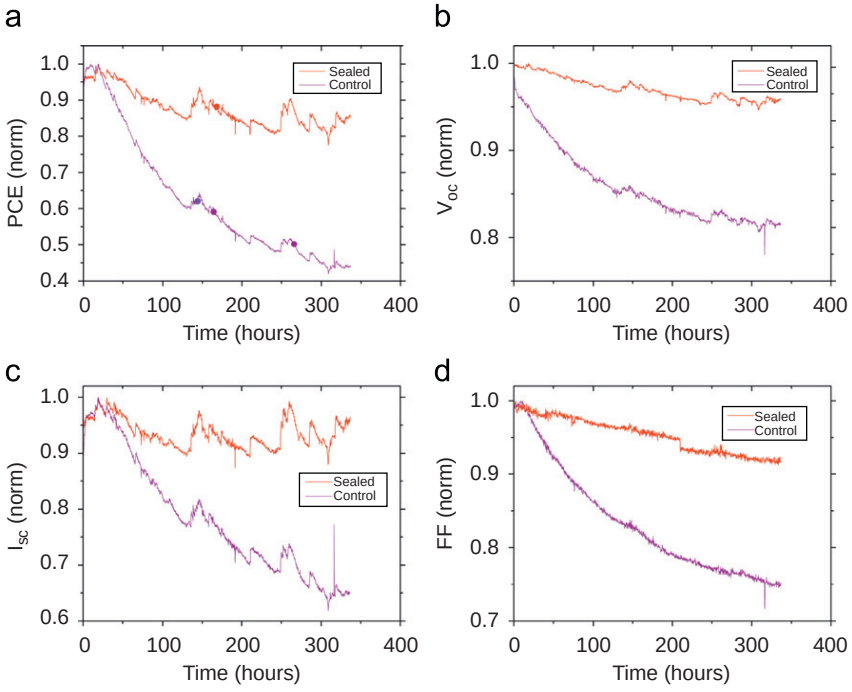

Fig. 7. Plots showing the set of key electrical characterization parameters, *PCE*, V_{oc}, I_{sc}, and *FF* over time for a second matched pair soaked for 330 h under a metal halide sun simulator (KHS 1200, AM1.5G, 1100 W/m^2). The edge sealed sample (red) shows a higher stability than the control sample (purple) for each parameter. Data are normalized to peak values to highlight the relative stability. (For interpretation of the references to color in this figure legend, the reader is referred to the web version of this article.)

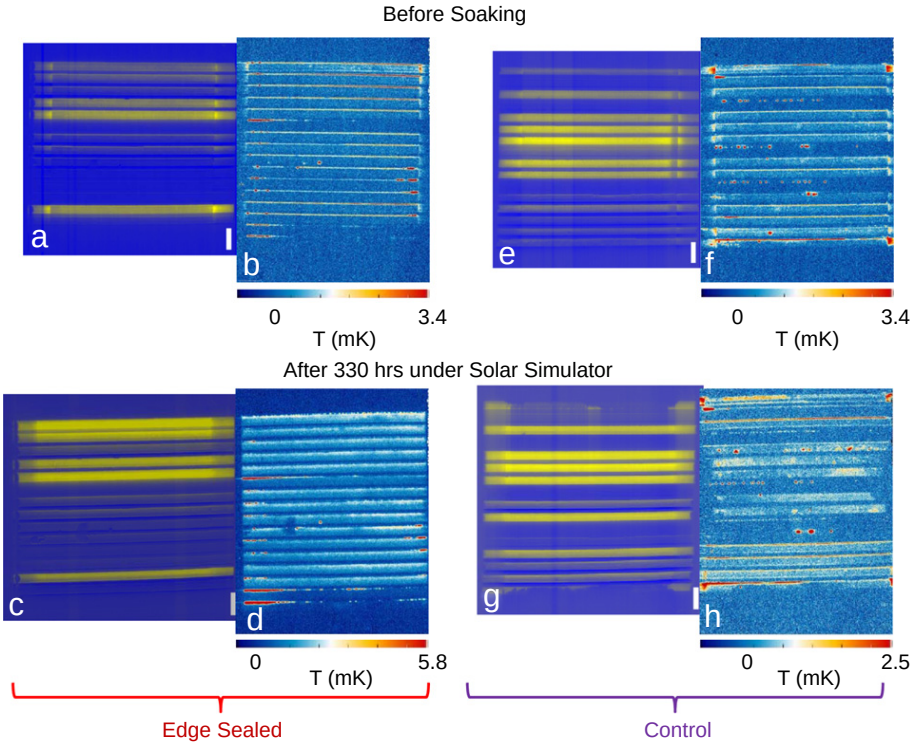

Fig. 8. DLIT and LBIC images of the same edge sealed (a–d) and control (e–h) samples measured in Fig. 7 both before (a,b,e,f) and after (c,d,g,h) soaking 330 h. As in Fig. 5, local hot (red) spots in the DLIT indicate probable shorts and correlate with weak LBIC signals. We can now observe temporal changes in the images as noted in the text. Note that in all images the color tables are optimized for a specific image and should not be compared between images. (For interpretation of the references to color in this figure legend, the reader is referred to the web version of this article.)

4. Discussion

While the dark storage shows no significant difference between the edge sealed and the control samples, Figs. 3, 6 and 7 demonstrate that edged sealed samples clearly degrade significantly less than control samples in use, independent of the source spectra. The relative degradation increases with the cell temperature during soaking presumably due to enhanced diffusion of atmospheric components through the modules. The typical degradation in *PCE* of the control samples shows an initial rise due to the activation of the ZnO nanoparticles as previously described [22] followed by a nonlinear decay. The exact mehcanisms of the degradation in OPV cells are complex and likely due to several competing phenomena including photo-oxidation, diffusion of molecular oxygen and water, degradation of interfaces, active materials, electrodes, and charge transport layers both from chemical and morphological changes [6,24]. In the case of inverted devices prepared by ProcessOne, Norrman, et al. identify changes in humidity and the hygroscopic nature of PEDOT:PSS on the phase separation of bulk PEDOT:PSS followed by oxidation at interfaces of the PEDOT:PSS as the dominant degradation mechanism [11]. After the initial 500 h of soaking, the degradation changes to a much more gradual linear decay in the *PCE*. The edge sealed modules in this study show a similar initial rise in *PCE* associated with the activation of the ZnO naonoparticles, but in dramatic contrast to the control samples, there is no nonlinear decay in the *PCE* over the first 500 h. Rather, the edge sealed modules display a slow linear decay, as seen in Figs. 3, 6 and 7a, which is consistent with the longer term decay seen in the control modules from 500 to 1000 h.

To further understand the nature of the degradation, one can look first at the key parameters extracted from the periodic characterization, which contribute to the final *PCE*. Fig. 7b–d shows the relative behavior of V_{oc}, I_{sc}, and *FF*, for the edge sealed (red) and the control (purple) modules shown in Fig. 8 over the intial 300 h of degradation. The trend is similar for the other module pairs in this study. It is clear that the relative decline in *PCE* of the control sample compared to the edge sealed sample is dominated by the decline in I_{sc}, but that there is also a contribution from the weaker decline in V_{oc}. In addition, we see a dramatic loss in the *FF* of the control module compared to the edge sealed sample, an indication that there is both a decrease in the shunt resistance and an increase in the series resistance in the modules.

The origins of these changes are a continuing area of study, but their spatial distribution in the modules can be examined by LBIC and DLIT imaging. There is a significant difference in complexity between individual cells and modules of 16 cells connected in series as in this study. Not only does the number of interfaces increases by a factor of 16, there is a mixing of series and shunt resistances, charging effects, and other complex phenomena. The LBIC and DLIT images clearly show that in many cases we are not getting equal contributions from the 16 cells in each module, nor is each cell itself homogenous. In high speed LBIC on modules without an applied bias voltage or flood illumination, the detailed mechanism for charge transport through dark cells is still under investigation. Similarly, the reverse bias DLIT of modules is complicated by the blocking of charge transport by cells in series. Despite these complexities, both the LBIC and forward bias DLIT of modules show clear and reproducible spatial maps that correlate with cell and module performance. The LBIC identifies regions of exciton creation and charge separation, while the DLIT identifies local heating associated with bias induced charge transport in the absence of illumination. In both imaging methods, the currents are significantly smaller than the currents generated under full sun illumination, and the measurements should not induce significant changes in the cells or modules. In both imaging techniques the ideal module would create largely

homogenous stripes for each of the 16 serial connected cells in the module. While our best modules have achieved this, many modules have some cells with imperfections including point defects, short circuits, layer misalignment, delamination, etc. Defects can be both localized within a cell or circumvent operation of an entire cell in the module.

Fig. 5 shows the dramatic difference of two modules soaked for 900 h in the solar simulator (same modules reported in Figs. 3 and 4) that were initially selected for their similar performance. In comparing the images, one should note that the signals from the edge sealed module are greater than for the control module but that color tables are optimized individually for each image. In the LBIC and DLIT measurements the driving stimulus (photon flux and applied forward bias) is the same for both modules. From the IV measurements we know that the drop in *PCE* of the control sample is dominated by the decrease in *FF* and I_{sc}. The most striking difference in the imaging data is localization of many hot spots along the left side in the DLIT image of the control sample, which are characteristic of shorts, which enable recombination and reducing the shunt resistance and current.

In an effort to understand the temporal changes in the images, we repeated the measurements with imaging both before and after soaking. The edge sealed module shows a relative improvement in the top two cells in the LBIC image (Figs. 8a and c) after soaking. The DLIT of the same sample (Figs. 8b and d) shows a corresponding loss of localized hot spots in the upper left edge of these same cells, suggesting that some shorts have been burned out over the 330 h of soaking. The LBIC images of the control sample (Figs. 8e and g) show that after 330 h of soaking there is a decline in the performance of the 8th cell and an improvement in the performance of the 4th cell as counted from the bottom of the images. Careful examination of the DLIT images of the control module in Fig. 8 shows an apparent decrease in the heat generated near the edges of the module after soaking. This suggests that the degradation is faster near the open edges as might be expected if atmospheric components are entering form the unsealed edges and slowly diffusing into the body of the module. However, this pattern is not consistently observed in all the control samples, suggesting that the rate of diffusion along the layer interfaces in some cases is faster than the rate of ingress from the edges.

The application of LBIC and DLIT imaging in this study makes it clear that these modules have many initial manufacturing defects prior to the soaking studies. It should be noted that these modules were manufactured as part of the ISOS-3 demonstration workshops where most of the workers were experiencing the processing techniques for the first time. The best modules from the workshops were used in other studies or given to the participants, and the modules in this study represent working devices, but not the optimal modules achievable from the process. The effect of the soaking on the LBIC and DLIT images (Fig. 8), demonstrates that the situation is complex, with some cells in the modules improving and others decaying within the same 16 cell module. Both techniques help us understand the spatial characteristics of the degradation process and reveal the high complexity of the range of processes underlying the changes observed in the IV characterization of the 16 cell modules represented by Figs. 3, 6 and 7.

The improved stability of the edge sealed samples in this study is consistent with previous encapsulation studies with full glass encapsulation, glass/adhesive/glass, or glass/adhesive/metal plate and other encapsulation schemes [13,14,25–30]. The focus in our work is on cost effective encapsulation for large scale production of solar cell modules. The double lamination edge seal process applied here was performed manually on samples, but industrial roll-to-roll equipment with a kiss cut to define the 1 cm wide edge seal around the modules *in situ* on the web prior to the second lamination step is common in the manufacturing sector, and makes this process economically viable for large scale production. This was the simplest edge seal technique and it significantly improves in module stability. A cold lamination adhesive formulated to have low permeability could enhance the process without additional processing complexity and cost.

5. Conclusion

We have observed significant improvements in the stability of flexible OPV modules consisting of 16 serial cells with a total active area of 35.5 cm^2 produced in an entirely roll-to-roll compatible and economically viable manufacturing technique. The application of a roll-to-roll compatible second level of lamination with a 1 cm wide edge seal is compared to control devices with exposed cut edges. This simple edge seal eliminates the initial phase of nonlinear degradation seen in all the key parameters extracted from the current voltage curves. Modules were studied for 1000 h and imaged by both high speed LBIC and DLIT to further understand the failure modes in these complex devices.

Acknowledgments

The authors acknowledge the support of Jan Alstrup in the fabrication of the modules during the ISOS-3 workshops, Suren Gevorgyan and Roar Søndergaard for useful conversations and initial sorting of modules created at the workshops, as well as all the workshop participants. DMT is grateful for the funding provided through the American Scandinavian Foundation. This work has been supported by the Danish Strategic Research Council (2104-07-0022) and EUDP (j. no. 64009-0050). Partial financial support was also received from the European Commission as part of the Framework 7 ICT 2009 collaborative project HIFLEX (Grant no. 248678). from the EU–Indian framework of the "Largecells" project that received funding from the European Commission's Seventh Framework Programme (FP7/2007–2013. Grant no. 261936) and from PV-ERA-NET (project acronym POLYSTAR). RR and HH are grateful for the financial support from the Thuringian Ministry of Culture and the German Federal Ministry of Education and Research in the Frameworks of FIPV II and PPP (Contract no. 13N9843), respectively.

References

[1] B.C. Thompson, J.M.J. Fréchet, Polymer–fullerene composite solar cells, Angewandte Chemie International Edition 47 (2008) 58–77.
[2] Jana Rothe, Moritz Riede, Karl Leo, Heliatek and IAPP achieve production-relevant efficiency record for organic photovoltaic cells, Retrieved 6/20, 2011, Accessed from 〈http://www.heliatek.com/uploads/19-en.pdf〉.
[3] Tracy Wemett, Konarka's Power Plastic Achieves World Record 8.3% Efficiency Certification from National Energy Renewable Laboratory (NREL), Retrieved 6/20, 2011, accessed from 〈http://www.konarka.com/index.php/site/pressreleasedetail/konarkas_power_plastic_achieves_world_record_83_efficiency_certification_fr〉.
[4] F.C. Krebs, Fabrication and processing of polymer solar cells: a review of printing and coating techniques, Solar Energy Materials and Solar Cells 93 (2009) 394–412.
[5] F.C. Krebs, T. Tromholt, M. Jørgensen, Upscaling of polymer solar cell fabrication using full roll-to-roll processing, Nanoscale 2 (2010) 873–886.
[6] M. Jørgensen, K. Norrman, F.C. Krebs, Stability/degradation of polymer solar cells, Solar Energy Materials and Solar Cells 92 (2008) 686–714.
[7] F.C. Krebs, S.A. Gevorgyan, J. Alstrup, A roll-to-roll process to flexible polymer solar cells: model studies, manufacture and operational stability studies, Journal of Materials Chemistry 19 (2009) 5442–5451.
[8] S.A. Gevorgyan, A.J. Medford, E. Bundgaard, S.B. Sapkota, H.F. Schleiermacher, B. Zimmermann, et al., An inter-laboratory stability study of roll-to-roll coated flexible polymer solar modules, Solar Energy Materials and Solar Cells (2011) 1398–1416.

[9] S.A. Gevorgyan, M. Jorgensen, F.C. Krebs, K.O. Sylvester-Hvid, A compact multi-chamber setup for degradation and lifetime studies of organic solar cells, Solar Energy Materials and Solar Cells (2011) 1389–1397.
[10] M.O. Reese, S.A. Gevorgyan, M. Jørgensen, E. Bundgaard, S.R. Kurtz, D.S. Ginley, et al., Consensus stability testing protocols for organic photovoltaic materials and devices, Solar Energy Materials and Solar Cells (2011) 1253–1267.
[11] K. Norrman, M.V. Madsen, S.A. Gevorgyan, F.C. Krebs, Degradation patterns in water and oxygen of an inverted polymer solar cell, Journal of the American Chemical Society 132 (2010) 16883–16892.
[12] M. Manceau, M. Helgesen, F.C. Krebs, Thermo-cleavable polymers: Materials with enhanced photochemical stability, Polymer Degradation and Stability (2010) 2666–2669.
[13] F.C. Krebs, Encapsulation of polymer photovoltaic prototypes, Solar Energy Materials and Solar Cells 90 (2006) 3633–3643.
[14] M.O. Reese, A.J. Morfa, M.S. White, N. Kopidakis, S.E. Shaheen, G. Rumbles, et al., Pathways for the degradation of organic photovoltaic P3HT: PCBM based devices, Solar Energy Materials and Solar Cells 92 (2008) 746–752.
[15] M. Lira-Cantu, K. Norrman, J.W. Andreasen, N. Casan-Pastor, F.C. Krebs, Detrimental effect of inert atmospheres on hybrid solar cells based on semiconductor oxides, Journal of the Electrochemical Society 154 (2007) B508–B513.
[16] T. Jeranko, H. Tributsch, N. Sariciftci, J. Hummelen, Patterns of efficiency and degradation of composite polymer solar cells, Solar Energy Materials and Solar Cells 83 (2004) 247–262.
[17] F.C. Krebs, R. Sondergaard, M. Jorgensen, Printed metal back electrodes for R2R fabricated polymer solar cells studied using the LBIC technique, Solar Energy Materials and Solar Cells (2010) 1348–1353.
[18] J. Bachmann, C. Buerhop-Lutz, C. Deibel, I. Riedel, H. Hoppe, C.J. Brabec, et al., Organic solar cells characterized by dark lock-in thermography, Solar Energy Materials and Solar Cells 94 (2010) 642–647.
[19] H. Hoppe, J. Bachmann, B. Muhsin, K.H. Drue, I. Riedel, G. Gobsch, et al., Quality control of polymer solar modules by lock-in thermography, Journal of Applied Physics 107 (2010) 014505-014505-4.
[20] F.C. Krebs, Polymer solar cell modules prepared using roll-to-roll methods: knife-over-edge coating, slot-die coating and screen printing, Solar Energy Materials and Solar Cells 93 (2009) 465–475.
[21] F.C. Krebs, M. Jørgensen, K. Norrman, O. Hagemann, J. Alstrup, T.D. Nielsen, et al., A complete process for production of flexible large area polymer solar cells entirely using screen printing—first public demonstration, Solar Energy Materials and Solar Cells 93 (2009) 422–441.
[22] M.R. Lilliedal, A.J. Medford, M.V. Madsen, K. Norrman, F.C. Krebs, The effect of post-processing treatments on inflection points in current-voltage curves of roll-to-roll processed polymer photovoltaics, Solar Energy Materials and Solar Cells 94 (2010) 2018–2031.
[23] C.J. Brabec, S. Gowrisanker, J.J.M. Halls, D. Laird, S. Jia, S.P. Williams, Polymer–fullerene bulkheterojunction solar cells, Advanced Materials 22 (2010) 3839–3856.
[24] K. Norrman, S.A. Gevorgyan, F.C. Krebs, Water-induced degradation of polymer solar cells studied by H218O labeling, ACS Applied Materials & Interfaces 1 (2008) 102–112.
[25] C. Lungenschmied, G. Dennler, H. Neugebauer, S.N. Sariciftci, M. Glatthaar, T. Meyer, et al., Flexible, long-lived, large-area, organic solar cells, Solar Energy Materials and Solar Cells 91 (2007) 379–384.
[26] G. Dennler, C. Lungenschmied, H. Neugebauer, N. Sariciftci, M. Latreche, G. Czeremuszkin, et al., A new encapsulation solution for flexible organic solar cells, Thin Solid Films 511 (2006) 349–353.
[27] J. Meiss, M. Hermenau, W. Tress, C. Schuenemann, F. Selzer, M. Hummert, et al., Tetrapropyl-tetraphenyl-diindenoperylene derivative as a green absorber for high-voltage stable organic solar cells, Physical Review B 83 (2011) 165305.
[28] S. Cros, S. Guillerez, R. de Bettignies, N. Lemaître, S. Bailly, P. Maisse, Relationship between encapsulation barrier performance and organic solar cell lifetime, Proc. SPIE 7048 (2008) 70480U, doi:10.1117/12.794986.
[29] S. Cros, R. de Bettignies, S. Berson, S. Bailly, P. Maisse, N. Lemaitre, et al., Definition of encapsulation barrier requirements: A method applied to organic solar cells, Solar Energy Materials and Solar Cells (2011) S65–S69.
[30] B. Zimmermann, H.F. Schleiermacher, M. Niggemann, U. Würfel, ITO-free flexible inverted organic solar cell modules with high fill factor prepared by slot die coating, Solar Energy Materials and Solar Cells 95 (2011) 1587–1589.

Morphological study of low band gap polymer:PCBM nanoparticles for organic photovoltaics (OPVs)

Henrik F. Dam[a], Natalie P. Holmes[b], Thomas R. Andersen[a], Thue T. Larsen-Olsen[a], Frederik C. Krebs[a], Paul Dastoor[b]*

Abstract

Nano scale particles consisting of polymer and acceptor material were investigated using scanning transmission x-ray microscopy (STXM) and transmission electron microscopy (TEM) with the purpose of identifying the inner structure of the nanoparticles and their shape and agglomeration. The low bandgap polymer PSBTBT (poly[4,8-bis(2-ethylhexyloxy)benzo(1,2-b:4,5-b′)dithiophene-alt-5,6-bis(octyloxy)-4,7-di(thiophen-2-yl)(2,1,3-benzothiadiazole)-5,5′-diyl]) is investigated and compared to the commonly used P3HT (poly[3-hexylthiophene-2,5-diyl]) polymer. A core-shell morphology was found from STXM data for nanoparticles consisting of PSBTBT polymer and PCBM similar to what has been reported for P3HT:PCBM nanoparticles, however with a difference in the shape of the nanostructures. Devices produced from the same materials have shown, for nanoparticle based polymer solar cells, a high efficiency of 1.29%.

[a] *Department of Energy Conversion and Storage, Technical University of Denmark, Frederiksborgvej 399, DK-4000 Roskilde, Denmark.*
[b] *Department of Physics, Newcastle University Australia, University Drive, 2308 Callaghan, Australia.*

Solar Energy Materials & Solar Cells ∎ (∎∎∎∎) ∎∎∎–∎∎∎

Contents lists available at SciVerse ScienceDirect

Solar Energy Materials & Solar Cells

journal homepage: www.elsevier.com/locate/solmat

A rational method for developing and testing stable flexible indium- and vacuum-free multilayer tandem polymer solar cells comprising up to twelve roll processed layers

Thomas R. Andersen, Henrik F. Dam, Birgitta Andreasen, Markus Hösel, Morten V. Madsen, Suren A. Gevorgyan, Roar R. Søndergaard, Mikkel Jørgensen, Frederik C. Krebs *

Department of Energy Conversion and Storage, Technical University of Denmark, Frederiksborgvej 399, DK-4000 Roskilde, Denmark

ARTICLE INFO

Keywords:
Tandem polymer solar cells
ITO free
Vacuum free
Flexible
Roll printed
Stability

ABSTRACT

We demonstrate a method for the preparation of multijunction polymer solar cells without the use of vacuum evaporation methods or indium tin oxide (ITO). The entire layer stack is prepared by printing or coating of each layer. The number of layers typically employed in complete devices exceeds ten and to efficiently identify layers and interfaces that are not robust we developed a double sided illumination method and demonstrate how layer thicknesses can be optimized with respect to the roll processing in the aim of achieving functional tandem devices. The devices were prepared directly on barrier foil and were later encapsulated. In this study the same active material comprising poly-3-hexylthiophene (P3HT) and phenyl-C_{61}-butyric acid methyl ester ([60]PCBM) was employed using nanoparticle based zinc oxide for electron selectivity and several different PEDOT:PSS formulations for hole selectivity, electrode- and recombination layer formation. A novel slanted comb silver grid electrode structure was employed to enable efficient double sided illumination and minimize shunts. The operational stability of the tandem devices evaluated under ISOS-D-2 conditions demonstrated less variation in stability between devices than similar single junctions prepared in the same manner for reference. We demonstrate lifetime studies for 480 h without any sign of degradation and estimate that the tandem or multijunction polymer solar cells are as stable as single junctions.

1. Introduction

The polymer tandem solar cell has been reviewed several times [1,2] and until now it has mostly been reported with a very small active area on rigid glass substrates using indium tin oxide (ITO) as the semitransparent front electrode and vacuum evaporated back metal back electrodes. In many cases the recombination layer has also been vacuum processed and thus only the two active layers have been solution processed. In some cases the recombination layer has been solution processed [1,2] but in the majority of cases most processing has been carried out in a glovebox and using vacuum deposition for many of the layers. The polymer tandem solar cell prepared without the use of semitransparent indium–tin-oxide electrodes and vacuum steps using only ambient conditions for roll-to-roll printing and coating on flexible substrates undoubtedly represents the ultimate challenge and the pinnacle of complexity within the field of printed and organic electronics [3]. It is also likely that all these requirements will be necessary before tandem polymer solar cells can become useful outside academic reports. The motivation for preparing the polymer tandem solar cell is clearly the desire to reach the highest achievable performance and the tandem approach or multi-junction approach to photovoltaics in general is the undisputed route to the highest performance in terms of power conversion efficiency. The tandem solar cell also presents the drawback of being more complicated with a significantly larger room for error and the effort is only justified provided that the process is robust and the extra effort required for its making is returned as a higher efficiency at lower process intensity and a lower embodied energy. The increased complexity is quite possibly also the reason why tandem polymer solar cells initially did not attract so much attention as compared to single junctions as shown in Fig. 1 where it is clear that the number of tandem solar cell publications did not increase significantly beyond 10 articles per year until 2010 [3]. In spite of this much lower number of publications by two orders of magnitude the tandem solar cell is rapidly approaching the best reported single junctions.

Printing and coating of polymer solar cells [4] has already been demonstrated to be a fast and viable approach to the manufacture of polymer solar cells while there has been a significant gap

* Corresponding author. Tel.: +45 46 77 47 99.
E-mail address: frkr@dtu.dk (F.C. Krebs).

0927-0248/$ - see front matter © 2013 Elsevier B.V. All rights reserved.
http://dx.doi.org/10.1016/j.solmat.2013.07.006

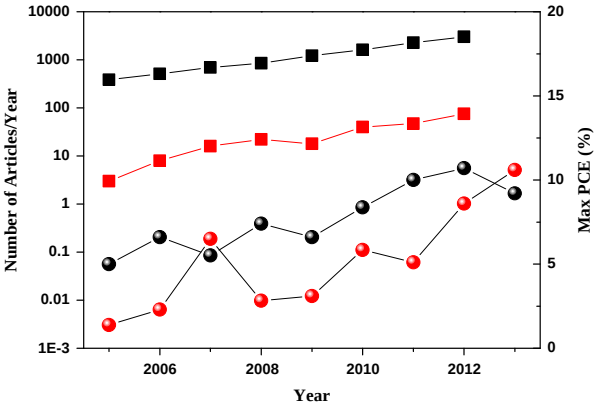

Fig. 1. The number of scientific reports on OPV as a function of time (black squares, left *y*-axis) as compared to the number of tandem solar cell reports (red squares, left *y*-axis) shown on a logarithmic scale. The maximum reported PCE (%) for each year for single junction cells (black spheres) and tandem cells (red spheres). (For interpretation of the references to color in this figure legend, the reader is referred to the web version of this article.)

between the reported record efficiencies for small laboratory cells and the well corroborated performance of large area polymer solar cell modules. In addition to this, early printed polymer solar cells still employed indium–tin-oxide as the semitransparent front electrode while several life cycle analysis studies showed that an alternative to indium based electrodes is mandatory for rational use of polymer solar cells including tandem polymer solar cells [5–8]. It was also established that vacuum processing steps require very high polymer solar cell performance to be justified and that printed or coated (vacuum free) polymer solar cells can reach much shorter energy payback times even with a lower performance [9]. While the justification for avoiding both vacuum and indium is compelling it has taken an enormous effort to find convincing alternatives due to the enormous complexity of printing and coating thin 2-dimensionally patterned multilayer films. Traditional processing has limited the number of wet coating steps and has employed vacuum processing wherever possible and this has elegantly avoided the unforgiving challenge of interfacing many thin layers without shunting. Recently a very efficient low cost flexible semitransparent electrode was developed which is in fact so cheap to process that it is freely available to academics [10]. This electrode and processing philosophy serves as the foundation in this work and is explored for processing of tandem polymer solar cells. The largest challenge for the tandem solar cell is how the thicknesses of the individual layers critically influence the overall device performance and imposes firm requirements on the processing conditions as subsequently processed layers must not adversely affect or change previously processed layers. This can to a certain extent be solved through vacuum processing of some layers such as the electrodes and oxide layers. The industrially relevant processes are however expected to employ only printing and coating which does represent a very challenging task and the successful development of functional tandem devices following that approach does require a novel protocol that enables fine tuning of the individual junctions and the interlayers such that a functional device is guaranteed during development even if the given device does not represent the optimal choice. There are two points that must be rationally addressed to achieve this, the first point is that one must be able to address the individual junctions optically such that their individual performance can be established and optimized and the second point is the optimization of the processing conditions for the secondly processed junction such that the performance of the first junction is not adversely affected.

We have in the past successfully prepared tandem solar cells through use of thermocleavable materials [11] whereby the active layers and the interlayers are insolubilized after processing thus enabling solution processing of subsequent layers without affecting underlying layers. The performance was however relatively poor for this approach and required temperature stable glass substrates. In a second embodiment full roll-to-roll processing was employed in all layers on flexible ITO substrates by use of water based emulsions for the back junction [12]. The performance was also found to be poor in this case even though the devices had a large active area.

In this work we present our approach to optimize fully printed and coated flexible tandem polymer solar cells and we successfully demonstrate how this method allows for establishing the process windows for new materials combinations in multilayer tandem polymer solar cells. The use of organic solvent based inks was deemed necessary and an optimization of the intermediate layer towards a higher degree of solvent resistance was achieved. For testing of the device performance, and in particular the efficiency of the intermediate layers, a specialized illumination geometry was developed where the device is illuminated from both sides thus enabling controlling the incident light intensity on each junction.

2. Experimental

Solar cells were manufactured on a barrier material substrate (Amcor) with a silver grid/conductive PEDOT:PSS/ZnO electrode. This ITO-free semitransparent electron accepting front electrode known as Flextrode has been previously described [10] and can be obtained freely at www.plasticphotovoltaics.org. Cells were prepared directly on the Flextrode and consisted of a fully slot-die coated layer stack. The final metal back electrode was printed using the flexo technique. The machinery employed has been described [13,14]. ZnO was employed as an electron transport layer, P3HT:PCBM as the active layer, the intermediate recombination layer with a compatibilizing layer comprising PEDOT:PSS and ZnO.

2.1. Materials

Poly-3-hexylthiphene (P3HT from Plextronics) had a M_n of 40.000 Da. Phenyl-C_{61}-butyric acid methyl ester ([60]PCBM, from Solenne) had a purity of 99%. The P3HT:[60]PCBM ink used was 20:20 mg mL^{-1} ink dissolved in chlorobenzene with 10% chloroform and 3% chloronaphtalene, for 100 nm thick active layer a 10:10 mg mL^{-1} solution was used for coating. Electron transport layers (ETL) were coated using a stabilized ZnO nanoparticle solution in acetone (49 mg/mL). Several hole transport layers (HTL) were employed in the process of optimizing the method. V_2O_5 was employed where stated as a HTL and compatibilizer layer between the first active layer and the poly(3,4-ethylenedioxythiophene):poly(styrenesulfonate) (PEDOT:PSS) layer and comprised of a vanadium(V)oxiiso-propoxide:isopropanol (IPA) (1:100; 1:1000; 1:2000) solution. Several PEDOT:PSS HTL formulations were used; Clevious P VP Al 4083 or Clevios F-010. In the case of AL 4083 PEDOT:PSS it was mixed in a ratio of 1:2 with IPA and 2% ethyl glycol. PEDOT:PSS (Clevios F-010) was diluted 7:3 with IPA to enhance wetting properties. A MoO_x precursor solution in isopropanol was employed as a second HTL and/or compatibilizer where stated from a neutralized IPA solution. The printable silver back electrode used was PV410 from Dupont. The substrate used was Flextrode with a honeycomb (as described in Ref. [10]) or line silver pattern as developed in this work (see Fig. 2). The cells were encapsulated between two 18 × 18 mm^2 glass slides with

Please cite this article as: T.R. Andersen, et al., A rational method for developing and testing stable flexible indium- and vacuum-free multilayer tandem polymer solar cells..., Solar Energy Materials and Solar Cells (2013), http://dx.doi.org/10.1016/j.solmat.2013.07.006

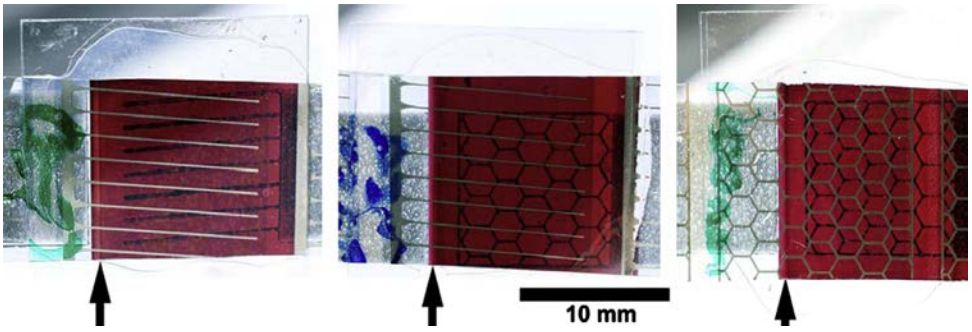

Fig. 2. Photographs of encapsulated tandem solar cells with our slanted grid design. In this left case each finger from front (light lines) and back-electrode (dark lines) has only one direct overlap. In the middle photograph the slanted front electrode has multiple overlaps with the printed honeycomb back electrode. The right photograph displays a tandem cell comprising two honeycomb electrodes. The arrows indicate the edge from the active layer of each subcell.

a UV curable epoxy resin (DELO LP655) adhesive and cured for 2 min under the solar simulator (1000 W m^{-2}, AM1.5G).

2.2. Printing and coating

The silver grids (bottom and top layers) were printed using flexographic printing whereas the remaining 9 layers all were fabricated by slot-die coating on lab scale roll-coater [13]. Flextrode comprising a large scale roll-to-roll processed silver grid, PEDOT:PSS (Heraeus Clevious PH1000) and ZnO on barrier material was used as substrate in all the experiments. The parameters presented are used as standard parameters with variations for the optimization of the individual layers. The first coated active layer had a thickness of 450–500 nm with a width of 13 mm and was coated with a web-speed of 1 m min^{-1} at 60 °C. The intermediate layer was coated in 3 steps; V_2O_5-layers were coated with a web speed of 2 m min^{-1} at 30 °C and a wet-thickness of 11.5 μm, the HTL PEDOT:PSS coating had a wet-thickness of 31 μm with a web speed of 1 m min^{-1} at 60 °C, and the last layer in the intermediate layer, ZnO, was coated at 60 °C with a web speed of 2 m min^{-1} and a wet-thickness of 7.7 μm. To minimize the risk of solvent penetration through the intermediate layer the second active layer was coated at 80 °C for faster evaporation. The thickness of this layer was approximately 200 nm coated with a web speed of 1 m min^{-1}. The top electrode also consisted of 3 layers; a MoO_x HTL coated with a web speed of 2 m min^{-1} at 70 °C and a wet thickness of 5 μm. On top of the MoO_x, a conducting F010 PEDOT:PSS from a 7:3 solution with IPA was employed, coated with a web speed of 1 m min^{-1} at 70 °C and a wet thickness 23 μm. The top silver grid was printed as previously reported [14]. In this study two versions of the Flextrode design was used. The already reported honeycomb pattern was used in the initial cells and as a reference, while we focused on the improved Flextrode with slanted grid lines (+5°) reported here. In combination with a slanted back electrode comb structure (−5°) we achieve maximum two direct overlaps (worst case) from each front and back electrode finger that minimizes the chance of silver–silver shorts. Since both sides of the solar cell present the same slanted comb structure and the same shadow loss this is optimal for double sided illumination and comparison of the two individual junctions. The design is also independent from the web-directional registration. Photographs of fully printed and coated tandem cells are shown in Fig. 2

2.3. External quantum efficiency

Quantum efficiency (QE) measurements of the tandem devices were performed. The approach of QE measurements for tandem devices is significantly more complex than that for the single junction devices. Tandem devices require measuring each subcell individually within the device and therefore, the process includes a set of additional steps (see e.g. Gilot et al. [15] or ASTM standard E2236-10 [16]). In particular, in order to measure the QE of one subcell in a multijunction device one has to saturate all the other subcells not being measured, which is done via a bias light. To do so, a light with spectrum in the absorption range of the subcells not being measured is used to bias these assuring that the tested sample is the one limiting the current within the multijunction. Additionally, a bias voltage is applied to the tandem device equal to the sum of V_{oc}'s of the subcells not being measured to cancel out the potential of all the junctions not being measured. This assures that the tested sample is at a state of short circuit when QE is measured. In our studies however the QE testing was significantly simplified by the property of double side illumination. Since only double junction devices were in question, it was possible to saturate the bottom subcell by illuminating it from the bottom using simple white light. Most of the light would be absorbed by the bottom subcell due to the thick film assuring that the top cell is the limiting one. This was proved by absorption measurements, which showed that most of the light was absorbed by the first subcell facing the illumination and thus, the second subcell limited the current. The QE was measured using an IPCE setup, which was calibrated with a photodiode with a calibration against NIST standard 1755. The tandem device was placed in the IPCE system such that the bottom subcell faced the bias light and the top subcell faced the testing monochromatic beam. Bias voltage was applied to the sample with the magnitude equal to the V_{oc} of the subcell not being measured. After measuring the QE of the front junction, the sample was flipped and the back junction was measured in the same fashion.

2.4. Stability measurements

To study the stability, the devices were encapsulated using a glass and a UV curable adhesive. ISOS-D-2 testing procedure [17] was used to make a quick assessment of the stability of the completed devices. For that purpose the samples were placed in the dark in an oven with temperature set to 65 °C and low relative humidity level. During the storage the solar cells were periodically (once every few days) removed from the oven and tested for photovoltaic performance using a class A solar simulator.

2.5. Bending test

A bending test was completed on flexible tandem cells encapsulated with Amcor barrier foil. The test was carried out to establish the resilience of the tandem devices towards bending. The test was completed on a Mecmesin Multitest 2.5-i tensile and

Please cite this article as: T.R. Andersen, et al., A rational method for developing and testing stable flexible indium- and vacuum-free multilayer tandem polymer solar cells..., Solar Energy Materials and Solar Cells (2013), http://dx.doi.org/10.1016/j.solmat.2013.07.006

compressive test bench, which was set in compression mode for 0, 1, 10, 100, 1000 times. The resulting bending radius was 10 ± 2 mm.

3. Results and discussion

3.1. Solvent resistance tests for the intermediate layer

One of the first obstacles of using printed electrodes is the inherent roughness of many of the coating methods. In the Flextrode substrate the general surface roughness is low, however distinct spikes are present in the flexographically printed silver grid in the range of 300–600 nm after printing of both PEDOT:PSS PH1000 and ZnO as seen in Fig. 3A. Fig. 3B displays a thin (200–250 nm) first coated active layer with the intermediate layer on top. A solubility test with chloroform on top of the intermediate layer selectively dissolves the active layer around the silver grid lines in the Flextrode. This led to a necessity for thick active layers to avoid dissolution and shunting of the first coated cell and intermediate layer in the tandem cell.

Since thick layers are necessary from a processing standpoint, tandem solar cells fabricated this way suffers from poor performance. This is the case since one active layer absorbs the main fraction of light, as seen in Fig. 4. This issue must of course be solved for tandem solar cells to be functional in a reasonable way.

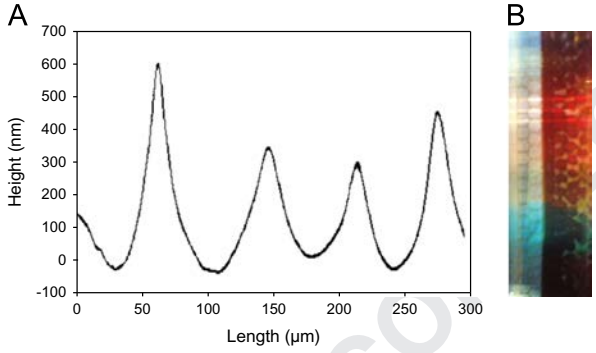

Fig. 3. (A) Height profile of the edge of a silver stripe on the Flextrode measured by a Dektak Profilometer. The height profile shows that four silver spikes are present within a scan-length of 300 μm, varying from around 300 to 600 nm in height. (B) The first coated active layer (thin 200–250 nm) dissolved around the silver grid when depositing chloroform on top of the intermediate layer.

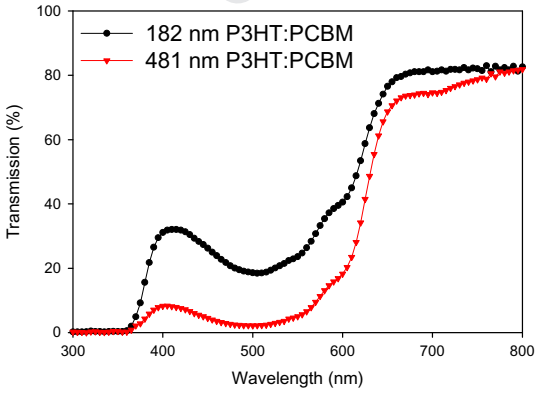

Fig. 4. Transmission through a P3HT:PCBM layer printed on Flextrode directly printed on barrier foil. The absorption of the P3HT film shows that less than 40% of the incoming light remains after a 182 nm layer while less than 10% is left after passage through a 481 nm layer (when integrating the transmission from 350–800 nm). This confirms the almost complete optical separation of the two subcells when using the same polymer in both layers.

Further, for tandem solar cells it is critically important that the materials absorb different parts of the spectrum since otherwise the tandem cell would not be an improvement over a standard cell. However before tandem solar cells can be developed to fulfill all operational requirements, useful information can be extracted from thick layered tandem cells during the development phase, especially when the aim is to be able to process functional multilayer stacks.

3.2. The double sided illumination method

The preparation of homo tandem cells with the same active layer material in both sub cells is the most rational way of testing losses incurred by intermediate layers and poor transport in the tandem cell. In order to do tests on these types of tandem solar cells illumination from both sides was found to be very useful and enabling the identification of failure in each discrete sub cell. This is of course only possible when both electrodes are somewhat transparent or ideally equally transparent.

For this study a mirror setup was constructed which allows double sided illumination under a standard solar simulator. The setup consists of two mirrors mounted 45 degrees to normal. When the cell is placed between the mirrors, light reflects from each mirror ensuring equal illumination from both sides.

3.3. Oxide based recombination layers

From previous publications reporting partially solution processed tandem devices, a stack as shown in Fig. 5 was used with the intermediate layer consisting of a vanadium-oxide layer and ZnO [18] or PEDOT:PSS 4083 and (Al)ZnO [19]. Firstly an intermediate layer comprising vanadium oxide and ZnO was attempted with limited success. Improvements, in single junction cells, have been shown by the use of molybdenum-oxide as a hole selective material [20] and has therefore been used as an alternative to vanadium-oxide. Trials with molybdenum-oxide was carried out with similar results and the main issue being cracks in the intermediate layer (shown in Fig. 6) leading to mixing of the first and second coated active layers. This resulted in poorly performing single junction cells following a device geometry as outlined in Fig. 7.

The same structure as presented in [19] was tried but dewetting occurred when attempting to slot-die coat the 4083 PEDOT:PSS layer on top the active layer, therefore the V_2O_5-layer was coated as a compatibilizer, which has been shown to work in the tandem stack by [18]. Using a PEDOT:PSS 4083 layer in the intermediate stack solved the issue seen with cracks forming as shown in Fig. 6B.

Optimization of the intermediate layer was conducted by variation of the thicknesses of all three components (p-type oxide, PEDOT:PSS, n-type oxide). Firstly, we varied the thickness of the V_2O_5 layer by varying the VTIP:IPA concentration and keeping the wet-thickness constant. The results for this thickness variation can be seen in Supplementary information Fig. S2A, the VTIP:IPA 1:1000 out-performed both the thicker and thinner V_2O_5 with a PCE of 0.83% where the largest enhancement is seen for the short circuit current with an increase from respectively -0.28 and -1.40 to -2.40 mA/cm^2. The lower performance for 1:2000 VTIP:IPA solution could be found in the loss of the ability to work as a compatibilizer, when coating the following 4083 PEDOT:PSS layer, as coating defects were observed. V_2O_5 films with different thicknesses can be seen in Fig. S2B and S2C. Fig. S2B is a V_2O_5 layer with a theoretical thickness of 60 nm, showing a film with discrete pinholes. Fig. S2C has a theoretical solid thickness of 3 nm, the film is however not fully covering and displays discrete crystals and island formation.

Please cite this article as: T.R. Andersen, et al., A rational method for developing and testing stable flexible indium- and vacuum-free multilayer tandem polymer solar cells..., Solar Energy Materials and Solar Cells (2013), http://dx.doi.org/10.1016/j.solmat.2013.07.006

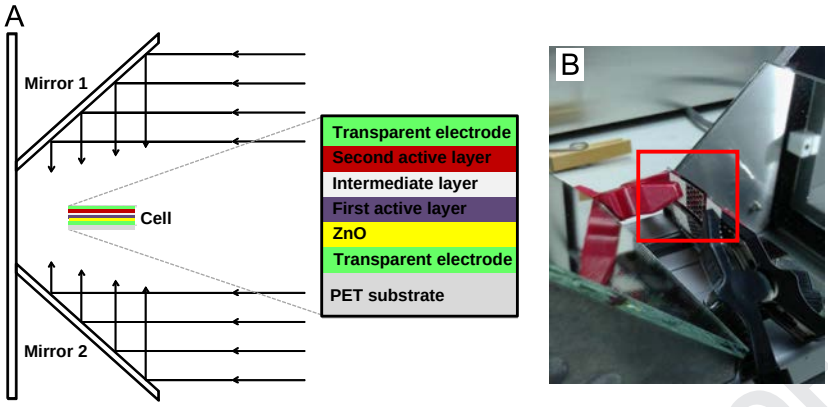

Fig. 5. (A) Illustration of the geometry used for illuminating the tandem solar cells when testing. The intensity received by the cell was effectively 1.4 suns with an equal distribution from both sides. The exploded view of the cell shows the stack of a standard tandem cell but with both top and bottom electrodes being transparent. (B) Image of the mirror test setup with a fully printed ITO-free flexible tandem solar cell in the center (red box). (For interpretation of the references to color in this figure legend, the reader is referred to the web version of this article.)

Q3

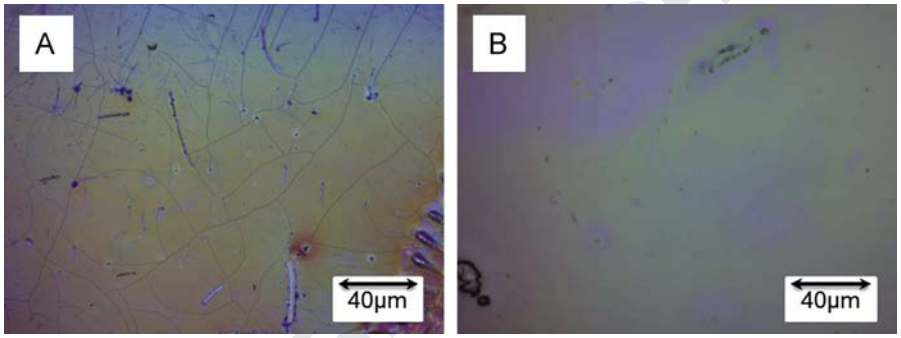

Fig. 6. Cracks in different intermediate layers. (A) Intermediate layer with only MoO_x and ZnO. (B) An intermediate layer containing MoO_x, PEDOT:PSS P VP AL4083 and ZnO.

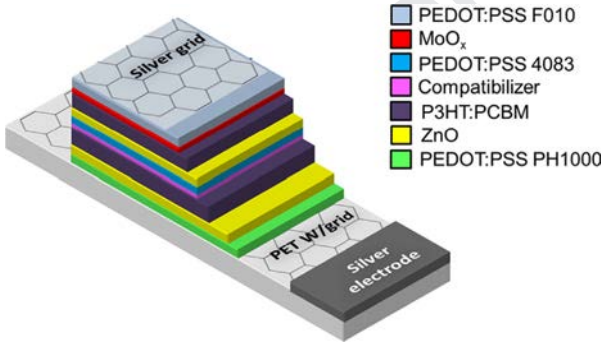

Fig. 7. The material stack first shown to work in a fully printed and roll coated flexible tandem stack on a honeycomb grid electrode. An intermediate layer consisting of a metal-oxide hole selector, PEDOT:PSS hole conductor and zinc-oxide electron selector was used.

IV-curves for devices prepared with a variation in the thickness of the intermediate 4083 PEDOT:PSS layer can be seen in Fig. 8A. They show a tradeoff between current and voltage. Thicker PEDOT:PSS layers yield devices with a higher current but lower voltage than those with a thinner 4083 PEDOT:PSS layer. The thinnest 4083 PEDOT:PSS however lost solvent resistance. Devices with different PEDOT:PSS thicknesses in the intermediate layer were coated from the same 1:2 (4083:IPA) solution by variation of the wet-thickness. The last layer in the intermediate layer is ZnO, Fig. 8B shows the *IV*-characterization for devices fabricated with two different thicknesses of the ZnO layer. The current appears to be unchanged by the thickness variation whereas there is a small difference in voltage that however can be explained by the need for less light soaking when activating the ZnO in the thinner layer. Once we had defined the process conditions and interlayers we found that a device geometry as illustrated in Fig. 7 was robust. It comprised a total of 11 printed and coated layers applied to a flexible barrier substrate.

3.4. EQE measurements of each junction

After examining the *IV*-curves obtained from the optimization of the intermediate layers it is seen that the currents are still very low. To investigate the reason for these low currents, EQE measurements were recorded on the fabricated devices for both the 1st and 2nd active layer. The EQE data obtained can be seen in Fig. 9, the data for the 1st active layer show a large peak which tops at 530 nm with an EQE of around 23%. The EQE data for the 2nd active layer however displays a drop in EQE from 420 to 500 nm. This drop in EQE correlated well with the absorption peak for P3HT, therefore the drop could be caused by strong absorption in the top of the 2nd active layer, making the distance from the dissociated electrons to the electrode long, giving larger possibility for recombination.

To avoid this drop in EQE in the 2nd active layer a variation of the layer thickness was conducted. Devices with a 2nd active layer estimated thickness of 100 nm, 200 nm, and 300 nm were coated. From the *I–V* curves presented in Fig. 10A it can be seen that a thickness of 200 nm outperforms both 100 nm and 300 nm.

Please cite this article as: T.R. Andersen, et al., A rational method for developing and testing stable flexible indium- and vacuum-free multilayer tandem polymer solar cells..., Solar Energy Materials and Solar Cells (2013), http://dx.doi.org/10.1016/j.solmat.2013.07.006

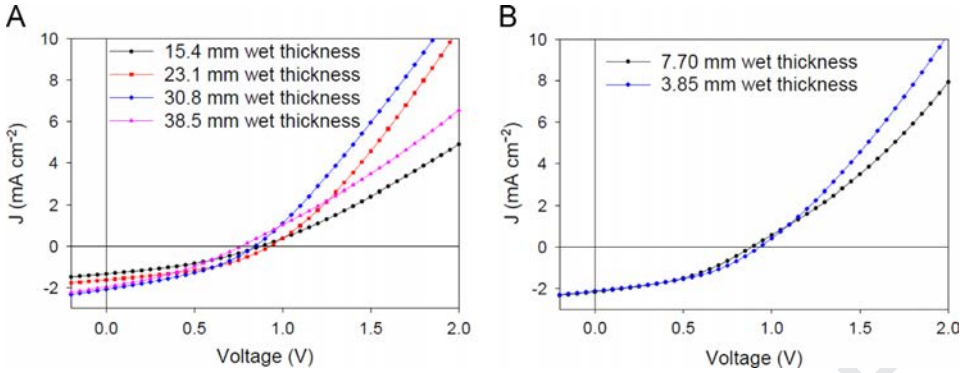

Fig. 8. (A) *I–V* curves for devices prepared with different thickness of PEDOT:PSS in the intermediate layer. (B) *I–V* curves from characterization of devices prepared with different thicknesses of the ZnO layer in the intermediate layer by varying the wet thickness in the coating but keeping the concentration constant.

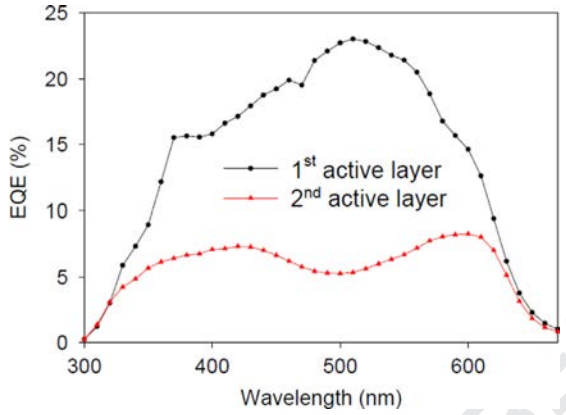

Fig. 9. EQE measurements of the 1st and 2nd active layer in a tandem device.

For the 100 nm thickness coating defects started to occur more frequently, leading to shorting through the active layer.

EQE measurements for the 2nd active layer with the thickness of 200 nm can be seen along with previously shown 480 nm thick 2nd active layer in Fig. 10B. The previously observed drop in EQE where P3HT absorbs the most has been effectively removed by reducing the layer thickness. As expected there is a minor peak in EQE around 340 nm, which is due to the illumination through the top electrode and thereby the light doesn't get absorbed in the ZnO layer.

3.5. The revised 12-layer tandem stack

Homo-junction tandem solar cells based on P3HT:PCBM were studied and achieved a maximum voltage of 1.00 V with a quite significant fill factor at 44% for initial devices with an active area of 1 cm^2. The current of -2.66 mA cm^{-2}, was however still very low, compared to a single junction P3HT:PCBM device at 700 W/m^2 illumination intensity. This was attributed to the thickness of V_2O_5, which was found to significantly influence the current that could be extracted from the device, as can be seen in Fig. S2 However, a minimum thickness was required to ensure wetting for the following 4083 PEDOT:PSS layer. This led to the investigation of whether MoO_x or F010 PEDOT:PSS could provide the same layer coating performance without the restriction in current. *IV*-curves for the tandem devices are shown in Fig. S3, which clearly shows that the tandem cells with the best overall performance are prepared with F010 PEDOT:PSS as compatibilizer for AL P 4083 (Fig. 11). Devices obtained have similar V_{OC} as devices with V_2O_5 but the currents are much higher, with a J_{SC} of -5.11 mA cm^{-2}, where devices containing V_2O_5 only have a J_{SC} of approx. -2.7 mA cm^{-2}. A reference single junction solar cell using the same electrodes, overall active layer thickness and active area is also shown. As expected the single junction perform better than the homo tandem junction and the deficit in performance is indicative of the losses incurred by the recombination layer and tandem stack processing. This loss of around 30% thus has to be counteracted by a wide bandgap/low band gap polymer couple for tandem devices that are more efficient than their individual single junction counterparts following the strategy and device geometry employed here.

This led to a simplified stack comprising silver, PEDOT:PSS, ZnO and P3HT:PCBM as shown in Fig. 12, with the intermediate layer stack offering good solvent resistance and an efficient recombination between holes from the 1st coated subcell and electrons from the 2nd coated subcell.

The specific coating parameters for the optimized tandem device with a stack as Fig. 11 can be seen in Table 1. It is noteworthy that all coating temperatures has been conducted at 60 °C, all speeds were 1 m per min. or faster, which for the small roll coater, where these experiments were conducted, is one minute or less per layer, and that the annealing step after coating of the first layer was found to be unnecessary.

3.6. Stability of 12-layer all printed flexible tandem solar cells according to ISOS-D-2

The best performing tandem cell structure, presented in Fig. 12, was chosen to evaluate the lifetime properties of the tandem devices. The stabilities of those were compared to the single devices (active layer thickness is around 480 nm) by performing testing of both types under the same conditions. Three samples of each structure were used for the studies. The efficiency for the single junction devices varied between 1.7 and 2.4%, while for the tandem devices between 0.8 and 1.3%, mainly due to the lower photocurrent of the latter, when measuring with the double illumination setup. For the stability measurement the light intensity were approx. 570 W m^{-2} pr. side. The comparison of the stability curves of the normalized PV parameters for the single and tandem devices are shown in Fig. 13. The results revealed a similar stability performance during the period of 20 days, which confirms that the additional layers in the tandem structure did not affect the stability for the devices with the studied configurations.

3.7. Stability of devices to bending

The devices were tested for their stability towards bending. It is well known that ITO does not support bending and device performance is normally significantly reduced or destroyed after

Please cite this article as: T.R. Andersen, et al., A rational method for developing and testing stable flexible indium- and vacuum-free multilayer tandem polymer solar cells..., Solar Energy Materials and Solar Cells (2013), http://dx.doi.org/10.1016/j.solmat.2013.07.006

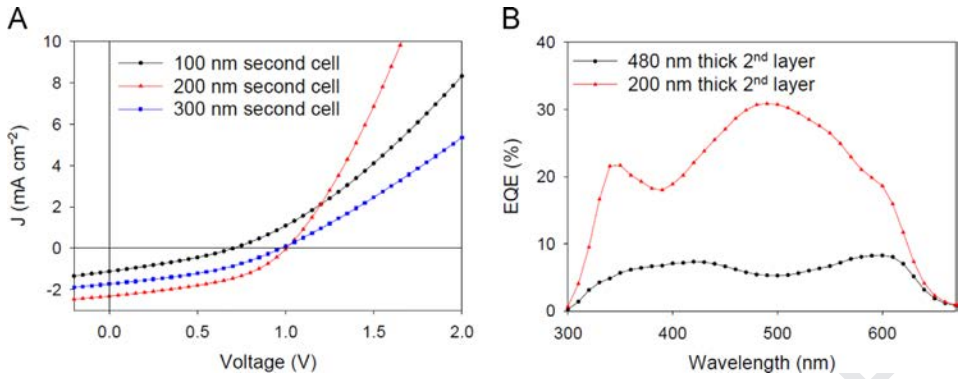

Fig. 10. (A) *I–V* curves from experiments with variation of the thickness of the 2nd active layer. The thicknesses given of the second cell are estimated from the concentration, wet thickness, and film density. (B) EQE measurements of the 2nd active layer of tandems cell prepared with two different thicknesses of the 2nd active layer.

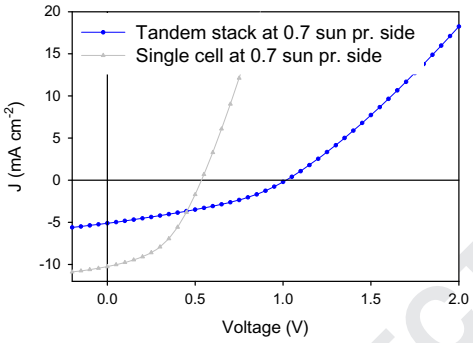

	Tandem	Single
V_{oc}	1.02 V	0.54 V
J_{sc}	5.11 mA cm^{-2}	11.4 mA cm^{-2}
FF	35.8 %	44.4 %
PCE	1.33 %	1.94 %

Measuredat 0.7 sunpr. side

Fig. 11. *IV*-curves for a cell based on the revised stack comprising F010-ALP4083-ZnO as the intermediate layer and a single junction cell with same active layer thickness as the combined active layer thickness of the tandem cell. The performance given in the curve and table are all shown for a measurement performed with a light intensity of 1.4 suns (700 Wm^{-2} pr. side).

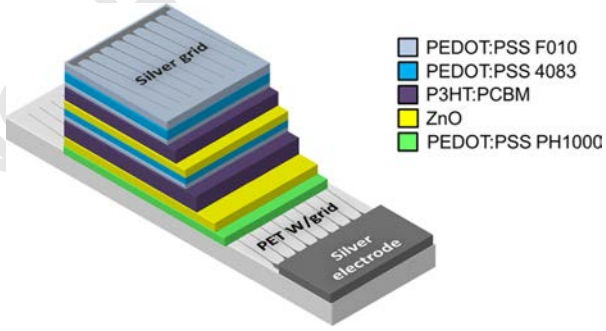

Fig. 12. The final stack, optimized by use of the mirror system, here shown with the slant type electrode.

Table 1
The coating parameters used for the developed coating stack as shown in Fig. 12.

Layer	Material	Concentration	Temperature (°C)	Speed (m/min)	Flow (ml/min)	T_{wet} (μm)
Substrate	Flextrode					
1st active layer	P3HT:PCBM	20:20 mg/ml	60	1.0	0.20	15
Compatibilizer	PEDOT F010:IPA	1:4 vol/vol	60	1.0	0.10	8
HTL	PEDOT 4083:IPA	1:2 vol/vol	60	1.0	0.30	23
ETL	ZnO	39 mg/ml	60	2.0	0.10	3.8
2nd active layer	P3HT:PCBM	20:20 mg/ml	60	1.0	0.08	6
Compatibilizer	PEDOT F010:IPA	1:4 vol/vol	60	1.0	0.10	8
HTL	PEDOT 4083:IPA	1:2 vol/vol	60	1.0	0.30	23
Conducting layer	PEDOT F10:IPA	1:1 vol/vol	60	1.0	0.40	31
Top electrode	Ag PV410		60	1.2		

Please cite this article as: T.R. Andersen, et al., A rational method for developing and testing stable flexible indium- and vacuum-free multilayer tandem polymer solar cells..., Solar Energy Materials and Solar Cells (2013), http://dx.doi.org/10.1016/j.solmat.2013.07.006

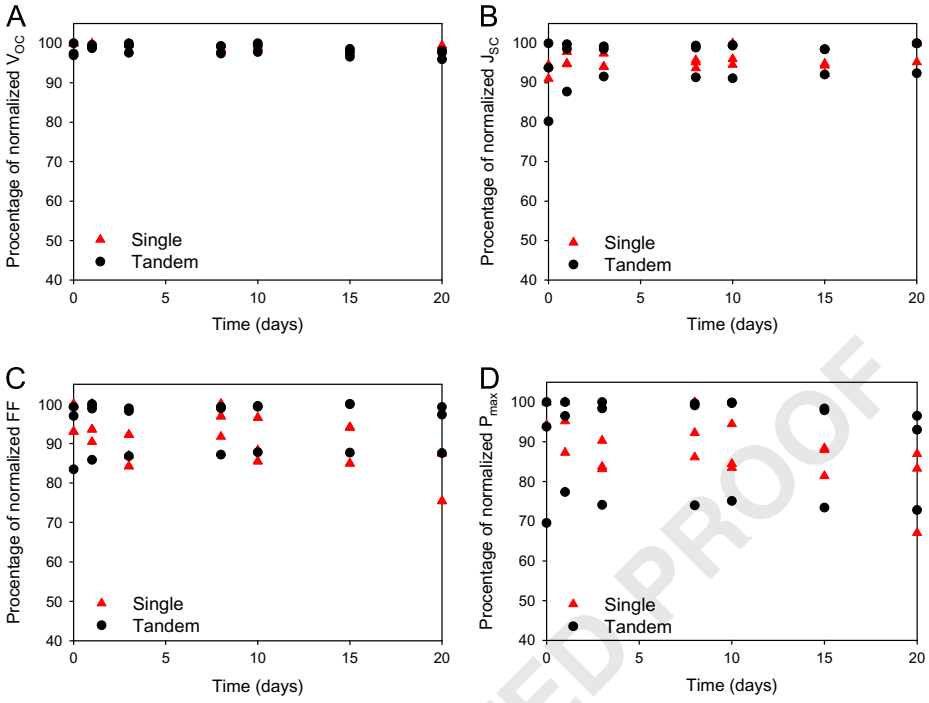

Fig. 13. A short accelerated shelf life stability study of 20 days of duration according to ISOS-D-2 conditions was performed to find if any increased degradation compared to single cell devices would be seen. No increased degradation was experienced for the tandem cells compared to the single cells, suggesting a stable interlayer. The figures are shown with normalized V_{oc} (A), J_{sc} (B), FF (C) and PCE (D).

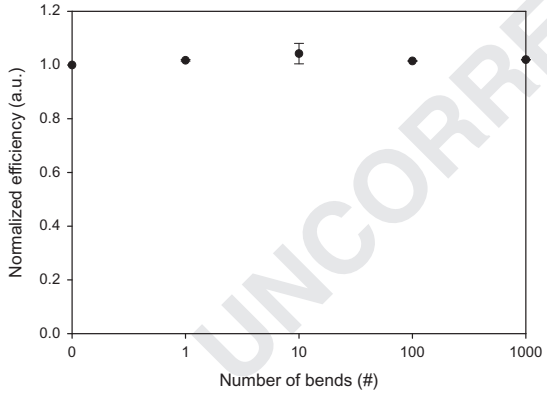

Fig. 14. Results of bending test of Amcor barrier encapsulated cells. Two samples were bended 0, 1, 10, 100 and 1000 times and *IV*-curves were recorded at each stage. The normalized efficiency shows that the bending has little influence on the performance of the cells for a range up to 1000 bends.

a couple of bending cycles [21]. In this case with the added number of layers and interfaces for the tandem stack there could be a higher risk of delamination or having layers cracking. The tandem cells however showed no signs of these effects, as seen in Fig. 14, suggesting that the stack, although being made up of twelve individual layers, have a good adhesion between the layers and that the layers are not damaged by crack formation or delamination during bending [22].

4. Conclusion

We have shown fully wet processed large area tandem solar cells comprising 12 layers on flexible substrates using only roll processing techniques and highlight a technique to optimize the individual sub cells in the tandem structure by starting with the use of thick active layer thicknesses with a gradual reduction in thickness until the optimum is found. This was enabled through use of transparent electrodes on both sides enabling double sided illumination. Different tandem cell architectures have been prepared with variations in both active layer thicknesses and intermediate layer composition and thicknesses with IV- and EQE-tests performed to show the variation in the tandem cell performance. Finally, a stability study according to ISOS-D-2 was carried out to test the tandem solar cell stability compared to the single cell structure. We found that the tandem solar cells were as stable as the single junctions and that they seemed to exhibit less variation in performance.

Acknowledgments

Henrik F. Dam and Thomas R. Andersen contributed equally to the work reported in this article. This work has been supported by Energinet.dk (Project no. 10728) and EUDP (J. no. 64012-0202). Partial financial support was also received from the European Commission as part of the Framework 7, from the EUIndian framework of the "Large cells" project that received funding from the European Commission's Seventh Framework Program (FP7/2007-2013. Grant nos. 261936 and INT/IRMC/EC-SOLAR/OISC/LARGE-CELLS:1/261936/2010), partial financial support was also received from the European Commission as part of the Framework 7 ICT 2009 collaborative project ROTROT (Grant no. 288565).

Appendix A. Supporting information

Supplementary data associated with this article can be found in the online version at http://dx.doi.org/10.1016/j.solmat.2013.07.006.

References

[1] A. Hadipour, B. de Boer, P.W.M. Blom, Organic tandem and multi-junction solar cells, Advanced Functional Materials 18 (2008) 169–181.
[2] T. Ameri, G. Dennler, C. Lungenschmied, C.J. Brabec, Organic tandem solar cells: a review, Energy and Environmental Science 2 (2009) 347–363.
[3] R.R. Søndergaard, M. Hösel, F.C. Krebs, Roll-to-roll fabrication of large area functional organic materials, Journal of Polymer Science Part B: Polymer Physics 51 (2013) 16–34.
[4] R. Søndergaard, M. Hösel, D. Angmo, T.T. Larsen-Olsen, F.C. Krebs, Roll-to-roll fabrication of polymer solar cells, Materials Today 15 (2012) 36–49.
[5] N. Espinosa, M. Hösel, D. Angmo, F.C. Krebs, Solar cells with one-day energy payback for the factories of the future, Energy and Environmental Science 5 (2012) 5117–5132.
[6] N. Espinosa, R. García-Valverde, A. Urbina, F.C. Krebs, A life cycle analysis of polymer solar cell modules prepared using roll-to-roll methods under ambient conditions, Solar Energy Materials and Solar Cells 95 (2011) 1293–1302.
[7] N. Espinosa, R. García-Valverde, F.C. Krebs, Life-cycle analysis of product integrated polymer solar cells, Energy and Environmental Science 4 (2011) 1547–1557.
[8] B. Azzopardi, C.J.M. Emmott, A. Urbina, F.C. Krebs, J. Mutale, J. Nelson, Economic assessment of solar electricity production from organic-based photovoltaic modules in a domestic environment, Energy and Environmental Science 4 (2011) 3741–3753.
[9] N. Espinosa, R. García-Valverde, A. Urbina, F. Lenzmann, M. Manceau, D. Angmo, et al., Life cycle assessment of ITO-free flexible polymer solar cells prepared by roll-to-roll coating and printing, Solar Energy Materials and Solar Cells 97 (2012) 3–13.
[10] M. Hösel, R.R. Søndergaard, M. Jørgensen, F.C. Krebs, Fast inline roll-to-roll printing for indium-tin-oxide-free polymer solar cells using automatic registration, Energy Technology 1 (2013) 102–107.
[11] O. Hagemann, M. Bjerring, N.C. Nielsen, F.C. Krebs, All solution processed tandem polymer solar cells based on thermocleavable materials, Solar Energy Materials and Solar Cells 92 (2008) 1327–1335.
[12] T.T. Larsen-Olsen, T.R. Andersen, B. Andreasen, A.P. Böttiger, E. Bundgaard, K. Norrman, et al., Roll-to-roll processed polymer tandem solar cells partially processed from water, Solar Energy Materials and Solar Cells 97 (2012) 43–49.
[13] H.F. Dam, F.C. Krebs, Simple roll coater with variable coating and temperature control for printed polymer solar cells, Solar Energy Materials and Solar Cells 97 (2012) 191–196.
[14] J.E. Carlé, T.R. Andersen, M. Helgesen, E. Bundgaard, M. Jørgensen, F.C. Krebs, A laboratory scale approach to polymer solar cells using one coating/printing machine, flexible substrates, no ITO, no vacuum and no spincoating, Solar Energy Materials and Solar Cells 108 (2013) 126–128.
[15] J. Gilot, M.M. Wienk, R.A.J. Janssen, Measuring the external quantum efficiency of two-terminal polymer tandem solar cells, Advanced Functional Materials 20 (2010) 3904–3911.
[16] E44 Committee, Test methods for measurement of electrical performance and spectral response of nonconcentrator multijunction photovoltaic cells and modules, ASTM International, 2010.
[17] M.O. Reese, S.A. Gevorgyan, M. Jørgensen, E. Bundgaard, S.R. Kurtz, D.S. Ginley, et al., Consensus stability testing protocols for organic photovoltaic materials and devices, Solar Energy Materials and Solar Cells 95 (2011) 1253–1267.
[18] T.T. Larsen-Olsen, E. Bundgaard, K.O. Sylvester-Hvid, F.C. Krebs, A solution process for inverted tandem solar cells, Organic Electronics 12 (2011) 364–371.
[19] N. Li, T. Stubhan, D. Baran, J. Min, H. Wang, T. Ameri, et al., Design of the solution-processed intermediate layer by engineering for inverted organic multi junction solar cells, Advanced Energy Materials 3 (2013) 301–307.
[20] C.-H. Chou, W.L. Kwan, Z. Hong, L.-M. Chen, Y. Yang, A Metal-Oxide, Interconnection layer for polymer tandem solar cells with an inverted architecture, Advanced Materials 23 (2011) 1282–1286.
[21] S. Na, S. Kim, J. Jo, D. Kim, Efficient and flexible ITO-free organic solar cells using highly conductive polymer anodes, Advanced Materials 20 (2008) 4061–4406.
[22] S.R. Dupont, M. Oliver, F.C. Krebs, R.H. Dauskardt, Interlayer adhesion in roll-to-roll processed flexible inverted polymer solar cells, Solar Energy Materials and Solar Cells 97 (2012) 171–175.

Please cite this article as: T.R. Andersen, et al., A rational method for developing and testing stable flexible indium- and vacuum-free multilayer tandem polymer solar cells..., Solar Energy Materials and Solar Cells (2013), http://dx.doi.org/10.1016/j.solmat.2013.07.006

FULL PAPER WWW.POLYMERPHYSICS.ORG JOURNAL OF POLYMER SCIENCE Polymer Physics

Manufacture and Demonstration of Organic Photovoltaic-Powered Electrochromic Displays Using Roll Coating Methods and Printable Electrolytes

Jacob Jensen,[1] Henrik F. Dam,[1] John R. Reynolds,[2] Aubrey L. Dyer,[2] Frederik C. Krebs[1]

[1]Department of Energy Conversion and Storage, Technical University of Denmark, Frederiksborgvej 399, DK-4000 Roskilde, Denmark

[2]The George and Josephine Butler Polymer Research Laboratory, Department of Chemistry, Center for Macromolecular Science and Engineering, University of Florida, Box 117200 Gainesville, Florida

Correspondence to: F. C. Krebs (E-mail: frkr@risoe.dtu.dk)

Received 15 November 2011; revised 16 December 2011; accepted 16 December 2011; published online 17 January 2012
DOI: 10.1002/polb.23038

ABSTRACT: Electrochromic devices (ECDs) were prepared on flexible substrates using spray coating and slot-die coating methods. The electrochromic materials were the conjugated electroactive polymers, poly((2,2-bis(2-ethylhexyloxymethyl)-propylene-1,3-dioxy)-3,4-thiophene-2,5-diyl) as a vibrantly colored active material (ECP-Magenta) and poly(*N*-octadecyl- (propylene-1,3-dioxy)-3,4-pyrrole-2,5-diyl) as a minimally colored, charge balancing material (MCCP). Two electrolyte systems were compared to allow development of fully printable and laminated devices on flexible substrates. Devices of various sizes, up to 7 × 8 cm^2, are demonstrated with pixelated devices containing pixel sizes of 4 × 4 mm^2 or 13 × 13 mm^2. The transmission contrast exhibited by the devices, when switched between the fully bleached and fully colored state, was 58% at a visible wavelength of 550 nm, and the devices exhibited switching times of <10 s. Additionally, we demonstrate the utilization of printed organic photovoltaic devices (with or without the use of a lithium-polymer battery) to power the devices between the colored and bleached state, illustrating a self-powered ECD. © 2012 Wiley Periodicals, Inc. J Polym Sci Part B: Polym Phys 50: 536–545, 2012

KEYWORDS: adhesion; conjugated polymers; coatings; electrochemistry; electrochromism; interfaces; processing; thin films

INTRODUCTION Thin, functional, organic, and polymeric films for electronic devices have attracted significant interest industrially due to the promise of enabling manufacture of equivalents to existing solutions much more efficiently and at much lower cost. Examples of this include organic light emitting diodes (OLEDs),[1] white OLEDs[2] and light emitting electrochemical cells,[3,4] light harvesting devices such as small molecule photovoltaics[5] and polymer photovoltaics (OPVs),[6] color changing devices for displays such as e-paper, LCDs, and electrochromics (ECs),[7] logic circuitry such as transistors,[8] diodes,[9] and memory elements,[10] and energy storage devices such as thin film batteries[11] and supercapacitors.[12] Advantages of the many organic-based materials discussed above, over their well-established inorganic counterparts, include processability to yield printable materials, mechanical flexibility to allow use of flexible and organic substrates, and lower power consumption in many cases.[13] Organic and polymeric ECs also fall into this category as, in the past decade, full classes of materials have been developed that are processable from common organic and aqueous solvents, the use of flexible and all-organic electrodes has been demonstrated, and the full color palette of polymeric electrochromes has been developed through use of structural modification to achieve the subtractive primaries, cyan–magenta–yellow and red–yellow–blue along with black.[14,15]

When considering organic materials for active devices, the use of roll coating and roll-to-roll printing methods is an advantage that would allow low-cost and high-throughput processing as demonstrated for OPV devices. These polymer solar cells have been demonstrated in product-integrated applications comprising the light energy harvesting polymer solar cell, a thin film battery for energy storage, and a LED as a light source.[16–18] The poor match between the relatively power hungry LED and low power density OPV is managed through the battery and the intentional use of the application where light is used intermittently.

In this work, we demonstrate the use of polymer solar cells to drive EC display devices. The EC devices (ECDs) were fabricated using roll coating methods onto indium tin oxide coated flexible substrates (ITO/polyethyleneterphthalate (PET)) and switch between a vibrantly colored magenta state and a near colorless bleached state with low current density. These devices exhibit switch times on the order of several

Additional Supporting Information may be found in the online version of this article.

seconds with use of a printed, crosslinked electrolyte. With the low current required to switch, combined with the bistability that the ECDs exhibit, we are able to show that there is a good match between the power density of an OPV and the power requirements of EC displays by integrating both into printed module devices wherein one OPV powers a switch to the colored state and a second OPV powers a switch to the bleached state. In situations where constant lighting is not available, modules were constructed and demonstrated where a lithium battery stores the charge harvested by the OPV and further powers the ECD.

EXPERIMENTAL

All chemicals and solvents were used as received unless otherwise noted. The polymer inks used for the poly(methylmethacrylate) (PMMA)/propylene carbonate (PC) devices had an electrolyte content equivalent to that of the electrolyte-binder layer (w/w) to avoid cracking in the polymer film. Chloroform was used as the solvent because of the solubility of both polymer and salt, while having a reasonably low vapour pressure for roll coating. The ElectroChromic Polymer (ECP)-Magenta had a M_n of 76 kDa and the MCCP had a M_n of 56 kDa. The concentrations of inks were varied according to coating method. Solutions of 5 mg/mL were used in the spray coating experiments. In the spin coating experiments, a 20 mg/mL concentration of polymer was used, whereas the concentration used for slot-die coating varied between 20 and 40 mg/mL in $CHCl_3$.

The electrolyte solution was a mixture of PMMA (M_n 80,000 kDa; 4.4 g), tetrabutylammonium-hexafluorophosphate ($TBAPF_6$; 2 g), and PC (40 mL). The suspension was stirred at 100 °C until the PMMA was completely dissolved (3–4 h). To this was added a UV curable binder mixture comprising of Ebecryl® 150 (44 g), Ebecryl® 116 (3.5 g), Additol® BCPK (tradename of Cytec) (2.5 g; all from Cytec), and Zonyl FSO (trade name of Dupont)-100 (1.5 g). A typical electrolyte:-binder solution was a 2:1 mixture, which was mixed well and sonicated before use.

The ionic liquid electrolyte solution was made according to Watanabe with a slight modification.[19] Methylmethacrylate (MMA) and the crosslinking agent ethyleneglycol-dimethacrylate was purified by distillation and degassed before use. Benzoylperoxide was recrystallized from chloroform/methanol before use. MMA (0.02 mol), the crosslinker ethylenedimethacrylate (2 mol %) and 1-ethyl-2-methyl-imidazolium-bis(triflouromethane sulfonyl)imide (0.02 mol) were mixed in a round-bottomed flask and benzoyl peroxide (BPO) (0.5 mol %) was added. A condenser was added and the solution stirred at 85 °C for 4 h, after which acetonitrile (10 mL) was added. Further stirring (12 h) at 85 °C yielded a slightly yellow viscous solution that was used without further purification.

Roll Coating

Roll coating was performed on a small-scale roll coater with PET foil substrates.[20] The foil came prepared with a 175 μm sputtered ITO layer, etched into stripes of 4 mm or 13 mm with a nominal sheet resistivity of 100 Ω/□. Lengths of 1 m were coated at a time and with a coating width of 50 mm, thereby overlapping three of the ITO stripes. ECP-Magenta, MCCP, and electrolyte were coated on the machine with a high degree of uniformity.

EC Assembly

The ECDs were assembled manually due to the adhesiveness of the electrolyte. The ITO covered PET substrate was cleaned with isopropanol prior to coating. After coating of the various layers, 1 cm of ITO was carefully made available for electrical contact by removing the polymer and electrolyte layer with isopropanol. The two films were assembled perpendicular to each other. After assembly, the device was run through a laminator effectively forming a laminate joint.

Polymer Solar Cells and Demonstrator Assembly

The polymer solar cell modules used in this study were fully roll-to-roll processed and has been described in use for the Organic Electronics Association (OE-A) demonstrator.[18] The typical performance when initially prepared comprised a power conversion efficiency of 2%, open circuit voltage of 7.5–8.5 V, a device short circuit current of 10–15 mA, and a fill factor of 30–35%.

RESULTS AND DISCUSSION

Over the last several decades, the availability of EC polymers exhibiting a wide range of neutral state colors, switching to highly transmissive, has made the use of these materials in vibrantly colored displays, such as e-paper and e-readers, a serious possibility.[14] What has advanced this possibility even further is that many of these materials are also solution processable, allowing for use of film casting and patterning methods not previously used, such as spray casting, inkjet printing, slot-die coating, and several others. However, as the processability has improved, the characterization methods have remained the same with application of the polymer film to a small transparent electrode (typically ITO/glass), immersed in a 1 cm cuvette, for electrochemical and optical characterization. Further application of these materials to device platforms has also remained relatively small, and on rigid substrates, while little effort has extended to the use of roll coating and roll-to-roll coating methods for large area, flexible devices, or demonstrators. Additionally, little effort has been put toward understanding the power and energy requirements for such devices regarding the needs for switching between extreme states or maintaining a constant state. It is expected that the energy requirements are relatively low, as these devices are redox devices and that they exhibit memory, in that a specific color state, after an initial voltage hold, will remain after taken to open circuit. [21–23] The extent of time allowed to pass at open circuit before a refresh pulse is needed can vary based on fabrication conditions and redox potential of the device, but the energy requirements are significantly lower than those seen for solution-based ECDs, such as viologens in solution.

Here, we present the development of a printed ECD in a demonstrator where the device is powered by printed OPVs. In general, there are several opportunities and challenges for EC technology as presented in Figure 1. We have these broken down into three main points (materials, addressability,

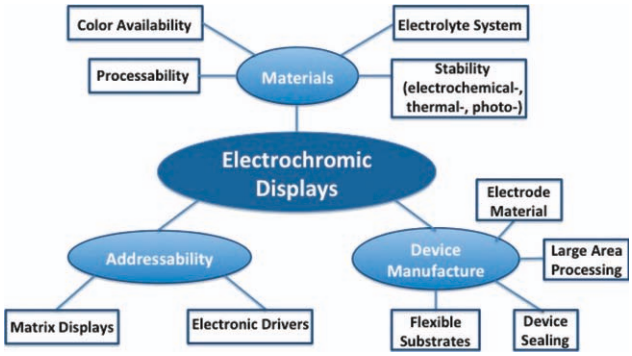

FIGURE 1 Challenges and possibilities in ECD development.

and device manufacture). As mentioned previously, recent work has addressed the challenges involving color availability and processing, allowing for a full color palette of solution processable polymers, not previously available. However, little effort has focused on using these materials in full device manufacture, looking at use of flexible substrates and large area processing, let alone addressability of matrix displays and integration of electronics drivers.[24] As an effort toward use of EC materials in commercial applications, such as currently available in auto mirrors, the development process for ECDs is at a stage where further progress has to center on efficient production methods combining high output, reliability, and low cost. To realize these important parameters, where conjugated polymers are concerned, the employment of roll coating onto flexible substrates emerges as the technique of choice. The success of using these techniques in polymer photovoltaics manufacture has stimulated the use of similar techniques in ECDs. The research presented in this article centers on the progress toward a demonstrator ECD with effort focused toward printable electrolyte development, printing methods, device lamination, and finally, incorporation into a photovoltaic-powered module, addressing several of the points illustrated in Figure 1.

Materials and Coating Methods

The EC polymers used in this work were reported previously by Reynolds et al. and were the poly((2,2-bis(2-ethylhexyloxymethyl)-propylene-1,3-dioxy)-3,4-thiophene-2,5-diyl) (ECP-Magenta) that switches between a vibrant magenta color when charge neutral and highly transmissive, nearly colorless when oxidized,[25] and the PProDOP-N-C18 (MCCP) was used as the counterpolymer wherein the polymer provides charge balance during device operation but lends minimal color to the device optical properties. Both polymers are highly soluble in common organic solvents and have been routinely processed from solution using spray casting. In this work, we examined use of spray processing and slot-die coating onto flexible substrates. We initially used spray casting, as this technique is known to create an open morphology in the film[14] and is advantageous as it easily allows ions from the electrolyte layer to be driven into the polymer film when a current is applied. In unpublished trials, slot-die coated films exhibited extensive cracking when switched between the two redox states. This is because the slot-die coated films are more dense than the spray cast films with a compact film morphology.[26] The observed cracking in slot-die coated films is explained by ions being forced into the dense polymer matrix on redox switching, causing swelling and creating stresses in the polymer film.[27] On reversal of the redox potential, the current reversed, and the matrix morphology collapses, resulting in cracking. Although the spray casting avoids this issue and is compatible with roll coating film formation, slot-die coating is a more reproducible method and was the method of choice for this work. The issue with film cracking was resolved by incorporating electrolyte ions into the polymer film during coating. A further advantage of incorporating ions in the polymer film during printing is minimization of the absorption change of the polymer when initially switched between the different redox states. This phenomenon, known as electrochemical annealing, results from the irreversible reorganization of the EC polymers caused by the initial applied current.[14,28] The setup used is shown in Figure 2(a–d) for roll coating, whereas the incorporation of spray processing on a roller is shown in Figure 2(e). For slot-die coating, the substrate is attached to the rotating drum and moved while the dispensing head is maintained stationary. The coating conditions are provided in the Experimental section. In short, both ECP-Magenta and MCCP were printed on ITO/PET films on a small-scale roll coater.[20] The coating solution contained the polymer dissolved to 20 mg/mL, $TBAPF_6$ to 4 wt % in chloroform. The electrodes consist of PET coated with 4 or 13 mm-wide ITO stripes or full ITO. The electrodes were coated with a layer of either MCCP or ECP-Magenta and afterward a layer of electrolyte mixed with a UV curable binder was applied.

Central to the preparation of an ECD that is flexible and roll-to-roll compatible is the development of a solid electrolyte system that enables laminate formation of the device while maintaining fast and robust switching. We explored two approaches in this work to establish advantages/disadvantages between the use of an electrolyte system comprised of a dissolved electrolyte salt in a printable/coatable photocurable prepolymer with a swelling agent and a system comprises a printable/coatable polymer mixed with ionic liquid. The need for a printable electrolyte is crucial if one wants to gain all the benefits of a roll coating process, where a liquid electrolyte will not work. The electrolyte layer in the ECD serves multiple purposes. The first being that it serves as a source of moveable charge carriers (i.e., ions), which are able to counterbalance the induced charges on the ECPs during redox switching. This is accomplished by dissolving an appropriate salt in an ion conducting solvent, typically PC. PC being a polar aprotic solvent is widely used in ECD studies, as it fulfils many of the requirements for an electrolyte solvent. The high polarity of PC allows it to dissolve the electrolyte salt and its high relative permittivity/dielectric constant introduces capacitance in the system allowing charge to build up on the ECPs. Additionally, its excellent properties as a plasticizer are used to modulate the plasticity of PMMA. The second role of the electrolyte in laminated devices is that it acts as an adhesive layer when sandwiched between

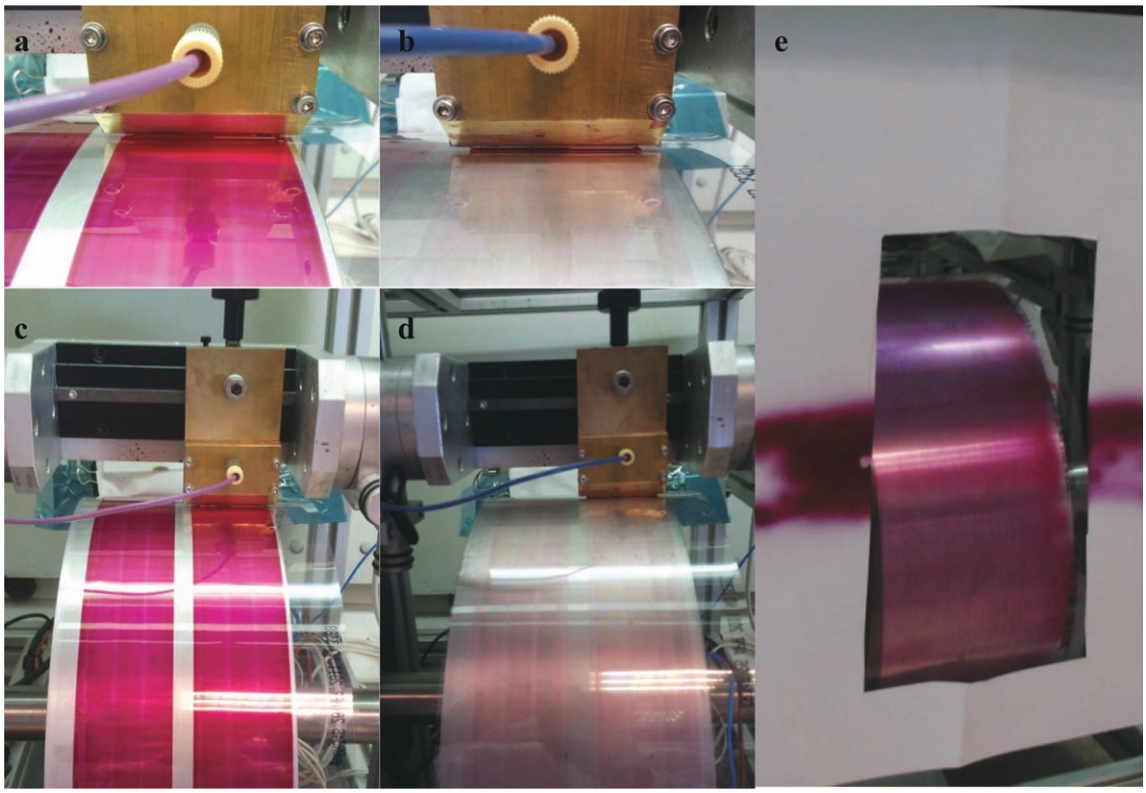

FIGURE 2 Roll coating of (a and c) ECP-Magenta from a 20 mg/mL solution and (b and d) MCCP from a 20 mg/mL solution. (e) A spray-coated substrate coated with 20 mg/mL ECP-Magenta.

the two active layers during lamination. The device presented in this report either made use of a PC/PMMA system or a PMMA/ionic liquid electrolyte. For the former, variation of the PC/PMMA ratio allows for an electrolyte system with a viscosity compatible with roll coating while enabling curing at a later stage for sealing. In the case of the PMMA/PC electrolyte system, the required viscosity was achieved by mixing of the PMMA/PC/salt system with an UV-curable acrylate oligomer, Ebecryl®. Subjecting this electrolyte layer to approximately 1700 mJ/cm^2 of UV light dosage made the surface adhesive, which allowed for curing of the laminate joint after lamination. When the devices were examined for function in outside light exposure (powered by OPVs), the curing process continued inside the device resulting in ECDs with limited switching abilities after full sun exposure for about an hour (1000 W/m^2, AM1.5G). The result was a hardened and brittle electrolyte layer with poor ion mobility and consequently poor switching. The challenge in using the electrolyte layer as a sealant in addition to the other required properties arises because of counteracting properties of ion mobility (switching speed) and adhesive properties. This was then addressed by exploring the use of ionic liquids as the swelling agent/plasticizer in combination with ion conducting properties of such agents. The latter approach proved superior due to the fact that the system was fully cured and no longer subject to photochemical crosslinking when the device was assembled, yet exhibited sufficient ion mobility to allow switching of the device. We thus present here data for the most successful method that uses a polymer (PMMA) mixed with ionic liquid where we found reliable and fast switching and good adhesion between the ECP-Magenta and MCCP electrodes. The binder mixture was used as a sealant as well, thereby avoiding the tedious and slow process of using double-sided adhesive or epoxy liner. When the binder was appropriately cured, as detailed in the Experimental section, the two electrodes were combined with the architecture detailed in the following section and shown in Figure 3.

ECD Assembly and Testing

One of the strengths in using polymers in ECDs lies in their mechanical flexibility and, as such, the electrode material ideally should posses this ability as well. The flexibility is challenged by use of inorganic oxides (i.e., ITO on PET) as electrode material, as cracking during extensive stressing can be a problem, in addition to availability of high quality coated ITO films.[29] In the literature, this has been addressed by use of polyethylenedioxythiophene-polystyrenesulphonate (PEDOT:PSS) as electrode material in all polymer ECDs.[30,31] However, as PEDOT:PSS electrodes exhibit a light blue hue and affect the ultimate bleached state achieved, as well as dissolving and cracking during processing and device curing, ITO/PET was chosen as the electrode material in this report.

The devices were assembled by coating individual layers onto the transparent ITO/PET electrodes from opposite sides, followed by sealing the device using a UV curable

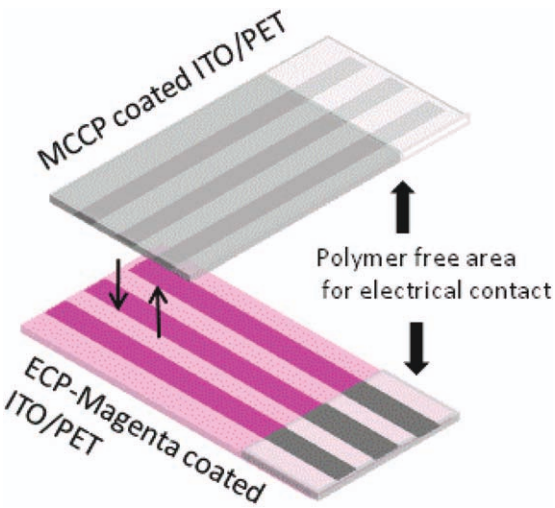

FIGURE 3 Assembly of the ECD. The foils consist of PET with ITO stripes or solid ITO. MCCP (top) and ECP-Magenta (bottom) is coated onto the foils followed by a layer of electrolyte. The foils are placed on top of each other with the ITO stripes perpendicular. An area of 1 cm on each foil is cleaned of polymer for connection to an external power source.

electrolyte binder. The electrolyte binder was chosen to act as a sealant for the device rather than peripheral adhesives as, from a production point of view, the use of double-sided adhesives is challenging in that they are not compatible with fast processing using batch methods (i.e., only a dedicated in-line machine can handle this efficiently). Fabricating the device in this way enables roll coating of the individual layers using either spray or slot-die coating as film forming techniques, followed by printing of the electrolyte-binder layer onto one electrode and laminating the two sides together. This multilayer approach is not without its limitations. Although it is possible to use roll coating with this assembly method, the multilayer approach is not directly roll-to-roll compatible, as the coated surfaces of two electrodes are to be joined through a lamination step with a sticky electrolyte. A "bottom-and-up" approach can solve this challenge but raises others regarding coating and manufacture. Building a device in one direction is the preferred method incorporating roll-to-roll coating techniques but the coating of individual layers needs to be orthogonal to each other.[32] This means that the coating of succeeding layers does not influence the already coated layer(s); typically by dissolution or oxidation. A typical challenge is dissolution of previous layers by the solvent as the materials used are often soluble in the same solvents. This can be solved by modification of the materials making them postcoating processable by hydrolysis[33] or heat[34] or by coating some layers from water and others from organic solvents.[32] Despite the aforementioned shortcomings, the multilayer approach was chosen as a starting platform for the development of the EC demonstrators.

The assembled devices switched efficiently with low current densities as illustrated for large area devices with an active area of >10 cm^2 as shown in Figure 4. As can be seen the initial voltage switch (± 2 V) induced a peak in the current with a maximum of 1 mA/cm^2, which decayed rapidly to a background current of $\sim$0.05 mA/cm^2. Between these two voltage extremes, the devices were switched from fully colored, vibrant magenta to fully bleached, nearly colorless, as shown in the photographs in Figure 4.

On monitoring the optical changes during switching, a change in transmission (ΔT) was found to be 44%, with a transmission in the clear state of $\sim$54% and a transmission as little as 10% in the colored state (at 550 nm) as shown in Figure 5(a). As seen in the figure, the response time remains constant for a period of 45 min with 30 s between switches (i.e., 90 switches), with minimal ΔT drop during that time.

To achieve 100% switching ($\Delta T = 44\%$), 10 s was required. As a substantial portion of the redox process occurs in the beginning of the voltage pulse, as seen by the initial current spike at the beginning of a switch, and the optical changes noticeable to the human eye are in the 90–95% range of the full switch, it is common to report the time periods required to reach these percentages of the full switch.[14] As shown in Figure 5(b), the full 100% switch is achieved in 10 s, whereas that for 95% of the full switch is reached in 5 s. These values are longer than those reported previously as we are using a crosslinked electrolyte with an expected ionic mobility less than that for the gel-type electrolytes. To determine the full ΔT across the visible region for this device type, a difference spectrum was measured and is shown in Figure 6. A difference spectral setup was used as there is difficulty in obtaining exactly matched sample and reference devices where optical effects (i.e., interference effects and reflective losses) are eliminated, especially where there are thin multilayer films as in these devices. We thus used a setup where two identical devices are counterdriven in, respectively, the reference and sample channel. We obtain the plot in Figure 6 that shows that the achievable ΔT with

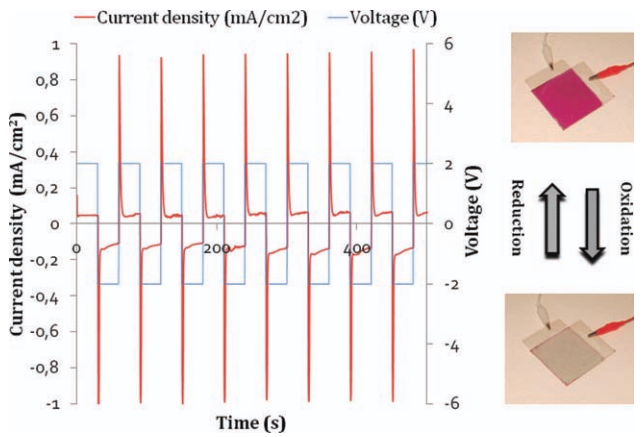

FIGURE 4 Current (left axis)/voltage (right axis) switching of a 10 cm^2 device, when switched between -2 and 2 V. The colored (reduced ECP-magenta) and bleached (oxidized ECP-Magenta) states for a device are shown in the photographs to the right.

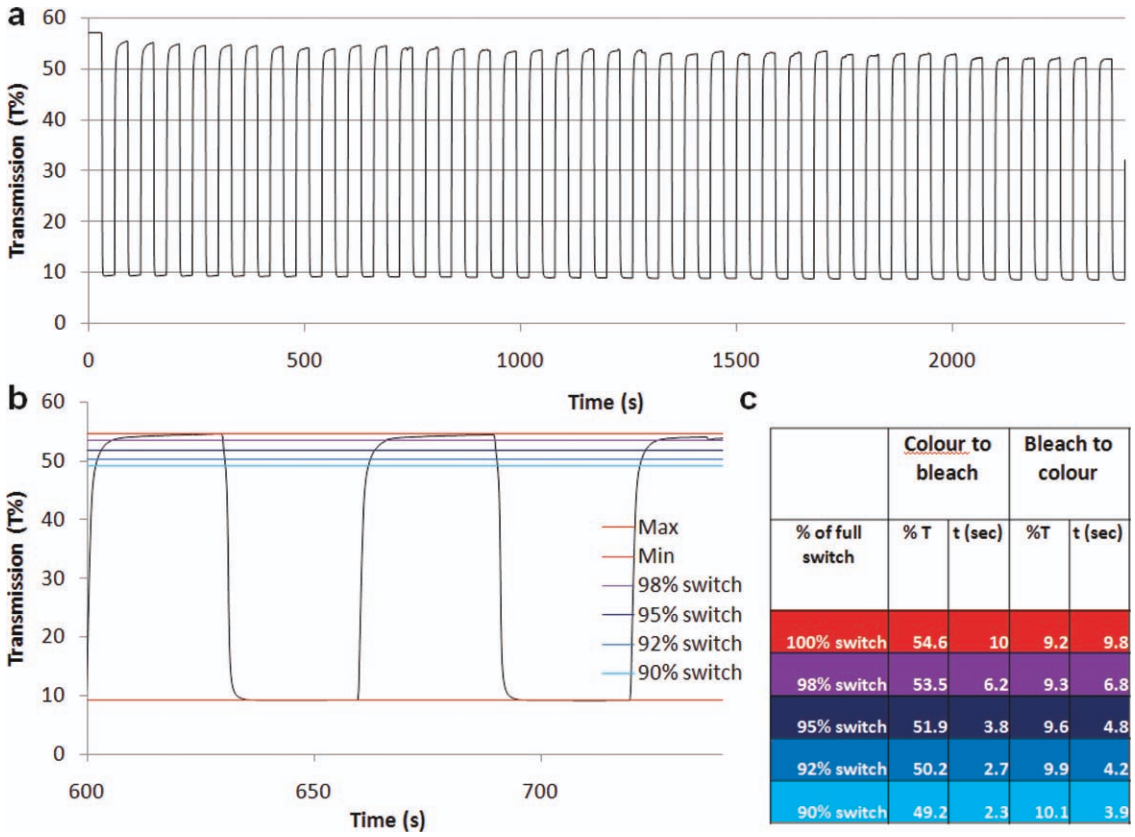

	Colour to bleach		Bleach to colour	
% of full switch	% T	t (sec)	%T	t (sec)
100% switch	54.6	10	9.2	9.8
98% switch	53.5	6.2	9.3	6.8
95% switch	51.9	3.8	9.6	4.8
92% switch	50.2	2.7	9.9	4.2
90% switch	49.2	2.3	10.1	3.9

FIGURE 5 Transmission of a device at 550 nm while switching from 2 to −2 V for 30 s at each potential. (a) Optical transmission data for a 45-min period (90 switches) causing a slight decrease in ΔT is observed. (b) Response times for the 600–750-s interval. The colors represent various degrees of switching. (c) Table showing response times corresponding to the lines in (b).

this device is around 58% at 550 nm. This value takes a bleached reference sample into account, thereby subtracting absorption by PET, ITO, reflections, and the polymeric electrolyte. The practically obtained ΔT of 44% [Fig. 5(a and b)] is obtained without a reference sample constituting the difference in transmission as seen by the eye. It is thus very satisfactory showing that our device is well constituted and unlikely to be improved much further. In addition, taking the inverse values of the plot where the reference is colored and the sample is clear (Fig. 6, green line), one should obtain values corresponding to a setup where the reference is bleached and the sample colored (Fig. 6, red line). Any difference between the values arises from nonmatched samples. For the values reported here, this corresponds to only 1%.

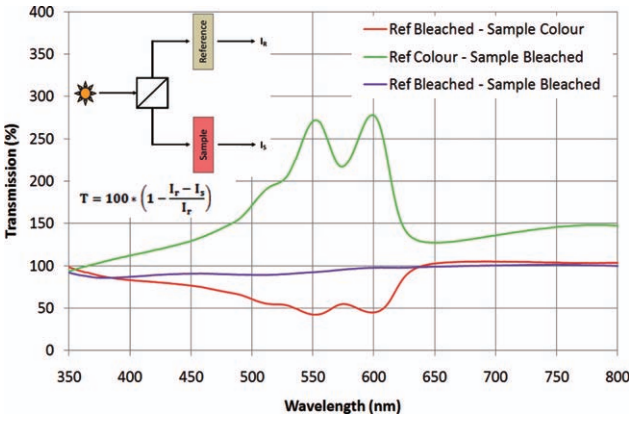

FIGURE 6 Difference plot. The green line results from the reference device being colored and the sample device bleached. The red line represents the opposite, that is, a bleached reference device and a colored sample device. The middle (purple) line results from both devices being bleached.

Demonstrator Assembly

As a large optical contrast can be effected by use of a relatively low voltage (+/−2 V) and low current (<100 μA/cm^2), use of polymer solar cells as power sources was ideal. The solar cell devices used in this study were prepared according to ProcessOne[35] following a device structure and outline as recently described for the OE-A demonstrator.[18] The polymer solar cell modules used to drive the ECDs in this study were prepared on a scale of more than 10,000 units and typically presented a V_{oc} in the range of 7.5–8.5 V and an I_{sc} in the range of 5–10 mA under illumination with 1 sun (AM1.5G, 1000 W/m^2). The solar cells were directly laser cut from the roll and used for direct incorporation into the prototypes developed here.

The demonstrator was prepared using printed electronic circuitry and assembly that was previously developed in an earlier study for an OPV/lithium-polymer battery powered

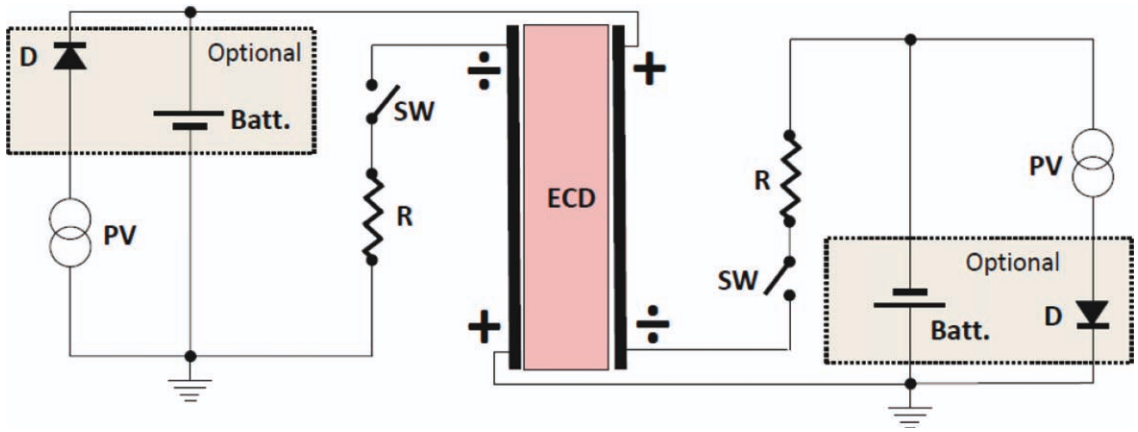

FIGURE 7 The electrical diagram for the demonstrator showing how the two independent circuits can be used to switch the ECD between the colored and transparent state. The switches are push buttons that are pressed alternately. In the case where the device is powered solely by the OPVs, the circuit elements marked optional are not included (top). The flexible printed circuitry is shown below for the version with battery and blocking diode (in dashed square box). The display area measures 40 × 40 mm^2.

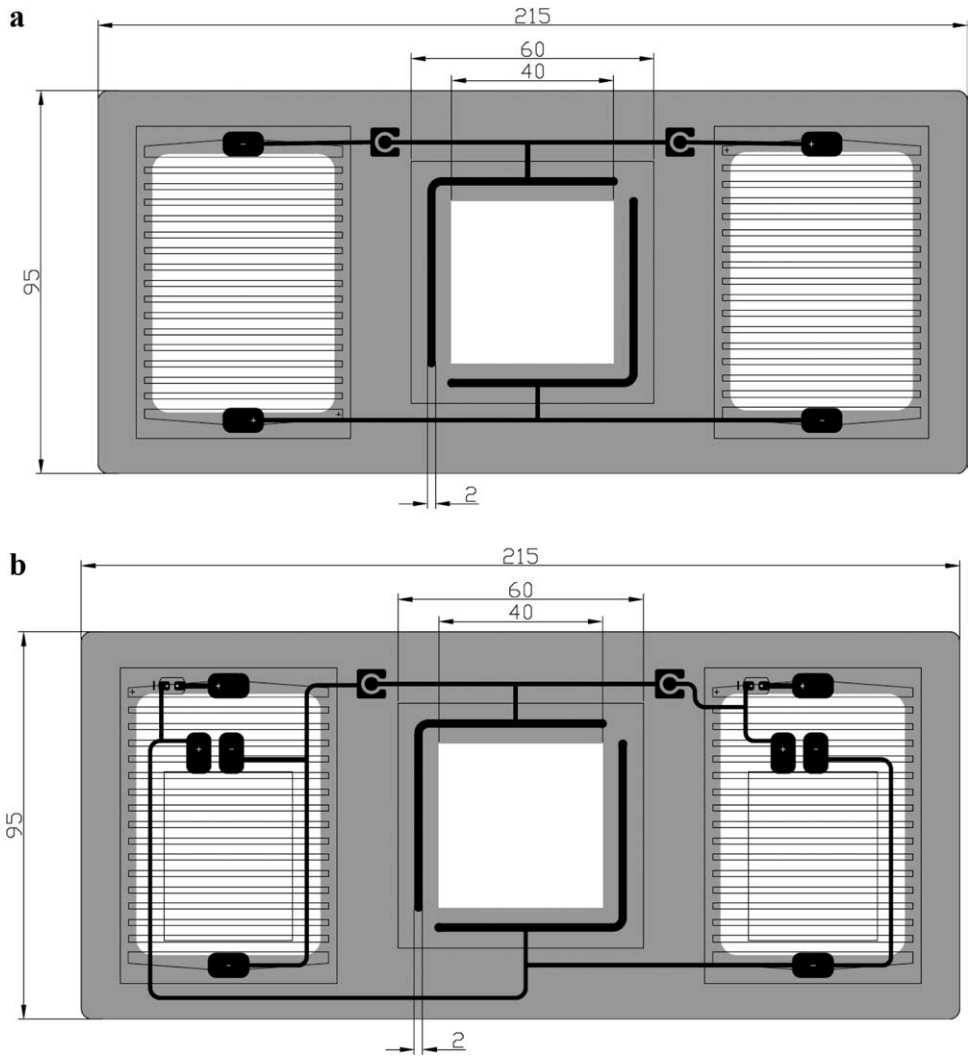

FIGURE 8 Illustration of the schematic circuit diagrams for devices powered by OPV alone (top) or OPV/lithium-polymer battery (bottom).

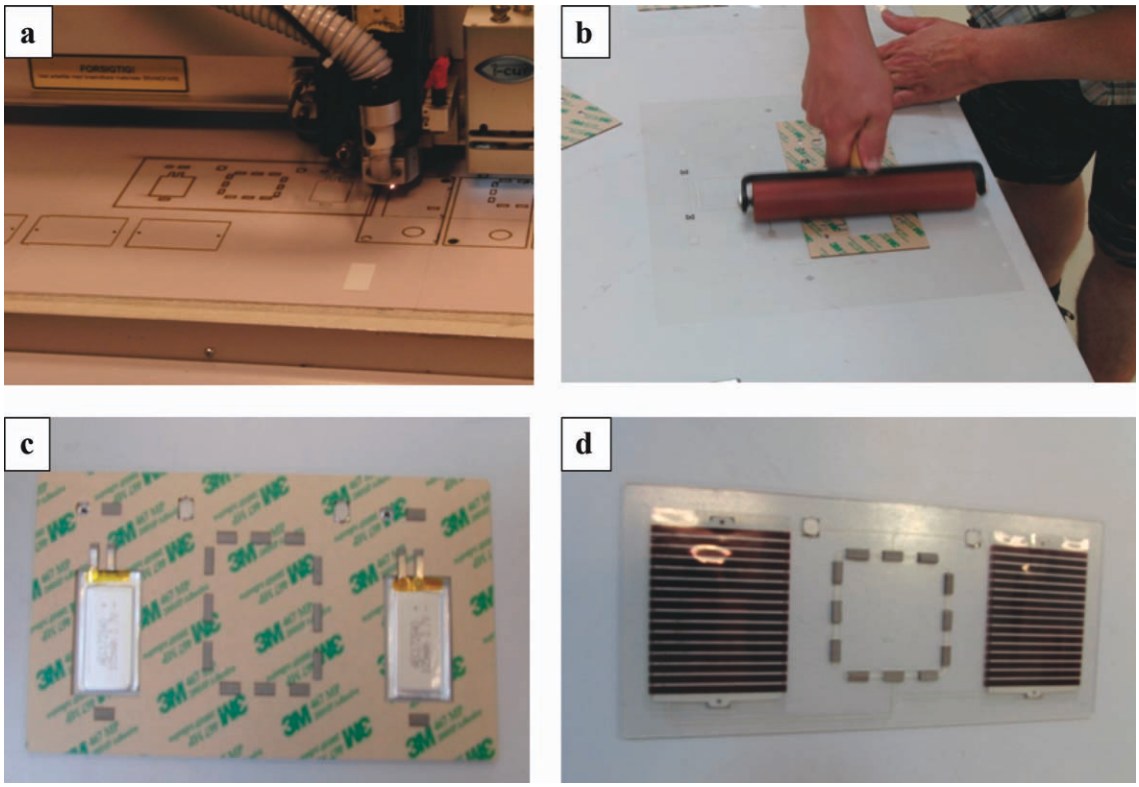

FIGURE 9 Demonstrator assembly. (a) Laser cutting of electrical circuit. (b) Lamination of adhesive polyester. (c) Polyester plate with lithium batteries and nickel sponges. (d) OPV module with on/off switches.

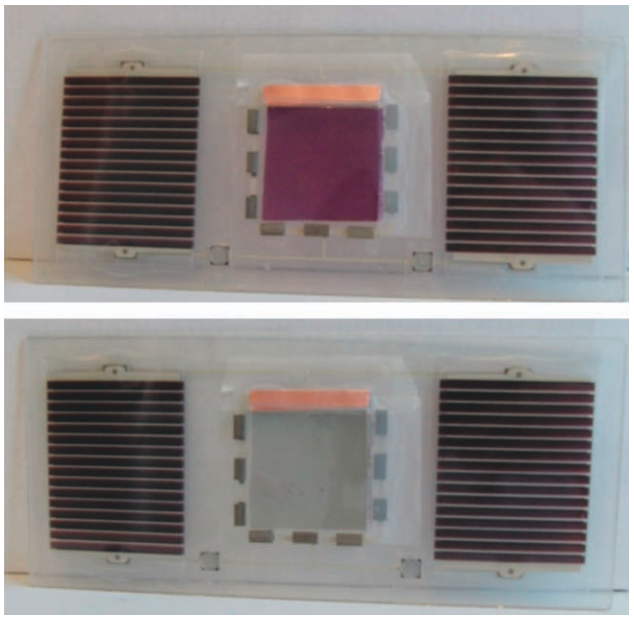

FIGURE 10 Demonstrator device, powered by polymer solar cells (far left and far right), with ECP-Magenta/MCCP ECD in the center. Contact to the ECD is made with printed circuitry from the solar cells to nickel sponges (seen around the periphery of the ECD), and the device is switched by pressing of buttons located at the bottom of the device.

flashlight[17] by replacing the white LED with the ECD. As the ECD needs to be driven electrically to switch states by passing a current through the device in opposite directions, we powered the ECD through two independent OPV circuits or OPV/lithium-polymer battery circuits as illustrated in Figure 7 where the circuit diagram is shown. The lithium-polymer battery presents a voltage in the range of 3.7–4.2 V depending on the state of charging and can supply a large current at this voltage. This resulted in fast switching times on the order of 2 s, but such large voltages can also lead to degradation of the various components in the device.[36] The switching times when powered by the solar cell alone depend on the incident light intensity and at full sun the switching time was on the order of 3 s.

The demonstrator circuitry was prepared by printing silver lines using sheet fed screen printing of a silver paste (Dupont 5007E) onto an optically clear polyester foil with a thickness of 130 μm that was cured at 140 °C for 10 min. A graphite paste was subsequently printed over the areas of the switch and the material again cured at 140 °C for 10 min. The circuit diagram for the devices is shown in Figure 8 for the demonstrators with the OPV alone [Fig. 8(a)] or with the OPV/lithium-polymer battery combination [Fig. 8(b)].

A 2.5-mm thick polyester plate was then prepared on each side with a 50-μm thick lined pressure sensitive adhesive (MP467 from 3M). The polyester sheets carrying the

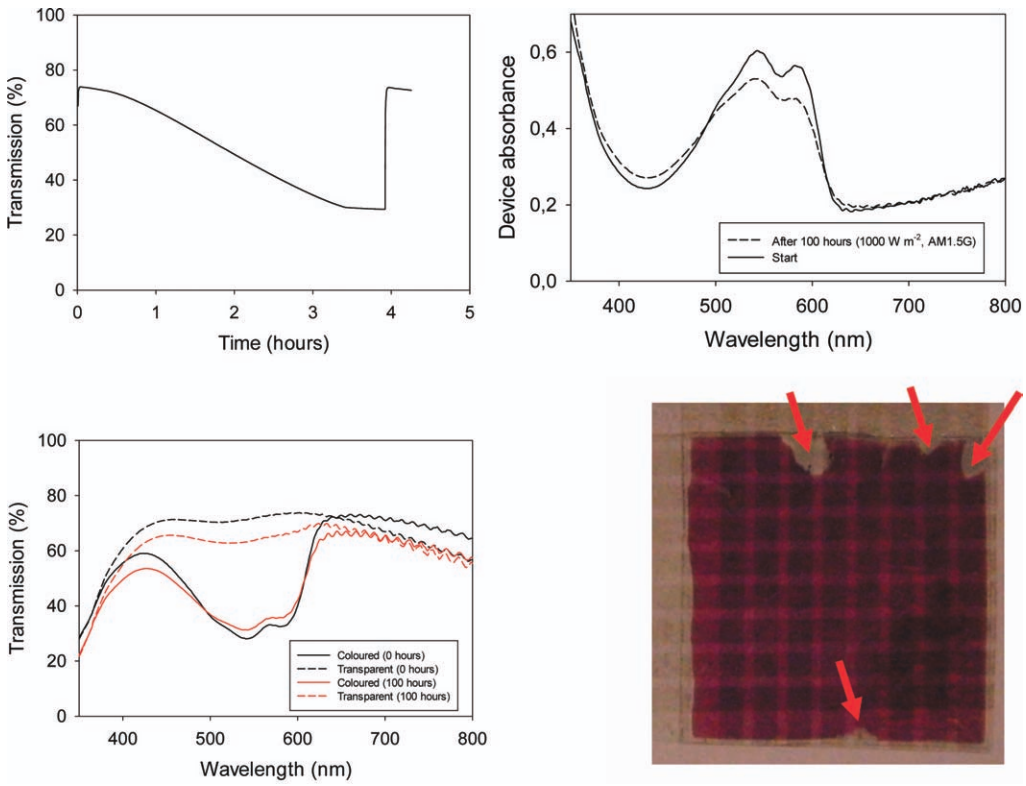

FIGURE 11 The hold time for a bleached device showing the gradual loss in transmission due to reversion from the oxidized to the reduced (colored) state when the electrical supply is removed (top left). A photobleaching experiment for a complete device under continuous illumination (AM1.5G, 1000 W/m^2, 45 °C) for 100 h leading to a 20% loss in absorbance (top right). The loss in switching capacity as a consequence of the 100-h illumination condition was 25% (lower left). The effect of photobleaching is shown with red arrows on a photograph of the photobleached device. It is also observed as ingress all around the edge (lower right).

adhesive was laser cut [Fig. 9(a)] into the desired shape of the demonstrator by cutting holes for the batteries, discrete component (1N4148 blocking diode), switches, and the nickel sponge via connections. The adhesive liner was then removed at one side and the printed circuit was applied to the adhesive [Fig. 9(b)] followed by mounting of the nickel via connections and the batteries [Fig. 9(c)]. Finally the solar cells [Fig. 9(d)] were applied over the batteries, the switch components inserted, and the ECD mounted followed by a final lamination to complete the device.

The completed device is shown in Figure 10 and movies of the device switching indoors (powered by the batteries) and outdoors (powered solely by solar cells) is supplied as Supplementary Information. Future work should address the possibility for crosslinking the electroactive polymers and electrolyte system or some other means of in-solubilization thus enabling both the bottom-and-up approach and ensure better thermomechanical properties such that the final devices become robust toward delamination during processing, handling, and operation. Although devices could be delaminated in the laminate joint by manual force, they are quite well joined and we estimate the fracture energy (G_c) to be significantly above >1 J/m^2 based on earlier studies for delamination of polymer solar cells.[37] Development of electrolyte systems with higher fracture energies would be a valid research goal.

Of significant importance is also the hold time and the temporal and photochemical stability of the devices during operation as these devices would be intended for use as variable shading of sunlight (e.g., in a window) or as a display unit (e.g., a billboard applied outdoors with backlight). We performed experiments to establish how long the bleached state is maintained after the power supply is removed from the device. The stable state for the ECD is the colored (reduced) state. Here, it is stable for extended periods of time. After bleaching, it takes on the order of 4 h to revert to the colored state (Fig. 11). This is of some importance for large area applications as a short hold time would use constant power consumption. Based on this result, it would seem that these ECDs have a large potential for display and shading applications with very low power consumption either through self powering using a solar cell as demonstrated here or through brief updates of the color state every 30 min. The devices prepared here were not encapsulated in a barrier to oxygen and water and in spite of that seem quite stable. We illuminated an operational device with a solar simulator (AM1.5G, 1000 W/m^2, 45 °C) for 100 h continuously and found that the degree of photobleaching was limited.

The device lost 20% in absorbance and when switching about 25% of the transmission change was lost (Fig. 11). The photobleaching was just visible to the eye and most significant in areas around the edges where slight delamination had occurred allowing for ingress of water and oxygen. This is a convincing result and we estimate that operation for many years is possible provided that water and oxygen are excluded from the ECD through a suitable barrier material. The shelf life is encouragingly long for practical development and use. We were unable to detect any decrease in absorbance or performance for devices stored or cycled in the dark for 4 months.

CONCLUSIONS

In this report, we have demonstrated that large area EC displays with high contrast and relatively fast response times can be achieved using EC polymers in combination with a printed and cured adhesive electrolyte. The devices were prepared by using roll coating methods on flexible substrates followed by lamination. The devices exhibited 58% ΔT when fully switched and $\sim$44% ΔT with switch times of $<$5 s. The power required for the devices were low with $+/-2$ V applied and <100 μA/cm^2 max current with a 5 μA/cm^2 background current. These low energy requirements paired well with the power output of printed polymer photovoltaic devices, allowing fabrication of a self-powered OPV/ECD module. We also established a preliminary assessment of the photochemical and temporal stability for the devices and found that full sun illumination (AM1.5G, 1000 W/m^2, 45 $^\circ$C) of an ECD for 100 h led to a decrease in absorbance of 20% and a loss in ΔT of 25%.

ACKNOWLEDGMENTS

The authors thank Jan Fyenbo at Mekoprint A/S for technical assistance during manufacture of the demonstrator and also acknowledge the funding of the electrochromics program at UF by BASF and for their supply of the two EC polymers used in this work.

REFERENCES AND NOTES

1 Greenham, N. C.; Moratti, S. C.; Bradley, D. D. C.; Friend, R. H.; Holmes, A. B. *Nature* **1993,** *365*, 628–630.

2 Reineke, S.; Lindner, F.; Schwartz, G.; Seidler, N.; Walzer, K.; Lüssem, B.; Leo, K. *Nature* **2009,** *459*, 234–238.

3 Pei, Q.; Yu, G.; Zhang, C.; Yang, Y.; Heeger, A. J. *Science* **1995,** *269*, 1086–1088.

4 Fang, J.; Matyba, P.; Edman, L. *Adv. Funct. Mater.* **2009,** *19*, 2671–2676.

5 Uchida, S.; Xue, J.; Rand, B. P.; Forrest, S. R. *Appl. Phys. Lett.* **2004,** *84*, 3013–3015.

6 Brabec, C. J.; Sariciftci, N. S.; Hummelen, J. C. *Adv. Funct. Mater.* **2001,** *11*, 15–26.

7 Mortimer, R. J.; Dyer, A. L.; Reynolds, J. R. *Displays* **2006,** *27*, 2–18.

8 Dimitrakopoulos, C. D.; Malenfant, P. R. L. *Adv. Mater.* **2002,** *14*, 99–117.

9 Katsia, E.; Huby, N.; Tallarida, G.; Kutrzeba-Kotowska, B.; Perego, M.; Ferrari, S.; Krebs, F. C.; Guziewicz, E.; Godlewski, M.; Osinniy, V.; Luka, G. *Appl. Phys. Lett.* **2009,** *94*, 143501.

10 Katsia, E.; Tallarida, G.; Kutrzeba-Kotowska, B.; Ferrari, S.; Bundgaard, E.; Søndergaard, R.; Krebs, F. C. *Org. Electron.* **2008,** *9*, 1044–1050.

11 Meyer, W. H. *Adv. Mater.* **1998,** *10*, 439–448.

12 Jayalakshmi, M.; Balasubramanian, K. *Int. J. Electrochem. Sci.* **2008,** *3*, 1196–1217.

13 Forrest, S. R. *Nature* **2004,** *428*, 911–918.

14 Amb, C. M.; Dyer, A. L.; Reynolds, J. R. *Chem. Mater.* **2011,** *23*, 397–415.

15 Dyer, A. L.; Thompson, E. J.; Reynolds, J. R. *ACS Appl. Mater. Interfaces* **2011,** *3*, 1787–1795.

16 Krebs, F. C.; Nielsen, T. D.; Fyenbo, J.; Wadstrøm, M.; Pedersen, M. S. *Energy Environ. Sci.* **2010,** *3*, 512–525.

17 Krebs, F. C.; Fyenbo, J.; Jørgensen, M. *J. Mater. Chem.* **2010,** *20*, 8994–9001.

18 Krebs, F. C.; Fyenbo, J.; Tanenbaum, D. M.; Gevorgyan, S. A.; Andriessen, R.; van Remoortere, B.; Galagan, Y.; Jørgensen, M. *Energy Environ. Sci.* **2011,** *4*, 4116–4123.

19 Susan, M. A.; Kaneko, T.; Noda, A.; Watanabe, M. *J. Am. Chem. Soc.* **2005,** *127*, 4976–4983.

20 Dam, H. F.; Krebs, F. C. *Sol. Energy Mater. Sol. Cells* **2012,** *97*, 191–196.

21 Heckner, K.-H.; Kraft, A. *Solid State Ionics* **2002,** *152–153*, 899–905.

22 Lampert, C. M. *Sol. Energy Mater. Sol. Cells* **2003,** *76*, 489–499.

23 Mortimer, R. J. *Annu. Rev. Mater. Res.* **2011,** *41*, 241–268.

24 Andersson, P.; Forchheimer, R.; Tehrani, P.; Berggren, M. *Adv. Funct. Mater.* **2007,** *17*, 3074–3082.

25 Reeves, B. D.; Grenier, C. R. G.; Argun, A. A.; Cirpan, A.; McCarley, T. D.; Reynolds, J. R. *Macromolecules* **2004,** *37*, 7559–7569.

26 Krebs, F. C. *Sol. Energy Mater. Sol. Cells* **2009,** *93*, 394–412.

27 Rajesh; Pandey, S. S.; Kumar, D.; Takashima, W.; Kaneto, K. *Thin Solid Films* **2004,** *467*, 227–230.

28 Welsh, D. M.; Kloeppner, L. J.; Madrigal, L.; Pinto, M. R.; Thompson, B. C.; Schanze, K. S.; Abboud, K. A.; Powell, D.; Reynolds, J. R. *Macromolecules* **2002,** *35*, 6517–6525.

29 Ginley, D. S.; Bright, C. *MRS Bull.* **2000,** *25*, 15–18.

30 Mecerreyes, D.; Marcilla, R.; Ochoteco, E.; Grande, H.; Pomposo, J. A.; Vergaz, R.; Sánchez Pena, J. M. *Electrochim. Acta* **2004,** *49*, 3555–3559.

31 Argun, A. A.; Cirpan, A.; Reynolds, J. R. *Adv. Mater.* **2003,** *15*, 1338–1341.

32 Larsen-Olsen, T. T.; Andersen, T. R.; Andreasen, B.; Böttiger, A. P. L.; Bundgaard, E.; Norrman, K.; Andreasen, J. W.; Jørgensen, M.; Krebs, F. C. *Sol. Energy Mater. Sol. Cells* **2012,** *97*, 43–49.

33 Reeves, B. D.; Unur, E.; Ananthakrishnan, N.; Reynolds, J. R. *Macromolecules* **2007,** *40*, 5344–5352.

34 Hagemann, O.; Bjerring, M.; Nielsen, N. C.; Krebs, F. C. *Sol. Energy Mater. Sol. Cells* **2008,** *92*, 1327–1335.

35 Krebs, F. C.; Gevorgyan, S. A.; Alstrup, J. *J. Mater. Chem.* **2009,** *19*, 5442–5451.

36 Ma, C.; Taya, M.; Xu, C. *Electrochim. Acta* **2008,** *54*, 598–605.

37 Dupont, S. R.; Oliver, M.; Krebs, F. C.; Dauskardt, R. H., *Sol. Energy Mater. Sol. Cells* **2012,** *97*, 171–175.

nature COMMUNICATIONS

OPEN

ARTICLE

Received 13 Apr 2012 | Accepted 11 Jul 2012 | Published 14 Aug 2012

DOI: 10.1038/ncomms2002

Ambient fabrication of flexible and large-area organic light-emitting devices using slot-die coating

Andreas Sandström[1], Henrik F. Dam[2], Frederik C. Krebs[2] & Ludvig Edman[1]

The grand vision of manufacturing large-area emissive devices with low-cost roll-to-roll coating methods, akin to how newspapers are produced, appeared with the emergence of the organic light-emitting diode about 20 years ago. Today, small organic light-emitting diode displays are commercially available in smartphones, but the promise of a continuous ambient fabrication has unfortunately not materialized yet, as organic light-emitting diodes invariably depend on the use of one or more time- and energy-consuming process steps under vacuum. Here we report an all-solution-based fabrication of an alternative emissive device, a light-emitting electrochemical cell, using a slot-die roll-coating apparatus. The fabricated flexible sheets exhibit bidirectional and uniform light emission, and feature a fault-tolerant >1-μm-thick active material that is doped *in situ* during operation. It is notable that the initial preparation of inks, the subsequent coating of the constituent layers and the final device operation all could be executed under ambient air.

[1] The Organic Photonics and Electronics Group, Department of Physics, Umeå University, Umeå SE-901 87, Sweden. [2] Department of Energy Conversion and Storage, Technical University of Denmark, Roskilde DK-4000, Denmark. Correspondence and requests for materials should be addressed to L.E. (email: ludvig.edman@physics.umu.se).

With tantalizing goals such as the projected multi-billion-dollar market for low-cost and environmentally friendly illumination panels in sight[1], it comes as no surprise that tremendous efforts have been directed towards the development of high-throughput and cost-effective fabrication methods of qualified lighting technologies. The organic light-emitting diode (OLED) is one such technology[2–7], and numerous scientific and company reports related to the partial fabrication of OLEDs under ambient air using low-cost printing and coating methods, such as inkjet[8–10], screen[11,12], and gravure[13,14], are today available. However, despite these achievements, to our knowledge, no single report on an uninterrupted fabrication of a functional OLED under ambient conditions has appeared to date. This is particularly problematic not only because it makes today's OLEDs prohibitively expensive for many large-scale applications[4] but also because the current dependency of OLEDs on, first, an electron-injection layer/cathode with low-work function and concomitant poor ambient stability, and, second, a thin active layer with extremely well-controlled thickness, make the future prospects for such a breakthrough bleak.

An alternative to the OLED is the more process-tolerant light-emitting electrochemical cell (LEC) technology. LECs are characterized by the existence of mobile ions in the active layer, which can redistribute to allow for electrochemical doping following the application of an external voltage. This *in-situ* electrochemical doping process brings the attractive consequence that the LEC operation is notably insensitive to the above-specified problematic requirements of the OLED, and that LECs thus can be expected to be well suited for the hitherto elusive uninterrupted manufacturing under ambient conditions. Relatively few studies on a potentially scalable fabrication of LECs can be found in the literature, but we note Mauthner *et al.*'s[15] report on inkjet printing of the active material in an open planar device geometry, and recent demonstrations of metal-free[16,17] and stretchable LECs[18,19].

Here we show that it is possible to fabricate large-area LEC sheets under uninterrupted ambient conditions using a purpose-built roll-coater apparatus. The constituent device layers consist of solely air-stable materials, which are deposited using the slot-die coating technique. The constituent device layers were found to be highly uneven, but the roll-coated LEC devices still exhibited uniform and strong light emission at low applied voltage. The realized LEC sheets are in addition flexible and feature bidirectional light emission as a result of the use of conformable and transparent electrode materials.

Results

Ambient fabrication using a roll-coater apparatus. For the fabrication of LEC devices, we used the technique of slot-die coating. Figure 1a depicts schematically the successive deposition of a (yellow) active layer and a (blue) anode on top of a (pink) flexible cathode-coated substrate mounted on a roll. The dissolved material to be coated (the ink) is transferred from an external container via a pump to the (orange) slot-die head, where the coating width is defined by the width of the head's bottom slot through which the ink flows onto the moving substrate, while the coating thickness is dictated by the ink flow rate and the substrate speed. The apparatus shown in Fig. 1b is a new type of slot-die roll coater specifically designed and developed for the challenging task of enabling a time- and material-efficient optimization of a continuous coating process[20]. The motorized roll can be heated to an elevated temperature of $>180\,^{\circ}C$ and has a diameter of 300 mm, so that a flexible substrate with 1 m length can be mounted and dried directly on the roll. By using a small slot-die head (Fig. 1c), and allowing the head to be translated perpendicular to the coating direction following every complete revolution of the roll, it is possible to coat several stripes on one substrate and enable for an effective substrate length of several metres (Fig. 1b). When the coating system is equipped with the small slot-die head it requires a very small amount of dead volume ($<50\,\mu l$), which makes the technique well suited for a screening of novel and expensive inks.

We prepared a relatively viscous active-material ink, free from binder and thickener additives, comprising a blend of the emissive conjugated polymer superyellow (SY) and the electrolyte KCF_3SO_3 in poly(ethylene oxide) (PEO). The ink was deposited as multiple stripes (typically three) on a flexible poly(ethylene terephthalate) substrate, precoated with ZnO-on-indium-tin-oxide cathodic stripes[21], at a coating speed of $0.6\,m\,min^{-1}$; see Fig. 1b,c. A matching number of anode stripes was thereafter coated on top of the active material from a diluted poly(3,4-ethylenedioxythiophene):poly(styrenesulfonate) (PEDOT:PSS) water dispersion at $0.6\,m\,min^{-1}$. The ink formulation and coating took place under ambient air, with the roller kept at $40\,^{\circ}C$ to facilitate the drying of the films. The coated layers had a wet thickness of $100\,\mu m$ and a dry thickness of 1–1.5 μm (Fig. 1d). The surface morphology map of the dry layers shown in Fig. 1e,f reveals rather uneven interfaces, with an root mean squared surface roughness for the cathodic and anodic interfaces of 4.5 and 20 nm, respectively. Figure 1g–i presents $2\times2\,\mu m^2$ phase-contrast maps of the constituent layers, and we note that the active material (Fig. 1h) displays a relatively minor phase separation on the order of a few hundred nanometres between the hydrophobic conjugated polymer and the hydrophilic electrolyte, which is of the same order of magnitude as for spin-coated LEC films with similar composition[22–24].

Performance of the roll-coated devices. Figure 2a,b shows the light emission from two roll-coated devices when driven with an applied voltage of $V=7\,V$. The emitting area is $\sim300\,mm^2$, and we call attention to the bidirectionality and the uniformity of the light emission. The former is a consequence of both the anode and the cathode being transparent, whereas the latter is a direct manifestation of the unique operational mechanism of LECs. In fact, an OLED comprising a similar thick and uneven layer for the active material (Fig. 1e,f) would emit with a much lower and non-uniform light intensity, if any. Moreover, as mentioned previously, the current generation of OLEDs depends on the existence of a highly air-sensitive (low-work function) material for the attainment of efficient electron injection, which on generic terms excludes a continuous fabrication process under ambient conditions.

So what is the key distinguishing feature between an LEC and an OLED that makes the former so much more fit for a low-cost continuous coating process in ambient conditions? The answer is the existence of mobile ions within the active layer (Fig. 2c)[25]. These ions redistribute following the application of a voltage to establish nanometre-thin electric double layers at the cathodic and anodic interfaces that allow for balanced and efficient electron and hole injection, respectively (Fig. 2d). The initial injected electrons and holes attract electrostatically compensating counter-ions in an electrochemical doping process—*n*-type at the cathode and *p*-type at the anode—and these two doping regions grow with time, eventually making contact in the bulk to form a *p*–*n* junction structure (Fig. 2e)[26,27]. Such an *in-situ* formation of a *p*–*n* junction is particularly attractive in the context of thick and uneven layers of active material that commonly result from a coating or printing process, as the *p*–*n* junction will form independent on the thickness of the active layer. In other words, the doped regions continue to grow until they make contact, at which point the limiting thickness of the device is the small and constant thickness of the *p*–*n* junction and not the large and spatially varying thickness of the active material.

The measured performance of the roll-coated LEC devices is quite promising, considering that these are the pioneering experiments in the field. Figure 3a shows optoelectronic data recorded during a voltage sweep at $0.1\,V\,s^{-1}$, during which the brightness reaches $B=150\,cd\,m^{-2}$ at $V=10\,V$. The turn-on voltage at which the device begins to emit visible light ($B>1\,cd\,m^{-2}$) is $V=3.7\,V$

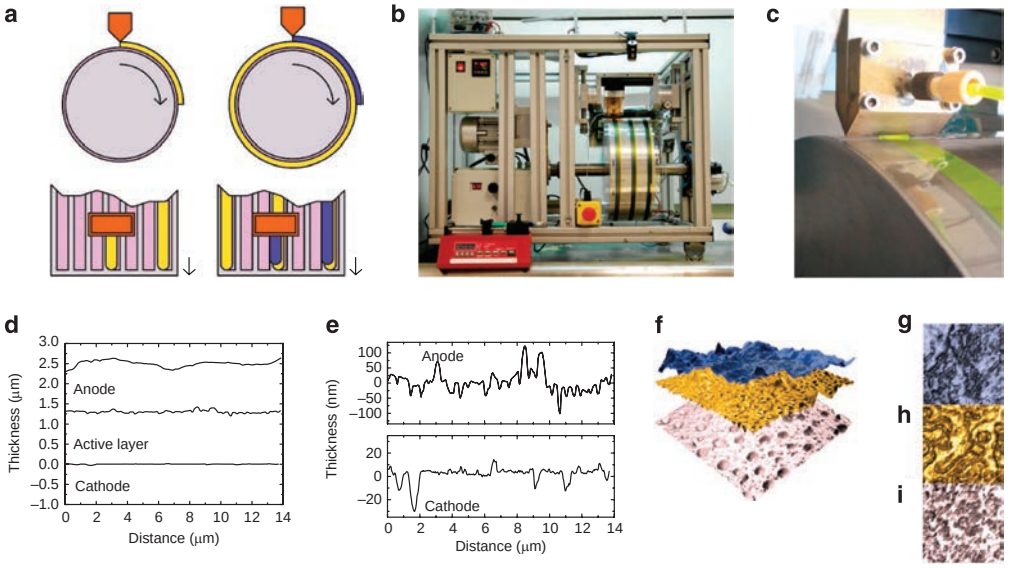

Figure 1 | Coating process and morphology and thickness of the coated films. (**a**) Schematic view of the slot-die roll coating of the (yellow) active layer and the (blue) semitransparent anode on top of a (pink) flexible cathode-coated substrate. The ink is transferred from an external container via a pump to the slot-die head (orange). (**b**) Photograph of the roll coater during the deposition of the active layer. (**c**) Close-up photograph of the slot-die head during coating of an active layer stripe. (**d**) Atomic force microscopy (AFM) data indicating the thickness of the anodic, active and cathodic layers in the LEC device stack. (**e**) Enlarged AFM data indicating the roughness of the anodic and the cathodic interfaces. (**f**) Exploded view of 10×10 μm^2 AFM height maps of the three constituent layers. (**g**–**i**) 2×2 μm^2 AFM phase-contrast images of (**g**) the PEDOT-PSS anode, (**h**) the active layer and (**i**) the ZnO cathode.

(see inset in Fig. 3a), which is close to the theoretical limit, as dictated by the band-gap potential of SY; V_{BG} (SY) = 2.4 V (refs 28, 29). The turn-on time is a critical and important parameter for LEC devices. Figure 3b presents the brightness versus time for a device driven at constant current density (j). We define the turn-on time as the time to reach $B > 10\,cd\,m^{-2}$ for a pristine device, and find that the turn-on time is ~2 s at $j = 770\,A\,m^{-2}$ (see inset in Fig. 3b). The operational stability of roll-coated LECs can be quantified by the time to reach half-maximum brightness[22,30], which we find to be ~8 h at a drive current density of $j = 77\,A\,m^{-2}$. The latter results were attained on devices that had been stored in a glove box for >6 months. The highest recorded current efficacy is $0.6\,cd\,A^{-1}$ at a brightness of $B = 50\,cd\,m^{-2}$. Finally, the fabrication yield of the roll-coated LECs is found to be very satisfying, primarily due to the fault-tolerant device geometry with a thick active layer and air-stable materials, and barring mistakes during transportation and contacting, all tested devices were functional and emitting light.

Discussion

In the above performance context, we mention that the herein used active material was chosen and optimized for the purpose of facile coating, but that, for example, its high electrolyte content has proven to be detrimental for the attainment of high efficiency and long-term stability[31]. We therefore foresee that the reported performance values can be significantly improved with further optimization of the constituent processes and the utilization of lower-electrolyte-content active materials, so that state-of-the art efficiency and operational stability values for polymer LECs of ~$10\,cd\,A^{-1}$ and several 1,000 h, respectively, can be attained also for roll-coated LEC devices[32–35].

The ink formulation and coating processes, as presented herein, were conveniently executed solely under ambient conditions, but during light emission the active material in LECs (and in OLEDs) must be free from oxygen and water vapour to enable a satisfying performance. This challenge should, however, be addressable in a manner compatible with ambient processing by including an efficient drying stage at an elevated temperature to drive out remnants of O_2/H_2O/solvents followed by an immediately subsequent encapsulation stage, where a flexible barrier material is attached to the device with, for example, a simple pressure-sensitive adhesive. Figure 3c shows a photograph of such an encapsulated roll-coated LEC device during operation at $V = 7$ V under ambient conditions. This device could be operated without any signs of deterioration in performance following 3 days of ambient storage, despite the fact that the encapsulation material exhibits rather limited barrier properties (see ref. 36). Considering the current prohibitive significant cost for high-performance barrier materials[37], this opportunity to utilize a material-conservative and time-efficient fabrication process and a low-cost barrier material could thus indicate a viable path towards conformable emissive devices for low-end applications, at a cost that could be accepted by the market.

To conclude, we demonstrate that the entire manufacturing of emissive LEC sheets—from the initial preparation of inks, to the coating of the constituent layers, to the final encapsulation—can be carried out in air using a slot-die coating technique that is directly compatible with high-speed and low-cost roll-to-roll fabrication. The fabricated devices are attractively robust and fault-tolerant due to the utilization of air-stable materials and a micrometre-thick emissive layer. Furthermore, the introduced roll-coating apparatus is particularly fit for further optimization of the constituent processes and the device performance. We anticipate that transparent and metal-free plastic applications with good light-emission performance should be a highly realistic option with the use of other available material combinations, and hope that our effort will pave the way so that long-term grand visions within the illumination community, notably an affordable 'light-emitting wall-paper', finally will turn into reality.

Methods

Materials and ink preparation. The dry materials, SY (Merck, catalogue no. PDY-132), PEO ($M_w = 5\times10^6\,g\,mol^{-1}$, Sigma-Aldrich), and KCF_3SO_3 (Sigma-Aldrich),

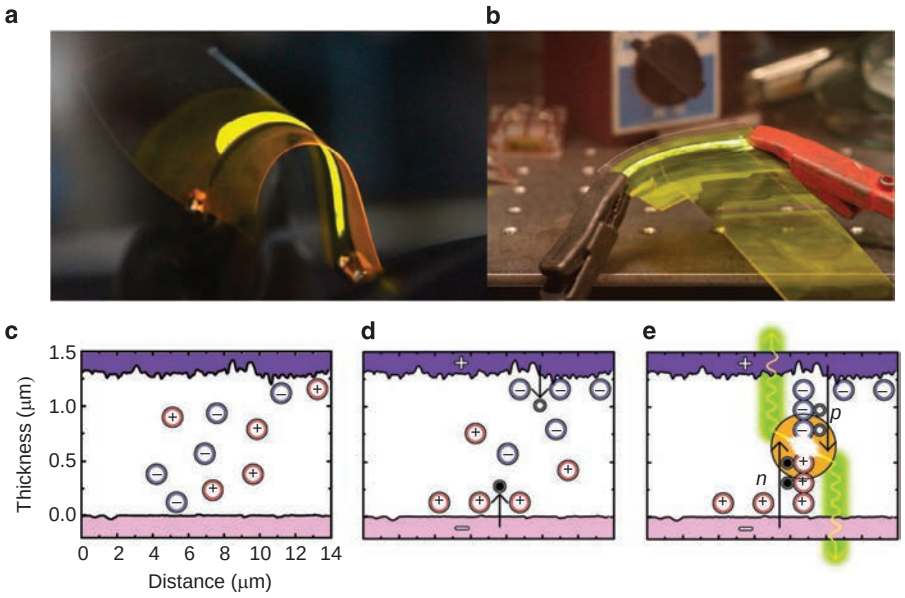

Figure 2 | Key aspects of LEC operation. (**a**) Photograph of a slot-die–coated LEC, illustrating the bidirectional light emission and the device conformability. (**b**) Light emission from a semitransparent slot-die–coated LEC following >6 months storage in a glove box. The devices depicted in **a** and **b** were driven at $V = 7$ V. (**c**) Schematic structure of a pristine LEC device, indicating the existence of mobile (red) cations and (blue) anions in the active layer and the rough (blue) anodic and (purple) cathodic interfaces. (**d**) The electric double-layer formation and the initial electron (solid circles) and hole (open circles) injection within the same device following the application of a voltage bias. (**e**) The light emission (yellow-green) from the *in-situ* formed *p*–*n* junction at steady state.

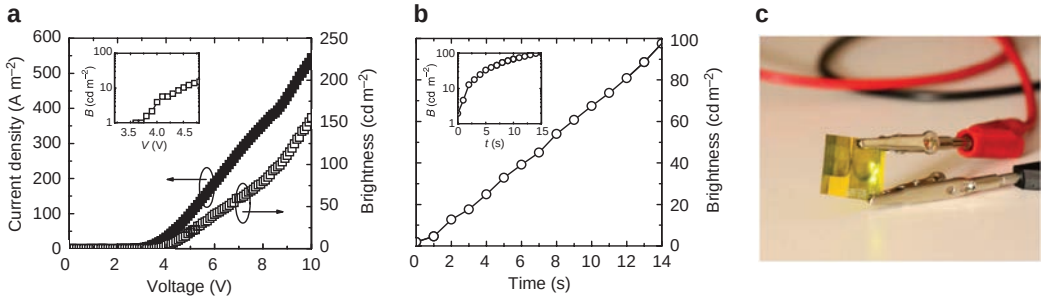

Figure 3 | Performance of roll-coated devices. (**a**) Optoelectronic data recorded on a roll-coated poly(ethylene terephthalate)/indium-tin-oxide/ZnO/{SY + PEO + KCF_3SO_3}/PEDOT:PSS device during a voltage sweep at 0.1 V s^{-1}. Inset: the brightness data plotted on a logarithmic scale. (**b**) The turn-on time for a nominally identical device driven in galvanostatic mode at $j = 770$ A m^{-2}. Inset: the brightness data plotted on a logarithmic scale. (**c**) Photograph of an encapsulated roll-coated device operating at $V = 7$ V under ambient conditions. Note that the device had been stored under ambient air for 3 days before the voltage was applied.

were separately dissolved in cyclohexanone in a 10 g l^{-1} concentration. These master solutions were stirred for 24 h at 70 °C, before being blended in a (SY:PEO:KCF_3SO_3) volume ratio of (1:1.35:0.25) to form the active-material ink. The ink was stored in 20-ml glass vials with Al lined screw caps for >5 days before deposition. The anode ink was a PEDOT:PSS dispersion (Orgacon 5015, Agfa) diluted with 75 volume % isopropanol. All ink formulation was done under ambient air.

Device fabrication. The LEC devices were manufactured on a slot-die roll coater developed at Risø DTU (Fig. 1b)[20]. A flexible poly(ethylene terephthalate) substrate (length = 1 m, width = 0.15 m) was roll-coated with a 14-nm-thick ZnO nanoparticle layer on indium-tin oxide (60 Ω/□) in a line pattern (line width = 4 mm, line separation = 1 mm)[38] and attached to the roller using pressure adhesive tape. The active-layer ink was deposited onto the ZnO cathode with an ink-flow rate of 4.0 ml min^{-1} at a substrate speed of 0.6 m min^{-1} using a 13- or 50-mm-wide slot-die head. Following a 5-min intermission, the anode ink was deposited on top of the active layer at 1.0 ml min^{-1} and 0.6 m min^{-1} using a 13-mm-wide slot-die head. The entire coating process was executed at 40 °C under ambient air. The LEC devices were additionally dried at 100 °C for 12 h under N_2 and thereafter stored under ambient air for >5 days before testing. Some devices were encapsulated on both sides with a 55-μm-thick barrier foil (U-barrier, Amcor Flexibles) to allow for light emission under ambient conditions, whereas non-encapsulated devices were tested in a N_2-filled glove box ($[O_2]$, $[H_2O]$ <10 p.p.m.).

Device characterization. The roll-coated LEC sheets were characterized using a computer controlled source-measure unit (Agilent U2722A) and a calibrated photodiode equipped with an eye-response filter (Hamamatsu Photonics) connected to a data acquisition card (National Instruments USB-6009) via a current-to-voltage amplifier. The AFM data were recorded in tapping mode under ambient conditions using a MultiMode SPM (Veeco) and the recorded micrographs were visualized using the software Gwyddion. The photographs were recorded with a digital camera (Canon EOS 300D) using the following settings: shutter speed = 1/8 s, aperture = f/5.6, sensor sensitivity = ISO-3200.

References

1. Sheats, J. R. Manufacturing and commercialization issues in organic electronics. *J. Mater. Res.* **19,** 1974–1989 (2004).
2. Tang, C. W. & Van Slyke, S. A. Organic electroluminescent diodes. *Appl. Phys. Lett.* **51,** 913–915 (1987).
3. Burroughes, J. H. *et al.* Light-emitting-diodes based on conjugated polymers. *Nature* **347,** 539–541 (1990).
4. Mertens, R. *The OLED Handbook* 1st edn (Metalgrass software, 2011).
5. Sun, Y. R. *et al.* Management of singlet and triplet excitons for efficient white organic light-emitting devices. *Nature* **440,** 908–912 (2006).
6. Reineke, S. *et al.* White organic light-emitting diodes with fluorescent tube efficiency. *Nature* **459,** 234–238 (2009).
7. So, F., Kido, J. & Burrows, P. Organic light-emitting devices for solid-state lighting. *MRS Bull.* **33,** 663–669 (2008).
8. Hebner, T. R., Wu, C. C., Marcy, D., Lu, M. H. & Sturm, J. C. Ink-jet printing of doped polymers for organic light emitting devices. *Appl. Phys. Lett.* **72,** 519–521 (1998).
9. Chang, S.- C. *et al.* Multicolor organic light-emitting diodes processed by hybrid inkjet printing. *Adv. Mater.* **11,** 734–737 (1999).
10. Suzuki, M. *et al.* A 5.8-in. phosphorescent color AMOLED display fabricated by ink-jet printing on plastic substrate. *J. Soc. Inf. Disp.* **17,** 1037–1042 (2009).
11. Pardo, D. A., Jabbour, G. E. & Peyghambarian, N. Application of screen printing in the fabrication of organic light-emitting devices. *Adv. Mater.* **12,** 1249–1252 (2000).
12. Birnstock, J. *et al.* Screen-printed passive matrix displays based on light-emitting polymers. *Appl. Phys. Lett.* **78,** 3905–3907 (2001).
13. Chung, D.- Y., Huang, J., Bradley, D. D. C. & Campbell, A. J. High performance, flexible polymer light-emitting diodes (PLEDs) with gravure contact printed hole injection and light emitting layers. *Organic Electronics* **11,** 1088–1095 (2010).
14. Nakjima, H. *et al.* Flexible OLEDs poster with gravure printing method. *SID Symposium Digest of Technical Papers* **36,** 1196–1199 (2005).
15. Mauthner, G. *et al.* Inkjet printed surface cell light-emitting devices from a water-based polymer dispersion. *Organic Electronics* **9,** 164–170 (2008).
16. Matyba, P. *et al.* Flexible and metal-free light-emitting electrochemical cells based on graphene and PEDOT-PSS as the electrode materials. *ACS Nano* **5,** 574–580 (2010).
17. Yu, Z. B. *et al.* Fully bendable polymer light emitting devices with carbon nanotubes as cathode and anode. *Appl. Phys. Lett.* **95,** 203304 (2009).
18. Yu, Z. B., Niu, X. F., Liu, Z. T. & Pei, Q. B. Intrinsically stretchable polymer light-emitting devices using carbon nanotube-polymer composite electrodes. *Adv. Mater.* **23,** 3989–3994 (2011).
19. Filiatrault, H. L., Porteous, G. C., Carmichael, R. S., Davidson, G. J. E. & Carmichael, T. B. Elastomeric emissive materials: stretchable light-emitting electrochemical cells using an elastomeric emissive material. *Adv. Mater.* **24,** 2673–2678 (2012).
20. Dam, H. F. & Krebs, F. C. Simple roll coater with variable coating and temperature control for printed polymer solar cells. *Sol. Energ. Mat. Sol. C.* **97,** 191–196 (2012).
21. Krebs, F. C., Fyenbo, J. & Jorgensen, M. Product integration of compact roll-to-roll processed polymer solar cell modules: methods and manufacture using flexographic printing, slot-die coating and rotary screen printing. *J. Mater. Chem.* **20,** 8994–9001 (2010).
22. Cao, Y., Yu, G., Heeger, A. J. & Yang, C. Y. Efficient, fast response light-emitting electrochemical cells: electroluminescent and solid electrolyte polymers with interpenetrating network morphology. *Appl. Phys. Lett.* **68** (1996).
23. Wenzl, F. P. *et al.* The influence of the phase morphology on the optoelectronic properties of light-emitting electrochemical cells. *Adv. Funct. Mater.* **14,** 441–450 (2004).
24. Matyba, P., Andersson, M R. & Edman, L. On the desired properties of a conjugated polymer-electrolyte blend in a light-emitting electrochemical cell. *Organic Electronics* **9,** 699–710 (2008).
25. Pei, Q. B., Yu, G., Zhang, C., Yang, Y. & Heeger, A. J. Polymer light-emitting electrochemical-cells. *Science* **269,** 1086–1088 (1995).
26. Matyba, P. *et al.* The dynamic organic p-n junction. *Nat. Mater.* **8,** 672–676 (2009).
27. Lenes, M. *et al.* Operating modes of sandwiched light-emitting electrochemical cells. *Adv. Funct. Mater.* **21,** 1581–1586 (2011).
28. Sandstrom, A., Matyba, P. & Edman, L. Yellow-green light-emitting electrochemical cells with long lifetime and high efficiency. *Appl. Phys. Lett.* **96,** 053303 (2010).
29. Becker, H. *et al.* Soluble PPVs with enhanced performance—a mechanistic approach. *Adv. Mater.* **12,** 42–48 (2000).
30. Costa, R. D. *et al.* Intramolecular π-stacking in a phenylpyrazole-based iridium complex and its use in light-emitting electrochemical cells. *J. Am. Chem. Soc.* **132,** 5978–5980 (2010).
31. Fang, J., Matyba, P. & Edman, L. The design and realization of flexible, long-lived light-emitting electrochemical cells. *Adv. Funct. Mater.* **19,** 2671–2676 (2009).
32. Tang, S. & Edman, L. Quest for an appropriate electrolyte for high-performance light-emitting electrochemical cells. *J. Phys. Chem. Lett.* **1,** 2727–2732 (2010).
33. Yu, Z. *et al.* Stabilizing the dynamic pin junction in polymer light-emitting electrochemical cells. *J. Phys. Chem. Lett.* **2,** 367–372 (2011).
34. Yang, Y. & Pei, Q. B. Efficient blue-green and white light-emitting electrochemical cells based on poly 9,9-bis(3,6-dioxaheptyl)-fluorene-2,7-diyl. *J. Appl. Phys.* **81,** 3294–3298 (1997).
35. Shao, Y., Bazan, G. C. & Heeger, A. J. Long-lifetime polymer light-emitting electrochemical cells. *Adv. Mater.* **19,** 365–370 (2007).
36. Krebs, F. C. *et al.* A round robin study of flexible large-area roll-to-roll processed polymer solar cell modules. *Sol. Energ. Mater. Sol. C.* **93,** 1968–1977 (2009).
37. Park, J. S., Chae, H., Chung, H. K. & Lee, S. I. Thin film encapsulation for flexible AM-OLED: a review. *Semicond. Sci. Technol.* **26,** 034001 (2011).
38. Krebs, F. C., Tromholt, T. & Jorgensen, M. Upscaling of polymer solar cell fabrication using full roll-to-roll processing. *Nanoscale* **2,** 873–886 (2010).

Acknowledgements

L.E. and A.S. are grateful to Kempestiftelserna, Energimyndigheten and the Swedish Research Council (Vetenskapsrådet) for financial support. L.E. is a Royal Swedish Academy of Sciences Research Fellow supported by a grant from the Knut and Alice Wallenberg Foundation. F.C.K. and H.F.D. are thankful for support from the Danish Strategic Research Council (2104-07-0022).

Author contributions

A.S., H.F.D. and F.C.K. carried out the experiments. L.E. and A.S. wrote the manuscript. A.S., H.F.D., F.C.K. and L.E. contributed to data analysis and project planning.

Additional information

Competing financial interests: The authors declare no competing financial interests.

Reprints and permission information is available online at http://npg.nature.com/reprintsandpermissions/

How to cite this article: Sandström, A. *et al.* Ambient fabrication of flexible and large-area organic light-emitting devices using slot-die coating. *Nat. Commun.* 3:1002 doi: 10.1038/2002 (2012).

Polymersolceller

AF

THUE T. LARSEN-OLSEN, HENRIK F. DAM, BIRGITTA ANDREASEN, THOMAS TROMHOLT og FREDERIK C. KREBS

Verdens samlede energiforbrug var i 2008 omkring 16,5 TW, og i de kommende år forventes det, at dette tal vil vokse støt [1]. I dag kommer størstedelen af energien fra fossile brændsler. Det er generelt accepteret, at der stadig er nok fossile brændsler tilbage til at understøtte dette forbrug i mange år. Da fossile brændsler kan have en katastrofal virkning på verdens miljø, er dette imidlertid ikke en langsigtet løsning. Derfor må vores fremtidige energi stamme fra vedvarende og miljøvenlige kilder. Solenergi er en af disse vedvarende energikilder. Solen er en meget pålidelig energikilde, og på ethvert tidspunkt modtager jorden ca. $1{,}2 \times 10^5$ TW fra solen. Dette alene ville i 2008 dække verdens energiforbrug mere end 10.000 gange [2].

Solcelleteknologien kan inddeles i tre generationer. Første generation (1G) er single junction-solceller, som hovedsageligt er baseret på (krystallinske) siliciumwafere, og disse har i dag en ydelse på lige over 20 %. 1G-solceller dominerer på solpanelmarkedet. Selvom disse solpaneler har en høj ydelse, er prisen for hver produceret energienhed stadig højere end samme energienhed produceret af fossile brændsler, blandt andet på grund af dyre materialer og produktionsmetoder.

Andengenerationssolceller (2G) prøver at imødekomme disse to faktorer ved brug af billigere materialer (f.eks. amorft silicium), som gør det muligt at reducere produktionsomkostningerne. 2G-solceller har en ydelse på op imod 14 %, men også her er prisen per produceret energienhed højere end for konventionelle fossile brændstofbaserede energikilder.

Tredjegenerationssolceller (3G) bruger alternative billige materialer. Blandt disse er plastik- eller polymersolceller, men 3G dækker samtidig også over dyre eksperimentelle og højtydende multi-junction-solceller. Polymersolceller tilbyder flere fordele såsom en enkel, hurtig og billig storskalaproduktion, som kan opnås ved at printe solcellerne med allerede eksisterende rulle-til-rulle (R2R)-teknologier. Selvom polymersolcellers ydelse og holdbarhed stadig er begrænsede i forhold til uorganiske solceller, har de stort potentiale. Forskningsinteressen inden for polymersolceller er steget markant de seneste år pga. en forventning om, at polymersolceller i fremtiden kan blive en konkurrencedygtig, vedvarende og miljøvenlig energikilde [2, 3].

POLYMERSOLCELLERS VIRKEMÅDE

Det, som gør en polymersolcelle anderledes end konventionelle solceller, er, at det materiale, som anvendes til at absorbere solens lys, udgøres af en polymer til forskel fra f.eks. silicium.

Det basale princip bag både polymersolcellen og andre former for solceller er dog det samme, nemlig omdannelsen af energien i elektromagnetisk stråling (lys) til elektrisk energi (en strøm og en spænding), et fysisk fænomen, der kaldes for den *fotovoltaiske effekt*. Denne energiomdannelse muliggøres af de særlige materialeegenskaber, som besiddes af såkaldte halvledere. En gruppe af materialer, der – som navnet antyder – befinder sig midt imellem at være en isolator og en leder. Dette skyldes materialernes helt særlige elektronstruktur, der er udformet med

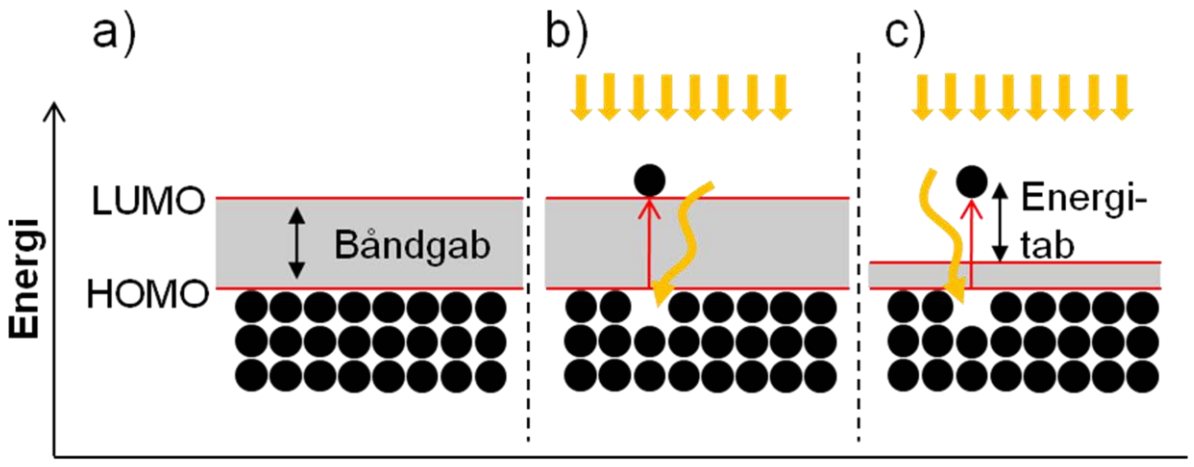

Figur 1. Solcellers virkemåde. Et halvledende materiale i mørke (a), hvor ingen strøm kan løbe, og i lys (b), hvor en foton exciterer en elektron til LUMO-niveauet og derved danner en fri elektron og et "hul", som muliggør strømledning. Til højre (c) ses et materiale med et lille båndgab i forhold til den absorberede fotonenergi, hvorved overskudsenergien går tabt.

et område af 'forbudte' energier mellem de besatte og frie elektrontilstande, et såkaldt *båndgab*. For en halvledende polymer defineres båndgabet som forskellen mellem den højeste besatte molekylorbital (highest occupied molecular orbital, HOMO) og den laveste frie molekylorbital (lowest unoccupied molecular orbital, LUMO). Så længe dette båndgab er større end de tilgængelige termiske energifluktuationer, vil elektronerne i materialet være 'låst fast' og materialet kan således ikke lede en strøm. Hvis en foton imidlertid rammer materialet, og denne besidder en energi, der er mindst lige så stor som energien i båndgabet, kan fotonen afgive sin energi til en elektron i materialet ved at excitere denne til en ikke-besat tilstand over båndgabet. Derved befinder elektronen sig i et område med frit tilgængelige tilstande, samtidig med at der er skabt et 'hul', hvor elektronen sad før. Dette gør, at elektronerne i materialet ikke længere er fastlåst, og materialet er derfor ledende. Dette princip er illustreret i Figur 1.

Elektronen og hullet kaldes tilsammen for en *exciton*, en såkaldt kvasipartikel, der betragtes som én enhed pga. den gensidigt tiltrækkende coulombkraft, der findes mellem sådanne to modsat ladede partikler. For at få solcellen til at generere strøm, skal elektronen og hullet løbe i hver sin retning og samles op ved hver sin elektrode. Dette kræver, at 'exciton-båndet' brydes. I en polymersolcelle gøres dette ved at kombinere to forskellige halvledende materialer med indbyrdes forskellig elektronegativitet og ioniseringsenergi i en såkaldt heterojunction. De to materialer kaldes henholdsvis for en *elektronacceptor* og en *elektrondonor*. Når forskellen i elektronegativitet over acceptor/donor-grænsefladen er tilstrækkelig til, at elektronen i excitonen hellere vil være i acceptor-materialet, vil der opstå en drivkraft, som adskiller elektroner og huller fysisk i hvert sit materiale. Elektroner og huller er derefter "frie" og drives mod henholdsvis katode og anode af den iboende gradient i det elektrokemiske potential, kaldet solcellens indbyggede elektriske felt. Det er netop dette indbyggede elektriske felt koblet med tilstede-

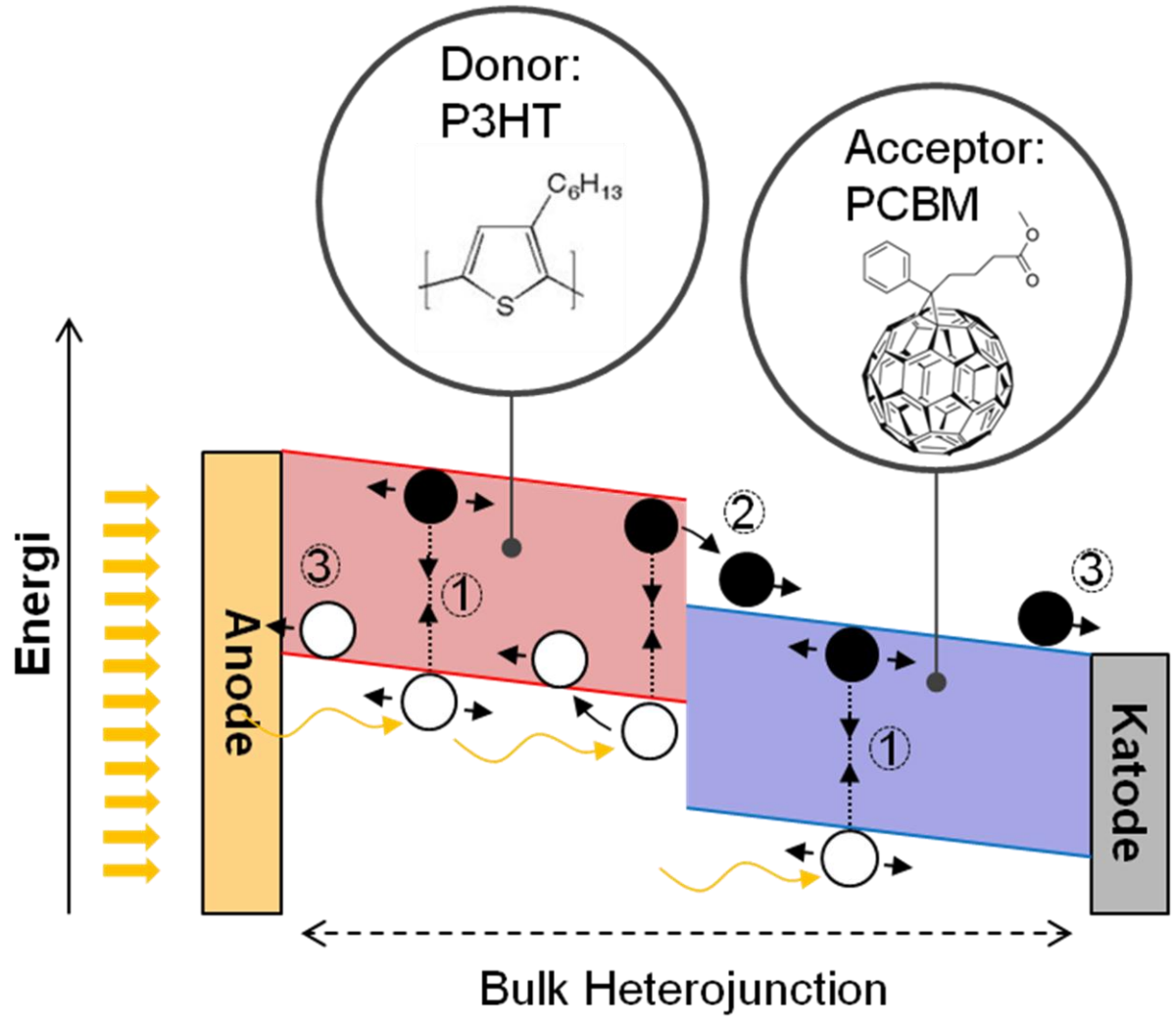

Figur 2. Skematisk tegning af polymersolcellens virkemåde. Lys absorberes og skaber excitoner (1). Disse diffunderer, indtil de møder en donor/acceptor-grænseflade, hvor excitonen deler sig i en elektron og et hul (2) som derefter drives mod og opsamles ved hver sin elektrode (3).

værelsen af frie elektroner og huller, der gør, at solcellen producerer strøm. Hele denne proces er illustreret i Figur 2.

En solcelle kan i sin simpleste form beskrives som en 3-lags sandwichstruktur på et substrat, hvor et fotoaktivt lag er placeret mellem to elektroder. En sådan struktur kan med fordel betragtes i et 2-dimensionalt tværsnit, som det er tilfældet i Figur 3. Det fotoaktive lag er der, hvor lyset absorberes, hvilket fører til generering af ladninger (elektroner og huller), som derefter opsamles og videredistribueres af elektroderne. Det særlige ved polymersolcellen er de halvledende polymerer, som bruges i det fotoaktive lag.

I Figur 3 er vist den til dato mest brugte materialekombination til polymersolceller, med polymeren P3HT som donor og en opløselig udgave af en C_{60} 'bucky-ball' kaldet PCBM som acceptor. Mens det er disse organiske molekylers særegne materialeegenskaber, der giver polymersolcellen dens mange fordele, sætter de også en række begrænsninger i forhold til udformningen af solcellen. En af

disse begrænsninger ligger i de lysgenererede excitoner, som i halvledende polymerer har en så begrænset levetid, at de kun kan nå at bevæge sig ca. 10 nm, inden de rekombinerer. Dette sætter dermed den maksimale afstand mellem en genereret exciton og den nærmeste donor/acceptor-heterojunction. Det er her, at det simple, men banebrydende, koncept kaldet en *bulk heterojunction* kommer ind i billedet. Ved at lave det fotoaktive lag af en opløsning, bestående af en makroskopisk set homogen opblanding af donor- og acceptor-materiale, fremkommer der en naturlig nanoskala-struktureret fase-adskillelse mellem de to typer af materialer, som det er illustreret i figur 3. Ved på den måde at lade naturen klare udform-ningen af sin polymer-heterojunction får man optimeret mængden af grænse-flade i det fotoaktive lag så godt, at det endnu ikke har været muligt at gøre det bedre på mere kontrolleret vis [4].

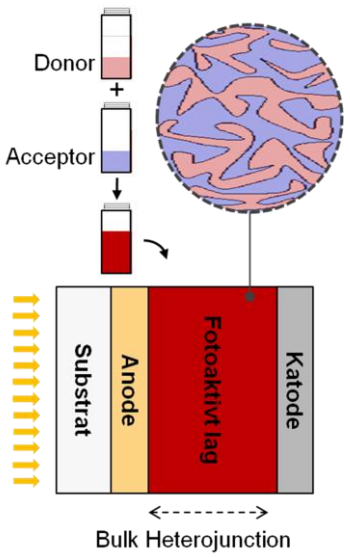

Figur 3. Polymersolcellens opbygning og lagstruktur. Det fotoaktive lag er en såkaldt bulk heterojunction, der udnytter den naturligt fremkomne finstrukturerede fase-adskillelse (vist i den stiplede cirkel) mellem donor- og acceptormateriale til at maksimere grænsefladearealet i laget.

FORSKNINGENS FOKUSOMRÅDER

De store udfordringer for polymersolceller centrerer sig omkring ydelsen, stabiliteten og produktionsteknikkerne. Disse er forskningsmæssige udfordringer, som skal løses, før teknologien kan blive konkurrencedygtig med eksisterende solcelleteknologier.

YDELSE

Kommercielle solpaneler baseret på siliciumsolceller ligger i området 10–20 % i ydelse, afhængigt af kvaliteten af solcellen. Polymersolceller optimeret i laboratoriet ligger derimod på 5−8 %, og større paneler overstiger ikke 4 % [3]. Forklaringen på denne store forskel ligger i selve det materiale, som absorberer lyset. I en siliciumsolcelle anvendes en siliciumskive på ca. 50 µm til at absorbere lyset. Herved absorberes nærmest alt lys, som rammer solcellens overflade. Desuden er silicium en halvleder med en langt højere ledningsevne end de halvledende polymertyper, som anvendes til polymer-solceller, bl.a. pga. den høje krystallinitet, som silicium har. Følgen af dette er, at mange ladninger tabes under en ladnings-ekstraktionsproces, hvorfor ydelsen reduceres yderligere.

Forskning i at øge ydelsen af polymersolceller er derfor i høj grad rettet mod at optimere de egenskaber, som kendetegner siliciumsolcellen. Disse egenskaber forsøges optimeret gennem syntese af nye polymerer, hvor andre kemiske grupper sammensættes for at efterligne siliciums egenskaber i polymermaterialerne – mere specifikt et energimæssigt lavere og bredere båndgab, højere absorptionsevne samt bedre ledningsevne. Figur 4a viser fire eksempler på halvledende polymerer deponeret på glassubstrater, hvor deres forskellige optiske egenskaber tydeligt ses i deres forskellige farver. De er alle ca. 100 nm tykke, men fremstår alligevel forholdsvis mørke, hvilket illustrerer polymerernes høje absorptionsevne. Figur 4b viser polymerernes absorption af synligt lys, sammen med solens spektrum. For alle de viste polymerer kan man se, at bindingstypen er skiftevis enkelt- og dobbeltbindinger på hovedkæden, hvilket giver materialet dets halvledende egenskaber, hvorfor polymererne kaldes *konjugerede* polymerer. Nogle po-

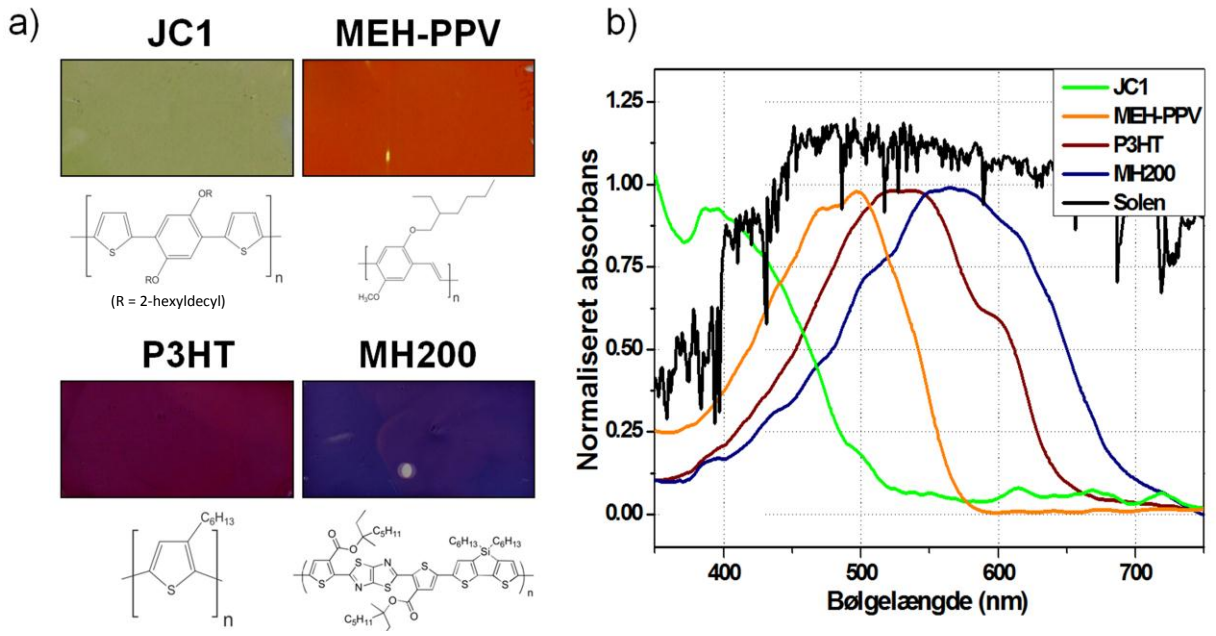

Figur 4. Halvledende polymerfilm og absorptionsspektre.
(a) 4 eksempler på halvledende polymerfilm med tykkelser på ca. 100 nm, hvor et billede af polymeren deponeret på glas er vist sammen med deres kemiske struktur. (b) Normaliserede absorptionsspektre af de 4 viste polymerer sammen med solens emissionsspektrum.

lymerer absorberer den højenergetiske blå del af det synlige lys og er derfor rødlige, hvorimod andre absorberer den lavenergetiske røde del af lyset og derfor fremstår blå. Tykkelsen af de polymerfilm, som anvendes i solceller, er et kompromis mellem at have en meget tyk film, der absorberer meget lys, eller en meget tynd film, hvor den elektriske ledningsevne gennem filmen er høj.

HOLDBARHED

Konventionelle siliciumsolceller forventes ved almindeligt brug at være stabile i mere end 20 år, dvs. at ydelsen i perioden ikke er faldet drastisk. Siden de materialer, som anvendes i polymersolceller, er overvejende organiske, er de langt mindre stabile end silicium. For de halvledende polymertyper gælder det som for de fleste organiske materialer, at eksponering til vand, varme, sol og ilt nedbryder materialerne – faktorer, der også kendetegner det miljø, hvor solceller anvendes.

Forskellige typer polymerer har forskellig holdbarhed i solceller under forskellige påvirkninger. Når en polymer udsættes for sollys, sker forskellige nedbrydningsmekanismer. Konjugationen af polymerkæden tabes gradvist ved, at kæden klippes over i mindre stykker. Dette kan observeres med det blotte øje ved at polymeren bleges, bliver mere transparent, og derfor absorberer færre fotoner. En anden udbredt nedbrydningsmekanisme indebærer oxidation af sidekæderne, så de spaltes fra monomeren,

Figur 5. Polymersolceller monteret på en soltracker.
Sensorer til monitorering af solens intensitet ses monteret på de røde plader i midten. Et system til koncentrering af sollys gennem en linse er monteret i den gule kasse.

hvorved de kemiske egenskaber ændres. Alt dette nedsætter polymerens ydelse i polymersolceller. Derfor testes nye polymerer for fotostabilitet såvel i solsimulatorer indendørs, der er lamper med lysspektrum og intensitet tilnærmet solens spektrum, som udendørs i sollys. Figur 5 viser en soltracker på Risø DTU, hvor paneler af solceller testes løbende udendørs i længere perioder.

Nogle polymerer er meget stabile, og en fuld analyse af holdbarheden på solcellen vil derfor overstige år, hvis solcellens holdbarhed testes på en udendørs tracker. For at opnå en hurtigere analyse af holdbarheden af disse materialer anvendes aggressive miljøer, hvor bl.a. høj varme, fugtighed og lysintensitet medfører en højere nedbrydningshastighed af materialet. På soltrackeren på Figur 5 ses et system til koncentrering af sollys monteret i den gule kasse. Den består af en glaslinse, som ved normalindfald fokuserer lyset ind i et bundt af optiske fibre. Disse leder lyset ind i et laboratorium, hvor det intense lys anvendes til accelererede nedbrydninger af polymerer. Herved kan tidsrammen for en analyse af stabiliteten af en polymer reduceres med en faktor 100, hvilket er en stor fordel, når potentialet af en ny polymer skal vurderes.

RULLE-TIL-RULLE

Solceller fremstillet *rulle-til-rulle* (R2R) er et forholdsvis nyt fænomen, sammen med fleksible solceller. I 1G- og til dels også 2G-solceller anven-

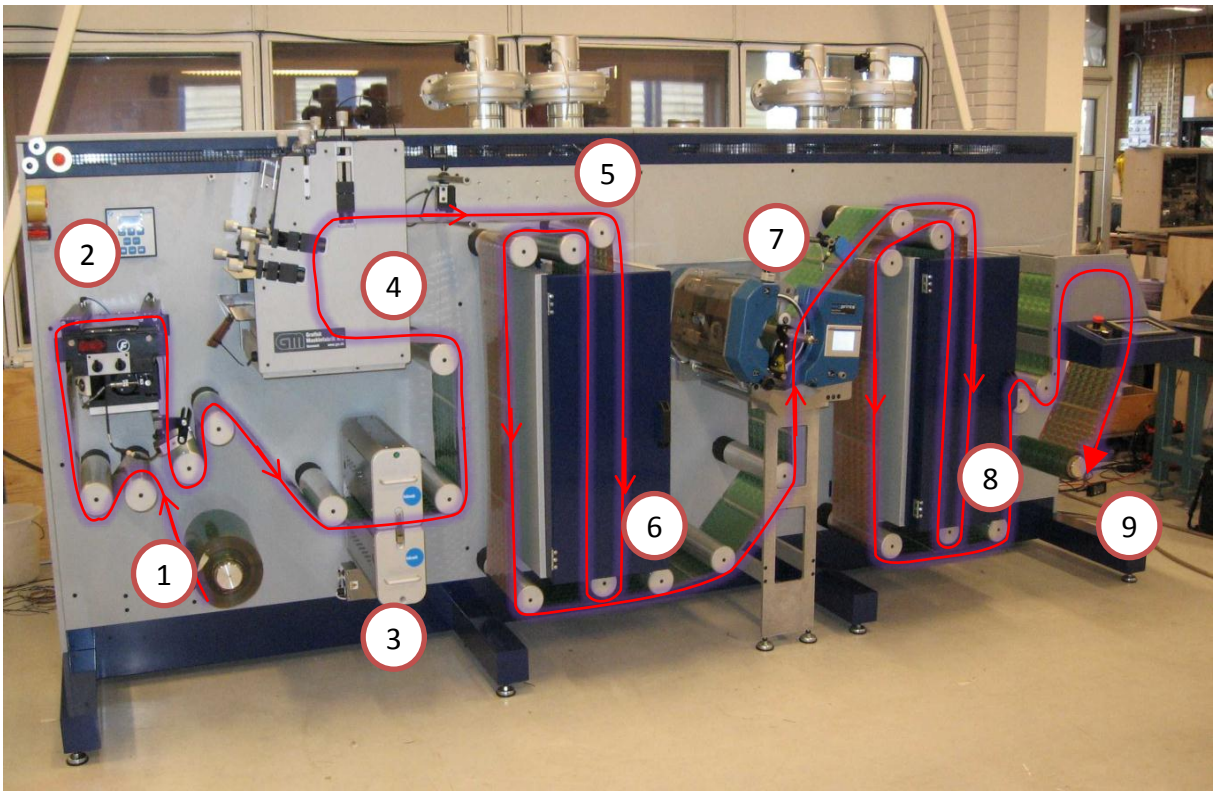

Figur 6. R2R solcellecoater installeret på Risø DTU.
Folien rulles af rullen til venstre (1) og gennem maskinens folietilretter (2), videre gennem en folierenser (3) og gennem et flexoprintmodul ved (4). Et slot-die-coatehoved er normalt monteret ved (5), hvorefter folien tørres ved to passager gennem den første ovn (6). Herfra løber folien gennem en silketryksenhed (7) for at forsætte igennem den anden ovn på maskinen (8) og til sidst at føres tilbage på rullen yderst til højre (9).

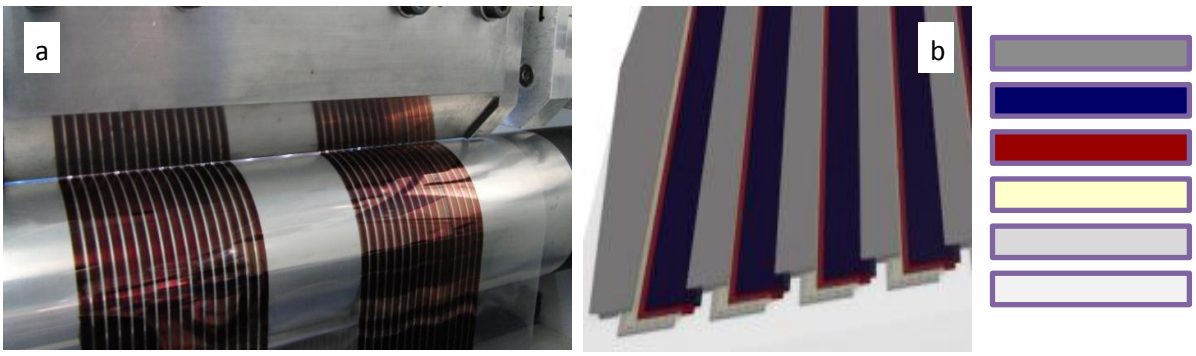

Figur 7. (a) Trykkehoved monteret på maskinen med 2 x 16 parallelle striber af polymer er ved at blive påtrykt substratet. (b) Illustration af opbygningen af et færdigtrykt solcellemodul med en opbygning af serielt forbundne solceller (4 ud af de 16 striber vist). Modulet trykkes på en PET folie. Opbygningen af cellerne består af indiumtinoxid (ITO), zinkoxid, P3HT:PCBM (fotoaktivt lag), PEDOT:PSS og en sølv-topelektrode. Modulet belyses gennem bagsiden (nedefra på illustrationen).

des stive substrater og materialer. Dette betyder, at meget af fabrikationen må foregå ved trinvise, serielle processer. Ved rullecoating af organiske solceller trykker man solcellen på et fleksibelt substrat af gennemsigtigt plastik (PET) og trykker kontinuerligt en rulle med nogle hundrede meter folie ad gangen.

R2R-begrebet kommer af, at man på maskinens indgangsside har en rulle med folie, som derpå rulles af og føres igennem trykkemaskinen, som ses i Figur 6, hvorefter den til slut rulles op i maskinens anden side.

Teknikken, der anvendes, er tilsvarende til trykning af en avis ved offset-print, hvor man påtrykker en avisside via på hinanden følgende tryk af de forskellige farver, som indholdet skal bestå af. I solcelletrykket er strukturen dog noget simplere, og i stedet for en maske med en avissides indhold bruges en teknik, der kaldes *slot-die coating*, hvor man tilfører en kontinuert strøm af blæk til et coatehoved. Blækket føres i coatehovedet ud over en dråbeguide, som styrer bredden af den resulterende stribe af materiale på substratet (se Figur 7a).

Fabrikationen af solceller ved rulle-til-rulle-coating er en mulig løsning til at sænke prisen på solceller. Der anvendes en begrænset mængde materiale, og spildet er lavt. Der pålægges lag på et substrat i rækkefølgen bundelektrode (katode), bufferlag for elektroner, aktivt lag, bufferlag for huller og til sidst topelektroden (anode). Efter hvert lag flyttes folien fra højre til venstre side af maskinen (se Figur 6). Derefter påføres det næste lag en smule forskudt på substratet for at danne en lagstruktur og celle, som ses i Figur 7, hvor man belyser cellen fra bagsiden gennem PET-folien, ITO-elektroden og zinkoxidlagene. Bufferlagene, ZnO og PEDOT, bruges for at forbedre solcellens ydeevne ved at blokere for, at elektroner og huller bevæger sig til den forkerte elektrode og rekombinerer.

De primære problemer ved rulle-coating er at finde materialer, der har både gode elektriske egenskaber, men også nemt kan coates. Problemer med *dewetting* kan ofte eksistere, hvor et følgende lag kan have problemer med at hæfte til det foregående lag. Derfor er det ofte nødvendigt at udforske et meget bredt parameterrum for at finde en velfungerende kombination af polymerer, elektroder og opløsningsmidler for at kunne foretage en vellykket coating.

Hastigheden, hvormed man kan coate opløsningerne på substratet, er en anden udfordring for fabrikationsproces-

sen. Det coatede lag skal selvfølgelig nå at tørre før det rulles på rullen på maskinens udgangsside. For nogle af lagene er det vigtigt, at de tørres hurtigt for at undgå gelering i laget, mens andre af lagene har brug for en langsom tørring for at danne gode strømførende baner.

ENERGIREGNSKAB OG BÆREDYGTIGHED

Den store udfordring for enhver ny energiteknologi er, at den skal levere bæredygtig og CO_2-neutral energi. Derfor fokuseres der på at kunne fremstille polymersolceller ved brug af mindst mulig energi og ved brug af miljøvenlige materialer. Dette kan opnås ved f.eks. at sænke produktionstemperaturen, udskifte giftige opløsningsmidler med vand og undgå brugen af sjældne grundstoffer. Et brugbart mål for bæredygtigheden er betegnelsen *energi-tilbagebetalingstid* (ETBT), som defineres ud fra den tid, det tager eksempelvis en solcelle at producere en mængde energi svarende til den totale energi brugt til at fremstille solcellen samt den energi, der er indeholdt i materialerne (den indlejrede energi). ETBT er derfor en vigtig parameter, når nye materialer skal bedømmes.

Et eksempel på et demonstrationsprodukt baseret på en organisk solcelle, som er udviklet på Risø DTU i samarbejde med trykkevirksomheden Mekoprint, er en solcellelampe til projektet "Lighting Afrika" (se Figur 8) [5]. Her er formålet at forlænge timerne med lys i lande, hvor elektricitet ikke er allestedsnærværende. Konkurrenterne til solcellelampen er lamper med batteridrift og petroleumslamper. På denne type produkt, hvor den forventede levetid er kortere end fastmonterede solpaneler og investeringen, som er mulig for brugerne, væsentlig mindre, viser ETBT sig at være bedre end for batteri- og petroleumslamper. F.eks. har solcellelampen indtjent sin indlejrede energi på under 1 måned ved substitution af batteribaserede lamper og under 2 måneder for petroleumsbaserede lamper [6]. Mekoprint A/S sælger i dag disse lamper.

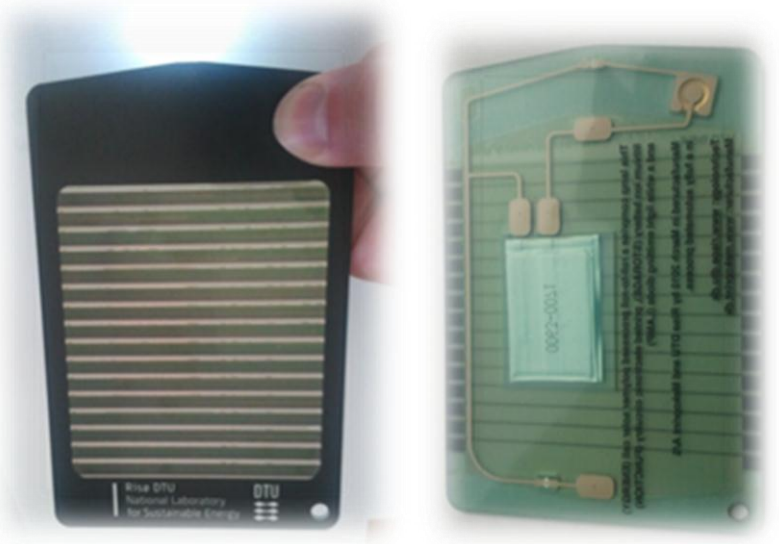

Figur 8. Eksempel på prototype af solcellelampe.
Lampen består af en plastiksolcelle produceret ved rulle-til-rulle-metoden (se Figur 7), et lithium-polymerbatteri, et trykt sølv-elektrodelag, en lysdiode og indpakning.

PERSPEKTIVET

Allerede nu er der et stort potentiale for polymersolceller ved implementering i mindre, forbrugerorienterede produkter. Her betyder teknologiens klare fordele, som lave produktionsomkostninger, fleksible materialer og generelle alsidige udformningsmuligheder, helt nye potentialer for produktudvikling i forhold til konventionelle solceller. Det langsigtede perspektiv er dog uden tvivl, at polymersolceller skal kunne bidrage væsentligt til verdens energiproduktion. Som beskrevet tidligere, ligger der dog stadig store udfordringer i at forbedre holdbarhed og effektivitet. Disse er faktorer, der skal forbedres væsentligt, før man vil se nettilsluttede polymersolceller monteret på hustage rundt

omkring eller i deciderede solfarme.

Om forfatterne

Thue T. Larsen-Olsen *er PhD-studerende ved Program for Solenergi, Risø DTU.*

Henrik F. Dam *er PhD-studerende ved Program for Solenergi, Risø DTU.*

Birgitta Andreasen *er PhD-studerende ved Program for Solenergi, Risø DTU.*

Thomas Tromholt *er PhD-studerende ved Program for Solenergi, Risø DTU.*

Frederik C. Krebs *er professor ved og stifter af Program for Solenergi, Risø DTU.*

Referencer og videre læsning

1. U.S. Energy Information Administration www.eia.gov
2. F. C. Krebs (red.): *Polymer Photovoltaics – a Practical Approach*, SPIE Press, Bellingham, Washington, USA, 2008.
3. F. C. Krebs (red.): *Polymeric Solar Cells – Materials, Design, Manufacture*, DES*tech* Publications, Inc., Lancaster, Pennsylvania, USA, 2010.
4. C. J. Brabec, M. Heeney, I. McCulloch, J. Nelson: "Influence of blend microstructure on bulk heterojunction organic photovoltaic performance", *Chemical Society Reviews* **40** (2011) 1185−99.
5. F. C. Krebs, T. D. Nielsen, J. Fyenbo, M. Wadstrøm, M. S. Pedersen: "Manufacture, Integration and Demonstration of Polymer Solar Cells in a Lamp for the "Lighting Africa" Initiative", *Energy Environ. Sci.* **3** (2010) 512–525.
6. N. Espinosa, R. García-Valverde, F. C. Krebs: "Life-cycle analysis of product integrated polymer solar cells", *Energy Environ. Sci.* **4** (2011) 1547–1557.

Forkortelser

1G, 2G, 3G Henholdsvis første-, anden- og tredjegenerationssolceller.

ETBT Energi-tilbagebetalingstid

HOMO Highest occupied molecular orbital. Højeste besatte molekylorbital.

ITO indiumtinoxid

JC1 Efter Jon E. Carlé, se Figur 4 for struktur.

LUMO Lowest unoccupied molecular orbital. Laveste frie molekylorbital.

MEH-PPV poly{[5-(2-ethylhexyloxy)-2-methoxy-1,4-phenylen]ethen-1,2-diyl}, se Figur 4 for struktur.

MH200 Efter Martin Helgesen, se Figur 4 for struktur.

P3HT poly(3-hexylthiophen), se Figur 2 for struktur.

PCBM 4-(1'-phenyl-1,2-methano-[60]fulleren-1'-yl)butansyre-methylester, se Figur 2 for struktur.

PEDOT poly{2,3-dihydrothieno[3,4-*b*]-[1,4]dioxin-5,7-diyl}

PET poly(ethylenterephthalat)

PSS poly(styrensulfonat)

R2R "Rulle-til-rulle" fremstilling, se s. 6 for beskrivelse.

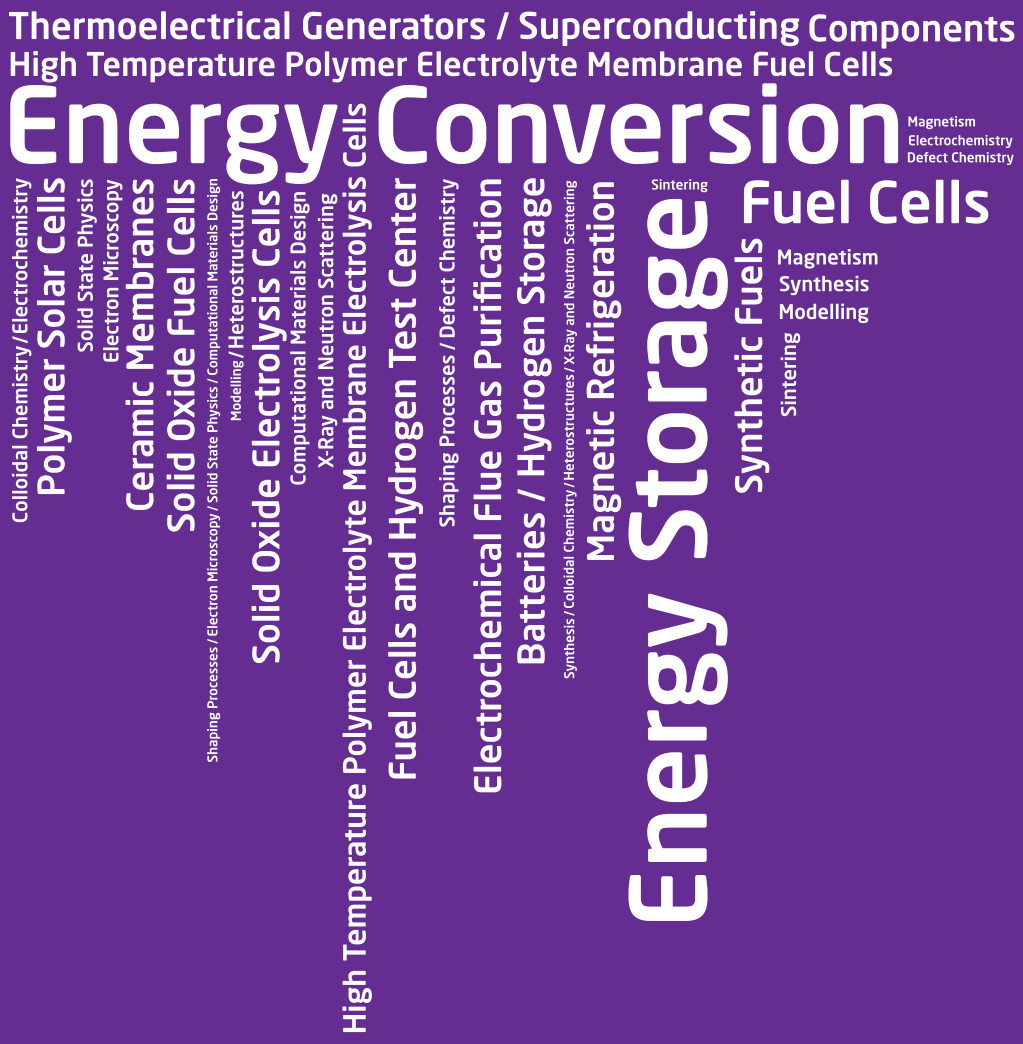

Department of Energy Conversion and Storage
Technical University of Denmark
Risø Campus
Frederiksborgvej 399
4000 Roskilde
Denmark
www.ecs.dtu.dk

ISBN 978-87-92986-06-1